University of Southampton

Faculty of Engineering and Physical Sciences

School of Electronics and Computer Science

Development and Validation of Optical Models for Predicting Solar Irradiance in Temperate Climates

by

Yazan J.K. Musleh

Thesis for the degree of Doctor of Philosophy in Electronic and Electrical Engineering

May 2025

University of Southampton

Abstract

Faculty of Engineering and Physical Sciences

School of Electronics and Computer Science

Thesis for the degree of Doctor of Philosophy

Development and Validation of Optical Models for Predicting Solar Irradiance Estimates in Temperate Climates

by

Yazan J.K. Musleh

As the global energy landscape shifts toward renewable sources, particularly photovoltaic (PV) technology, PV installations are expanding rapidly, covering larger areas and integrating advanced innovations. This growth poses new challenges for feasibility software used to evaluate solar projects, especially as diverse regions adopt emerging PV technologies. Accurate solar irradiance prediction plays a crucial role in ensuring the reliability of feasibility assessments and financial forecasting, as these predictions form the backbone of feasibility software's performance. This research delves into advanced PV technologies, including bifacial panels, tracking systems, and AgriPhotovoltaics (AgriPV), focusing on their behavior under the dynamic sky conditions typical of temperate climates, with high-resolution, minute-by-minute irradiance measurements. A major focus of this work is the evaluation of feasibility software limitations, specifically in its ability to estimate Diffuse Horizontal Irradiance (DHI) and Direct Normal Irradiance (DNI) from Global Horizontal Irradiance (GHI) using decomposition models, as well as its transposition models for calculating Plane of Array (POA) irradiance.

The contributions of this research are fourfold: firstly, this thesis develops a robust benchmarking framework to evaluate decomposition models using tests for temporal resolution, spatial homogeneity, and the influence of dataset periods. Since many locations lack dedicated weather stations for DHI and DNI measurements, such as the case study in the UK, this framework becomes essential. Initially, 5 decomposition models were identified as robust. To broaden the range, this research introduces the effect of clear-sky GHI (GHI_{Clear}) by altering 10 variations, expanding the pool of viable models from 5 to 15. Secondly, through the separation of sky conditions into clear, intermediate, and overcast days, the study evaluates the performance of transposition models within feasibility software. The DISC decomposition model, when paired with the Skartveit-Olseth (SO) transposition model, demonstrated consistent performance for both a fixed-tilt (FT) system at 55 degrees and a tracking system. Additional testing, using six distinct cloud intervals and feeding in measured GHI, DHI, and DHI, further confirmed the robustness of the SO model. Thirdly, work in this thesis assesses the reliability of six clear-sky irradiance model iterations using data from 67 global stations and different data sources, including measured values from AErosol RObotic NETwork (AERONET), Modern-Era Retrospective analysis for Research and Applications, Version 2 (MERRA2), and Copernicus Atmosphere Monitoring Service (CAMS). The analysis focuses on key atmospheric parameters such as precipitable water (PW), the Ångström exponent (AE), and Aerosol Optical Depth at 550 nm (AOD550). MERRA-2 data outperformed CAMS in all 3 parameter estimations and was second only to AERONET's measured data when coupled with the REST2 proprietary model. Among open-access model services, McClear proved superior to ERA5, making it the most reliable option.

Lastly, with the growing adoption of AgriPV systems, there is an increasing demand for accurate estimation of Photosynthetically Active Radiation (PAR) irradiance, a critical aspect currently underrepresented in existing feasibility software for AgriPV applications. A new model, the Musleh-Rahman (MR) model, is introduced to accurately predict PAR in temperate climates using easily accessible input parameters. This model is designed to enhance the accuracy of PAR estimations and was benchmarked against 10 other PAR models, outperforming them all. The combined findings of this research provide a foundation for enhancing sub-hourly irradiance prediction accuracy. These insights are expected to support the PV industry's expansion into new regions and facilitate the seamless integration of advanced PV technologies into feasibility software, ultimately driving the growth of renewable energy deployment.

Table of Contents

Table of Tables

Table of Figures

Research Thesis: Declaration of Authorship

Print name:

Title of thesis:

I declare that this thesis and the work presented in it are my own and has been generated by me as the result of my own original research.

I confirm that:

1. This work was done wholly or mainly while in candidature for a research degree at this University;
2. Where any part of this thesis has previously been submitted for a degree or any other qualification at this University or any other institution, this has been clearly stated;
3. Where I have consulted the published work of others, this is always clearly attributed;
4. Where I have quoted from the work of others, the source is always given. With the exception of such quotations, this thesis is entirely my own work;
5. I have acknowledged all main sources of help;
6. Where the thesis is based on work done by myself jointly with others, I have made clear exactly what was done by others and what I have contributed myself;
7. #Delete as appropriate#None of this work has been published before submission #or# Parts of this work have been published as:- #please list references below#

[Add references here] #otherwise delete#

Signature: ..... Date:.....

#Important note:

The completed signed and dated copy of this form should be included in your print thesis.

A completed and dated but unsigned copy should be included in your PDF/A-3 thesis#

Acknowledgements

Firstly, I would like to express my sincere appreciation and respect for the tremendous support and guidance that my supervisory team has kindly provided throughout my journey. Their unwavering encouragement and expert advice have been pivotal to my development. Dr. Tasmiat Rahman has been exceptionally generous and supportive since the beginning of my time as his PhD student. His willingness to entrust me to be his first PhD student alongside having faith in me in leading the team that established the pioneering outdoor testing facility, speaks volumes about his faith in my abilities. I am immensely grateful for his consistent support in both my professional and personal life - his guidance has been a cornerstone of my academic journey. Similarly, Dr. Stuart A. Boden has provided invaluable mentorship and support. His insights and advice have been crucial not only to my PhD research but also to my personal development. His calm demeanour and thoughtful guidance have been a tremendous source of comfort and inspiration. *Tas* and *Stuart*, since joining in September 2021, you have been more than supervisors to me; you have become mentors and friends. Thank you ever so much to both of you - I deeply appreciate your kindness and consider myself fortunate to have such a wonderful PhD journey with you two.

Words cannot describe how grateful I am for the invaluable contributions and collaboration from Dr. Carlos D. Rodríguez-Gallegos of RINA Tech Renewable in Australia, and Dr. Christian A. Gueymard from Solar Consulting Services in the USA. Working with such esteemed experts has been both an honour and a profoundly enriching experience. *Carlos* and *Chris* - collaborating with you has been incredibly meaningful, and I value the chance we had to contribute to our field together. Additionally, my sincere thanks go to Dr. Silvana Oviatt from the National Renewable Energy Laboratory in the USA. I first met her at BifiPV 2022 in Ankara, and we've stayed in touch ever since. Her insightful responses to my questions and her unwavering support across our conversations have been truly invaluable. Thanks *Silvana*!

I am immensely thankful to Corrie Energy Partners and especially Dr. Jonathan Fleming for providing their trackers for my data collection efforts. I would also like to express my gratitude to Mr. Anthony Duffin and Mr. Thomas Duffin for their ongoing support and engaging discussions about my research. *Tony* and *Tom*, thank you for not only being mentors but also a dear friends, and for the memorable visits to the Oxford Farm Shop where I could see the operations of your trackers firsthand. At Chilbolton, my appreciation extends to Mr. Darcy Ladd for his generosity, and to Dr. Keith Dumbell and Dr. Christopher Walden for their assistance with data access. Their help has been invaluable in advancing my work. Thank you, *Darcy*, *Keith,* and *Chris*.

Prof. Harold Chong, Mrs. Laura Everett, and Prof Paolo Rapisarda have been ever so nice to me during my PhD - a special thank you to them. *Harold*, you graciously shared invaluable insights

about pursuing a PhD, which were incredibly inspiring even outside my specific field of study. *Laura*, your outstanding warmth and kindness have made you an indispensable pillar of our administrative team. Your welcoming presence consistently fosters a positive atmosphere. *Paolo*, many thanks for your kindness in allowing me to lead the mathematics demonstrations and for our occasional chats about our shared passion for Italian football (calcio). Furthermore, I extend my heartfelt thanks to Prof. Rishad Shafik and Dr. Martin Johnston of Newcastle University. *Rishad* and *Martin*, your warm welcome during my return visit to the cherished Geordie-land, along with the priceless guidance they offered regarding my PhD pursuits, has made a profound impact.

The steadfast support of my childhood friends in Doha and the friendships I built during my time at university in Newcastle have been a foundation of strength throughout my journey. They have celebrated each of my achievements with genuine joy and provided steady emotional support during the toughest moments of my PhD. Their belief in me has been a powerful source of motivation, helping me navigate challenges with resilience and confidence. But their impact goes beyond words of encouragement - the memories we have shared through trips, gaming marathons, and long conversations have been a source of joy and strength. Even with many miles between us, their frequent check-ins have brought immense comfort and a sense of closeness that has enriched my journey, reminding me of our shared experiences and aspirations.

I am truly grateful to have friends like them, and as much as it may sound like a cliché, I genuinely believe I would not have made it this far without them. There's a saying in Arabic (الصديق وقت الضيق): *a friend in need is a friend indeed* - and these past few years have been living proof of that. I type this with a full heart, knowing how blessed I am to have their friendship. When things got difficult and I felt overwhelmed, they would always check in at just the right moment, cheering me on and telling me how proud they were of me. I love each and every one of them, and this journey wouldn't have been possible without their presence in my life.

I would also like to express my heartfelt gratitude to my beloved football club, AC Milan. Being a *Rossonero* has taught me the virtues of patience, resilience, and hard work - qualities embodied by the club, often seen as a sleeping giant, just as my PhD journey has felt at times. I vividly recall my first year, the most challenging period of my PhD, where I found solace in dedicating my weekends to watching you play. The joy you brought me when you won the Scudetto was immeasurable. Watching my favourite players push forward with relentless determination ignited within me the motivation and passion I needed to persevere through the tough times. I began my PhD journey with you lifting the Italian league title, and now, as I reach the end of this chapter, you have crowned the journey with another victory to be the Supercoppa Italiana champions. We began with shared success, and now, as you've done your part, I am doing mine - culminating in

the submission and defence of this PhD. Thank you for being my constant companion and inspiration along the way.

Above all, my deepest gratitude is extended to my family - my beloved parents and my supportive brother, whose unwavering presence and encouragement have been a beacon of hope and guidance. During the toughest times, when the path ahead seemed clouded with uncertainty, their profound empathy and consistent support were the forces that lit my way and strengthened my resolve to continue. My mother, Hiba Abu-Al Ragheb, has been an inexhaustible source of love and comfort. *Ommi*, your presence, even from a distance, has been a constant embrace, wrapping me in the warmth and security of home. Your nurturing words and boundless affection have been my sanctuary, guiding me through challenges with grace and resilience. You are the epitome of unconditional love, and truly the best mother a son could ever hope for. My father, Jihad Kamil Musleh, the person I admire the most, has always been a pillar of wisdom. *Abooy*, your advice, frequent check-ins, and unconditional love have not only helped me achieve my dreams but also fulfill your aspirations of seeing your eldest son pursue advanced education up to the PhD level - a proud milestone for our family. Abdullah Jihad Kamil Musleh, my cherished brother, has always been there with his straightforward and honest advice when I needed it most. *Abood akhoy*, your support and love have been a source of comfort and pride, knowing you are also proud of my achievements.

Together, my family's contributions have shaped my journey, providing a foundation of love and support that has enabled me to strive for and achieve my academic and personal goals. Mum, Dad, and Abdullah - your daily photos of our cats, Iz and Looli, brought so much joy and support throughout this process. Also, your profound understanding and encouraging words have not only sustained me but also given me the strength to persevere against all challenges. The influence you've had on my journey is beyond measure, and for that, I am eternally grateful.

I want to take a moment to recognise the resilience that has carried me through this journey. Along the way, I encountered countless challenges that tested my limits and often left me feeling overwhelmed. There were moments when it seemed as though obstacles were deliberately placed to block my path. Yet, despite the struggles, I tapped into a well of inner strength, confronting each hurdle with persistence (and lifting my spirits with a lot of Coldplay!). This PhD was never just about achieving a goal; it was about growing through the challenges that shaped my journey. I am truly proud of my ability to press on and progress, even when the odds seemed against me.

Walking daily to university through Southampton Common, I would often lose myself in thought, gazing at the trees and reflecting on where I could summon the strength to endure the toughest moments. These past three and a half years have been more challenging than words could ever

fully convey. There were times when I found myself almost in tears, desperately calling upon the fire within to reignite. Yet, the fact that I stayed the course despite these challenges is an achievement I deeply cherish. This resilience, hard-earned through countless trials, is a reflection of my character. For me, acknowledging this growth is essential, as it highlights the personal strength and determination that have been just as meaningful as any milestone I have reached.

In closing, I dedicate this work to my beloved uncle, Zahed Abu-Al Ragheb, who left us during my doctoral journey. Throughout my studies, he was a steady source of encouragement, always radiating positivity and lifting me up whenever I needed it. *Khalo Zahed*, I hope you're looking down with a smile, knowing I finally achieved this. This accomplishment is in honour of you.

To Khalo Zahed, this is for you.

Nomenclature

AE	Ångström exponent
$AM1.5$	Air Mass for the standard terrestrial solar spectrum
$AOD(\lambda)$	Aerosol Optical Depth at a specific wavelength
$AOD550$	Aerosol Optical Depth at 500nm
AOI	Angle of Incidence (Degrees)
$Area_{All}$	Total Area (m^2)
$Area_{shaded}$	Total shaded Area caused by solar panels (m^2)
$Area_{unshaded}$	Total unshaded Area (m^2)
BG_{Energy}	Energy Bifacial Gain
BG_{irr}	Irradiance Bifacial Gain
BOA	Back of Array Irradiance (W/m^2)
CW	Collector Width of the total Solar Panels within a row (m)
DHI	Diffuse Horizontal Irradiance (W/m^2)
DNI	Direct Normal Irradiance (W/m^2)
DNI_{Clear}	Clear-Sky Direct Normal Irradiance (W/m^2)
$dPAR$	Diffuse Photosynthetically Active Radiation (W/m^2)
E_a	Extraterrestrial Horizontal Irradiance (W/m^2)
E_{Bifi}	Energy Produced by a bifacial system (Wh)
E_{mono}	Energy Produced by a monofacial system (Wh)
$elev$	Site elevation above sea level (m)

GHI	Global Horizontal Irradiance (W/m^2)
GHI_{Clear}	Clear-Sky Global Horizontal Irradiance (W/m^2)
GHI_{cda}	Clean, and dry Global Horizontal Irradiance (W/m^2)
G_{STC}	Irradiance under standard testing conditions (W/m^2)
h	Elevation height of a module (m)
k	Extinction coefficient (nm)
K_d	Diffusion Fraction
K_t	Sky Clearness Index
MAD	Mean Absolute Deviation (%)
$NO2$	Total Nitrogen Dioxide amount (cm)
$Ozone$	Total Ozone amount (cm)
PAR	Photosynthetically Active Radiation (W/m^2)
P	Pressure (mbar)
P_{IDEAL}	Dataset DC Power at standard testing conditions (W)
P_{SYSTEM}	DC Power of the modules (W)
$P_{max-front}$	Rear side Power of a bifacial module (W)
$P_{max-rear}$	Front side Power of a bifacial module (W)
POA	Plane of Array Irradiance (W/m^2)
PPF	Photosynthetic Photon Flux (µmol/m^2/s)
PR	Performance Ratio
PW	Precipitable Water (cm)
SSA	Single Scattering Albedo

STC	Standard Testing Conditions
SZA	Solar Zenith Angle (Degrees)
ψ_{sun}	Solar Azimuth (Degrees)
ψ_{system}	System Azimuth (Degrees)
R_d	Transposition Factor
RHI	Reflected Horizontal Irradiance (W/m^2)
R^2	Coefficient of Determination
ρ	Albedo
T	Temperature (K)
T_d	Dewpoint Temperature (ºC)
T_L	Linke Turbidity Factor
α	Solar Altitude (Degrees)
β	System Tilt (Degrees)
δ	Solar Declination (Degrees)
Δ	Perez Sky Brightness Coefficient
ε	Perez Sky Clearness Coefficient
φ	Latitude of Location (Degrees)
λ	Wavelength (nm)
ω	Hour Angle (Degrees)
τ	Broadband Optical Depth
Φ_{bifi}	Bifaciality Factor
f_{Hay}	Hay Modulation Factor

$f_{Hay\ 1993}$	Hay-1993 Modulation Factor
f_K	Klucher Modulation Factor
f_R	Reindl Modulation Factor
B_t	Beam Tilted Irradiance Component
D_t	Diffuse Tilted Irradiance Component
R_t	Reflected Tilted Irradiance Component

Abbreviations

AATSR ..... Advanced Along-Track Scanning Radiometer

AERONET ..... Aerosol RObotic NETwork

AgriPV ..... Agricultural Photovoltaics

AM ..... Air mass

ASTM G173..... American Society for Testing Materials G173 Spectra

AVHRR ..... Advanced Very High Resolution Radiometer

BSRN ..... Baseline Surface Radiation Network

CAELUS ..... Classification Algorithm for the Evaluation of cLoUdiness Situations

CAMS..... Copernicus Atmosphere Monitoring Service

CEDA ..... Centre for Environmental Data Analysis

CIE..... International Commission on Illumination

CSD ..... Clear-Sky Detection

DAT..... Dual Axis Tracking

ECMWF..... European Centre for Medium-Range Weather Forecasts

FT..... Fixed-Tilt

HPC ..... High-Performance Computing

HSAT..... Horizontal Single Axis Tracking

IEA ..... International Energy Agency

IEC..... International Electrotechnical Commission

ICOS ..... Integrated Carbon Observation System

IPCC ..... Intergovernmental Panel on Climate Change

IRENA ..... International Renewable Energy Agency

ISO..... International Organization for Standardization

ITRPV ..... International Technology Roadmap for Photovoltaics

LCOE..... Levelized Cost of Electricity

LER ..... Land Equivalent Ratio

LJ ..... Liu-Jordan

ML..... Machine Learning

MERRA-2..... Modern-Era Retrospective analysis for Research and Applications, Version 2

MISR ..... Multi-angle Imaging SpectroRadiometer

MODIS ..... Moderate Resolution Imaging Spectroradiometer

MR ..... Musleh-Rahman

PV ..... Photovoltaics

RT ..... Ray-Tracing

Si ..... Silicon

SMARTS ..... Simple Model for the Atmospheric Radiative Transfer of Sunshine

SO..... Skartveit-Olseth

SPA ..... Solar Position Algorithm

TBO ..... Tracking-the-Best-Orientation

TC ..... Temps-Couslon

TS..... Tracking-the-Sun

UTC..... Coordinated Universal Time

VF ..... View-Factor

Chapter 1 Introduction

1.1 Motivation

An expanding global population and geopolitical disputes are causing a pressing energy crisis. Alternative sources of energy are needed to meet this growing demand. A viable alternative is necessary due to the limited nature of finite sources and the emission of excessive amounts of carbon. It has become increasingly important to find abundant yet sustainable alternative sources of energy to satisfy such extensive demand. In order to adhere to the 1.5°C cap goal set forth by the Paris Agreement [1], carbon dioxide emissions must decrease by 45% prior to 2030. Furthermore, the Intergovernmental Panel on Climate Change (IPCC) [2] highlights the necessity for renewable energy to comprise a minimum of 70% of the energy supply by 2050. A shift from fossil fuels will be facilitated by the growth and widespread adoption of renewable energy solutions within industrial, commercial, and residential domains.

Despite perceptions that the volatile energy market has a high degree of competitiveness, renewable sources of energy are gaining a foothold [3]. Solar energy, hailing from the sun's virtually limitless reserves, is instrumental in mitigating the escalation of average global temperatures. Solar panels work on the principle of photovoltaics (PV), in which sunlight is converted into electricity by using semiconductors, typically silicon (Si), that absorb photons through transitions of electrons across an energy gap. The International Energy Agency (IEA) stated that certain solar power projects deliver historic cost-effective electricity [4], making PV one of the most affordable and environmentally friendly energy sources available.

In examining the global landscape of PV technology, a historical overview reveals noteworthy growth in solar energy adoption. According to data from the International Renewable Energy Agency (IRENA), solar capacity experienced a significant increase from 175,039 MW in 2014 to 1,411,139 MW by the end of 2023, surpassing the 1 TW mark [5]. This expansion means that solar energy now represents over a quarter of the global installed renewable energy capacity, comprising more than 36% of all renewable energy installations [5]. There are several factors that have contributed to such expansions, ranging from government policies to incentives, aiding in the broader adoption of solar energy.

Temperate climates, known for their fluctuating sunlight and predominantly diffuse irradiance, pose distinctive challenges for the adoption of PV systems. Nonetheless, these regions also offer substantial opportunities for integrating solar energy into the national energy framework. Within

the framework of its new British Energy Security Strategy, the UK aims to build a cumulative solar PV capacity of 70 GW by 2035 [6]. Yet, despite a consistent increase, the growth rate observed over the past decade suggests that by 2035, the actual capacity may only slightly exceed 27 GW. This would leave the UK more than 42 GW below its ambitious target. Therefore, it is crucial to promote the adoption of advanced PV technologies to accelerate the expansion of solar capacity, a step that must be taken promptly.

The advent of bifacial solar technology, which utilizes advanced cell technologies to capture irradiance simultaneously from the front and the rear, coupled with tracking solutions, may provide solutions to these climatic challenges [7]. Moreover, these advancements may prove instrumental in supporting the UK's ambitious target of 70GW. By harnessing the potential of breakthrough solar technologies, the UK can solidify the position of solar power in its renewable energy landscape and achieve its goals.

Recent advancements in PV technology have positioned bifacial solar panels as potential disruptors in the market, poised to challenge the dominance of traditional single-sided modules. According to the 15th edition of the International Technology Roadmap for Photovoltaics (ITRPV), bifacial modules currently command approximately 63% market share. This figure is expected to increase by an additional 10%, reaching 73% over the next decade. The same edition of ITRPV predicted that tracking solutions would also be used in more than 55% of PV systems by 2030 [8]. Tracker systems that adjust module orientation with respect to the sun's motion are proving to be effective at improving module performance. Furthermore, such solutions may decrease the number of modules required per kWh of output [9]. This development is especially critical due to the high costs and limited availability of land - a challenge that Agricultural Photovoltaics (AgriPV), which combines agriculture with photovoltaics, regularly encounters [10]. Projections from the ITRPV 2024 indicate that AgriPV is poised to secure a growing portion of the market [8].

Despite advances in PV technologies, there remains a significant gap in research concerning the validity of optical models for irradiance estimation in temperate climates. This gap is primarily due to the complex dynamics of light harvesting, which complicates the optimization of bifacial PV and AgriPV technologies. Without robust validation of these models, particularly in temperate regions, the broader adoption of diverse PV technologies could be impeded.

Currently, a variety of prediction models, ranging from empirical to physical, are employed within different simulation software to estimate irradiance on PV modules [9][11], including the rear side for bifacial modules, and the irradiance utilized by plants for photosynthesis. Accurate irradiance estimations are crucial as they serve as a foundational metric that attracts investor interest [11].

Most models have been developed (and thus validated) using daily or hourly irradiance measurements. However, there is a pressing need to predict irradiance on a minute-minute scale as it provides more precise information on the variability and quality of solar irradiance, enabling more reliable PV power output estimations [12][13][14] and performance metrics [15]. Such data offer a more accurate reflection of weather conditions and events that may impact PV systems and provide enhanced information for the optimal control and management of PV systems [16]. If the temporal resolution of solar resource data is too coarse, such as hourly or daily, it will fail to capture short-term fluctuations or peaks in solar irradiance, which can significantly affect a project's energy production and financial returns. Consequently, 1-minute solar resource data are vital for financiers to secure realistic and dependable estimates of energy production and the profitability of solar projects, as they capture the variability and frequency distribution of solar irradiance, influencing the revenue of PV projects [12][17].

There is an urgent need to refine the precision of solar irradiance models within temperate climates through diligent development and comprehensive validation of new empirical methods. Accurate solar irradiance estimations are crucial inputs for feasibility software, which drives the bankability and viability of PV farms. Feasibility software serves as a critical tool for engineers, enabling them to design, simulate and analyse the performance of various PV systems. Feasability software assist in evaluating both the technical and financial potential of a project by modelling expected energy production. They also help users optimise system configurations, estimate energy yields, and carry out in-depth performance assessments, ultimately supporting informed decision-making prior to project deployment. A variety of feasibility tools are available, each offering different levels of complexity and tailored to meet diverse project requirements. These estimations not only inform technological choices and project design but also pinpoint primary sources of uncertainty in energy production forecasts, impacting financing conditions and investment returns. Thus, validating and integrating diverse irradiance estimation models with commercially available software on a minute-by-minute basis is essential. Failure to address these needs could hinder the widespread implementation of these technologies in such climates.

1.2 Aims and Objectives

The primary goal of this research is to boost the integration of solar energy within the energy market. This goal is pursued by enhancing the accuracy of solar irradiance estimates, which are essential for evaluating the performance of PV systems. These refined estimates are incorporated into widely used feasibility software employed to inform investment. The research focuses on

improving the precision of solar irradiance models in temperate climates through rigorous development and comprehensive validation of new empirical methods. By providing a robust and validated approach to estimating solar irradiance, applicable across a range of technologies - from traditional fixed-tilt to innovative bifacial and AgriPV systems - this study aims to strengthen investor confidence in these emerging technologies, particularly in regions like the UK.

To achieve this, this research will involve on validating optical models to enhance the selection of appropriate solar irradiance models for use in temperate climates. The methodology will explore the limitations of current optical models integrated into feasibility software and aim to improve these models through the identification and rectification of prevalent errors. All assessments will be conducted on a minute-by-minute scale to ensure precision. The outcomes of this study are expected to serve as crucial tools for model validation in temperate climates and will provide a necessary framework that can be adapted for use in other climatic conditions. Additionally, this work will establish a benchmark that can guide technological advancements in the field. As a result, the experimental methodology will be employed to achieve the following objectives:

1. Develop a comprehensive framework for a series of tests designed to evaluate and select optimal methods for solar irradiance components.
2. Validate and quantify current solar irradiance models, including decomposition and transposition methods, to identify and thoroughly document their limitations.
3. Strengthen the precision and reliability of clear-sky irradiance models by employing varied satellite data sources.
4. Construct a predictive model for photosynthetically active radiation irradiance, incorporating innovative and readily available input parameters.

1.3 Overview of Research Contributions

The following are portions of this work that have been presented to the wider scientific community in various forms:

Journal Paper Publications:

- Y. J. K. Musleh and T. Rahman, "Predictive models for photosynthetic active radiation irradiance in temperate climates," Renewable and Sustainable Energy Reviews, vol. 200. Elsevier BV, p. 114599, Aug. 2024. doi: 10.1016/j.rser.2024.114599.
- Y. J. K. Musleh, W. Herring, C. D. Rodríguez-Gallegos, S. A. Boden and T. Rahman, "Subhourly Error Analysis of Decomposition–Transposition Model Pairs for Temperate Climates," in *IEEE Journal of Photovoltaics*, vol. 15, no. 1, pp. 164-172, Jan. 2025, doi: 10.1109/JPHOTOV.2024.3483262
- Y. J. K. Musleh, C.A. Gueymard and T. Rahman, "Worldwide impacts of satellite-based atmospheric conditions on solar irradiance modelling." *Under Preparation*.

Oral Presentations

- Y. J. K. Musleh, S.A. Boden and T. Rahman, "A Comprehensive Examination of Decomposition Models for Solar Radiation Forecasting in Temperate Climates." 17th Photovoltaic Science, Application and Technology Conference, London, England, 2023.
- Y. J. K. Musleh, S.A. Boden and T. Rahman, "Irradiance Estimation for Vertical Bifacial AgriPV Systems: Integrating Regression Analysis and Decomposition-Transposition Matrix in the UK Context." Photovoltaic Science, Application and Technology Conference 2024, Glasgow, Scotland, 2024.
- Y. J. K. Musleh, S.A. Boden and T. Rahman, "Analyzing Bifacial AgriPV Systems in Temperate Climates with Advanced Mathematical Modelling for Irradiance Estimation." BifiPV 24 Conference, Chambéry, France, 2024.

Poster Presentations:

- Y. J. K. Musleh, S.A. Boden and T. Rahman, "Developing Outdoor Testing Equipment for Insolation Measurement of Bifacial Solar Tracking Systems", 16th Photovoltaic Science, Application and Technology Conference (PVSAT-16), Salford, England, 2022.
- Y. J. K. Musleh, S.A. Boden and T. Rahman, "Developing Outdoor Testing Equipment for Insolation Measurement of Bifacial Solar Tracking Systems", Institute of Physics: Advances in Photovoltaics, London, England, 2022.
- Y. J. K. Musleh, S.A. Boden and T. Rahman, "An Empirical Study of the Plane-Of-Array and Back-Of-Array Solar Irradiance of a Dual-Axis Tracker in Oxford, UK", BifiPV 22 Conference, Ankara, Türkiye, 2022.
- Y. J. K. Musleh, S.A. Boden and T. Rahman, "An Empirical Study of the Plane-Of-Array and Back-Of-Array Solar Irradiance of a Dual-Axis Tracker in Oxford, UK", Institute of Physics: Advances in Photovoltaics, London, England, 2022.

1.4 Structure of Report

Chapter 2 presents a comprehensive review of the existing literature and provides a theoretical background on solar irradiance resource assessment. It discusses the fundamental principles of solar irradiance and emphasizes the significance of accurate estimation methods. This chapter also outlines prior studies on the mathematical modelling of irradiance, including decomposition, transposition, and clear-sky models, and explores their application in bifacial, tracking, and AgriPV systems. The methodology for assessing solar resources is introduced, establishing a clear benchmarking framework for selecting solar irradiance estimates in Chapter 3. This framework aims to enhance the accuracy and reliability of solar resource assessments. Chapter 4 delves into the limitations of current models in the context of decomposition and transposition. It examines the application of model pairs in feasibility software and discusses the dynamics of transposition techniques for predicting PV performance based on measured irradiance inputs. Chapters 5 and 6 focus on refining models and introducing new methodologies. Chapter 5 evaluates predictions of clear-sky irradiance, considering both measured and modelled atmospheric data by assessing the sources of satellite data. Chapter 6 introduces an empirical model for estimating Photosynthetically Active Radiation (PAR) irradiance and develops a new mathematical model tailored for temperate climates using readily available data, moving away from reliance on extensive measurements. Finally, Chapter 7 summarizes the findings, draws conclusions, and identifies areas for future research, aiming to further advance the field of solar irradiance assessment.

Chapter 2 Theoretical Background and Review of Related Literature

2.1 Foundations of Solar Irradiance

2.1.1 Comprehending the Solar Resource

Climate conditions vary globally due to differences in temperature, weather patterns, and geographical positioning. These all affect solar irradiance levels based on the sun's path and other variables [18]. The Köppen-Geiger climate classification system categorizes global land climates into five primary groups using thresholds related to air temperature and precipitation levels. This classification provides a structured approach to simplifying complex climate data into actionable insights.

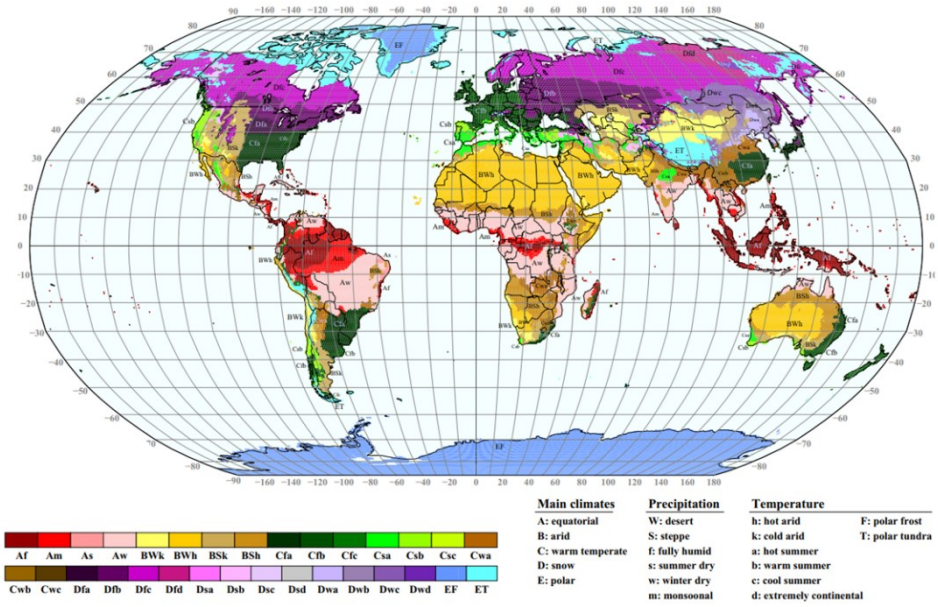

Figure 1: The Köppen-Geiger climate map is provided with a spatial resolution of 0.5º, adapted from [18].

The Köppen-Geiger system employs a three-letter code, as per Figure 1, to define climatic zones based on temperature, precipitation, and their seasonal occurrences. Each letter refines the classification further: the first letter indicates the main climate type, with "C" representing temperate climates where the warmest month has an average temperature that exceeds 10ºC and the coldest month's average temperature ranges between -3ºC to 18ºC. The subsequent letters describe precipitation and temperature patterns. For example, much of the UK is

classified under "Cfb," indicating a temperate climate with no dry season and mild summers where the warmest month's average temperature remains below 22 ºC.

It is crucial to comprehend the sun's movement in relation to a site location, as this knowledge is vital for maximizing a PV system installation's performance. This movement is described by a two-dimensional coordinate system consisting of azimuth, ψ and altitude angles, α [19].

$$\cos\psi = \cos\varphi \cdot \sin\delta - \cos\omega \cdot \cos\delta \cdot \sin\varphi \quad (1)$$

$$\alpha = 90 + \varphi - \delta \quad (2)$$

Here, ψ, signifies the angle between the sun and the north axis in a clockwise direction. This angle can be calculated using Equation 1, which incorporates trigonometric functions that involve the location's latitude φ, the declination angle δ, and the hour angle ω. α, represents the angle between the horizon and the center of the solar disc, as shown in Equation 2 [19].

An alternative method for pinpointing the sun's position involves the zenith angle, SZA, which is the angle between the sun's disc and a vertical line (see Figure 2). This angle is a 90-degree phase shift from α due to its basis on the orthogonal axis, as outlined in equation 3. Determining SZA is crucial for estimating the solar radiation that reaches the Earth's atmosphere across a range of solar configurations [20].

$$\cos SZA = \sin\alpha \quad (3)$$

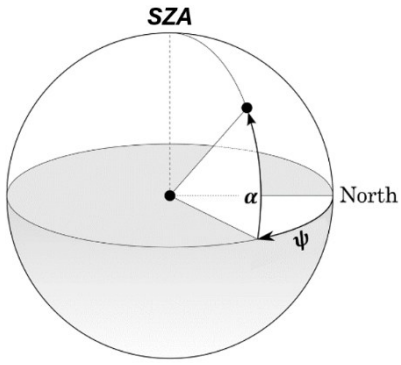

Figure 2: A two-dimensional coordinate system represents the assortment of solar angles. Adapted from [20].

Here, φ and time of year significantly impact ψ, α, and subsequently SZA, due to the sun's path [21]. The sun's trajectory changes more drastically at higher φ, as depicted in Figure 3. In such locations, during the summer solstice, the ψ range expands, and the α range ascends higher in the sky, which results in extended daylight exposure. In contrast, during the winter solstice, the

sun's path becomes compressed as a result of ψ and α becoming more limited, leading to reduce sunlight hours. At the equator, while the solar declination angle oscillates between ±23.45º, the sun's apparent movement remains relatively symmetrical across both the northern and southern hemispheres. As a result, seasonal fluctuations in sunlight duration and intensity are significantly less pronounced than at higher latitudes. A precise comprehension of the sun's path is crucial for assessing PV systems performance [7], as it directly influences the design and optimisation of tracking systems.

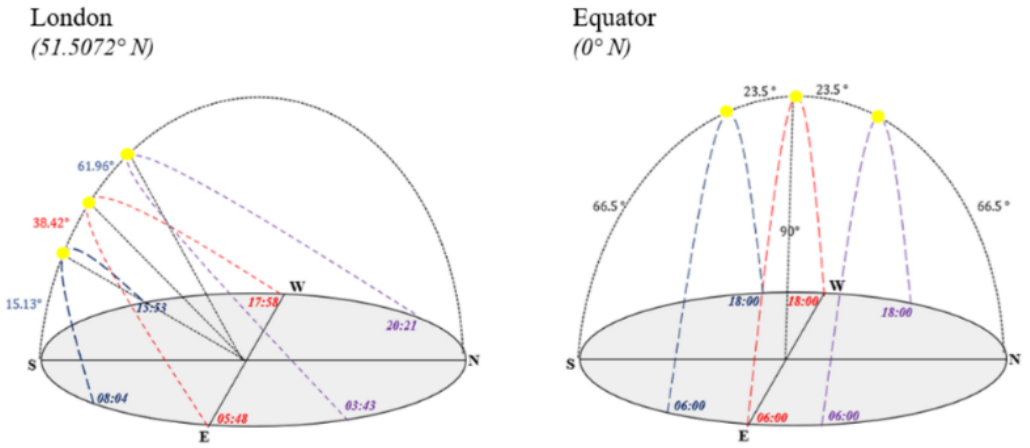

Figure 3: Trajectory of the sun throughout the winter, summer, and spring solstices observed in London and at the equator.

The location of a site influences the optical air mass (AM), which denotes the path length of the direct beam traversing the atmosphere compared to the overhead sun [20]. AM0 pertains to the irradiance at the atmosphere's apex, and AM1.5 (conforming to the ASTM G173 standard [22]) is a crucial component of standard testing conditions (STC) employed to rate PV modules [23]. This particular value is utilized as a standard due to its representation of the annual average for mid-φ regions, as determined through an analysis of solar irradiance data in the US. Referring to Figure 4, the ASTM G173 AM1.5 spectrum can be observed, showcasing dips at specific wavelength values. These dips occur due to Fraunhofer lines, a collection of spectral absorption lines resulting from gas absorption in the photosphere and absorption in the atmosphere [24]. These lines are crucial in understanding the composition of the sun and the way solar radiation interacts with the Earth's atmosphere. The presence of these lines can influence the performance of PV modules, which is essential to consider during system design.

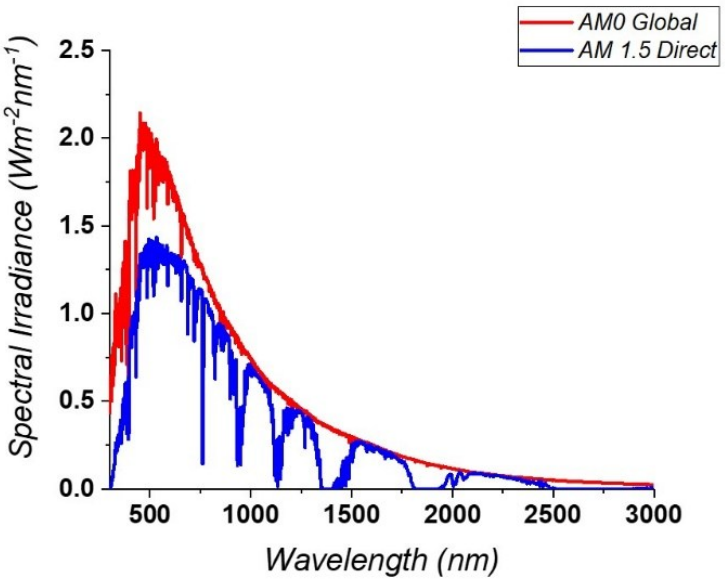

Figure 4: Solar extraterrestrial spectrum (in red) and the direct solar irradiance at the ground, ASTM G173 AM1.5 (in blue) using SMARTS software [25].

Possessing an understanding of the irradiance is critical. Such information is procured either through terrestrial observations from local meteorological stations or via satellite-derived data [26][27]. Focusing on temperate regions, satellite data exhibits diminished accuracy due to persistent cloud formations, rendering it less suitable [28]. It may also be outdated.

Solar irradiance can be segregated into three components. Direct Normal Irradiance (DNI) refers to the component of solar radiation that strikes a surface positioned perpendicularly (normal) to the sun's rays. It represents sunlight that reaches the surface directly from the solar disk, without undergoing scattering. DNI transpires when sun rays are traveling directly from the position of the sun. Diffuse Horizontal Irradiance (DHI) represents the quantity of irradiance dispersed by atmospheric elements such as clouds, or aerosols, rather than emanating directly from the sun. Global Horizontal Irradiance (GHI) is received by a surface oriented parallel to the ground, encompassing both DHI and DNI as constituents, as mathematically illustrated in the closure equation (equation 4) [29]:

$$\mathrm{GHI} = \mathrm{DHI} + \mathrm{DNI}\cos(SZA) \tag{4}$$

Solar irradiance overall spans a wide range of wavelengths, covering the ultraviolet, visible and infrared regions of the spectrum. This spectral distribution plays a critical role in the performance of PV systems, as different materials absorb and convert solar energy with varying efficiencies across different parts of the spectrum. Irradiance varies with the time of day due to sunlight reflection angles and the influence of Earth's atmosphere on light transmission. Solar noon, when the sun reaches its highest α, exhibits a peak in irradiance as sunlight traverses the minimal

atmospheric distance and experiences the least reflection. Conversely, during early mornings and late afternoons, SZA is near its maximum, the sun resides at its lowest α, and an increased quantity of light is reflected.

Moreover, there are additional components of solar irradiance that are important in the solar resource, which use different combinations of GHI, DHI and DNI. Irradiance reaching the surface of a module is known as Plane-Of-Array (POA) irradiance, a critical metric for evaluating system performance of PV [7][9][30]. Conversely, Back-Of-Array (BOA) irradiance refers to the irradiance that impacts the rear surface of a PV module. As the AgriPV sector expands its market presence, it becomes essential to measure the irradiance suitable for plant growth, termed Photosynthetically Active Radiation (PAR) [31]. Similar to GHI, PAR comprises both diffuse and direct components with diffuse irradiance prevalent in shaded environments and direct irradiance emanating straight from the sun [32][33].

Sky conditions, which influence solar resources, can fluctuate rapidly, demanding adaptable design, development, and management strategies to accommodate such variability. The constant and often swift changes in sky conditions complicate the accurate characterization of prevailing conditions and subsequently challenge the evaluation of model performance, especially at high frequencies [12][34]. On a daily timescale, the classification of the average sky conditions is feasible using a definition of sky clarity [19]. The clearness of the sky is often determined using GHI in conjunction with the extraterrestrial horizontal irradiance (E_a), as delineated in equation 5 to calculate the clearness index (K_t). This index is pivotal in solar resource applications and is widely acknowledged for its significance [20].

$$K_t = \frac{GHI}{E_a} \tag{5}$$

Daily aggregated sky conditions are categorized based on K_t values as per previous research conducted [35][36]. A K_t value below 0.30 indicates overcast conditions, above 0.68 signifies clear skies, and values between 0.30 and 0.68 are classified as intermediate. This acknowledges the findings of Page et al. who noted a typical decline in K_t values at higher ϕ [37]. It is important to highlight that at low solar altitudes (during early mornings and late afternoons), the values of E_a diminishes due to its dependence on the sine of the solar altitude (refer to Equation 3). As a result, the dominator of K_t becomes smaller, which may artificially elevate K_t values even under relatively poor atmospheric conditions. Additionally, during these times, sun rays must pass through a longer atmospheric path, increasing the influence of scattering by atmospheric molecules (i.e., aerosols). This extended optical path leads to notable attenuation of GHI relative to the extraterrestrial component. However, because of the sine of the solar altitude is very small at low

angles, its impact on the denominator can outweigh the GHI reduction, occasionally producing anomalously high Kt values during these periods.

The condition of the sky significantly influences solar irradiance, primarily dictated by cloud coverage, which affects both the quantity and variability of the irradiance reaching the ground [38][39]. Understanding the cloud dynamics is essential to evaluate how these variations impact PV systems. Developed by Ruiz Arias-Gueymard, the Classification Algorithm for the Evaluation of cLoUdiness Situations (CAELUS) effectively categorizes sky conditions into six distinct classes: cloud enhancements, cloudless, overcast, thin clouds, thick clouds, and scattered clouds [40]. This algorithm is informed by data from 54 radiometric stations across diverse climates, utilizing GHI measurements and SZA. It integrates four bespoke solar irradiance indices that gauge the magnitude and variability of GHI. Classifications are determined based on specific threshold values for these indices, refined through empirical testing for distinguishing between different types of cloud coverage. At the core of CAELUS are the clear-sky index (which compares observed GHI against modelled clear-sky GHI) and two indices derived from GHI variability, which are instrumental in classifying cloud impacts more accurately than the clear-sky index alone. These indices include the magnitude index, which compares a 30-minute moving average of GHI to the theoretical clear-sky GHI in a pristine atmosphere, and the variability index, which quantifies the cumulative minute-to-minute GHI fluctuations over a 30-minute span, aiming to capture short-term variations. A more finely tuned version of this index calculates variations over a 10-minute window to detect even more subtle fluctuations. Through this sophisticated, threshold-based approach, CAELUS advances the understanding of sky conditions by minimizing errors and stabilizing classifications, offering a more realistic portrayal of atmospheric dynamics.

Clear sky irradiance is a crucial parameter in assessing solar resources, referring to the solar radiation, whether GHI or DNI, that reaches a specific location on Earth's surface under cloudless conditions [41]. This parameter serves as a foundational element in evaluating the viability of PV systems, as these systems derive significant energy from such unobstructed conditions [42]. A key challenge in solar energy studies is accurately determining whether the sky is clear. The de facto method for Clear-Sky Detection (CSD) established in this field is the BrightSun algorithm, developed by Bright et al [43]. This CSD model has been developed by analysing irradiance data collected at minute intervals from 5 radiometric stations of varying climatology. The methodology encompasses two principal stages, culminating in detection analysis coupled with additional duration filtering. Initially, it employs a clear-sky model to establish baseline irradiance under clear conditions, which is then compared against measured irradiance. Subsequently, the algorithm enhances the clear-sky irradiance by fitting it to a curve and performing

multidimensional nonlinear optimization to fine-tune a linear correction factor. This approach directly aligns clear-sky curves with measured irradiance data, minimizing reliance on local atmospheric conditions and accommodating uncertainties such as aerosol presence. Rather than using absolute thresholds, it compares the differences between measured and clear-sky irradiance in normalized units or ratios, enhancing robustness across different irradiance levels and SZA. However, for BrightSun's criteria to classify a period as clear, it necessitates consensus among GHI, DNI, and DHI, alongside SZA, indicating the requirement for these four inputs. CAELUS can also be deemed as a CSD model, where its definition of a cloudless moment is synonymous with clear conditions.

2.1.2 Methods for Accurate Irradiance Assessment

Pyranometers, which function based on the Seebeck effect, can measure various types of solar irradiance, contingent upon orientation and mount [44]. When mounted horizontally, GHI is measured. By obstructing the sun's direct path using a shadow ball and a sun tracker, DHI can be obtained. DNI measurements can solely be acquired if utilizing the same tracker, without the shadow ball, using a pyrheliometer as evident in Figure 5a. An evaluation of PV performance considers factors like irradiance incident on a defined tilt-angle (β) and system-azimuth (ψ_{sys}). Placing instruments in-plane or inverted captures POA or BOA measurements, respectively. However, in such an assessment context, opinions emerge in deciding whether to utilize pyranometers or reference cells. The latter is designed to quantify the irradiance available to a PV module for transforming into electrical data. Table 1 offers a synopsis of both options [45][46][47].

Table 1: *Comparison of the use of solar reference cells and radiometers for two different types of measurements.*

Characteristics	Measurement of PV system performance at reference conditions (POA or BOA)		Solar Radiometric measurements (GHI or DHI)	
	Reference cell	**Pyranometer**	**Reference Cell**	**Pyranometer**
Spectral response	Similar to PV	Broadband response	Narrow wavelength response	Broadband response
Angle of Incidence	Similar to PV	Response to all angles	Response falls off at SZA > 70 °	Wide angle acceptance, up to SZA = 85°
Temperature Response	Linear, Similar to PV	Minimal sensitivity to temperature	Temperature correction required	Minimal sensitivity to temperature
Time Response	< milliseconds, Similar to PV	< 30 seconds	< milliseconds, Similar to PV	< 30 seconds
Standards	IEC 60904	IEC 9847, ISO 9845, ISO 9846	IEC 60904	IEC 9847, ISO 9845, ISO 9846
Other Issues	-	Problems At low irradiance conditions	-	-

Accurate measurements of GHI using spectrally flat class A pyranometers are exceedingly uncommon [12][39], and it is even rarer to find installations that measure DHI or DNI with a tracking and a pyrheliometer [43][44]. These methodologies are limited due to the significant challenges in maintenance, including the continuous need for calibration and recalibration [60][79]. As a result, there is a growing need to develop reliable estimations for these parameters. Consequently, researchers are exploring alternative methods, with mathematical modelling emerging as a pivotal approach [234]. While GHI is more accessible and can be measured using pyranometers, in cases where such equipment is unavailable, it can be estimated through satellite imagery combined with clear-sky GHI (GHI_{Clear}) estimates. Once GHI is determined, other parameters from DHI, DNI to complex configurations of POA and BOA irradiance can be estimated using various mathematical techniques [7][9][79][80]. This complex, interlinked model structure underscores the critical importance of comprehensive solar irradiance estimations. Additionally, within the specific spectral range of photosynthetically active radiation (400-700 nm), photodetectors, though even rarer than GHI measurements, are employed to meet the critical demand for precise Photosynthetically Active Radiation (PAR) estimates [31][265].

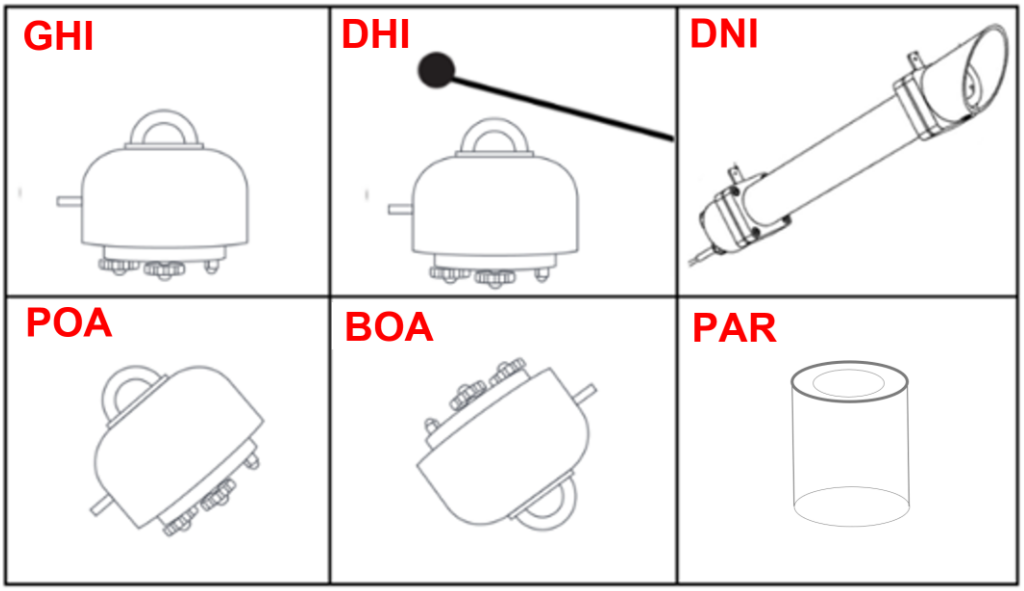

Figure 5: Various types of irradiance measurements are conducted using different instruments, including pyranometers for measuring GHI, DHI, POA, and BOA, pyrheliometers for DNI measurements, and photodetectors for capturing PAR measurements.

A crucial metric for evaluating PV performance is the Performance Ratio (PR), which is essential for gauging the overall quality of PV systems [49]. This assessment aligns with the IEC 61724 standard [50]. This location-independent metric describes the relationship between the actual and theoretical energy outputs of PV plants. A key application of the PR is to demonstrate the energy proportion that can be utilized operationally or exported to the grid at a premium rate. Higher PR is synonymous with higher quality in terms of overall performance, but a value of 100% is never possible due to unavoidable losses or eventual degradation. Several PV systems with PR between 60-90% were described in the literature as high-performance systems [49][51]. PR is computed as seen in Equations 6a and 6b, which is a ratio of POA and the irradiance under standard testing conditions, G_{STC} [50]. P_{SYSTEM} is the DC power of the modules (in Watts), and P_{IDEAL} is the DC power from the datasheet at STC (in Watts).

$$PR = \frac{P_{SYSTEM}}{P_{IDEAL}} \tag{6a}$$

$$P_{SYSTEM} = P_{IDEAL} \times \frac{POA}{G_{STC}} \tag{6b}$$

Monofacial PV with a defined β are configured to meet this requirement. However, it is essential to explore the implications of incorporating bifacial modules. Issues arise when utilizing the previously mentioned formula, as a definitive standard for assessing bifacial modules has not been established, as the current method only evaluates the front-side power. However, as per

Figure 6, IEC 61724-1 emphasizes that a station should have at least three BOA measurement instruments, positioned in representative locations to capture the effects of non-uniformities at the rear side while avoiding shading or reflections that could impact readings. Alternatively, it suggests placing two BOA sensors 20% from the module width's edge, as this provides a measurement comparable to average values in irradiance models [48]. Thus, it is evident that quantifying BOA irradiance presents significant challenges, and this is where the role of mathematical modelling becomes critical. This process initiates a cascade effect, starting from the foundational GHI measurements and progressively building towards accurately estimating BOA and PAR irradiance.

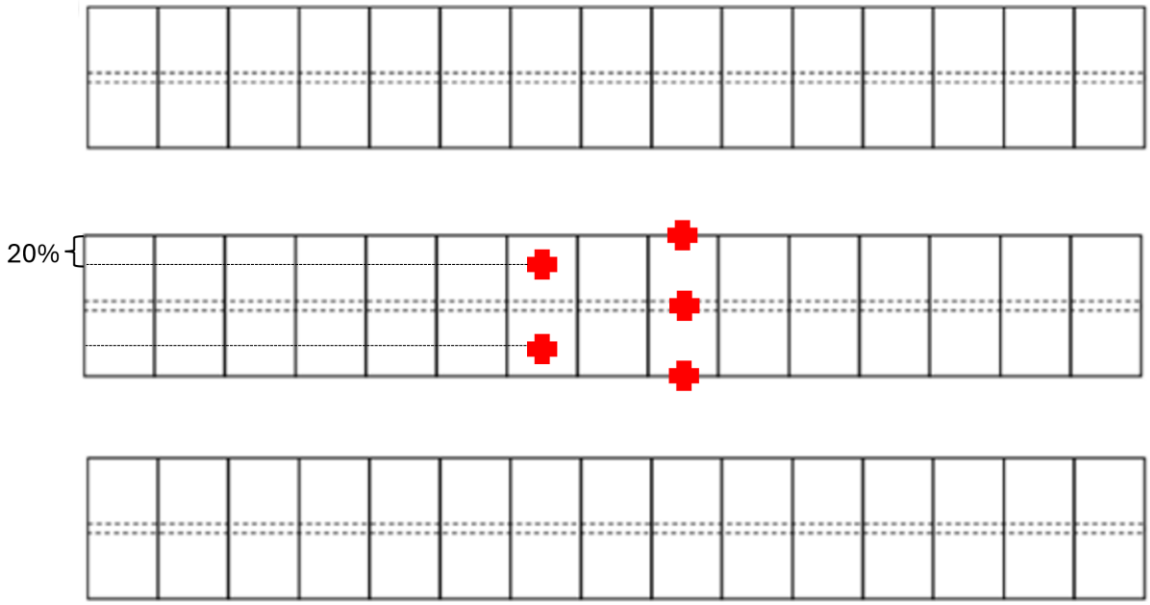

Figure 6: Suggestions for rear-side irradiance sensor placement as per [48].

2.1.3 Data Filtration Implementation

In the process of estimating solar irradiance, several data manipulation and handling steps are required. Especially since, when conducting solar irradiance measurements, the accuracy and reliability of these measurements are influenced by several crucial factors [52]. These factors must be thoroughly eradicated before the data is used for model development or validation [12]. Understanding these variables is essential for accurately assessing modelled irradiance data [44]. Therefore, it is imperative to implement the quality control procedure for solar irradiance measurements to ensure their precision and validity. Firstly, the establishment of a precise method for utilizing and predicting solar geometry has consistently relied on the most effective approaches found in the literature. This is done through the use of NREL's Solar Position Algorithm (SPA), which calculates solar angles such as SZA; critical to the closure equation (see

equation 4). The SPA is noted for its exceptional precision, with a minimal uncertainty of only 0.0003◦, applicable from the year 2000 to 6000 [53].

Although the Baseline Surface Radiation Network (BSRN) has initiated some quality control protocols, a comprehensive quality control framework remains under development [54][55]. Drawing inspiration from existing studies, a robust data quality procedure is required. The initial step involves identifying and quantifying missing timestamps and values (e.g., empty values) across data parameters such as GHI, DHI, or DNI. This assessment helps determine each station's data completeness, and any identified gaps or anomalies are excluded from further analysis to maintain data integrity [56]. Before implementing any quality control measures, it is critical to address potential thermal offsets in the pyranometers used. Hence, it is a fundamental prerequisite for quality control processes to ensure that any thermal offsets are either absent or have been correctly adjusted. The method for correcting thermal offsets involves using nighttime irradiance readings [57]. Specifically, negative irradiance values recorded after midnight until SZA reaches 100◦, and similarly post-sunset until midnight, are used. By averaging these values, an absolute adjustment is applied to the daytime observations of GHI and DHI to correct for any discrepancies caused by thermal offsets. This step is crucial to ensure that the data reflects accurate solar irradiance measurements, free from instrumental biases [52].

Once thermal offset issues are addressed, the next steps in this quality control process focus on measurements with SZA less than 85◦. This restriction helps eliminate instances of low irradiance from the dataset. It is also critical to evaluate the performance of the solar tracker used for DHI and DNI measurements. Tracker malfunctions, which can stem from electromechanical issues, misalignment, or timestamp inaccuracies, directly impact measurement reliability. Detecting these faults, especially subtle misalignments, requires careful analysis. This involves comparing recorded data against estimated values of irradiance to identify discrepancies. To further validate tracker accuracy, "tracker-off" tests are performed, adhering to established protocols. Moreover, the constant value of 1361.1 W/m^2 for extraterrestrial horizontal irradiance is utilized as a reference point throughout this research, as specified in [58] and the ASTM E490-22 standard [59]. Additionally, K-tests help not only in identifying potential issues with the tracker but also in correcting any physical misalignments that might skew the data. Addressing past constraints, which sometimes led to incorrect data exclusions during cloud enhancement scenarios, is another key aspect of this approach. Implementing "Extremely rare limits tests" as recommended by the BSRN is essential for projects requiring high-accuracy data. Finally, ensuring that the absolute value from the closure equation remains below 5% is vital, as it highlights the benefits

of using both DNI and DHI measurements over relying solely on GHI. This approach not only aligns with but also enhances the methodological rigor of these data quality protocols.

2.1.4 The Use of Satellite Data

Assessing solar irradiance at ground level is essential for analysing atmospheric components [60][61]. The atmosphere's constituents scatter and absorb solar radiation, leading to the attenuation of both direct beam and diffuse sky radiation. The decrease in solar irradiance through the atmosphere follows the principles outlined in the radiative transfer equation [62], as specified in equation 7a. In this equation, $E(\lambda)$ represents the irradiance at a particular wavelength (λ), κ denotes the extinction coefficient, and x refers to the distance traveled through the atmospheric volume.

$$dE(\lambda) = -\kappa(\lambda) \cdot E(\lambda) \cdot d(x) \tag{7a}$$

$$E(\lambda) = E_0(\lambda) \cdot e^{-\kappa(\lambda) \cdot x} \tag{7b}$$

Assuming $E_0(\lambda)$ represents the initial irradiance entering an atmospheric volume, it aligns directly with the Beer-Lambert-Bouguer law [63], thus evident in equation 7b. Furthermore, if $\kappa(\lambda)$is dependent on the distance, x; this introduces the definition of optical depth, $AOD(\lambda)$, and it is defined as the integral of extinction over a specified path, as outlined in equation 7c.

$$AOD(\lambda) = \int_{SZA1}^{SZA2} \kappa(\lambda, x) \cdot d(x) \tag{7c}$$

It should be noted that the formula presented in equation 7c applies to every wavelength due to κ (which encompasses both scattering and absorption) being highly dependent on the wavelength. The dynamics between solar irradiance and aerosols are critical to understand because aerosols significantly influence the attenuation and scattering of incoming solar radiation [64]. According to equation 7c, the wavelength-specific scattering by air molecules (via Rayleigh scattering) and aerosol particles (via Mie scattering), as well as the absorption by atmospheric gases marked by Fraunhofer lines, occurs in sharply varying absorption bands (refer to Figure 4). Additionally, data on aerosols and precipitable water (PW) can enhance cloud condensation formation, thereby impacting incoming radiation through changes in optical properties and cloud coverage [65]. Accurate prediction of surface solar irradiance necessitates the incorporation of aerosol data alongside other solar irradiance measurements. Ideally, aerosol levels should be monitored using a sunphotometer, though this equipment is typically only available within the AErosol RObotic NETwork (AERONET), which offers a global, yet limited, database of aerosol and radiative properties [66].

Historically, the primary sources of large-scale aerosol data have been derived from remote sensing observations conducted by spaceborne instruments [67]. These multispectral sensors monitor the reflected radiance from the surface-atmosphere system and employ algorithms to retrieve Aerosol Optical Depth (AOD) at various wavelengths. Estimations of AOD enable the calculation of the Ångstrom exponent (AE), an empirical measure crucial for inferring AOD at wavelengths not directly measured, or for identifying aerosol types by their size distribution through an inverse relationship [68]. AE effectively indicates the dominant particle size, with lower values (approaching 0) associated with larger coarse particles like dust, and higher values (up to 2.5) typical of finer aerosols such as those found in urban pollution. α can be derived from a linear fit following the linearization of the Ångstrom law [68][69], utilizing predetermined wavelengths, with AERONET typically measuring at 440, 500, 675, and 870 nm. AOD at 550 nm has become the standard reference for assessing turbidity and can also be calculated using this approach as outlined in equation 8, where λ_0 is the reference wavelength.

$$\ln(AOD_\lambda) = \ln(AOD_{\lambda 0}) - AE \cdot \ln\left(\frac{\lambda}{\lambda_0}\right) \tag{8}$$

However, the use of AOD and AE data from spaceborne remote sensing in surface irradiance modelling is hindered by their intermittent availability. AOD measurements are unreliable under cloudy conditions, over brightly reflective surfaces like sand or snow, or when clouds are mistakenly identified as clear skies. Additionally, the temporal discontinuity of aerosol data, due to the nature of polar-orbiting satellites, poses a significant challenge. This limitation has sparked considerable interest across various scientific communities in AOD modelling, leading to the development of satellite datasets that provide AOD and AE estimates for use in mathematical models, such as those estimating GHI and DHI under clear sky conditions [68]. With DNI being particularly sensitive to AOD, and GHI is also affected by AOD, the impact is less severe compared to DNI, and it is influenced by PW as well [70].

To mitigate these challenges, forecasters utilize satellite data from resources like MERRA-2 (Modern-Era Retrospective Analysis for Research and Applications, Version 2) [71][72][73] and CAMS (Copernicus Atmosphere Monitoring Service) [74][75][76][77]. Satellite datasets integrate historical data from satellites and weather stations with climate model outputs, offering a comprehensive and consistent record of atmospheric conditions over extended periods and across various ϕ [58][78]. This data is essential for understanding weather patterns, climate trends, and atmospheric disturbances, providing a global perspective that enhances the financial viability of solar energy projects. Different satellite data result in different approximations of AOD and AE hence, there is a need to see the difference and the effect that they have.

2.1.5 Metrics Deployed in Feasibility Software

The swift advancement and deployment of various PV technologies necessitate significant investments, financial risk assessments, and strategic policy decisions regarding the prioritization of technology deployment [11][12][52]. The energy output of a system is closely linked to POA (and to some extent BOA in bifacial systems and PAR in AgriPV systems), underscoring the impact of these factors on the system's energy production and design parameters. This inherent uncertainty in energy output directly correlates with uncertainties in POA (BOA, and PAR), making financial risk evaluation and the assessment of project bankability and feasibility crucial for future PV projects [9]. Numerous feasibility software applications exist that utilize various irradiance estimations to project values for POA, BOA, and PAR.

An accurate appraisal of PV performance is central to the economic viability of systems [6][7]. The wide range of optical model combinations, where decomposition and transposition models are paired together, can lead to errors and elevate the risk during the deployment of photovoltaic (PV) systems. Feasibility software offers a multitude of model combinations, but there is no established standard for their use [79]. Previous research indicate that applying the same meteorological information and system definitions can lead to differing POA irradiance predictions [80]. POA is crucial for making knowledgeable choices, spanning various domains from analyzing shade effects to assessing economic feasibility [81]. ITRPV estimates show that by 2030, 40% of PV systems will incorporate tracking technologies [82]. Reinforcing this, the International Energy Agency (IEA) highlights the growing use of single-axis trackers in the USA, surpassing Fixed-Tilt (FT) systems within PV farms [83]. Moreover, it demonstrates the growing global market for PV trackers. The pursuit of tracking technologies in the PV landscape holds the potential for enhanced energy output and therefore reduction in the number of modules required per kWh [84][85]. However, tracking solutions in PV systems often necessitate increased physical space, which could be a hurdle in space-limited areas [82]. Therefore, precise modelling is essential to ensure that the benefits provided by these solutions surpass their spatial needs. Furthermore, the use of trackers introduces concerns about return on investment.

It is documented that the accumulation of modelled results over longer periods tends to reduce their random errors (referenced in sources [86][87]). Thus, assessing model performance over an appropriate averaging period is critical. Traditionally, hourly and monthly radiation data have been standard in the simulation and design of PV systems. However, recent developments have introduced new requirements and opportunities. Many radiometric stations now offer data at much finer resolutions (i.e., 1 minute), facilitating model validation at higher frequencies. This high-frequency data is crucial for simulating PV systems that operate under rapidly changing

conditions, such as those found in the temperate climate of the UK. Additionally, solar resource characterization over specific areas is often reported in terms of mean annual irradiation, a vital factor in estimating the long-term energy production of PV systems and an essential component for the financial analyses required to determine a project's bankability using feasibility software.

Utilising high temporal resolution data, such as solar irradiance data at one minute intervals, allows for more precise characterisation of irradiance variability driven by transient atmospheric conditions. This includes the movement of clouds, aerosol events, and brief changes in solar position. This granular level of detail is particularly beneficial for assessing the dynamic response of PV systems under real-world sky conditions, as it captures rapid fluctuations in irradiance that are often obscured in coarser, hourly datasets. This is particularly true for tracking systems, where an hourly dataset my underpin the overall gains relative to its fixed-tilt counterpart. Moreover, employing minute-resolution data enhances the accuracy of time-series simulations by supporting the detection of systematic biases and enabling more precise calibration of both decomposition and transposition models. From a system operation perspective, high-frequency data facilitates more advanced forecasting methods and informs grid-integration analyses. This is especially true for scenarios with high levels of PV deployment. Integrating such data strengthens system design, refines operational planning and increases confidence in energy yield projections, all of which contribute to minimising investment risks in PV projects.

Given the scarcity of solar irradiance measurements in areas critical for large-scale developments, both general and specific project analyses often must rely on modelled datasets. This reliance raises several important considerations about the accuracy of these datasets compared to actual, locally measured high-quality data, and the level of confidence investors might place in such information. Additionally, comparisons between different models, are necessary to establish their relative accuracy and reliability. This discourse sets the stage for the extensive use of various metrics designed to quantify the errors inherent in irradiance modelling used by feasibility software. The literature on solar irradiance modelling is rich, and there is a wide range of methods for assessing the performance of these models through validation studies. These studies typically explore different components of irradiance, with most components being validated and some developed. Consequently, this thesis will establish a benchmark for comparing modelled data against measured data, for different solar irradiance estimations, aiming to set a standard for this evaluation.

The review of existing literature highlights a broad spectrum of evaluation methods, emphasizing the necessity for selecting suitable performance metrics. This thesis, like most previous research on this topic, employs Mean Absolute Deviation (MAD) as the key figure of merit as per equation

9a [88]. The term “deviation” is used here rather than “error” to emphasize that the performance of any radiation model is evaluated against irradiance measurements that are affected by low, but non-negligible, experimental uncertainties [52]. MAD is instrumental in quantifying discrepancies between observed data and predictions by irradiance models, offering a gauge for the model’s fidelity in reflecting real-world conditions. It proves especially useful in pinpointing how much the model’s estimates deviate from actual observations in general. MAD calculations provide insights into the absolute deviations a model exhibits compared to its measured values and are endorsed as Class A indicators [11]. The evaluation of deviation in the estimated irradiance is a key component of solar resource assessment, as it directly impacts the uncertainty in the predicted output of PV systems and their bankability. One key advantage of MAD is its robust measurement of average error, which remains unaffected by extreme outliers (unlike Root Mean Square Deviation) and prevents error cancellation, a common issue with Mean Bias Deviation. MAD evaluates the absolute size of deviations, providing a more comprehensive perspective on overall variation with measured data. This thesis underscores the uniform contribution of each site. For example, the MAD across a diverse station database is calculated as the arithmetic mean of all individual MADs as specified in [12]. The statistical results are expressed in percent rather than in W/m^2 to adhere to the recommendations in [40]. A good combination of irradiance models should have a low MAD, close to 0%.

$$\mathrm{MAD} = \frac{100}{Irr'_{Measured}} \sum_{i=1}^{i=N} |Irr_{Modelled} - Irr_{Measured}| \tag{9a}$$

$Irr_{Modelled}$ represents the irradiance value from the specific model for the ith data point and $Irr_{Measured}$ conveys the measured irradiance value from the instrument deployed for the ith data point. The number of data points is depicted as *N*. The $Irr'_{Measured}$ represents the mean of the measured irradiance value and $Irr'_{Modelled}$ represents its modelled mean counterpart. Another useful metric is the coefficient of determination (R^2), as outlined in equation 9b. R^2 is a measure of the variability of an irradiance model relative to actual measurements. Hence, it indicates how well a model capture the overall trend in the data. R^2 values closer to 1 indicating a higher level of accuracy in the model’s predictions.

$$\mathrm{R}^2 = \left(\frac{\sum_{i=1}^{i=N} (Irr_{Modelled} - Irr'_{Modelled})(Irr_{Measured} - Irr'_{Measured})}{\sum_{i=1}^{i=N} (Irr_{Modelled} - Irr'_{Modelled})^2 (Irr_{Measured} - Irr'_{Measured})^2} \right)^2 \tag{9b}$$

Bifacial Gain, or BG, is a metric frequently found in literature to characterize the performance of bifacial systems, but its usage is not uniform. At times, it is referred to as the ratio of irradiance collected on the front and rear of the panel [89][90]. Nonetheless, the energy yield version of BG

is employed in the industry [91][92], which quantifies the increase in energy yield for a bifacial module in comparison to a monofacial module under identical circumstances. To avoid confusion, the terms BG_{irr} and BG_{Energy} will be used distinctly. These concepts are outlined in equations 10a and 10b, where E_{Bifi} represents the total energy produced by a bifacial system (in Watt-Hours), and E_{mono} corresponds to the energy output from a monofacial system (in Watt-Hours).

$$BG_{irr} = \frac{BOA}{POA} \tag{10a}$$

$$BG_{Energy} = \frac{(E_{Bifi} - E_{mono})}{E_{mono}} \tag{10b}$$

Bifacial modules are classified using the bifaciality factor, ϕ_{bifi}, which conforms to the IEC 60904-1-2 standard [93]. A spectral mismatch correction factor is added as per IEC 60904-7 [94]. The rear-to-front side power ratio is measured at STC conditions: 25 °C, 1000 W/m^2, and AM1.5 and is defined by equation 11. The module rear side is covered with a non-reflective sheet through a solar simulator, ensuring less than 3 W/m^2 at any point on the non-illuminated side of the PV, and the front power ($P_{max-front}$)is measured. Similarly, the front side is covered with the same material to measure the rear side power ($P_{max-rear}$).

$$\phi_{bifi} = \frac{P_{max-rear}}{P_{max-front}} \tag{11}$$

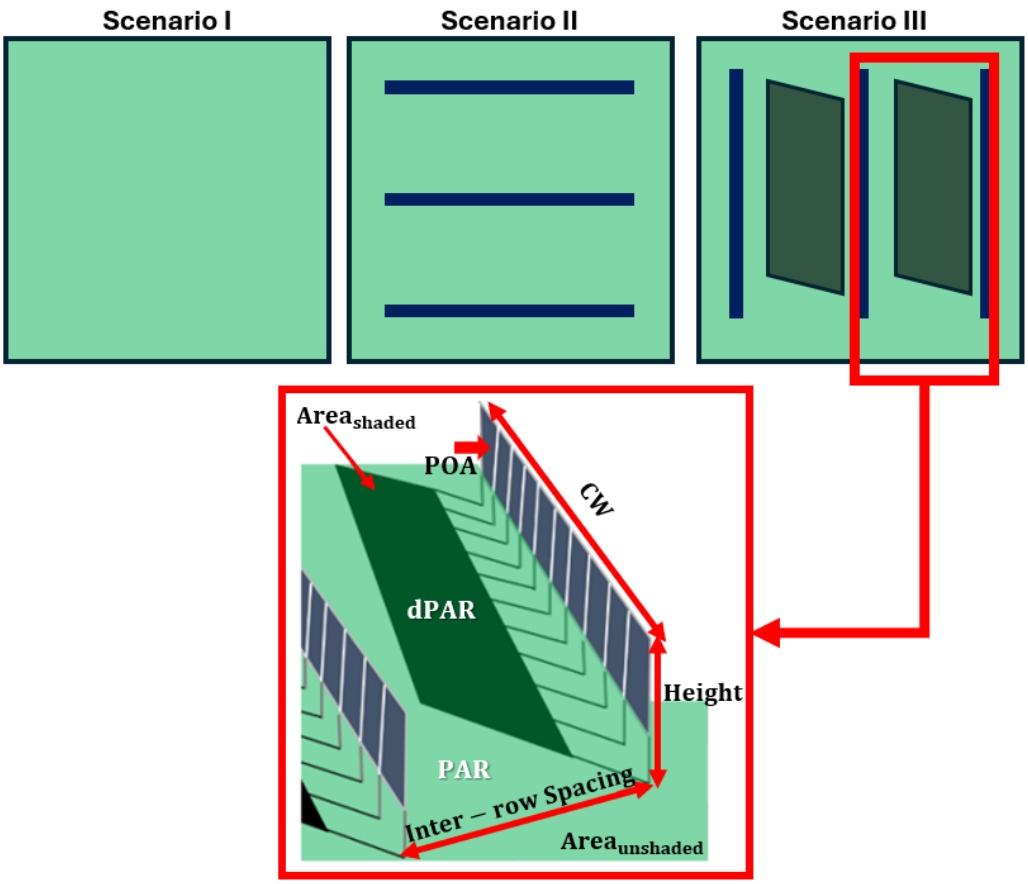

Figure 7: Three distinct scenarios illustrate the methods for calculating the land equivalent ratio: Scenario I involves dedicating the entire area to crop cultivation, Scenario II allocates the land exclusively for PV energy generation, and Scenario III combines both agriculture and PV energy generation to explore their synergistic potential.

$$LER = \frac{X_{Scenario\ III}}{X_{Scenario\ I}} + \frac{Y_{Scenario\ III}}{Y_{Scenario\ II}} \tag{12a}$$

$$X_{Scenario\ III} = dPAR \cdot Area_{shaded} + PAR \cdot Area_{unshaded} \tag{12b}$$

$$X_{Scenario\ I} = PAR \cdot Area_{All} \tag{12c}$$

$$Y_{Scenario\ III} = \mathrm{CW} \cdot N \cdot \sum_{N}^{N=Rows} POA_{Scenario\ III} \tag{12d}$$

$$Y_{Scenario\ II} = \mathrm{CW} \cdot N \cdot \sum_{N}^{N=Rows} POA_{Scenario\ II} \tag{12e}$$

Land costs are increasingly high and projected to rise further, prompting some to argue that arable land should primarily serve to feed the growing population amidst escalating hunger. AgriPV presents a solution by enabling the dual use of farmland for both crop growth and energy

generation, addressing the food-energy-water nexus. A critical metric in this approach is the Land Equivalent Ratio (LER) [95], which measures the combined yield of crops and energy as opposed to their separate cultivation across three scenarios as per Figure 7: Scenario I utilizes the land solely for agriculture, Scenario II dedicates it entirely to energy generation, and Scenario III integrates both uses. Equation 12a defines the LER, calculating the normalized value of combining land productivity for agriculture and PV energy in terms of production. Equation 12b focuses on Scenario III, quantifying the crop production by assessing the irradiance available for PAR, alongside the irradiance for PV deployment on the same agricultural land, as detailed in equation 12d Conversely, equation 12c corresponds to Scenario II, which reserves the land exclusively for agriculture, while equation 12e applies to Scenario I, where the land is used only for PV energy generation. In the equations below, dPAR connotes the diffuse component of PAR, $Area_{shaded}$ represents the shaded area caused by the PV panels, $Area_{unshaded}$ is the area that is unshaded and $Area_{All}$ is the total area of the land. CW is the collector width of the panels in a row in meters.

2.2 Exploring Bifacial, Tracking and AgriVoltaic Systems

2.2.1 Bifacial Technology

With the growing popularity of solar energy, choosing the right solar panel is crucial for maximising energy production and return on investment. Traditionally, monofacial panels have been the standard choice, designed to capture sunlight exclusively from the front side of the panel. In contrast, bifacial panels, as the name implies, are capable of absorbing sunlight from both the front and rear sides [96]. As shown in Figure 8, bifacial modules achieve this by replacing the opaque backsheet found in monofacial panels with a glass layer. This modification allows sunlight, reflected off the ground or nearby surfaces, to penetrate and be absorbed by the rear side.

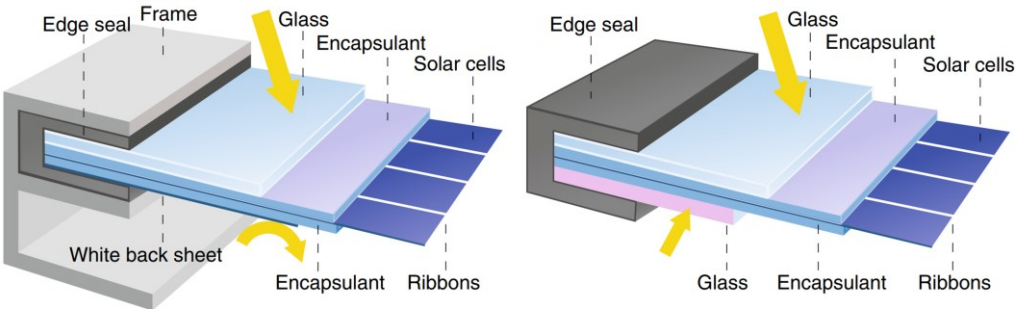

Figure 8: Monofacial and bifacial modules consist of multiple layers, with a key distinction being the replacement of the opaque backsheet in monofacial modules with a glass layer in bifacial modules [91].

The addition of this rear-side irradiance collection sets bifacial modules apart from their monofacial counterparts. The glass layer or in some cases, a transparent backsheet, takes the place of the conventional backsheet [85], reducing infrared light absorption. This reduction lowers operating temperatures, ultimately extending the panels' lifespan, as highlighted by Hubner et al. [100]. Although bifacial modules offer advantages such as increased durability and enhanced performance under diffuse light conditions, their overall efficiency depends on several environmental and system-specific factors. Consequently, a transition to a bifacial modules architecture can improve energy yield by up to 30% [98]. Calculations by Deline et al. have shown that such architecture options can be achieved at a reasonable increase in production costs while guaranteeing an increase in power production [99].

The visual distinction between monofacial and bifacial modules is just one aspect of a broader set of functional differences. Bifacial modules absorb irradiance from the rear side as well as the front side due to the use of bifacial-compatible solar cell architecture. This is due to the fact that various cell architectures are evolving away from completely covering the back end of a cell. Instead, metallization is applied only partly on the back side - thereby improving photon absorption [99]. This allows for bifacial technology to be integrated due to their metallization.

Aside from the different optical designs between monofacial and bifacial modules, they also exhibit distinct lifetime behaviour. Bifacial modules are constructed with glass on both sides, which enhances the mechanical strength and operational lifetime when compared to the more conventional glass-back sheet configuration of monofacial modules. An essential aspect affecting bifacial system performance is the elevation height, *h* of the module [101]. To optimize sunlight collection at the rear, *h* should be adequate. This is defined as the height of the distance between the lowest part of the module and the surface. There is a positive correlation between *h* and performance, indicating that the higher the bifacial module is positioned, the more likely the rear side will be exposed to reflected sunlight [102]. In addition, for energy yield considerations,

a uniform distribution of reflected irradiance is preferred on the rear side of a bifacial module [48]. Shadows cast by the module's own rear side cause irradiance variations resulting in mismatch loss, which impacts the system's energy yield.

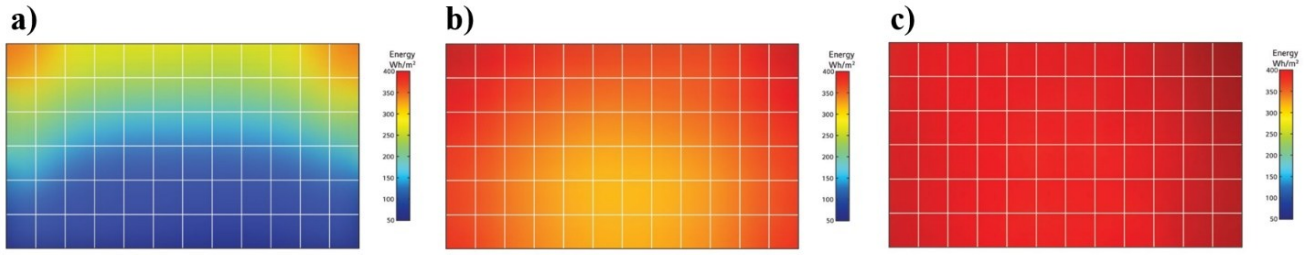

Figure 9: The distribution of rear side irradiance in a single module changes as per different h **(a)** 0.08m **(b)** 0.58m (c) 1.08m. This figure is adapted from [103].

Kreinin et al. conducted an experiment to investigate the irradiance distribution of a single south-facing bifacial module set at $\beta = 30°$ at φ = 32°, exploring various *h* [103], as depicted in Figure 9. Berrian et al. [104] used a simulation to study the effects of different *h*, employing the same β, but situating the system at φ = 42°, ultimately reaching a similar conclusion. Although there is general agreement in the literature that a saturation point regarding rear uniformity will eventually be achieved, there remains a noticeable research gap concerning the extent of rear side nonuniformity in diffuse regions, and whether differing saturation points would be reached in said conditions.

In the context of bifacial solar panels, a crucial factor that quantifies the amount of light reflected is albedo (ρ) [105]. Regarded as a dimensionless metric, ρ symbolizes the portion of light reflected off a surface. This value can range between 0 and 1, where 0 signifies a completely black, absorptive substance, and 1 indicates an ideal reflector. Through the use of a pair of pyranometers placed back-to-back, equation 13 is utilized to calculate ρ from measured GHI and Reflected Horizontal Irradiance (RHI). Various parameters influence the overall value of ρ, such as surface type, moisture levels, roughness, and solar angular light distributions [105][106]. As stated by Gostein et al., most PV software computes ρ as a single figure, but some applications calculate monthly ρ values that may fluctuate due to ground dampness and other environmental factors [47].

$$\rho = \frac{RHI}{GHI} \tag{13}$$

As notably seen in Figure 10, ρ of materials depends on the wavelength of incoming sunlight, often referred to as spectral albedo in literature [107]. Previous research has investigated the spectral properties of plants due to PAR, which denotes the light spectrum portion used by plants for photosynthesis [108] ranging from 400 nm to 700 nm. In temperate regions, a significant amount

of land is designated for agriculture, and such vegetation areas can accommodate bifacial panels to tackle the food-energy-water nexus [109]. However, calculating ρ under one-sun calibrated pyranometers, which yield a single aggregated value related to shortwave radiation (typically 0.20), does not provide a comprehensive understanding, and introduces uncertainty. As most bifacial solar panels employ crystalline silicon, operating between 400 and 1100 nm [110], BOA estimation are said not to be accurate if they are measured using pyranometers.

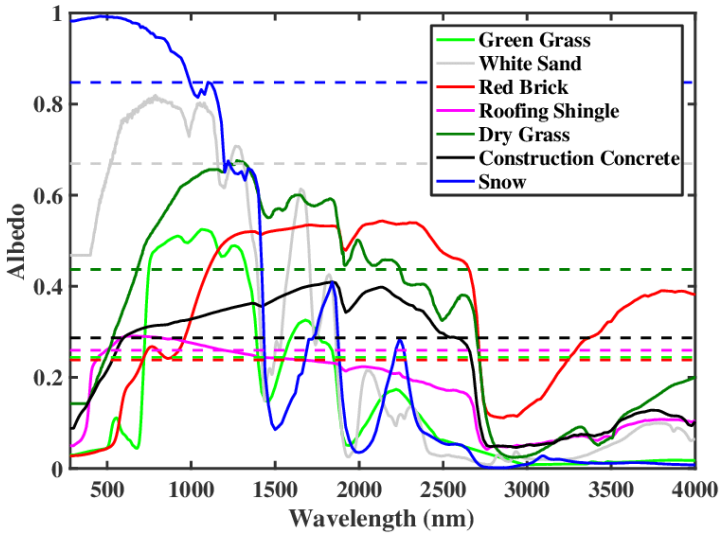

Figure 10: A study of the spectral albedo of a few commonly used surfaces [111]. The dashed horizontal lines refer to the broadband albedo value using a back-to-back pyranometer.

Moreover, simulation software that uses specific wavelength ranges might produce inaccurate results, especially if there are assumptions made about the ground's Lambertian isotropic scattering. Investigations show that neglecting spectral and angular details can lead to significant deviations in PV performance [112]. Consequently, research has concluded that spectral albedo effects can significantly impact BOA estimations, and these effects must be considered in simulations [46][113].

2.2.2 Tracking System Varieties and Algorithmic Approaches

While more cost-effective, the limitations of Fixed-Tilt (FT) systems (Figure 11a) become apparent in light of the cosine effect. This effect means that the sun will not always be at a right angle to the panel, resulting in power losses as the PV module aligns with the SZA-axis for only a brief period. To mitigate such issues to an extent, tracking can be employed, with Horizontal Single Axis Tracking (HSAT, see Figure 11b) being the primary tracking method. As the name depicts, this technology permits one degree of motion, contingent upon one parameter. If it is configured to face south, ψ_{sys} is tracked (known as HSAT-EW). Conversely, if $\psi_{sys} = 90°$, α is tracked (termed

HSAT-NS). HSATs are believed to be on the rise, as IHS Markit anticipates increased tracker shipments due to the expected adoption of bifacial technology in the coming years [114].

Regarding bifacial HSAT, research has shown that irradiance gains ranges between 6.5-7.9% due to uneven soil moisture and grass texture [115][116] at φ = 36°. The 1.7 MW La Silla power plant at φ = 29° compared monofacial and bifacial HSATs over a nine-month period, determining that BG_{Energy} varies between 10.4% and 12.4% at an unspecified ρ (which likely ranges from 0.2 to 0.3 due to desert conditions) [117]. Patel's simulations [118] found that bifacial HSAT orientation matters depending on φ. HSAT-NS gain an additional BG_{Energy} of at least 5% compared to HSAT-EW at φ > 50°, whereas at φ < 50°, HSAT-EW outperforms HSAT-NS by a minimum of 10%. This is attributed to the more pronounced inclined sun path at higher φ and the greater variation in α throughout the year. Moreover, it was concluded that HSAT-NS is more effective in winter, while HSAT-EW is superior in summer [118]. However, it is important to note that these findings were based on simulated weather data; they may not accurately represent real-world conditions in temperate climates due to insufficient validation, which underlines the significance of validating models for more reliable conclusions.

In comparison to FT systems and HSATs, the use of Dual Axis Trackers (DATs) effectively eradicates the cosine effect, as the panels continuously align with the sun. DATs can move in response to both ψ_{sys} and β as seen in Figure 11c. Although they offer an increase in energy production, DATs are generally viewed as expensive options due to their upfront capital costs, with Rodriguez et al. estimating a 31% additional energy output, which is only 5% more than an HSAT at a price that investors find difficult to justify [7]. This is especially true when factoring in the economic aspects of DATs, such as maintenance expenses throughout their lifespans. However, bifacial modules might be the catalyst that changes these hesitant opinions, as bifacial DATs could boost energy production by 40% in comparison to monofacial FT systems and potentially more if BOA-specified algorithms are employed. Kelly et al. also suggested that with increasing ρ levels and sun path angles, bifacial DATs may become a more desirable alternative to FT systems [119].

Burnham [120] analyzed the performance of bifacial DATs in a high ρ environment at ϕ = $44°$, over a two-year timeframe. In comparison to its monofacial FT counterparts, there was an uplift of 41% energy increase. This heightened energy yield could be due to the study location receiving an average of 200 cm of snow yearly, dispersed over six months, as the high ρ of snow would generate additional energy on the panels' back side. Furthermore, the consistently lower ambient temperatures year-round would improve operating efficiency. However, Gueymard [121] argue

that up to 90% of the sun's potential energy comes from DNI , with the remaining 10% originating from DHI scattered by atmospheric aerosols. In overcast conditions, much of the radiation is derived from DHI; therefore, tracking the sun in temperate regions is less beneficial.

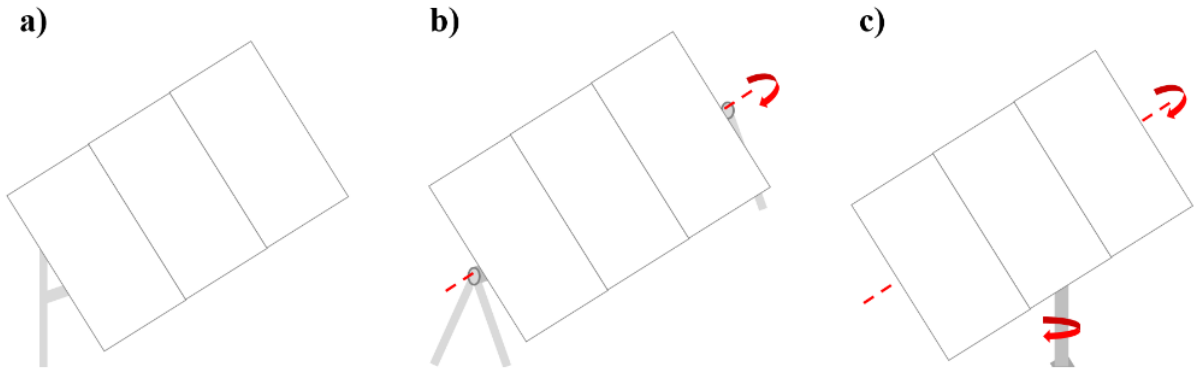

Figure 11: There types of tracking solutions: **a)** FT, **b)** HSAT-EW, and **c)** DAT. This figure was adapted from [102]

Tracking control schemes are of considerable importance in terms of the potential energy they can provide, depending on both the tracker's overall movement strategy and its response to shading on its modules. All tracking algorithms can be classified into two primary categories: closed-loop and open-loop. The open-loop control, synonymous with tracking-the-sun (TS) [122], employs a mathematical algorithm that automatically adjusts the tracker's position to follow the sun based on the site's geolocation, maximizing DNI collection. Although the module's position can be determined regardless of location, it does not account for weather conditions. In contrast, closed-loop algorithms consider atmospheric conditions using irradiance sensors that determine the module's optimum orientation, often referred to as "tracking-the-best-orientation" (TBO). Modules are oriented toward the area receiving the most solar insolation, considering reflective and diffuse components. Mousazadeh [123] suggested that in overcast conditions, little DNI insolation reaches the modules, in line with Gueymard statements [121]. Thus, modules should have been positioned horizontally on trackers to collect more energy compared to those using celestial tracking. However, the optimal tracking movements under stated conditions are yet to be developed. As a result, it is essential to further explore the impact of diffuse components on tracking and develop equations that maximize irradiance capture. Researchers are advised to integrate short-term irradiance control schemes, thereby highlighting the crucial requirement for precise solar irradiance estimations. This need encompasses the utilization of DHI, DNI, or GHI estimates, as well as more complex calculations such as POA and BOA estimations.

Trackers are deemed more effective when they integrate backtracking algorithms into their control schemes [90]. This is especially relevant when the α is low, potentially causing one panel to shade the one behind it, resulting in hot spot generation. This is particularly important in temperate climates due to the inclined solar path. Backtracking enables trackers to adjust their position to eliminate inter-row shading, considering the sun's position relative to the site topography and panel dimensions, albeit at the expense of cosine losses. Lorenzo detailed the backtracking geometry and how it varies for monofacial tracking technology [124]. Since current algorithms do not include ρ and, consequently, BOA, backtracking algorithms may require modifications in the context of bifacial technologies. This is especially at high φ, where the inter-row spacing will be extensive due to the angled sun path and the requirement to raise the system higher to optimize BOA uniformity.

Table 2 presents a comprehensive synopsis of the literature review on bifacial tracking, emphasizing the impact of various factors on irradiance or energy performance. There is a growing interest in studying bifacial tracking systems [102], [117], [125-131], with energy gains up to 41% in climates with lower latitudinal angles than the UK [120]. This highlights the need for research on potential gains in temperate environments.

Table 2: *An examination of the literature pertaining to bifacial gains demonstrated by various tracking systems, including their critical parameters and methods of data collection. Unless otherwise indicated, the gains reported are of the monofacial counterpart. Bifacial Gain outcomes from simulations are denoted by 's,' while 'm' indicates outcomes from real-world system measurements.*

Tracking System			Data Collection			ρ	ϕ_{bifi}	Duration (Months)	φ	BG_{Energy}	BG_{Irr}	Comments and References
Type	Algorithm	Backtracking	Solar Irradiance	Temperature	Power							
FT^m	β = 40°, ψ_{sys} = 180°			✓	DC	0.05	0.83	12	58.00	0.05		[281]
FT^m	β = 30°, ψ_{sys}= 180°		✓	✓	DC		0.75	1	32.00	0.10	0.16	[125]
FT^m DAT^m	β = 30°, ψ_{sys}= 180° ψ_{sun} , α				DC	0.20		21	44.00	0.41 0.14		Monofacial Fixed-Tilt vs Bifacial DAT Monofacial DAT vs Bifacial DAT [120]
DAT^m	ψ_{sun} , α				DC	0.16 0.23		2	30.00			Bifacial DAT under 2 surfaces [282]
$FT^{s,m}$	β = 30°, ψ_{sys}= 180°, h =3m		✓	✓	DC	0.30	0.90	6	48.86			[283]
FT^s	β = 12°, ψ_{sys}= 180°				DC	0.30	0.84	6	32.09			[283]
$HSAT^{s,m}$	α	✓	✓	✓	DC	0.32		6	37.77			[283]
$FT^{s,m}$	β = 10°, ψ_{sys}= 180°, h = 0.82m		✓			0.70		8	39.76		0.20	Test bed with reference cells, no modules [90]
$FT^{s,m}$	β = 20°, ψ_{sys}= 180°, h = 1.20m		✓			0.30	0.91	5	27.00		0.21	[92]
$FT^{s,m}$	β = 10°, ψ_{sys}= 165°, h = 0.52m		✓			0.55		-	35.00			[208]
$FT^{s,m}$	β = 45°, ψ_{sys}= 165°, h = 0.58m		✓			0.30		-	49.00			[208]
$FT^{s,m}$ $HSAT^{s,m}$	β = 25°, ψ_{sys}= 180° α		✓	✓	DC	0.21	0.67	12	55.60		0.06 0.08	[127]
FT^m	β = 60°, ψ_{sys}= 180°		✓	✓	DC, AC	0.70	0.94	13	64.00	0.21		[128]
FT^m $HSAT^m$ DAT^m	β = 15°, ψ_{sys}= 180° α ψ_{sun} , α		✓	✓	DC	0.35 0.20 0.55		12 1 < 1	35.08 35.23 44.20	0.33 0.20	 0.11 	[129]
FT^m	β = 45°, ψ_{sys}= 180°, h = 1m		✓		DC	0.10 0.30 0.50 0.70		12	55.95	- 0.11 0.12 0.20	0.08 0.15 0.19 0.26	[283]
$HSAT^m$	α	✓	✓		DC	0.26	0.73	-	39.73	0.26		[102]
$HSAT^m$	α	✓	✓	✓	DC, AC	0.30	0.85	12	29.00	0.13		[117]
$HSAT^m$	α	✓	✓	✓	DC	0.16	0.75	6	38.54	0.05		[130]
FT^m	β = 30°, ψ_{sys}= 180°, h = 1m				DC	0.06 0.12 0.21	0.82	1 2 1	35.82	0.05 0.11 0.14		[131]
FT^m	β = 35°, ψ_{sys}= 180°, h = 1.5m				DC	0.30 0.85 0.60	0.96	7	33.84	0.09 0.23 0.23		[284]

2.2.3 Integration of Agriculture and Photovoltaics through AgriVoltaics

Economic growth coupled with increasing population sizes significantly contributes to the escalating demand for energy, leading to an energy crisis in numerous nations [10]. This situation has sparked important discussions regarding energy use and agricultural practices worldwide [132]. The concept of the food-energy-water nexus underscores the interconnectedness of water, energy, and food security, emphasizing the urgent need for beneficial strategies that align agricultural and energy policies [133]. Contrary to the widespread belief that energy and agricultural production are incompatible, meaning one cannot be pursued without sacrificing the other, the integration of energy transition into societal norms is becoming a pivotal aspect of developing energy generation systems, such as PV farms [134]. Efforts are being directed towards addressing several of the United Nations Sustainable Development Goals (UN SDGs), particularly focusing on UN SDG 2, which aims to achieve zero hunger through agricultural improvements, and UN SDG 7, which promotes affordable and clean energy, notably through advancements in photovoltaic technology. AgriPV presents a notable solution that bridges the perceived divide between energy production and farming [135]. It integrates PV energy generation with agricultural activities, allowing for both crop cultivation and energy production to occur on the same piece of land simultaneously. This innovative approach enables the expansion of PV energy without encroaching on valuable agricultural space, and it also offers the added benefit of protecting crops with the installation of PV modules [136][137]. This coexistence potentially enhances crop yields through the shared use of sunlight, depending on climatic conditions and crop varieties [5]. In certain instances, this arrangement proves mutually advantageous, as the evaporation from crops can lower the operating temperatures of PV modules [138][139].

The agricultural sector faces several challenges beyond land scarcity and high costs. These include water shortages, constrained resources, and increasing demands for quality food. Additionally, climate change is exacerbating these issues with rising temperatures, altered precipitation patterns, and more frequent extreme weather events like droughts and floods, all of which adversely affect farm productivity. To cope, farmers are adopting strategies such as crop diversification, improved soil management, enhanced water efficiency, and selecting crop and livestock varieties better suited to harsh conditions. Limited access to arable land, water, and cost-effective energy is driving the agricultural sector toward innovative technologies such as AgriPV. These systems offer a viable solution by generating new avenues for solar energy development across diverse climates and simultaneously resolving the conflict between agricultural and photovoltaic demands on valuable land.

The role of PV systems situated on agricultural lands in advancing renewable energy objectives is becoming increasingly recognized in various regions. For example, France can deploy up to 5 GW of solar power by utilizing just 0.1% of its agricultural lands, which constitute a significant portion of the country's area. Similarly, the possibility of harnessing 1% of the European Union's agricultural land could lead to the generation of 410 GW through PV, although only 29.3 GW had been achieved in 2021. European nations have established guidelines for integrating agriculture and PV, with Italy allocating substantial funds for the development of 2 GW in AgriPV projects [84]. Furthermore, calls for AgriPV project proposals have been made in various countries, with France targeting approximately 300 MW, Germany 150 MW, and the Netherlands 45 MW. Additionally, progress has been made in tracking systems, which are increasingly prevalent in the market [82] and are being tailored for AgriPV initiatives to maximize the performance of PV energy for farming needs. Through leveraging the superposition of energy and food production for mutual benefit, studies have demonstrated the successful cultivation of various crops under AgriPV configurations. This helps mitigate risks of food scarcity and market volatility, particularly for rain-fed agriculture. Research by Edouard et al. on integrating tracking systems to optimize crop production within AgriPV setups has shown LER at 1.51 in temperate climates at ϕ = 48.3º, highlighting AgriPV's efficacy [140]. Furthermore, in temperate climates, optimal placement of PV panels requires significant inter-row spacing to minimize shading. This strategic positioning of crops within these spaces exploits the extensive areas surrounding and underneath the panels, further enhancing crop yield. This was supported by Campana et al., who reported an LER of 1.39 in similar conditions at ϕ = 59.55º, reinforcing the viability of AgriPV systems [141].

While AgriPV has garnered increasing interest, challenges persist due to the lack of comprehensive parameters and models. Despite its potential, the AgriPV sector remains niche, constrained by scarce data and installations that could broaden its impact. Moreover, the growing interest in PV systems has led to land competition, prompting investigations into land dual-use as a solution, especially in regions where land is at a premium [84]. Precise calculation of available irradiance for crops is essential to determine the viability of AgriPV, utilizing metrics such as LER [142]. Consequently, this necessitates modelling, which hinges on accurate assessments or predictions of irradiance components relevant to photovoltaics and agriculture [143]. Moreover, there is a lack of feasibility software for AgriPV mainly due to the challenges of estimating PAR irradiance.

Addressing the challenge of accurately modelling AgriPV systems involves understanding the critical role of PAR in plant growth. PAR represents a fraction of the spectral range (400 – 700 nm) [144] captured by common radiometer measurements of GHI. The integration of PV panels into

agricultural lands necessitates ensuring that crop yields do not fall below acceptable thresholds, thus underlining accurate PAR estimations [145]. Photosynthesis rates hinge on the energy accessible to plants and are expressed either in terms of flux density (i.e., μml photons/m^2/s) as it is a quantum process or in terms of flux density (i.e., irradiance W/m^2) [12]. While plants predominantly absorb radiation within the 360 and 760nm wavelength, their efficiency varies across this spectrum [146]. The way that PAR is measured is deploying photodetectors that assumes that the critical absorption range for stimulating photosynthesis lies between 400 to 700 nm, treating all wavelengths within this range as equally effective. Compared to its counterpart GHI, information on PAR irradiance is sparse [147]. There exists a critical demand for PAR data, essential for both agricultural applications and propelling AgriPV technologies forward, as it serves as a vital parameter in various modelling tools. This is particularly so in temperate regions like the UK, where integrating AgriPV offers a solution to deploying PV without sacrificing arable land, would aid in achieving the ambitious 70GW target by 2035. Moreover, quantifying PAR data is essential for estimating its diffuse component (dPAR), paralleling the roles of GHI and DHI, thereby highlighting the need for precise PAR irradiance predictions through mathematical modelling [33].

2.3 Mathematical Solar Irradiance Modelling

2.3.1 Comprehensive Analysis of Decomposition Models

GHI is the most frequently recorded solar radiation variable, obtained through ground-based meteorological stations or satellite imagery. In contrast, DHI is less commonly measured and not as easily accessible. Acquiring accurate DHI data is crucial for its use in advanced mathematical models within feasibility software, informing decisions about optimal β and tracking algorithms for PV deployment. Decomposition models, which calculate DHI from GHI using various parameters in conjunction with the K_t, offer an alternative to direct DHI measurements, addressing a critical need [148]. The closure equation (equation 4) in conjunction with SZA can then be deployed to estimate DNI [166].

The scientific community has responded to the demand for DHI without high start-up costs, ongoing calibration, or maintenance [148-152] by developing mathematical equations. Liu and Jordan [153] laid the groundwork by connecting K_t with the diffuse fraction, K_d (which is the ratio of DHI to GHI). Subsequent researchers expanded upon their work, incorporating geo-specific parameters and time resolution from daily to hourly [154]. Orgill and Hollands' model [155] used irradiance data from a single meteorological site (ϕ = 43°), generating DHI predictions from K_t,

resulting in three-order polynomials. The Erbs model [156], built upon earlier work, utilised four years of measured data across 31° ≤ ϕ ≤ 42° to establish its constants and parametric functions. Reindl et al. proposed distinct piecewise index intervals based on the assessment of measured climatic variables for 28° ≤ ϕ ≤ 59°, varying in input data and complexity [157]. Additionally, Ridley et al. [158] developed a five-parameter predictive model, as opposed to piecewise functions, for 7 ϕ values in the range of 12° to 51°. Decomposition models are developed based on data collected from specific locations, thus, they must be evaluated thoroughly before they can be applied elsewhere.

Previous studies have centered on determining the most suitable decomposition model by comparing data from diverse weather stations across the globe using several statistical measures [159]. An investigation by Yao et al. [160] scrutinized 108 decomposition models, based on hourly and daily data. It was discovered that intricate polynomial models, dependent on sunlight hours, could accurately depict locations with climates and geographical positions similar to Shanghai. One might speculate that models of greater complexity, encompassing more parameters, would deliver superior accuracy. However, Behar et al. discovered a contrary conclusion in a desert climate at ϕ = 28° [161]. After reviewing 17 models, it was found that simpler models outperformed the more complex ones. Further confirmation of this came from work by Zhou et al. who modelled hourly diffuse fraction based on apparent solar time and sky conditions clustering [162]. This conclusion aligns with the general agreement reached by Gueymard [12] and Stein [163], with the latter assessing 30 sites in North America, with 34° ≤ ϕ ≤ 48°. A recent study by Yin et al. focused on developing models for DHI estimations by categorizing sky conditions at five locations in China [164]. The discrepancy in findings and the lack of consensus between Yao, Behar, and Gueymard can be attributed to the K_d of the sky at each location. In a dry climate, K_d is low, implying that the diffuse component is minimal. Hence, most of the horizontal irradiance sum would originate from DNI. This observation helps to rationalize Behar's argument that simpler models excel in such environments. On the other hand, Shanghai is recognized for the high presence of diffuse irradiance, necessitating the use of more complex models.

Abreu et al. [34] examined 121 distinct models across 48 radiometric stations worldwide, with 25 stations classified as temperate climates. The conclusion drawn was that 13 out of the 121 models were suitable. Gueymard and Ruiz [21] reviewed 140 decomposition models across 54 stations, on a minute-by-minute basis, dividing them based on the count of predictors. Half of these stations were situated in locations with a temperate climate. It was found that complex models with additional inputs outperformed simpler ones. It was highlighted that the Engerer2a model [159], with its extensive set of predictors, is particularly suitable for both global and

temperate climates. Subsequently, the Engerer2a model, originally validated using minute-by-minute irradiance data from Australia, inspired Bright et al. to develop seven newer models [165]. These models, named Engerer2b to Engerer2h in this thesis, were each tailored for specific temporal resolutions (ranging from 1 minute to daily irradiance) using a global dataset, with adjustments made to their coefficients. Notably, these new models incorporated the TJ model [234] for clear-sky global horizontal irradiance (GHI_{Clear}) estimates.

Following this, several models emerged. The Starke1 and Starke2 models [167] were introduced, adjusting coefficients for Australian and Brazilian data respectively, employing the Simplified Solis GHI_{Clear} model in their piecewise equations [168]. Concurrently, Paulescu presented a model combining regression with indicator functions [169]. Starke et al. proposed the Starke3 model, examining one-minute data from global stations [170]. Simultaneously, Every et al. introduced the Every1 model, a quasi-global model adjusting the Boland-Ridley-Lauret (BRL) model [171], alongside Every2, which modified BRL coefficients for different Köppen-Geiger climate zones [172].

Yang [173] introduced the Yang4 model, which was developed using minute-by-minute data collected from various stations and integrated with the McClear GHI_{Clear} model [174]. The primary aim of Yang4 was to reduce reliance on satellite-derived data for input, a common practice across differing satellite-derived irradiance databases as outlined in [175]. This model included enhancements such as the incorporation of albedo effects, cloud coverage data, and an advanced physical representation of radiative transfer processes. Notably, when compared against ten different machine learning (ML) models, the Yang4 model demonstrated superior accuracy [176]. Building on this, the Yang5 model was launched [177], which incorporated new coefficients that consider cloud cover frequency, aerosol optical depth, and surface albedo climatology derived from satellite imagery. Like its predecessor, Yang5 utilized the same GHI_{Clear} model and exhibited improved performance in DHI estimation across more than 70% of the 126 stations tested.

Palmer et al. [178] assessed three decomposition models at three UK locations, using two stations previously utilized by [12], as well as one in Loughborough (φ = 52.76°). Their motivation stemmed from the lack of consensus regarding model complexity found in the literature. Through their evaluation of the Erbs [156], BRL [171], and De Miguel [179] models against hourly irradiance data, there is a tendency to underestimate DHI, indicating potential for model improvement. Additionally, Munoz et al. [180] analyzed historical GHI and DHI data from 1982 to 1999 under stringent data quality control to evaluate six different models across three UK locations,

employing error histograms. It was found that the Reindl [157] model performed best in an hourly-based context, although the other five models were in close competition.

Table 3: Various Optical Model pairs deployed in different feasibility software [181][182].

Decomposition Model	Transposition Model	Abbreviation	Software
Erbs [156]	Perez [185]	Erbs-Perez	INSEL [193] PVSyst [192]
	Liu-Jordan [186]	Erbs-LJ	PVToolbox [195] INSEL [193] RETScreen [194]
	Skartveit-Olseth [187]	Erbs-SO	INSEL [193]
	Temps-Coulson [188]	Erbs-TC	
	Willmot [189]	Erbs-Willmot	
	Bugler [190]	Erbs-Bugler	
	Hay [191]	Erbs-Hay	PVSyst [192] INSEL [193]
Reindl [157]	Perez [185]	Reindl-Perez	PVSOL [201] TRNSYS [196]
	Skartveit-Olseth [187]	Reindl-SO	PVSOL [201]
	Hay [191]	Reindl-Hay	TRNSYS [196]
DIRINT [183]	Perez [185]	DIRINT-Perez	SolarAnyWhere [197] SolarGIS [198]
DISC [184]	Hay [191]	DISC-Hay	Meteonorm [199]
	Perez [185]	DISC-Perez	
	Skartveit-Olseth [187]	DISC-SO	
BRL [171]	Liu-Jordan [186]	BRL-LJ	Summa [200]

It is essential to develop a comprehensive and transparent benchmarking framework to evaluate the wide variety of decomposition models available. This need arises from the scarcity of solar irradiance data in temperate climates, especially in regions such as the UK, where further detailed research is urgently needed. Currently, only three modern weather stations in the UK provide open access to both GHI and DHI data. Identifying the most effective decomposition model for these specific conditions and determining if particular decomposition models are ideally suited for certain datasets represent significant opportunities for future research. The diversity of models underscores the importance of establishing a standardized framework to

support accurate DHI estimation. It is critical to adopt a framework that can be implemented in other regions. Such a shift is consistent with prevailing solar energy guidelines, underscoring the significance of considering global implications in any model developed for widespread application [40][202]. Furthermore, a thorough evaluation of decomposition models is crucial because various feasibility software applications, as detailed in Table 3, utilize different decomposition methods to estimate DHI (or DNI) prior to transposing these estimates to calculate POA.

2.3.2 The Importance of Transposition Modelling

The economic viability of PV systems, be they categorized as FT or tracking, largely relies on accurate POA estimations. This evaluation is typically executed using a View-Factor (VF) method, implemented through feasibility software. Due to the unpredictability of PV systems' performance, precise modelling is crucial, irrespective of geographical location. The primary approaches to modelling irradiance involve Ray-Tracing (RT) and VF methods [203]. RT is a rendering technique that traces light rays from their origin, calculating the impact of light to render objects. RT applies radiative transfer theory in reverse, emitting rays at the sampling point and directing them from the module to the sky. This approach entails creating a ray at the sampling point, which passes through the view plane to the object (e.g., the hemisphere or other introduced geometries). By accounting for complex geometries, such as racking or obstructions, and analyzing shading, these modelling techniques can evaluate edge effects in bifacial modules. Due to its increased complexity and longer run times, reverse RT demands the use of High-Performance Computing (HPC) [204].

VF models are grounded in the thermal radiation heat transfer theorem and employ an etendue geometric quantity to gauge the flux-gathering ability of an optical system [205]. This quantity is essentially a mathematical product of the solid angle projected from the source as seen from the collector, the source, and the collector's area. The use of VF models has gained traction across a wide range of software applications due to their unique benefits. These advantages include faster computation times, lower computational resource requirements, seamless integration with other industry software and tools, and adherence to the standard used for PR calculations [192].

Prior research has compared between RT and VF methods. For example, Pelaez et al. [89] compared three models (two VF and one RT) with actual measurements under various inter-row spacing, β, and ρ, finding that all models demonstrated good agreement with BG_{Energy} with a 2% error. In a similar study, Sanchez et al. [101] compared three models across two locations (φ = 51.77° with a south-facing $\beta = 35°$ and φ = 9.85° with $\beta = 15°$), both with a system setup

featuring h = 1m. The comparison with measured data revealed that the VF method produced results closest to the actual measurements when considering β and ψ_{sys}. Further research [206] compared a single VF model and an RT model under various conditions, including β, ρ, and h, at φ = 41.64°. The study concluded that the VF model outperformed the RT model in all cases, except for inter-row spacing, where the difference was equal to 1.77%.

A key aspect of VF models is their reliance on transposition models, which are often used interchangeably with sky diffuse models. These models separate POA and BOA estimations. However, it is important to note that BOA estimation necessitates POA verification for the site of interest [7]. Equation 14a calculates POA using components of Beam Tilted Irradiance (B_t), Reflective Tilted Irradiance (R_t), and Diffuse Tilt Irradiance (D_t) [207]:

$$\mathrm{POA} = B_t + R_t + D_t \tag{14a}$$

B_t, through equation 14b, employs DNI and the angle of incidence (AOI) as seen Figure 12:

$$B_t = DNI \cdot \cos AOI \tag{14b}$$

The approach to calculate R_t in equation 14c assumes isotropic conditions, meaning that regardless of AOI, all rays exhibit the same intensity. The simplified ground re-emission of rays is treated as a Lambertian surface, where the amount of ground re-emission relies on ρ [208]. In this context, an infinite array is assumed, with the ground visible to the array from the intersecting slope extending to an infinite horizon.

$$R_t = GHI \cdot \rho \cdot \frac{(1 - cos\beta)}{2} \tag{14c}$$

$$D_t = \mathrm{DHI} \cdot R_d \tag{14d}$$

Equation 14d shows that D_t consists of DHI and R_d, which is the transposition factor. R_d heavily relies on the type of transposition model employed, be it isotropic or anisotropic. For a tilted inclined surface, the intensity of the D_t depends on the fraction of the sky dome it observes, as isotropic models assume uniform diffuse sky radiation across the sky dome. In contrast, an anisotropic sky model makes different assumptions. It considers diffuse sky radiation to be anisotropic near the circumsolar region (i.e., the area surrounding the solar disk) and introduces various horizon brightening factors, while maintaining isotropic conditions for the rest of the sky dome.

Numerous transposition models have been developed and presented for POA applications [185-1910, [209-217]. As indicated in the literature, these models can predict solar irradiation with

adequate accuracy [218-220]. However, it remains challenging to pinpoint a reliable transposition model that can serve as a standard reference, especially on a minute-by-minute basis. Generally, transposition models are site-dependent, given that they are based on various assumptions about sky distribution and have empirical origins. The selection of the best-performing model typically involves comparing it to measured POA data at a specified FT setups, with minimal focus on tracking systems [79].

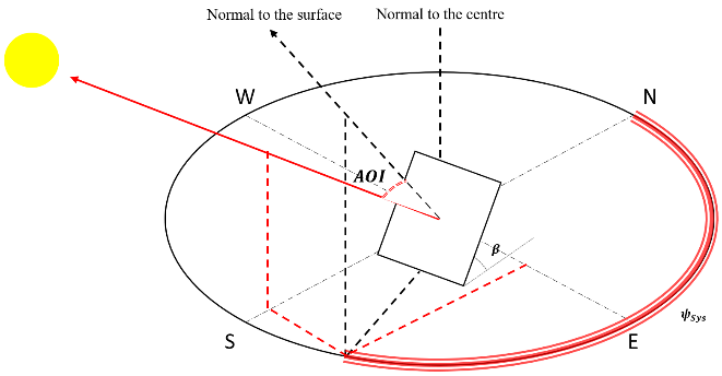

Figure 12: For AOI determination, the sun coordinates are correlated with the FT orientation. This figure was adapted from [20].

Limited research has been conducted on transposition validation for differing installations. Nonetheless, a noticeable inconsistency exists in the literature. Raptis et al. [221] analyzed four distinct transposition models for a south-facing $\beta = 38°$,and φ = 43.67°, concluding that the Perez model [185] was optimal. Mubarak et al. [222] compared five models at β =10° to 70° in 10° increments and at φ = 52.38°. They discovered that the Liu-Jordan model [186] best matched measured data up to 30°, after which the Hay [191] model performed best. Yang [223] evaluated 26 models against measured data that consisted of south-facing setup with β =45° at φ = 53.14° and determined that the Reindl [221] model was the top performer.

Furthermore, Wlodarczyk-Nowak [224] conducted a study on 14 models at two β, ($35°$ and $50°$), and at a similar φ, finding that the Temp-Coulson [188] model worked best for the former and Bugler [190] for the latter. It is evident that no consensus has been reached for FT installations. When tracking is incorporated, whether through HSAT or DAT, various ψ_{sys} and β combinations are introduced, necessitating further research to identify the ideal transposition model or a combination of models that most accurately approximate measured data.

The computation of BOA, it shares similarities with its front-side counterpart (POA), as demonstrated in equation 15. Both the reflected beam and diffuse components, B_{tr} and D_{tr},

follow the same methodology outlined in equations 14b and 14d, but consider a 180-degree adjustment for β [92][225]; as illustrated in Figure 13. Nonetheless, the ground-reflected component, R_{tr}, can no longer rely on the same initial assumptions due to influential factors such as shading, h, ψ_{sys}, ρ, and notably, the spectral effect and non-uniformity [208][225]. There are multiple methods for calculating this component, varying in complexity, but their applicability is contingent on specific case circumstances [208][226][227].

$$\text{BOA} = B_{tr} + R_{tr} + D_{tr} \tag{15}$$

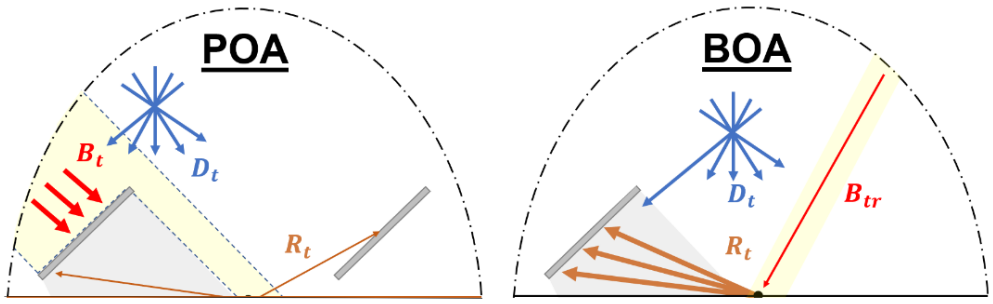

Figure 13: Differences between POA and BOA irradiances due to tilted components.

Obtaining POA (and consequently BOA) estimates relies on measured GHI, DHI, and DNI data, but it is uncommon for all three components to be measured. Consequently, decomposition must occur to obtain DHI, which can then be input into transposition models. No single combination of decomposition and transposition is universally recognized as a standard for converting GHI to POA; a variety of combinations are utilized. Therefore, during the incorporation of both decomposition and transposition models, as carried out in feasibility software, errors tend to escalate. This is attributable to a cascading effect where an underestimated DHI stemming from decomposition models, could result in an overestimated DNI, and subsequently, POA when these irradiance components are transposed. Conversely, an overestimated DHI would yield the opposite behaviour. This inconsistency results in differing POA (and thus BOA) predictions, even when the same GHI input is provided.

There are limited studies evaluating decomposition-transposition model pairs. For example, Lave et al. examined two model pairs across 9 locations in the US for FT systems (predominantly with a south-facing β = 25º), concluding that regardless of the decomposition model used, the choice of transposition model resulted in differing outcomes. The Hay model showed less error compared to its Perez counterpart [79]. In their research, Sun et al. implemented the Orgill and Hollands decomposition model [115], coupled with the Perez transposition model. Their validation exercises focused solely on FT systems set at β = 15° and 30° at φ = 35°, revealing a

variation in modelled irradiance BG of 6.40% compared to measurements [227]. Furthermore, the DIRINT-Perez model pairing was leveraged in an additional investigation [7], wherein Levelised Cost of Electricity (LCOE) calculations served as a validation criterion. An identical model pairing was used across six locations for an irradiance BG study [226].

The collection of 6 sites involved an HSAT and south-facing FT at φ = 35°, resulting in a 6% error from modelled BG. The setup at location 2 compromised an FT system of β = 34°, supplemented by two SATS at φ = 37.5°, resulting in a 5% error from the model. Location 3 was near the equator and featured a 10° β. Location 4 maintained β=24°, identical to its φ, whereas location 5 (φ = 51°) featured an FT setup with β = 35°. The BG from locations 3, 4, and 5 showed considerable consistency with the model, displaying errors of only 1%, 3.16%, and 1.65% respectively.

Yang et al. assessed ten transposition and five decomposition models under tropical conditions at φ = 1.3° [228]. It was discovered that combining both types of models leads to increased prediction errors when converting irradiance from horizontal to tilted surfaces, with the error magnifying as β increases. This highlights the need to explore the percentage error in the modelling results at higher tilts, which is important for bifacial systems or monofacial systems requiring greater β for optimal incident angle. Maani et al. noted that limiting studies to a single model combination might result in less accurate model chain indicators [229]. Roberts et al. conducted a year-long study at φ = 52.7°, analyzing 16 pairs of optical models using hourly data. Their research highlighted that the DISC decomposition model paired with the Liu-Jordan isotropic model delivered superior accuracy compared to other combinations; validated on a FT system (β = 45° with ψ_{system} of 12° relative to the South). It was recommended that future research delve into the empirical derating factors employed in PV modelling today, considering diverse system configurations with various β -ψ_{system} combinations [230].

Despite these findings, it is notable that the majority of the optical model pair validation studies use hourly data and FT systems. This leaves a knowledge gap concerning their utility for a range of angles, a prerequisite for tracking systems, along with a higher temporal resolution and under temperate climates. Additionally, Gueymard showed that most of the error in predicting POA irradiance at a sunny location stems from the empirical separation of direct and diffuse components when these are not measured locally [231]. Hofmann et al. noted that decomposition models tend to produce a broader range of outcomes, whereas transposition models significantly influence these results. Nevertheless, additional validation is necessary for areas with diffuse climates, and a range of β needs to be considered [232]. These findings raise a critical question about whether similar conclusions can be drawn for locations with high levels of diffuse light, and which has a greater impact on POA irradiance: the decomposition or the

transposition aspect. It is essential to explore not only the optical model pair but also the transposition process, particularly in environments with variable conditions such as the temperate climate of the UK. Even when rare measured values of DHI, DNI, and GHI are available, it remains crucial to determine which transposition model exhibits the smallest deviation. Investigating both the input of decomposed data to obtain DHI and DNI, and then their transposition (a process already implemented by various feasibility software as indicated in Table 3), as well as using measured DHI and DNI, could help elucidate why certain transposition models underperform in a temperate climate.

2.3.3 Evaluation of Clear-Sky Modelling Accuracy

Clear sky models are designed to predict the solar irradiance that reaches the Earth's surface in cloudless conditions [233]. These models are pivotal for estimating the potential maximum energy output of PV systems. Moreover, the general estimation of all-sky irradiance is derived from these clear sky calculations, adjusted by an attenuation factor that accounts for the solar position. By integrating time series data from satellite-derived irradiance with clear-sky model outputs, and a transmittance function reflecting the cumulative effects of clouds and surface interactions, a comprehensive irradiance profile is constructed. This transmittance is routinely assessed through the observation of atmospheric reflectance via satellite sensors. As a result, all-sky irradiance retains a proportional relationship to its clear-sky counterpart, forming the basis for all subsequent irradiance modelling. Additionally, GHI_{Clear} and Clear sky DNI (DNI_{Clear}) serve as essential inputs in various irradiance models, including decomposition types like Engerer2a [159] and Yang5 [177], underscoring their significance in solar irradiance forecasting.

Clear sky irradiance models, similar to decomposition models, utilize empirical relationships that circumvent the complexities inherent in detailed radiative transfer modelling. For instance, the Threlkeld-Jordan model utilizes three coefficients, based on the SZA, to estimate GHI_{Clear} [234]. El Mghouchi et al., utilizing three years of data collected every ten minutes in a dry, northern Moroccan climate (ϕ = 35.6º), refined this model to also factor in SZA and E_a [235]. Furthermore, with the same input parameters as El-Mghouchi's model, Kumar's model expanded upon this by incorporating atmospheric pressure to detail the attenuation effects on solar irradiance, tested with half-hourly data at a ϕ of 36.5º [236]. The Ineichen-Perez model introduced an innovative approach by integrating the Linke turbidity factor, aiming to reduce the model's reliance solely on solar geometry. This model was validated using hourly data from seven stations across ϕ: 35.1º to 45.8º, considering the impact of aerosols and water vapor [237]. Similarly, the Simplified Solis model employs the Bouguer-Lambert-Beer law, with variables like AOD at 700 nm, PW, and

atmospheric pressure [168]. Bashahu further developed this model using annual data from a ϕ of 14.7 º, adding AOD550 as a novel parameter, showing considerable accuracy at a nearby ϕ of 14.7º [238]. Moreover, the MAC2 model enhances transmittance calculations, simplifying Rayleigh scattering calculations relative to air mass and incorporating AOD data. It considers direct transmittances for Rayleigh scattering, ozone, aerosols, and a term for water vapor absorptance [239]. The Iqbal C model is another advanced example, incorporating eight parameters, including ozone concentration and nitrogen dioxide levels in the atmosphere, alongside the Angstrom exponent and AOD550 [20]. The REST2 model, developed by Gueymard in 2008, separates its analysis into two spectral bands (0.3 - 0.7 μm and 0.7 - 4.0 μm), using parameterizations from the SMARTS spectral radiation model to account for various atmospheric transmittances including Rayleigh scattering, mixed gas absorption, ozone, nitrogen dioxide, water vapor, and aerosol extinction [240]. Lastly, the McClear model stands out as a comprehensive, model-based approach utilizing a vast library of radiative transfer outputs to simulate detailed calculations [174]. As a part of the freely accessible CAMS, McClear operates as a "black box", providing users with results directly tied to extensive atmospheric data, without the option for alternative data inputs.

Generally, simplified models can yield acceptable results in regions where atmospheric and environmental conditions align with the model's foundational assumptions, which typically presume low to moderate levels of water vapor and aerosols [233]. A significant challenge with more advanced Clear Sky models is their dependency on detailed atmospheric data inputs. Often, the availability and quality of such data are constrained, limiting the models' accuracy. Consequently, deploying more complex models does not guarantee enhanced accuracy and might, under circumstances of inadequate or erroneous data inputs, lead to decreased model performance [241]. Validation studies for these models vary in their temporal resolution and geographical scope. For example, Badescu et al. examined 54 models at two sites (ϕ = 44º and 46º) using hourly data, identifying six clear-sky models capable of approximating GHI_{Clear} and developed an empirical model named after the author [242]. In contrast, Cros et al. assessed four models across three sites on a minute-by-minute basis, finding McClear to be the most accurate [243]. Similarly, Segupta et al.'s research across seven sites compared models for both DNI and GHI on a minute scale, highlighting REST2 as the superior model [244]. These findings underscore the necessity for more comprehensive validation studies, particularly focusing on spatial variability and minute-by-minute temporal resolution, to address existing gaps in model validation.

Ruiz-Arias and Gueymard reviewed 36 validation studies, creating a consensus around 15 robust clear sky models [245]. These models were assessed across different temporal resolutions and climates, pinpointing major discrepancies caused by high aerosol loads, elevated site locations, and low solar altitudes. This review underscores the need for more refined validation studies that integrate measured irradiance and sunphotometer data at the same locations to advance the development of a universally effective model, particularly in temperate climates. Moreover, Sun et al. systematically reviewed variables used in 75 clear sky models across diverse global sites, with the REST2 model emerging as one of the top performers [246]. Although REST2 is deemed as a proprietary, its efficacy underscores the critical role of high-quality input data in determining model accuracy.

Research has explored how satellite variables such as AOD, AE and PW impact the precision of solar irradiance predictions [247],[248]. For example, Gueymard found that PW data from MERRA2 introduces some uncertainty into clear-sky GHI estimates, although the effect is not marked numerically [249]. A significant finding by Ruiz-Arias et al. is that the error in DNI_{Clear} predictions could increase sixfold when substituting AERONET AOD measurements with those from MERRA-2 [250]. Additionally, a study by Salamalikis et al. on the uncertainties in DNI induced by CAMS AOD, using AERONET AOD as a baseline, highlighted regional differences, ranging for Mean Bias Deviation (MBD) -4.1% to 5.3%, with the latter in high AOD locations and the former in desert climate locations [251]. These findings underscore the variability in error propagation from satellite data to solar irradiance estimates across different geographical and climatic contexts. However, there has been limited research on the selection of satellite data products for optimizing clear-sky irradiance modelling. Sun et al. evaluated 95 clear sky models for clear-DNI at 100 radiometric sites and reiterated that REST2 provided the most accurate estimates [252]. However, it was noted the necessity for further research to assess the sensitivity of top models to variations in input data sources, highlighting ongoing challenges in the field.

The literature on clear sky models is extensive and diverse, reflecting a range of complexities designed to manage solar transmittance. These models vary from simplistic ones that use basic inputs like SZA in the Threlkeld-Jordan model, to more intricate physical models like McClear or REST2, which incorporate multiple atmospheric variables, including complex factors such as the AE and AOD550. Accurate satellite data are crucial for these models since atmospheric conditions directly impact the attenuation of solar irradiance. Gueymard highlights that prediction errors in these models mainly arise from two sources: errors in aerosol input data and the model's inherent limitations in accounting for aerosol effects, especially under high aerosol conditions [253]. Notably, these inaccuracies have a more pronounced impact on DNI

predictions, due to how errors in aerosol representation affect direct and diffuse irradiances differently.

2.3.4 Insights into Photosynthetically Active Radiation Irradiance Modelling

PAR irradiance is essential for evaluating the feasibility of AgriPV systems. Regulations specify that crop yields must maintain certain thresholds to ensure the successful integration of photovoltaics with agricultural land use [31][139][141]. This requirement highlights the critical nature of accurate PAR measurement. Unlike more common irradiance measurements such as GHI (as well as DHI and DNI), PAR irradiance data are not as readily accessible. This scarcity might stem from the relatively recent prominence of AgriPV in renewable energy discussions [258]. Accurate estimation of PAR irradiance is hence crucial. Such data is utilized in various modelling programs, such as CropWat [254], which predict crop yields based on defined mathematical relationships.

The significance of PAR irradiance in crop development is well-known, yet there is a notable scarcity of PAR measurements. This is compounded by the absence of a global network for measuring PAR that adheres to standardized quality control protocols. This situation has led to fewer studies on PAR compared to the more frequently analyzing GHI or DHI. Although atmospheric radiative transfer models can estimate PAR components, these models are often highly complex and demand substantial computational resources. As a result, researchers have increasingly relied on empirical mathematical methods for estimation. Accurate determination and comprehensive understanding of PAR irradiance are essential, yet measurements remain limited. Consequently, researchers have endeavored to estimate PAR irradiance using various conversion factors by multiplying different parameters. Numerous studies have identified PAR ratios as dependent on variables such as location, season, sky conditions, and altitude [255]. However, there is no agreed-upon consensus, making it challenging to predict reasonable PAR ratio values for specific sites and seasons. This lack of clarity underscores the importance of incorporating meteorological and solar position parameters in research.

The detailed analysis by Nwokolo et al. outlines various methods for estimating PAR irradiance, as identified in literature, focusing mostly on daily predictions with some hourly assessments. Since then, advancements have been achieved in predicting PAR irradiance by leveraging GHI and additional parameters [255]. Wang demonstrated the impact of sky clarity on PAR across China, introducing a validated model in two central locations [256]. Wang further elaborated on this by incorporating solar geometry into their research, covering 39 different locations on both hourly and daily scales. Similarly, Peng et al. developed a versatile PAR model suitable for temperate

climates in China [257]. Furthermore, Aguiar ventured into modelling PAR in Southwest Amazonia, employing methods ranging from simple ratios to complex formulas integrating sky clarity and precipitable water, suitable for all sky conditions [259]. Ferrera-Cobos explored 22 models for estimating daily PAR in oceanic and Mediterranean climates, employing site adaptation techniques and variables like relative humidity, temperature, and extraterrestrial irradiance [260]. Their study compared regression models and an ML approach, finding negligible differences in performance. Similarly, Proutsos et al. examined a high-altitude Mediterranean forest in Greece, developing models for estimating ultraviolet radiation and PAR based on hourly data, highlighting the importance of optical thickness and temperature [261]. Similarly, Escobedo et al. differentiated parts of the electromagnetic spectrum, in Brazilian climates using daily observations [262]. Furthermore, Akitsu et al. explored models incorporating GHI, precipitable water, and pressure alongside sky clarity under all sky conditions to demonstrate the interplay between said parameters and PAR [263]. These models, however, demonstrated diminished accuracy in winter conditions and in environments rich in aerosols, which are typical characteristics of temperate climates.

Studies suggest that models incorporating DHI or employing Perez coefficients (that are deployed in transposition modelling [185], which are direct derivatives of DHI and DNI), tend to exhibit improved performance [264-266]. Garcia-Rodriguez et al. incorporated meteorological indices for PAR irradiance modelling, using the International Commission on Illumination (CIE) [267] standard sky classification alongside Perez brightness and clearness coefficients for all sky conditions [268]. Reliance on DHI and similar metrics complicates analyses due to their sporadic measurement. When data are lacking, the need for specialized decomposition models becomes crucial, as these models vary significantly depending on temporal resolution and geographical location. Furthermore, inaccuracies in initial predictions can be exacerbated in subsequent stages, resulting in notable discrepancies in the final results. Although numerous decomposition models exist in the literature, their integration can introduce complexities. This is due to the varied ways these models function across different climatic zones, temporal resolutions, and input parameters, not to mention their divergent estimates of these parameters. Such complexities can lead to inaccuracies, particularly when using these models to calculate Perez coefficients. Errors may arise, for example, from overlapping ranges of sky brightness that the models may not correctly distinguish. Lu et al. emphasize the importance of advancing PAR prediction methodologies across various global climates [33]. This advancement is critical for expanding the market penetration of AgriPV [145]. It should be noted that while PAR irradiance models are necessary, said models should also be readily available and accessible.

There is a crucial demand to derive PAR estimates from GHI and other available parameters. Conversion ratios from GHI to PAR under conditions of high solar irradiance indicate a reliance on the sky's optical path, yet this relationship becomes complex under overcast conditions or variable weather, requiring multiple parameters for precise PAR conversion, a significant factor in high-ϕ temperate regions. While numerous studies have explored the conversion of GHI to PAR across various climates, the application of these models in new, especially temperate, environments has been scarcely explored. This deficiency is notable because models validated in diverse climates might not consider the unique sun path effects vital for accuracy in higher ϕ, temperate regions, where latitudinal differences substantially affect sun angles and model precision. Atmospheric conditions also vary by location, altering the scattering and absorption of solar radiation, and thus affecting PAR values. Moreover, the impact of cloud cover on GHI and subsequently on PAR is substantial, with many models overlooking regional differences in cloudiness due to local weather patterns, leading to potential errors in solar irradiance predictions. Furthermore, the reliance on limited datasets, typically focusing on daily or hourly solar irradiance for specific climates, highlights the need for more comprehensive models that account for the various factors influencing PAR in sub-hourly intervals. To address these challenges, it is essential to develop a mathematical model that predicts PAR irradiance in temperate regions without depending on conventional DHI or Perez coefficients, and instead utilizes readily available data. This approach would improve the accessibility of PAR estimations, thus facilitating the adoption and market growth of AgriPV systems where PAR data are critical for LER calculations.

2.3.5 Summary

A comprehensive review of the literature has revealed several critical research gaps in the field of solar irradiance estimation, particularly at a minute-level resolution within temperate climates. These gaps revolve around understanding the limitations of current models, identifying areas of improvement, and developing enhanced approaches to bridge existing shortcomings. One key area of focus involves evaluating the limitations of feasibility software, specifically in terms of the types of models employed and their overall performance. Additionally, the decomposition process presents a challenge due to the extensive variety of available models. A systematic approach is needed to identify and benchmark the most robust models by narrowing down this large pool and establishing a reliable evaluation framework. The evaluation of transposition models also remains essential, with particular attention given to their performance under diverse sky and cloud conditions. Examining these models from multiple perspectives can help assess their adaptability and effectiveness in different scenarios. Enhancing GHI_{Clear} and DNI_{Clear}

estimations represents a key area of research. This improvement involves integrating different satellite-derived data to refine crucial parameter inputs, thereby increasing the precision and reliability of clear-sky models. Identifying the most suitable satellite data is essential to achieving these enhancements. Furthermore, the development of AgriPV systems necessitates a tailored model for predicting PAR at sub-hourly intervals in temperate regions. This model should prioritize ease of use by relying on readily accessible inputs rather than complex or data-intensive requirements. Addressing these research gaps is essential for advancing the accuracy and applicability of solar irradiance models and supporting the widespread deployment of PV systems.

Chapter 3 Benchmarking Framework for Decomposition Models

3.1 Introduction

The chapter addresses the considerable variety of decomposition models that have emerged from differing inputs, data durations, and meteorological empirical foundations. This diversity is driven by the continual need for researchers to develop mathematical models that can approximate DHI from various parameters as a function of K_t. As a result, a multitude of models exist, each requiring rigorous validation to establish their robustness. This necessitates the implementation of a benchmark framework to identify robust models effectively. The chapter introduces a clear and structured benchmarking framework to evaluate decomposition models, using the United Kingdom as a case study. This choice is due to the challenges faced by many locations globally, which lack open access to weather stations or require complex maintenance and calibration of pyranometers and pyrheliometers for DHI and DNI measurements, respectively. The evaluation will cover 104 promising decomposition models identified in earlier studies in temperate climates. The assessment includes four series of tests to determine the most reliable models, examining the effects of varying temporal resolutions, spatial homogeneity, dataset influence, and changes in clear-sky irradiance inputs on the decomposition models.

3.2 Establishment of the Transparent Framework

Due to their empirical foundations, many decomposition models have traditionally relied on hourly irradiance data. However, as industry and research shift towards minute-by-minute irradiance values, it becomes crucial to assess the impact of temporal resolution on these models in both time domains. Particularly in a temperate climate such as the United Kingdom, where weather conditions can change significantly, hourly irradiance levels may not adequately capture the nuances of sunlight variations, including the amounts of diffuse and scattered irradiance. Therefore, an examination of the shift from hourly to minute-level inputs is vital. The first test in the proposed framework assesses the impact of temporal resolution on model accuracy. Additionally, the increasing demand for high-frequency solar irradiance data in PV simulations underscores the need for this focus. This framework is especially pertinent for larger SZA, where tracking systems provide distinct advantages, highlighting the limitations of using

hourly data for precise applications. The second test focuses on the spatial homogeneity performance of decomposition models. This involves evaluating the reliability of models across various geographic locations within temperate zones. An essential aspect of this assessment is determining whether a model performs consistently well across different locations or if its effectiveness is location-specific. The goal is to identify models that are inclusive of diverse geographic conditions, which is especially crucial in regions with limited access to open weather stations. Such an evaluation ensures that the models account for environmental variables, such as sun angles, and set a standard for geographical inclusivity in their performance.

The dataset period influence constitutes another critical test. This assessment investigates the effectiveness of models using data from different years, addressing the challenge of limited data availability from specific weather stations. Comparing models across diverse datasets is essential for evaluating their consistency over time and their adaptability to changing weather conditions and varying sky scenarios. This approach adds a vital dimension to understanding the robustness of decomposition models, emphasizing their performance stability across different temporal spans. Transitioning to one-minute irradiance data introduces new parameters that are distinct from those used in traditional hourly decomposition models. A key feature of these finer-resolution models is the incorporation of clear-sky irradiance, an essential element for their functionality. The fourth test here is to examine the influence of varying clear-sky irradiance approximation equations, which differ based on the number of input levels, ranging from one to ten. This exploration aims to identify the optimal clear-sky model that, when used in conjunction with decomposition models, could significantly enhance accuracy levels and hence, the number of robust models. Earlier studies [12] have identified models with an MAD value under 30% as highly effective. Among the 104 models evaluated in this study, a large number conform to this statistical benchmark (see Table A1 in Appendix A). For this research, the criterion is more stringent, setting a threshold below 15% as the sole measure of acceptable performance in each test.

Table 4: An overview of the locations and datasets used in this framework . The Köppen Climate Classification of Cfb is defined as a "Temperate", "without a dry season" and with a "warm summer" [38].

Site	Latitude (°)	Longitude (°)	Köppen Climate Classification [38]	Study Period
Camborne	50.21	-5.32	Cfb	June 1, 2015 - June 1, 2017
Chilbolton	51.15	-1.44	Cfb	June 1, 2015 - June 1, 2017 June 1, 2021 - June 1, 2023
Lerwick	60.14	-1.18	Cfb	June 1, 2015 - June 1, 2017

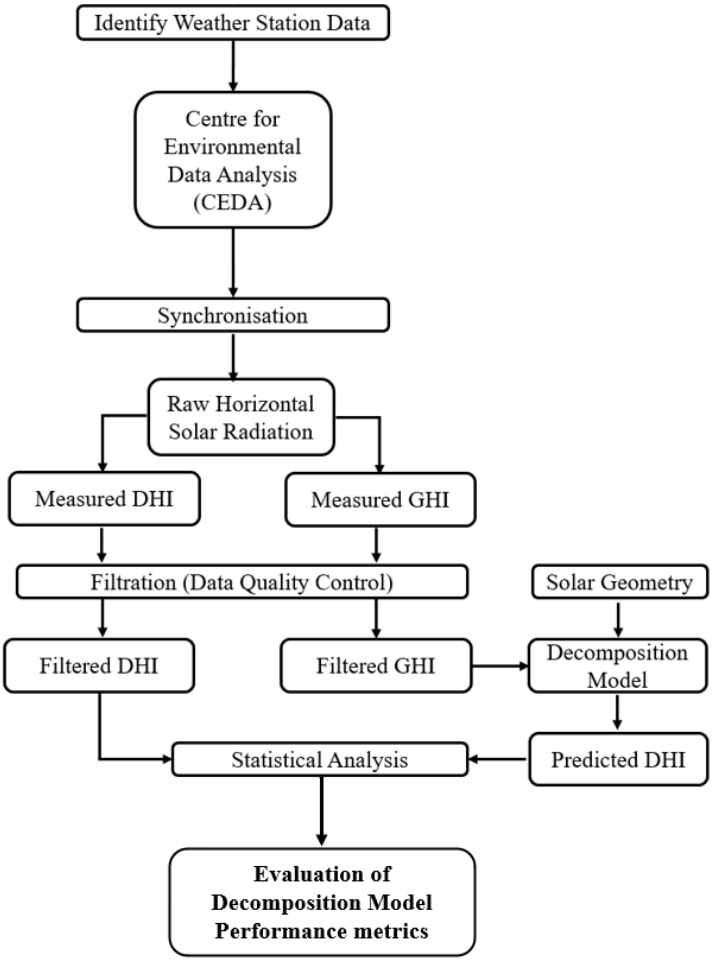

Figure 14: Evaluation method for the 104 decomposition models using open-source data based on horizontal irradiance measurements.

A search revealed 14 different DHI datasets from diverse ϕ areas across the UK in hourly format. These, however, have been retired owing to their requirement for steady operation and maintenance [269]. Three open-access locations (as per Table 4) were selected as they are capable of simultaneously recording both GHI and DHI in a minute-minute format. These include Lerwick and Camborne, from the Baseline Surface Radiation Network (BSRN) [54], and Chilbolton from the Centre for Environmental Data Analysis (CEDA) Archive [270]. Given this context, it becomes crucial to identify resilient decomposition models that exhibit strong alignment across these three locations, marking this as an important research area. The three selected sites adhere to standards set by the ISO [271], which has specific requirements and compliance guidelines. All data were measured using Spectrally Flat Class A Pyranometers (and their corresponding shadow ball trackers for DHI). As per Figure 14, the data is synchronized to coordinated universal time (UTC). The geometry of the sun (SZA, E_a, etc.) was sourced from the National Renewable Energy Laboratory's (NREL) Solar Position Algorithm (SPA) [53].

Table 5 presents the specific GHI_{Clear} models utilized in the respective 15 decomposition models. This consistent application of GHI_{Clear} across the study was driven by two primary considerations. Firstly, the coefficients within each decomposition model were originally derived based on these particular GHI_{Clear} implemented, hence maintaining consistency is essential for accurately assessing their effectiveness. Secondly, the study aims to investigate the potential for enhanced performance by exploring the feasibility of substituting different GHI_{Clear} models in a pair-matrix formation. This aspect examines whether the selection of which GHI_{Clear} model could potentially lead to improvements in DHI estimation.

Table 5: The 15 decomposition models studied, with their respective GHI_{Clear} models, as it relies on the decomposition model's specific coefficients calculation process.

Decomposition Model	GHI_{Clear}	Comment
Engerer1	REST2 [240]	
Engerer3		
Engerer2a	TJ [234]	Referred to Engerer2 in [159]
Engerer2b		Referred to New 1-min Engerer2 in [165]
Engerer2c		Referred to New 5-min Engerer2 in [165]
Engerer2d		Referred to New 10-min Engerer2 in [165]
Engerer2e		Referred to New 15-min Engerer2 in [165]
Engerer2f		Referred to New 30-min Engerer2 in [165]
Engerer2g		Referred to New 1-h Engerer2 in [165]
Engerer2h		Referred to New 1-day Engerer2 in [165]
Yang4	McClear [174]	
Yang5		
Starke1	Simplified Solis [168]	
Starke2		
Starke3		

A comprehensive analysis was conducted employing various GHI_{Clear} models, each characterized by distinct parameters [246]. Selection criteria for the models prioritized the highest-performing ones within each parameter category, ensuring a rigorous evaluation of GHI_{Clear} impacts as seen in Table 6. In this work, the Ineichen-Perez GHI_{Clear} model incorporated data specific to London, particularly the monthly T_L values. This model was used alongside averaged data from September and November to compensate for the absence of October values [272]. Moreover, this thesis opted for the TJ GHI_{Clear} model over the AHRAE model [46], aligning with the methodologies applied in the Engerer2b – Engerer2h evaluations. To calculate the parameters effectively, satellite data from MERRA2, provided by NASA's Global Modelling and Assimilation Office, served

as a crucial data source [274]. This approach mirrors the methodologies used in reference [246] for GHI_{Clear} assessments and allows the framework to be employed easily.

Certain limitations are apparent with this approach, firstly, due to the specific calibration conditions of the pyranometers used (namely, SZA of approximately 45º). This calibration specificity leads to increased measurement uncertainties under low irradiance conditions, such as during overcast weather, potentially compromising the accuracy of the collected data. Additionally, the assessment and validation of the models across three sites might not accurately reflect the broader characteristics of temperate climates, as different regions exhibit unique climatic traits that could affect the model's precision and relevance. This may prompt concerns about the broader applicability of the conclusions to all temperate climates. However, the primary goal here is not to generalize the results to all regions but to emphasize the urgent need to establish a series of tests for an effective benchmarking framework. Presently, a diverse array of decomposition models exists, yet there is a notable lack of transparent methodologies for their evaluation. Given the scarcity of one-minute irradiance data from UK stations (treated here as a case study) there is a critical need to identify robust decomposition models. This transparent framework can be applied in various settings, not limited to the UK or within temperate climates alone. Additionally, re-parameterization (altering the coefficients of present models) was not undertaken because it would entail an empirical approach that might unnecessarily complicate an already effective model or duplicate existing methods, rather than enhancing scalability.

Table 6: A list of the essential input parameters for each GHI_{Clear} model, including the following variables: the Solar Zenith Angle (SZA) in degrees, the extraterrestrial Horizontal Irradiance (E_a) in W/m^2, atmospheric pressure in millibars (P), site elevation above sea level in meters ($elev$), Linke Turbidity Factor (T_L), total precipitable water vapor in centimeters (PW), broadband optical depth (τ), Ångström exponent (AE), Aerosol Optical depth at 550nm (AOD550), single-scattering albedo (SSA), total ozone amount in atmospheric centimeters ($Ozone$), total nitrogen dioxide amount in atmospheric centimeters ($NO2$), and temperature in Kelvin (T). The global and temperate ranking is depicted in the table as per [44].

GHI_{Clear}	SZA	E_a	P	$elev$	T_L	PW	τ	AE	$AOD550$	SSA	$Ozone$	$NO2$	T	Global Ranking	Temperate Ranking	Reference
TJ	✓													62	47	[234]
El Mghouchi	✓	✓												68	67	[235]
Kumar	✓	✓	✓											61	59	[236]
Ineichen Perez	✓	✓		✓	✓									33	5	[237]
Simplified Solis	✓	✓	✓			✓	✓							34	21	[168]
Bashahu	✓	✓	✓			✓		✓	✓					4	3	[238]
MAC2	✓	✓	✓			✓		✓	✓	✓				1	1	[239]
IqbalC	✓	✓	✓			✓		✓	✓	✓	✓			7	8	[20]
REST2	✓	✓	✓			✓		✓	✓	✓	✓	✓		2	4	[240]
McClear	✓	✓	✓	✓		✓	✓	✓		✓	✓		✓	35	58	[174]

The irradiance measurements obtained from BSRN and CEDA were initially in .nc format. These were converted into individual .csv files, each named using the yyyymmdd.csv convention. For datasets recorded at one-minute intervals, no temporal adjustment was necessary. However, for hourly datasets, averages were computed over a sliding window from 30 minutes before to 29 minutes after the target timestamp (e.g., the 13:00 value represents the period from 12:30 to 13:29), aligning with recommendations from established PV feasibility tools [102]. All decomposition models utilized in this chapter were custom-developed in Python. A total of 104 models were implemented, with Python libraries such as NumPy and pandas facilitating data handling and batch processing across multiple CSV files. Data preprocessing followed a rigorous cleaning protocol, previously outlined in Section 2.1.3. This included applying quality-control filters and removing invalid or out-of-range values. The overall process adhered to a structured four-step workflow to ensure full transparency and reproducibility: (1) importing raw data, (2)

synchronizing timestamps to UTC+0, (3) applying the defined filtering criteria, and (4) running the in-house Python implementations of the models. Model outputs were evaluated using statistical tools from the scikit-learn library, with performance metrics calculated after each iteration. Lastly, the clear-sky reference model used during the final stage of the framework was adapted from source code originally written in R in [246], which was carefully translated and re-implemented in Python. The script generates an .xlsx file containing the results of all 104 implemented decomposition models. To ensure reproducibility, the Python code for all 104 models is provided in Appendix B.

3.3 Discussion of Performance and Results

3.3.1 Temporal Resolution

The first test of this framework is to examine the performance of decomposition models under hourly and minute rates, with a specific emphasis on the unpredictable climatic fluctuations in the UK. Such rapid shifts in weather can lead to notable changes in the K_t value over short periods of time. It is crucial, therefore, to delve into data more frequently than on an hourly basis. This test pinpoints models that meet the MAD threshold criterion for both hourly and minute-level domains.

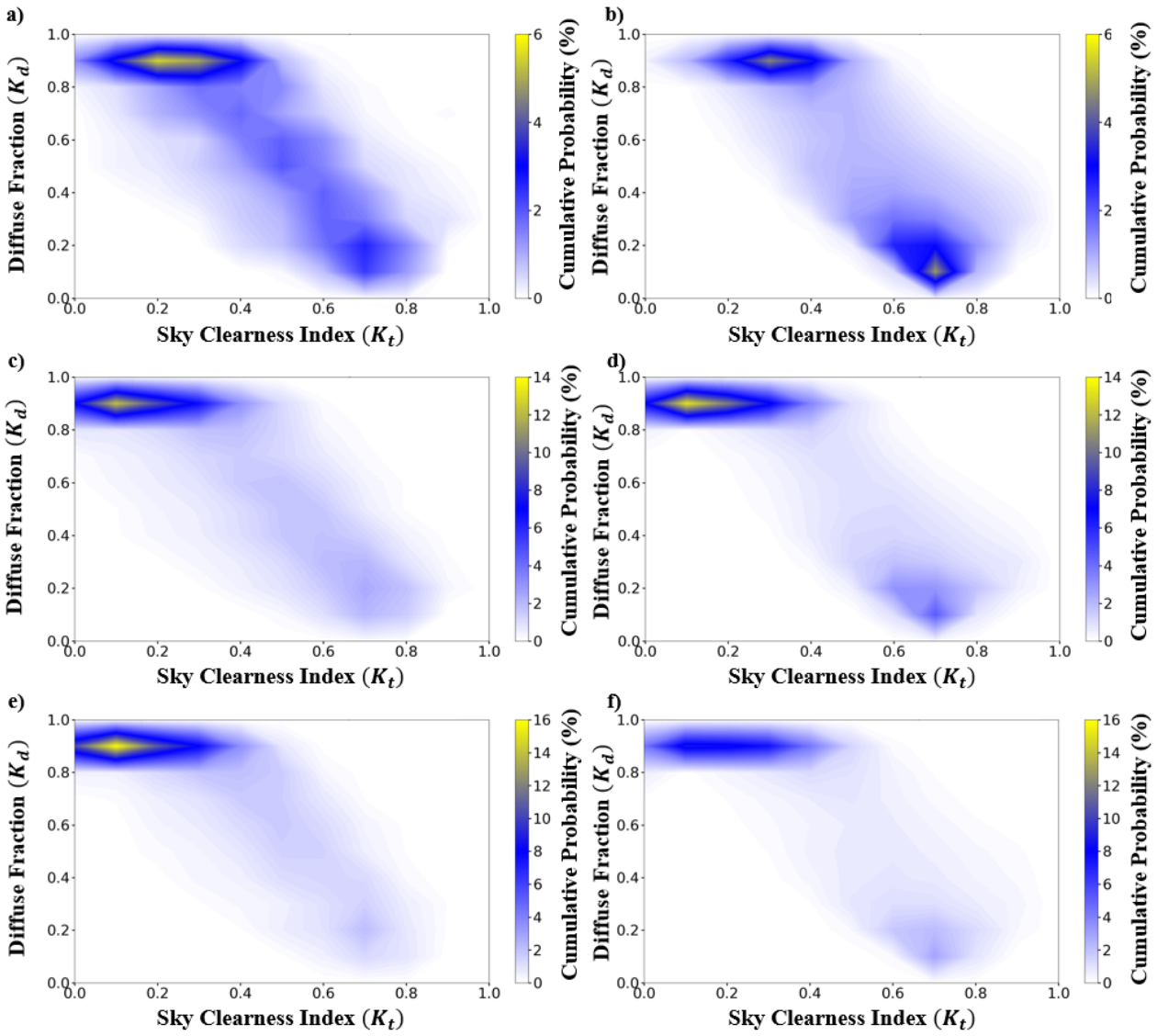

Figure 15: The combined probability matrix for Kt-Kd is segmented for various locations and intervals as follows: **a)** hour **b)** minute for Camborne, **c)** hour **d)** minute for Chilbolton, **e)** hour and **f)** minute for Lerwick during June 1, 2015 – June 1, 2017.

Figure 15 displays the combined joint distribution of K_t and K_d for three sites in the United Kingdom (Camborne, Chilbolton, and Lerwick) using two temporal resolutions; hourly and one-minute. A clear picture of the K_t distribution for each site is offered in the appendix (see appendix C). While K_t is not the sole factor influencing K_d, Figure 15 clearly illustrates that a single K_t value can correspond to multiple K_d values. To gauge the extent to which K_t values correspond to K_d, a cumulative probability percentage is employed. Essentially, this is a measure of the likelihood that data points will occur in a two-dimensional structure defined by K_t and K_d. The shift in the hourly basis (Figures 15a, 15c, and 15e) to that gathered every minute (Figures 15b, 15d, and 15f) suggests a heightened responsiveness to quick-changing conditions in the more granular level. In minute data, swift variations in cloud cover and positioning lead to notable fluctuations in both

K_t and K_d, resulting in a more dispersed array of data points. Conversely, the hourly data tends to represent average conditions over extended periods, thereby obscuring these brief variations. This process generates a more uniform pattern, as short-lived events are evened out, culminating in a closer grouping of K_t-K_d values. This may indicate why a large number of hourly decomposition models opt for a simple cubic mathematical regression.

Focusing on specific sky conditions, the more confined cluster for overcast scenarios ($K_t \leq 0.30$) indicates uniformity in the diffused component of solar radiation due to thick cloud coverage and the fact that there is little to no direct irradiance. Under such conditions, K_d shows less variation as the dense clouds distribute sunlight more evenly, resulting in a consistent diffuse fraction throughout the observation area. In contrast, under clear skies ($K_t \geq 0.70$), K_d values suggest a stronger impact from direct sunlight. Variables like the time of day, sun position, and the presence of atmospheric components like aerosols and water vapor, and thus, may introduce more variation in sunlight diffusion, leading to a more defined distribution. The fluctuating nature of cloud coverage and type during intermediate conditions leads to a broad and less predictable spectrum of K_d values. Moreover, the sun's angle relative to cloud edges can create sharp contrasts in both DNI and DHI, adding to the dispersion of K_t-K_d values in this range.

When examining the transition from minute to hourly data for each location, distinctive insights emerge about the behavior of K_d and K_t values within different climatic and geographic contexts. In Camborne, the shift from minute to hourly data shows a convergence of data points around the median K_d values. In Figure 15b, at the minute level, the maritime climate significantly influences solar irradiance, with the sea's proximity causing rapid cloud cover changes due to local weather systems. These changes can lead to notable shifts in K_d as clouds swiftly move across the sun. However, in the aggregated hourly data (see Figure 15a), this coastal variability is averaged out, resulting in a more stable and predictable K_d range. This suggests that although Camborne may experience short-term cloud cover variability, the overall solar irradiance across an hour tends to normalize to the area's average cloudiness level. Moving to Chilbolton, as evident in Figure 15d, the minute-level data captures a broader range of both K_t and K_d, indicative of a more continental climate. The hourly data, however, shows a more concentrated cluster of values, particularly at lower K_t levels, suggesting that overcast conditions, when present, tend to be more enduring and less subject to rapid changes compared to Camborne. This consistency over the hour signifies a reduced variability in cloud cover, possibly due to slower-moving weather systems inland. For Lerwick, located at a higher northern ϕ, the minute-level data displays a broad spread significantly influenced by the local climate's tendency for quick weather shifts, intensified by its island geography as indicated in Figure 15f. The transition to hourly data reveals a notable

concentration of K_d values, especially in the higher ranges of K_t. This could indicate a balancing of both diffuse and direct solar irradiance over time, as short-term cloud cover variations caused by the island's interaction with maritime air masses are averaged out. The more focused K_d values in the hourly data suggest a consistent cloud cover pattern, despite potential rapid weather changes. The transition from minute to hourly intervals in these three locations underscores the impact of broader weather patterns over immediate local conditions and the time-based averaging effect on solar irradiance measurements. It emphasizes the need to consider temporal resolution in solar irradiance analysis, as it can profoundly alter the interpretation of the relationship between the K_t and DHI.

One of the clearest differences between the hourly and minute-based datasets lies in the level of detail captured within the distributions. Hourly data tends to smooth out rapid fluctuations in irradiance, often cause by intermittent cloud cover or shifting atmospheric conditions. The hourly plots in Figure 15 (a, c and e) tend to smooth out rapid fluctuations in irradiance caused by short-lived meteorological phenomena such as passing clouds or sudden clearings. This average effect compresses K_t values into a narrower range, between 0.3 and 0.6 and thus, reduces the observed diversity in K_d. As a result, the joint distributions appear more generalised, with localised clusters. By contrast, the one-minute resolution data (see Figures 15b, 15d, and 15f) captures a richer and more detailed representation of atmospheric variability. Distinct peaks emerge across K_t-K_d space, especially near K_t = 0.20; indicative of overcast conditions, and around K_t=0.70, which reflects clearer skies. These features point to high-frequency changes that are lost in hourly averages but are crucial for the understanding of solar irradiance.

This pattern is further reinforced when examining the induvial histograms provided in the appendix (see appendix C). The hourly distribution are generally flatter, while the one-minute versions revel sharper distributions. In particular, sites like Lerwick and Chilbolton show prominent peaks at both low and mid-range K_t values in the minute-based plots, indicating the presence of intermittent sky conditions that are otherwise obscured when data is aggregated hourly. It must be noted that these differences are not trivial, especially considered in the context of solar energy applications. Many solar modelling frameworks (I.E., CSD) require detailed knowledge of short term irradiance behaviour. High resolution input data is also vital for classification tools like CAELUS [40], which depend on transient cloud pattern detection. Failing to account for this variability by relying on hourly data may lead to underrepresentation of key atmospheric states, resulting in biased energy estimates or misclassified sky conditions. In examining the performance, it is observed that a number of these models meet the MAD < 15% threshold, particularly in hourly analysis. This is especially true for models developed for or

effectively applied in temperate climates. In Camborne, 18 models fell within the acceptable MAD range, which varied from 13.63% to 14.91%. Chilbolton showed 32 models meeting the threshold, with MADs spanning 12.57% to 14.99%. Lerwick, although having the fewest, still presented 13 models within the threshold, with MADs from 13.86% to 14.89%. However, when data was examined at a more granular level, changes were noted. Lerwick's count was reduced to 9 models for the minute domain, with 5 models being effective in both the minute and hourly scales as per Figure 16a. Chilbolton saw a decrease to 5 models for minute data, with MADs ranging from 13.04% to 14.00%, and with 2 models effective in both time scales as per figure 16b. Camborne's adherence to the model decreased to 6 when analyzing minute-level data, showing MAD ranging from 12.74% to 14.52%. Only two models demonstrated effectiveness across both hourly and minute resolutions. As depicted in Figure 16, Paulescu consistently performed across all locations at both temporal resolutions. In Lerwick, Engerer models proved effective. These models are equipped to adeptly manage the variability in cloud coverage by incorporating a factor that adjusts for deviations from clear sky conditions to the actual sky clarity observed. Notably, Engerer models excel in adapting to shifts in cloud density and the influence of the SZA. Conversely, Chilbolton, which is located further inland, shows a different scenario. In Chilbolton, the Paulescu model performs well and stays within acceptable thresholds, unlike the Engerer models, indicating that the Paulescu model is highly effective across various climate conditions. Additionally, while the Starke1 model meets the threshold in both Lerwick and Camborne, Starke3 is unique to Chilbolton because it factors in hourly, rather than daily, calculations of K_t. The Starke1 model, meeting the threshold in both Camborne and Lerwick, underscores its flexibility across diverse environments, ranging from temperate coastal to harsher northern settings. Moreover, the consistent effectiveness of the Paulescu model across all three sites also underscores its versatility beyond purely geographical considerations. This model shifts focus from short-term local conditions to broader irradiance trends, adjusting its parameters based on varying thresholds of K_t. Hence, only the Paulescu model, out of a total of 104 models, adheres to said examination.

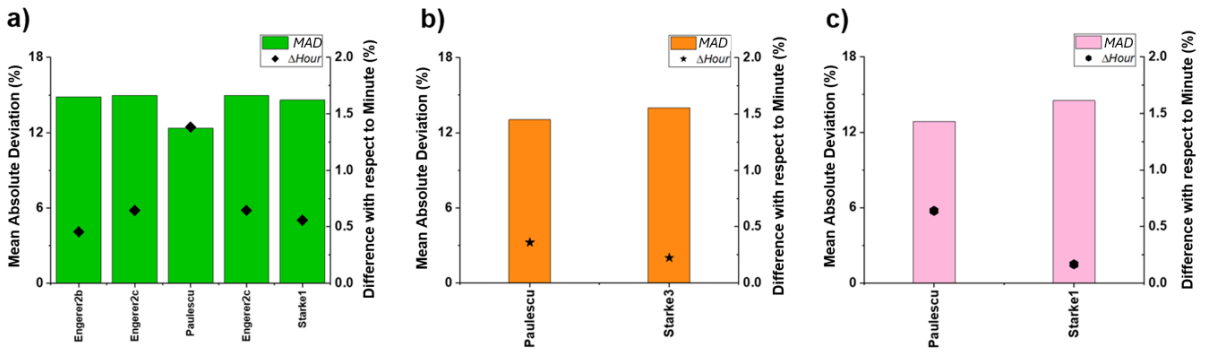

Figure 16: The minute MAD for decomposition models that meet the threshold for both hourly and minute-level analyses. It includes a comparison of the changes when shifting from minute to hourly intervals for **a)** Lerwick, **b)** Chilbolton, and **c)** Camborne, highlighting the percentage discrepancies observed during these transitions. Engerer models here use the default REST2 GHI_{Clear} model.

3.3.2 Spatial Homogeneity

Assessing the interplay among different models across three regions, utilizing publicly available minute data is needed. Prior analysis indicates that only the Paulescu model is effective across all locations when examined on the mutual inclusivity in the temporal resolution (i.e., adhering to the threshold both on an hourly and minute basis for all locations). Among the five models demonstrating spatial consistency (Paulescu, Suehrcke-McCormick (SM), Yang4, Starke3, and Yang5), Paulescu emerges as the most effective, with an MAD of 12.76% as per Figure 17a. This is illustrated in a radar chart (Figure 17), depicting each model's MAD at each location using minute-by-minute data.

The analysis shows that the models primarily depend on two variables: GHI and K_t, along with a parameter that identifies trends in overall solar irradiance. Paulescu and SM utilize three parameters; Paulescu incorporates daily K_t, while SM considers the SZA, each applying distinct mathematical approaches to explore their relationships and quantify the atmosphere.

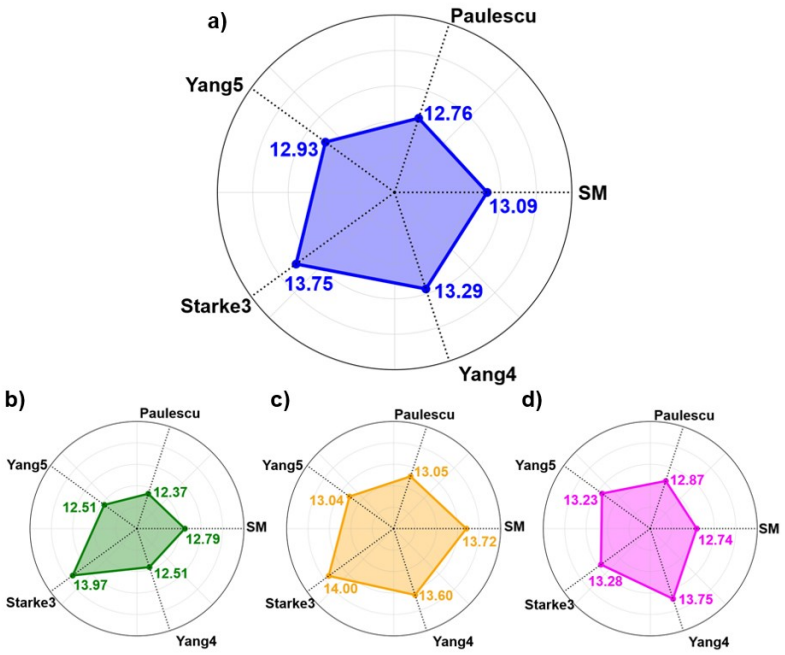

Figure 17: A radar chart displays the performance metrics of various decomposition models, highlighting the MAD (%) values for the following locations**: a)** overall average, **b)** Lerwick, **c)** Chilbolton, and **d)** Camborne using minute data.

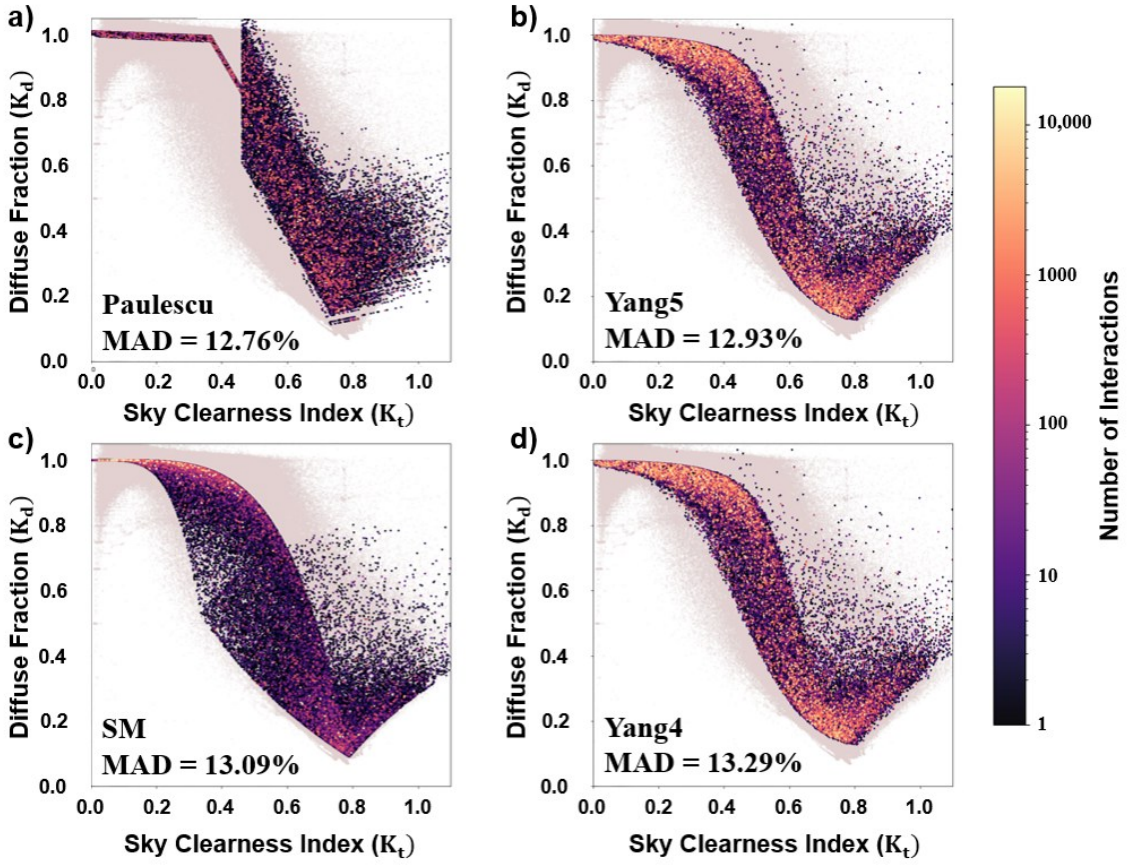

Figure 18: An illustration of one-minute datapoints from all three locations of Kd-Kt plots using 4 selected models that meet the criteria for spatial homogeneity. In this visualization, actual measurements are depicted by a grey backdrop, while the model results are displayed using a magma colour gradient.

According to Figure 18a, it initially establishes a baseline using linear effects of K_t and daily K_t, then applies additional empirical adjustments activated when K_t surpasses certain thresholds. These modifications enhance the estimation of conditions potentially linked to specific atmospheric occurrences or solar positions. In essence, the Paulescu model also incorporates the daily average K_t, which accounts for daily variations in solar clarity alongside instantaneous readings. It uses a segmented function defined by empirical constants to reflect day-long trends in solar irradiance. In contrast, the SM model uses the SZA to calculate air mass - the length of the path that sunlight travels through the atmosphere, normalized to the shortest path. Like Paulescu, SM includes a threshold that adjusts estimates when solar radiation becomes significantly diffuse due to atmospheric scattering and absorption. Unlike Paulescu's use of daily K_t, SM integrates air mass directly, beginning with a simple mathematical relationship at lower Kt values and becoming more complex at higher values, as depicted in Figure 18c.

The Yang4 and Yang5 models, although they share a structural basis by utilizing the GHI_{Clear} to GHI ratio as a metric for atmospheric quantification, differ in their coefficient values. Both models demonstrate extensive parameter ranges, leading to identical MAD values in Lerwick, as shown in Figure 17b. However, Yang5 performs better in Chilbolton and Camborne, owing to refined coefficients that effectively consider cloud clustering, aerosols, and albedo - making it a regime-dependent refinement of Yang4.

3.3.3 Period Influence

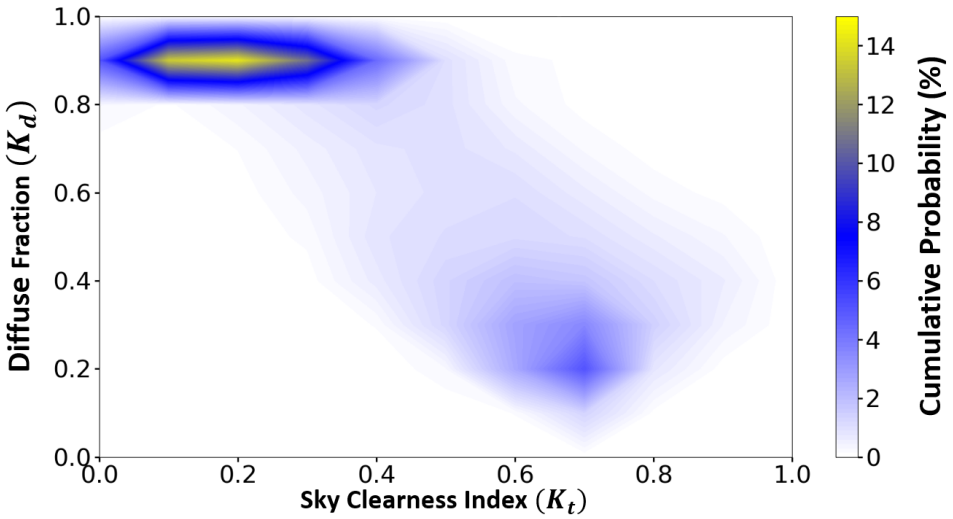

Figure 19: The combined probability matrix for K_t-K_d for minute data for Chilbolton during June 1, 2021 - June 1, 2023.

Examining the performance of models across different datasets, focusing on the unique challenges faced by weather stations with limited historical data is needed. The study involves a comparison of two datasets to evaluate the consistency, adaptability, and responsiveness of models over time. It explores whether models that achieved benchmark classification in an initial

dataset (June 1, 2015 – June 1, 2017, hereinafter referred to as the 2016 dataset) maintain similar performance in a later dataset (June 1, 2021 - June 1, 2023, hereinafter referred to as the 2022 dataset). Two models met the threshold on the 2016 dataset from Chilbolton , similar to the number of models in the 2022 dataset. A notable difference is the mean DHI, with the 2016 dataset at 136 W/m^2 and the 2022 dataset at 155 W/m^2, implying more overcast conditions in the latter period. Analysis of Figure 19 compared with Figure 15d reveals that the 2016 dataset exhibits a narrower concentration in overcast conditions than the 2022 dataset, with a wider spread of intermediate conditions in 2016.

Figure 20 illustrates the distribution of the K_d values across various models for two datasets from 2016 and 2022. In the 2022 dataset depicted in Figure 20a, the median K_d values are generally lower for almost all models, when compared to the 2016 values in Figure 20b. For instance, the median K_d for Yang4 drops from 0.956 in 2016 to 0.937 in 2022, suggesting a trend toward reduced diffuse fractions in conditions of lower DHI. This trend may reflect model adaptations to increasingly overcast skies, which elevate the ratio of diffuse to direct solar radiation. The downward shift in median K_d values signals a systemic change in the models' sensitivity to altered radiation scenarios as illustrated in Figure 19. Moreover, examining models like Gonzalez6 in 2022, which strictly meets the MAD <15% criterion only for the 2022 dataset reveals that the median reduces from 0.919 in 2016 to 0.856 in 2022. This substantial decrease in median alongside a maximum value that remains constant at 1.153 across years suggests that while the model is capable of reaching high K_d values, its general output has shifted downwards. This shift could be attributed to the model's sensitivity to higher DHI, where the presence of clouds increases the proportion of diffuse to direct sunlight, affecting the overall model performance.

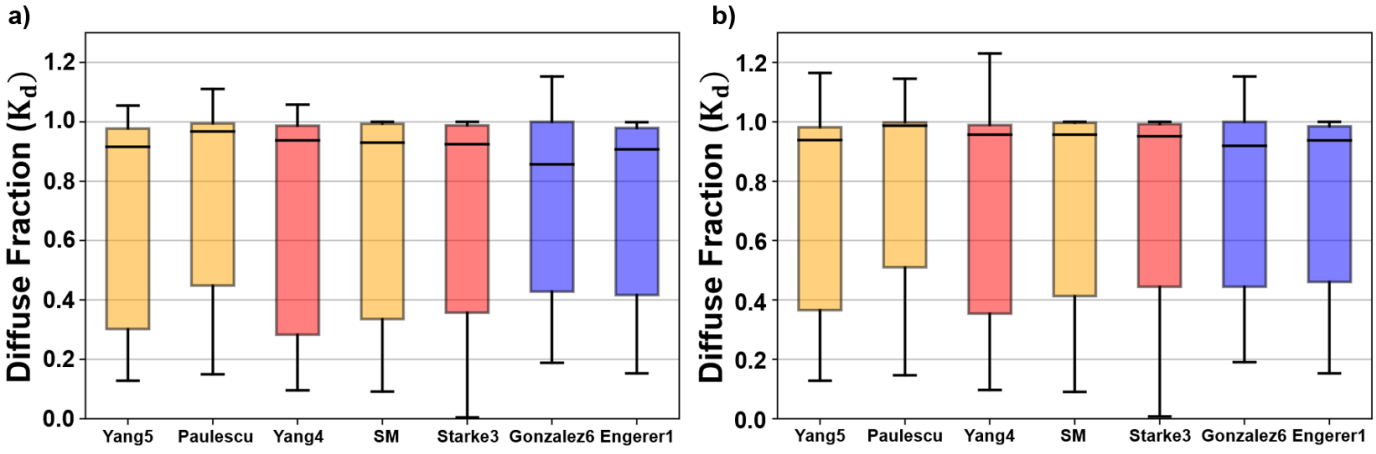

Figure 20: Box plots showcasing the comparative performance of various decomposition models against specified thresholds for two distinct datasets: a) the 2022 dataset and b) the 2016 dataset. Models that meet the threshold criteria exclusively for the 2016 dataset are marked in red, while those meeting the threshold solely for the 2022 dataset are highlighted in blue. Models that successfully meet the threshold for both datasets are distinguished in orange.

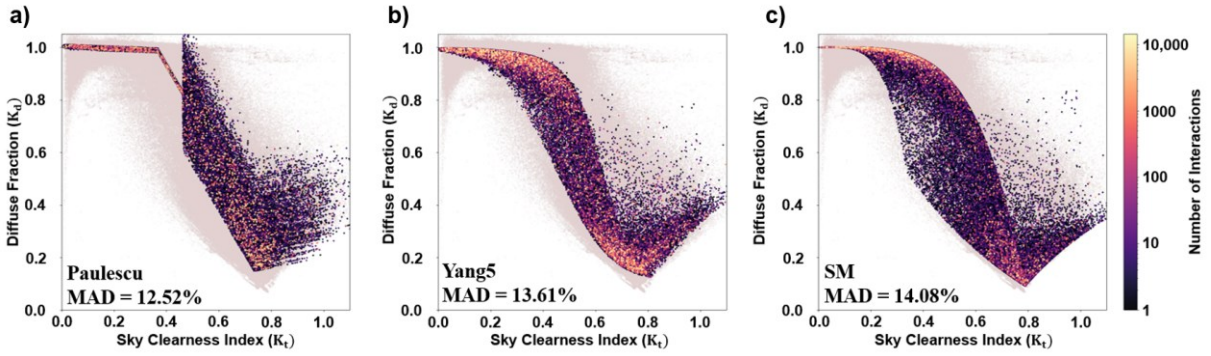

Figure 21: An illustration of one-minute datapoints of K_d-K_t plots using three selected models that meet the MAD maximum threshold for the 2016 and 2022 datasets. In this visualization, actual measurements are depicted by a grey backdrop, while the model results are displayed using a magma colour gradient.

The interquartile range (IQR) provides insights into the data spread around the median, indicating significant differences between the datasets. For instance, Yang5's IQR narrows from 0.615 (ranging from 0.366 to 0.981) in 2016 to 0.674 (from 0.303 to 0.977) in 2022. This increase in IQR in a higher DHI scenario implies not only a decrease in the estimated diffuse fraction but also greater consistency in model output, which may suggest enhancements in model accuracy and reliability under variable cloud conditions, possibly due to algorithmic improvements or better acclimatization to the prevailing climate conditions of 2022. Colour coding in the box plots provides further clarity on model adaptability, with orange indicating consistent performance across both datasets and red and blue denoting dataset-specific behaviors. Models coloured orange, like Paulescu, show remarkable stability, with median values of 0.987 in 2016 and 0.968 in 2022, demonstrating minimal variability despite different atmospheric influences. This stability implies a strong mathematical ability to compensate for variations in solar radiation due to cloud cover and other atmospheric factors, maintaining a tight clustering around the median K_t value as seen in Figure 21a. Conversely, models highlighted in blue, such as Energer1, optimize their performance for the specific conditions of 2022, achieving a median near the third quartile, indicative of an optimal setting for higher mean DHI (155 W/m^2 in 2022). This suggests that such models may not adapt as dynamically to fluctuating cloud cover and might perform poorly in 2016 but excel in conditions typical of 2022.

3.3.4 Effect of Clear-Sky Input Parameter Matrix

The objective centered on pinpointing models that align with all evaluation benchmarks, with MAD below the threshold of 15%. This endeavor led to the selection of five distinct models that are not only spatially homogenous, but robust to dataset selection and temporal resolution: Paulescu, Yang5, SM, Starke3, and Yang4. Their respective average MADs for the specified tests are 12.57%, 13.24%, 13.42%, 14.12% and 14.22%. Notably, three of these models (Starke3, Yang 4 and Yang5) incorporate GHI_{Clear} in their formulations. The focus now shifts to exploring the impact of modifying GHI_{Clear} approximation equations. This is to broaden the scope beyond the robust models, aiming to increase the number of models that meet the MAD threshold.

Table 7: Across the 15 decomposition models, an alternate distinct GHI_{Clear} is substituted, displaying the MAD (%) in minute-minute data. Bold figures denote the initial GHI_{Clear} model used. Yellow markings indicate a reduction in the MAD, though not conforming to the established threshold, whereas green highlights denote that the model pairs have improved and comply with the established threshold.

Decomposition Model \ GHI_{Clear} Model	TJ	ElMghouch	Kumar	Ineichen-Perez	Simplified Solis	Bashahu	MAC2	Iqbal C	REST2	McClear
Engerer1	19.36	18.46	19.36	18.47	18.96	17.74	17.84	17.00	**17.26**	17.86
Engerer2a	17.55	19.84	16.35	19.75	16.08	18.92	16.74	29.70	**17.66**	12.77
Engerer2b	**15.52**	17.10	16.52	17.05	16.58	15.95	15.88	16.52	12.97	14.75
Engerer2c	**15.68**	17.24	16.77	17.19	16.82	16.09	16.08	16.29	13.09	14.44
Engerer2d	**15.90**	17.44	17.01	17.40	17.07	16.30	16.32	16.32	13.28	14.69
Engerer2e	**16.00**	17.54	17.14	17.50	17.19	16.40	16.43	16.36	13.40	14.82
Engerer2f	**16.24**	17.73	17.46	17.70	17.49	16.61	16.68	16.28	13.56	15.13
Engerer2g	**16.64**	18.03	18.10	18.04	18.04	16.99	17.10	16.14	13.92	15.69
Engerer2h	**25.53**	26.54	26.39	26.66	25.72	25.88	25.05	28.05	21.55	22.67
Engerer3	73.33	74.50	72.94	74.38	73.28	73.17	72.91	74.47	**72.60**	71.75
Starke1	16.64	17.28	16.33	17.19	**15.17**	15.97	15.96	17.08	14.45	14.21
Starke2	19.21	20.15	18.84	20.06	**17.80**	18.78	18.70	20.04	17.27	16.65
Starke3	14.60	16.20	14.38	16.10	**14.12**	14.92	14.68	15.84	13.44	13.07
Yang4	17.85	19.14	16.72	19.14	16.28	18.71	16.46	28.45	16.21	**14.22**
Yang5	17.65	19.02	16.38	19.03	16.00	18.36	16.29	27.49	16.00	**13.24**

Tables 5 and 6 present detailed listings of 15 decomposition models and 10 GHI_{Clear} models, each differing in parameter complexity. To increase precision, a detailed analysis involving a matrix of 150 GHI_{Clear}-decomposition combinations is executed, as detailed in Table 7. Of these, modifying the input GHI_{Clear} model enhances 30 models, with 15 combinations maintaining MAD below 15%. According to Table 7, significant enhancements predominantly utilize REST2 or McClear as the GHI_{Clear} inputs, suggesting inaccuracies in conclusions that rank other models above those utilizing GHI_{Clear} due to the variability in GHI_{Clear} models applied. For the models ranging from Engerer2b to Engerer2e, regardless of whether REST2 or McClear was used as the GHI_{Clear} model, all modifications meet the MAD threshold. This consistency also extends to all Starke1 and Starke3 models. The Yang models (Yang4 and Yang5) initially paired with the original McClear show MAD values of 14.22% and 13.24%, respectively, indicating robust performance without the need for adjustments from the other nine GHI_{Clear} models in temperate regions. It is crucial to

recognize the intricate relationship between the coefficients in decomposition models and their comparative effectiveness in the GHI_{Clear} model, particularly in temperate zones, underscoring a significant interaction where a lower GHI_{Clear} model ranking does not necessarily imply reduced accuracy in the decomposition model, as shown when comparing Tables 6 and 7.

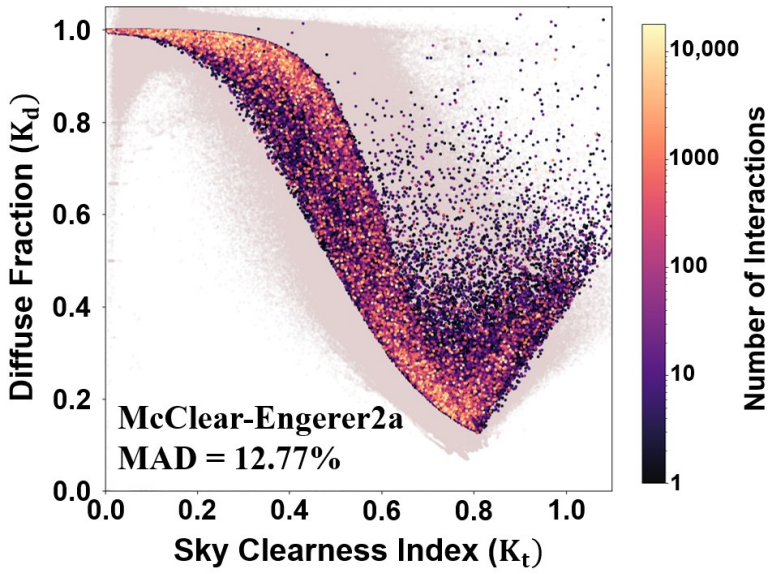

Figure 22: An illustration of one-minute datapoints of K_d-K_t plots using a model that show improvements that still meet the criteria for all tests. In this visualization, actual measurements are depicted by a grey backdrop, while the model results are displayed using a magma colour gradient.

Further analysis involves identifying the most robust decomposition model, regardless of the specific GHI_{Clear} model employed. This involves noting the MAD variation for each decomposition-GHI_{Clear} model combination. Engerer2b to 2g models show MAD fluctuation between 4.13% and 4.18%, indicating minimal change with GHI_{Clear}. This is expected due to their coefficients being based on the one-parameter TJ model. Furthermore, Yang models, as well as Engerer2a, demonstrate significant fluctuations due to their complex parameter GHI_{Clear} choice, which may result in underfitting when using different GHI_{Clear} due to the nature of REST2 and McClear. Analyzing top-performing decomposition models post GHI_{Clear} model adjustment reveals that Engerer2a with McClear achieves the lowest MAD value of 12.77 as per Figure 22; second to Paulescu.

3.4 Conclusion

In conclusion, this chapter introduces a clear and transparent framework that presents a sequence of evaluations designed to validate robust decomposition models across a series of tests addressing temporal resolution, spatial homogeneity, dataset period influence, and the

effect of altering clear-sky irradiance equations. This is particularly vital in regions lacking direct solar irradiance data. Therefore, utilizing the UK as a case example, this research comprehensively analyzed 104 decomposition models, mainly from or tested in temperate climates, for estimating DHI. The methodology employed a MAD limit of 15% as a metric for the success of a model. The approach included both hourly and minute-by-minute analysis. In Camborne, the number of models meeting hourly standards dwindled from 18 to 6 when assessed per minute, with only 2 models demonstrating consistent performance across both. Similarly, in Chilbolton, 32 models met the threshold on hourly data, decreasing to 5 for minute-to-minute data, with just two models satisfying the threshold for both periods. For Lerwick, suitable models were reduced from 13 to 9, and 5 models retained their performance in both timeframes. This chapter also identified specific models that proved effective in multiple locations for both hourly and minute-by-minute intervals. The Paulescu model demonstrated consistent performances across all three sites, yielding MADs of 12.37% for Lerwick, 13.05% for Chilbolton, and 12.87% for Camborne. In Camborne and Lerwick, the Starke1 model stood out, mainly because of its effectiveness in coastal areas by incorporating daily K_t to assess atmospheric changes. On the other hand, Starke3 was significant only in Chilbolton, where it enhanced the analysis by integrating both hourly and daily K_t measurements. Spatial homogeneity analysis across Lerwick, Camborne, and Chilbolton revealed only five models surpassing the threshold, with Paulescu showing the lowest average MAD at 12.76%. The study further investigated the impact of dataset periods in Chilbolton, finding Paulescu, Yang5, and SM consistently meeting the threshold across datasets collected over different periods. These models, examined by box plots, were identified as the most robust, with average MADs of 12.52% for Paulescu, 13.61% for Yang5, and 14.08% for SM. Lastly, this research delved into the transformative effect of modifying the GHI_{Clear} model, which increased the tally of robust models from 5 (Paulescu, Yang5, SM, Starke3, and Yang4) to a further 15. Specifically, integrating REST2 or McClear as the GHI_{Clear} model basis yields improved accuracy, with 15 models within MAD < 15%. Upon adjusting the GHI_{Clear} model, an analysis of the leading decomposition models indicates that the Engerer2a model combined with McClear yielded the lowest MAD value of 12.77%, ranking second to Paulescu by 0.25%.

Chapter 4 Exploring Transposition Techniques for In-plane Solar Irradiance Estimation in Temperate Setting

4.1 Introduction

Validating mathematical models embedded within PV system feasibility software is especially critical in temperate climates due to the empirical nature of these models. Accurate estimation of POA irradiance cannot be overstated, as it significantly influences the economic viability of deploying PV systems. The analysis is twofold: initially, an evaluation of 15 pairs of optical models involving decomposition-transposition processes is presented. Optical model pairs are utilized to calculate DHI and DNI before these values are transposed to estimate POA irradiance. The analysis is segmented based on the average clearness index of the day, including overcast, intermediate, and clear conditions, ensuring a comprehensive analysis across a spectrum of sky clarity. This structured approach allows for a detailed exploration of the intricacies inherent in optical model pairs, offering fresh insights into their functionality and application under differing environmental conditions. Furthermore, the chapter examines 16 transposition models, half of which are employed in software and others not typically used, by leveraging measured GHI, DHI, and DNI data. Despite the rarity of such detailed irradiance measurements, their inclusion is vital for assessing model performance across six distinct cloud conditions. This novel methodological approach not only enhances the understanding of model behavior under diverse weather scenarios but also refines the models used in feasibility software, ensuring they provide reliable and accurate predictions essential for the successful implementation of PV systems in a temperate climate.

4.2 Methodology

Table 8: Specifications of the actuator-based tracker and the FT system.

System	Type	Experimental Duration	ψ_{system} (°)	β (°)
1	Tracker	Apr 14, 2023 – Apr 13, 2024	126 -247	33 - 68
2	FT		180	55

Transposition models are inherently empirical, developed from a range of experimental results tailored to specific climates. Essentially, such models can be divided into two categories: isotropic and anisotropic. Isotropic models depict DHI as a consistent distribution of rays across the entire sky dome, signifying equal irradiance in every direction. On the other hand, anisotropic models (e.g. Perez [185]), are considerably more intricate as they break away from the restrictive assumption of complete isotropy. They divide solar irradiance into distinct elements: circumsolar (rays within a spherical cone with a 2.5° half angle), and horizon brightening (rays emanating from a planar beam) built on top of an isotropic foundation. Traditionally, these models utilize hourly irradiance data as their finest temporal resolution. However, there is a shift towards utilizing minute-by-minute data, raising critical questions about their effectiveness in temperate climates characterized by fluctuating weather conditions and at such granular irradiance levels. This shift necessitates an evaluation of whether these refined temporal resolutions maintain accuracy and reliability in predicting solar irradiance under variable atmospheric dynamics. Further, the examination of the optical model pairs and transposition pairs are performed at one-minute intervals, an approach designed to seize the variety inherent in the tracking combinations (i.e., $\beta - \psi_{system}$) that an hourly computation would not facilitate [275]. The 15 optical model pairs under scrutiny are outlined in Table 3 in the earlier section. Moreover, in the later stages of this research, 8 supplementary transposition models (Badescu [217], Hay 1993 [210], HDKR [211], Jimenez [215], Klucher [212], Koronakis [214], Ma-Iqbal [20], Reindl [211], and Tian [216]) will be evaluated alongside those already utilized in the feasibility software.

This research explores a diverse array of tilt and azimuth combinations, equipping a pyranometer on two distinct systems. The first, a conventional, south-facing static system, with a fixed tilt of 55º. In contrast, the second system incorporates a tracking mechanism that adjusts the solar panel array's tilt angle along the East-West axis using an actuator control system. This tracker aligns the panels according to the sun's altitude and azimuth within a two-dimensional

coordinate system. However, due to actuator length limitations, it aims the panels within predefined boundaries during its tracking cycle, as outlined in Table 8. This tracking system provides valuable insights into tilt and azimuth combinations that extend beyond the empirical basis of most existing transposition models. Both systems utilize spectrally flat class A pyranometers, conforming to the IEC 61724 standard, which covers aspects from calibration to sensor placement, ensuring the consistency and accuracy of data collection.

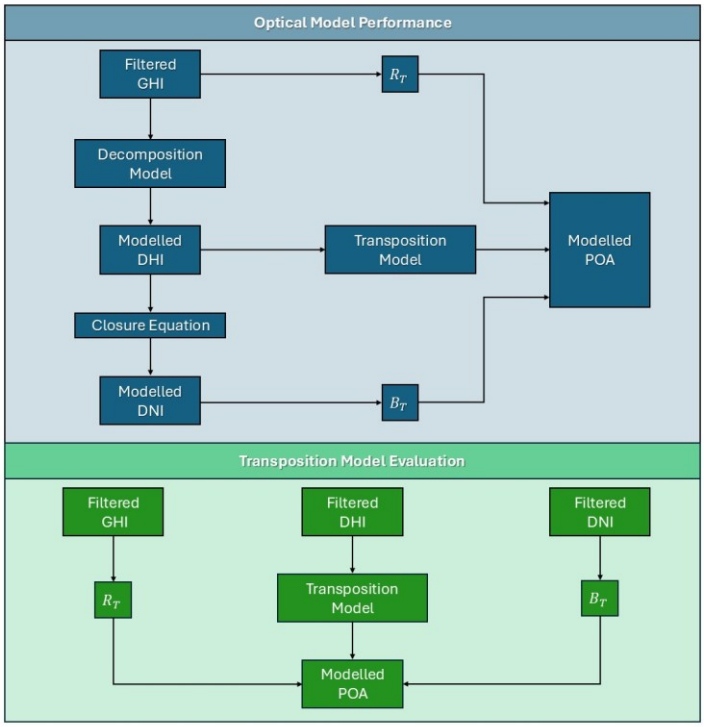

Figure 23: The flowchart provides a visual representation of the performance evaluation process for optical models, illustrating how DHI and DNI are derived through decomposition and subsequently combined with GHI to estimate modelled POA. Additionally, it depicts the evaluation of transposition models using actual measurements of DHI, DNI, and GHI. This dual approach helps in assessing both the models deployed in feasibility software.

Using Equation 5, sky conditions are classified into clear, overcast, or intermediate categories, as explained in earlier sections. To mitigate errors in misidentifying daily average sky conditions, K_t values were calculated only when the SZA was below 75º. This approach avoids the early morning periods between 75.1 and 85º, which could be inaccurately classified as overcast due to misleadingly low K_t values below 0.30. By employing average K_t values, each day can be accurately categorized under specific conditions, enhancing the understanding of how 15 optical models, deployed in feasibility software, perform under clear, overcast, and intermediate conditions. At φ = 51.1°, where the prevailing condition was deemed to be intermediate (with an average K_t equal 0.48), clear conditions were observed on 31 of the 364 days, with an average K_t

of 0.70, while overcast conditions (average K_t = 0.19) were reported on 101 days as per Figure 24a and 24b.

Despite the rarity of measured GHI, DHI, and DNI data, this research also leverages these measurements to evaluate the performance of 15 transposition models, seven of which are implemented in feasibility software while the remaining eight are not. This analysis aims to understand how these models perform under optimal conditions when provided with precise input data as seen in Figure 23. To deepen the understanding, the CAELUS algorithm's cloud coverage detection mechanism categorizes clouds into six distinct conditions: cloud enhancement, cloudless skies, thin clouds, scattered clouds, thick clouds, and overcast skies. Figure 24c illustrates that scattered clouds are the most frequent condition, totaling 175,847 occurrences. This is followed by cloudless skies, which appear 19,079 times. Both thin clouds and cloud enhancements show comparable frequencies, recorded at 14,660 and 14,848 instances, respectively. Similarly, overcast and thick clouds have nearly equal counts, with overcast conditions noted 5,944 times and thick clouds appearing 5,788 times. This classification adds a layer to the analysis, examining how clouds at minute-level irradiance impact the functionality of transposition models. Additionally, solar position is considered to further elucidate the interactions between cloud coverage and transposition model efficacy. It is important to note that the established figure of merit for both the optical model pairs and the transposition model evaluation is a MAD of less than 5%, aligning with common practices for evaluating the accuracy of irradiance models.

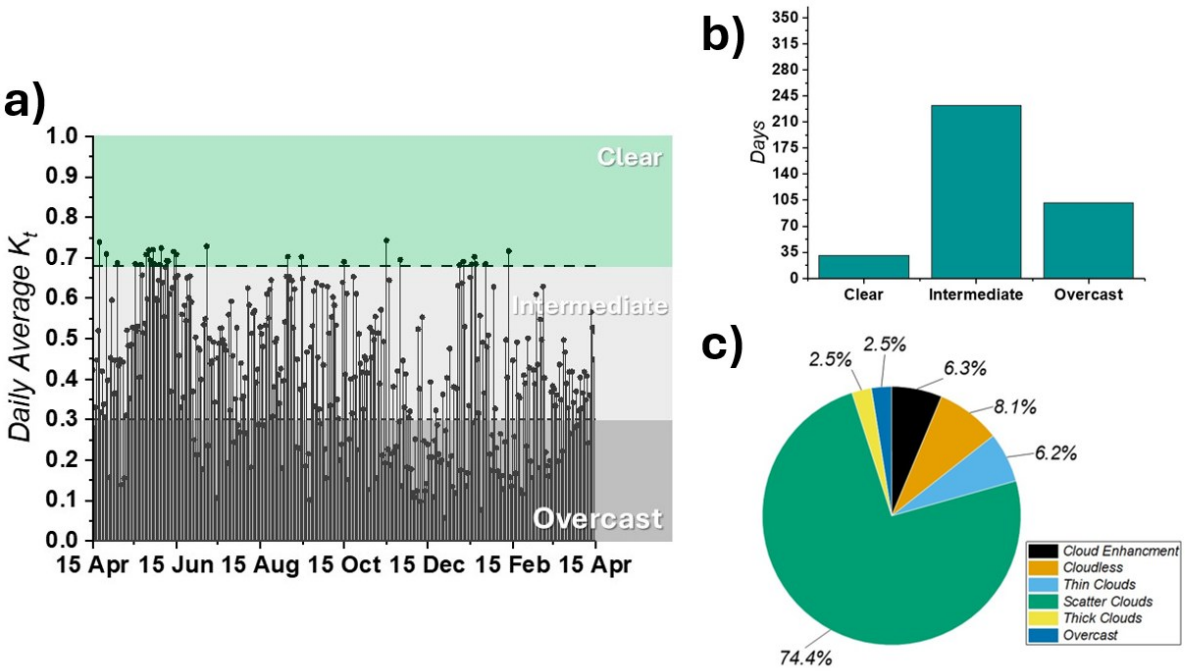

Figure 24: Different sky classification methods have been applied to a year's worth of data (April 15th, 2023, to April 14th, 2024) collected at the University of Southampton PV Outdoor Testing Facility. The analysis includes **a)** the daily average clearness index, **b)** the total number of accumulated days per condition, and **c)** minute-by-minute cloud instances evaluated using CAELUS.

Irradiance data, comprising GHI, DHI and DNI were sourced from the CEDA archive, measured via pyranometers installed at the Chilbolton Observatory. These instruments were positioned approximately 4 meters from the POA pyranometers associated with both the FT and tracking systems. It is important to note that while the GHI, DHI, and DNI datasets were provided through CEDA, the POA measurements originated from the University of Southampton's outdoor solar testing facility. The POA measurements were acquired using Spectrally flat Class A CMP10 pyranometers [285], which were connected to a CR1000X datalogger [286]. Data logging was conducted at one-minute intervals, capturing high-resolution irradiance data essential for model validation. All transposition models evaluated in this chapter (whether commonly integrated in PV feasibility tools or otherwise) were independently implemented using Python. These models were not simulated through proprietary software tools, as such platforms typically provide energy yield estimates rather than direct irradiance outputs, limiting their transparency and scientific reproducibility. Therefore, custom Python scripts were used for all decomposition models, with the exception of DISC and DIRINT, which were accessed through the open-source pvlib library. The data preprocessing methodology applied a stringent cleaning protocol, as outlined in Section 2.1.3. This included correction for thermal offsets across GHI, DHI, DNI, and POA measurements for both FT and tracking configurations.

Model outputs were statistically assessed using the MAD as a percentage, with evaluations performed using tools from the scikit-learn library after each model iteration. The CAELUS cloud classification algorithm was also employed, implemented through the open-access Python package caelus (available on GitHub) [40]. This algorithm requires three inputs: clear-sky irradiance (derived from McClear), SZA computed using NREL's SPA and measured GHI from the CEDA database.

Certain limitations must be declared in this methodology. The analysis here did not incorporate ρ measurements but instead specified a constant ρ = 0.20 for grass surfaces within the feasibility software. This could influence the comparative performance of the model pairs, particularly the FT system which is affected by its steep AOI. Unfortunately, this limitation is dictated by the constraints of the feasibility software, hence its adoption in this methodology. Moreover, the results presented here are based on standalone data from a single location. Another drawback is that the measurements focus solely on global in-plane POA, excluding diffuse and/or direct. This exclusion makes it challenging to determine the extent to which DHI or DNI contribute to errors in the analysis of in-plane POA. Aligning pyranometers with the POA is challenging, often resulting in alignment errors of several degrees. These errors increase as the AOI to the POA widens. Consequently, systems with a lower AOI, such as the tracker system, tend to exhibit fewer error percentages from POA and pyranometer misalignment compared to the FT system. However, it is important to acknowledge the impact of different elevation heights and the inherent nature of movement in tracking systems contributing to unavoidable errors in systems with varying AOI.

4.3 Optical Models Pairs Deployed in Feasibility Software

4.3.1 Clear Conditions

The MAD for the 15 model pairs, across the three conditions for both the tracked and FT systems, are presented in Figure 25 and 26, respectively. The performance seems to hinge on the fundamental aspects of either the initiation of the decomposition segment or the implementation of the transposition component within the optical model combination. A total of 4 models conform to MAD < 5% for the FT setup, with MAD fluctuating between 3.21% and 25.45%. Both Erbs and Reindl employ similar equations, exhibiting a negative linear gradient for the latter and a negative exponential-like shape for the former in clear instances. Comparing Erbs-Perez and Reindl-Perez, it is evident that their errors to measurement are closely aligned at 5.11% and 3.21%, respectively. The same can be observed with Skartveit Olseth (referred to as SO), where the Erbs model results in MAD of 17.25% and the Reindl model yields 14.88%.

Optical Model	Daily Sky Condition: Clear	Intermeidate	Overcast
BRL-LJ	3.70	7.20	4.81
DIRINT-Perez	2.82	3.28	45.22
DISC-Hay	3.94	6.18	5.72
DISC-Perez	2.78	3.31	44.56
DISC-SO	3.31	3.12	3.23
Erbs-Bugler	8.08	6.24	10.69
Erbs-Hay	4.17	6.93	7.08
Erbs-LJ	3.42	5.62	5.05
Erbs-Perez	4.97	4.37	38.81
Erbs-SO	6.00	5.73	8.90
Erbs-TC	8.36	12.95	51.07
Erbs-Willmot	13.92	7.14	37.66
Reindl-Hay	4.79	5.20	13.01
Reindl-Perez	4.41	3.33	35.95
Reindl-SO	7.70	6.44	9.30

Figure 25: The MAD (%) performance of 15 different decomposition-transposition model pairs is evaluated across clear, intermediate, and overcast conditions for the tracker. Underlined numbers signify that the pair meets the specified threshold.

Optical Model	Daily Sky Condition: Clear	Intermeidate	Overcast
BRL-LJ	7.44	10.81	7.42
DIRINT-Perez	4.96	5.53	31.73
DISC-Hay	6.80	5.89	7.28
DISC-Perez	3.73	4.99	30.23
DISC-SO	3.22	2.87	2.67
Erbs-Bugler	15.27	10.39	10.82
Erbs-Hay	10.60	6.10	8.86
Erbs-LJ	11.03	9.23	7.02
Erbs-Perez	5.11	8.91	26.79
Erbs-SO	17.25	10.93	10.93
Erbs-TC	16.44	19.35	40.47
Erbs-Willmot	25.45	17.31	8.73
Reindl-Hay	15.01	11.01	12.25
Reindl-Perez	3.21	9.09	25.76
Reindl-SO	14.88	9.72	6.72

Figure 26: The MAD (%) values of 15 different decomposition-transposition model pairs is evaluated across clear, intermediate, and overcast conditions for the FT system. Underlined numbers signify that the pair meets the specified threshold.

For the tracker, 10 of the 15 models conform to the figure of merit. Using a simple isotropic transposition model (in this case, Liu-Jordan or LJ) offers a more accurate portrayal of POA; mainly due to DHI being minimal, resulting in a low error from the measurement. Still, all models using Perez as the transposition part, adhere to the threshold, albeit producing overestimations rather than underestimations possibly due to the mathematical contributions of the model coefficients of the sky clearness bins found within the lookup table of the Perez model.

4.3.2 Overcast Conditions

By their nature, overcast conditions imply that a considerable segment of total irradiance will originate from DHI. Hence, the role of decomposition models becomes similar to their function in clear conditions but reversed - now focusing on D_T. According to Figure 26, all combinations for the FT system except for the DISC-SO pair have MAD >5%. Moreover, the range of percentage errors for the tracked system extends from 3.23% to 51.07%, while for FT, it spans 2.67% to 40.47%. For the tracked system, the number of models meeting the error threshold in overcast conditions decreased from 10 to 2. This reduction is primarily because the function of cos(AOI) nears one in clear conditions, where B_T dominates. Notably, employing LJ in the transposition role performs similarly in overcast conditions. Comparing BRL-LJ and Erbs-LJ, both assume D_T computation is uniformly distributed over the sky and their percentage errors to the measurement for the tracked system are quite similar, with a difference of only 0.24%. This further validates the use of isotropic models under overcast conditions, where diffuse irradiance scatters homogeneously.

The only model pair within the established threshold in both systems is the DISC-SO combination. However, it is important to note that the optimal estimation of DHI does not necessarily come from the DISC among the 5 decomposition models, as other transposition models using DISC still display substantial errors from the measured POA. In addition, regardless of the decomposition model used or the system type examined, combinations incorporating Perez consistently perform poorly. Extreme MAD ranges from 25.76% to 45.22%, possibly due to unsuitable constants defined in the lookup function for low sky brightness coefficients, suggesting a calibration necessity. The TC transposition model also presents the most significant POA percentage errors in both systems, with 51.07% for the tracker and 40.47% for the FT setup, respectively. The cause of this low performance is not attributed to the Erbs component, but primarily to the transposition aspect. The methodology is simplified, which can lead to inadequate results when horizons are darker during overcast conditions. The TC model results

from an integrated segment of the sky, exposed to these specified $\beta - \psi_{system}$ combinations. However, only a limited set of measurements from the 49 combinations in clear skies were taken, specifically from late January to early April at a $\varphi < 50°$.

4.3.3 Intermediate Conditions

Similar to the conditions of both clear and overcast conditions, the number of model pairs meeting the threshold is higher in the tracked system (Figure 25) compared to the FT setup (Figure 26). The tracked system features 5 model pairs with MAD within 5%, while the FT system includes only 2. For the FT system, these are DISC-Perez, which falls just 0.01% within the threshold, and DISC-SO with MAD of 2.87%. Meanwhile, the tracked system also includes these two pairs, in addition to DIRINT, DISC, and Reindl paired with Perez.

The Erbs-Willmot and Erbs-TC model combinations had the most significant percentage errors relative to the measured POA. The former had 7.14% and 17.31% for the tracker and FT system, respectively, while the latter combination showed a percentage variance of 12.95% and 19.35%. The TC model employs trigonometric principles to track D_T variability rooted in solar position, while the Willmot model exhibited a modification of the Hay model, incorporating its unique sky clarity definition and a second-order polynomial as a function of β. The conception of both the Willmot and TC models accepts that enhancements can better the approximations for dispersed clouds, as brightening on the horizon in these circumstances stem from a seemingly larger sky coverage due to clouds overlapping near the horizon. Naturally, the error percentage of Willmot and TC is reduced in a tracked system because the $\beta - \psi_{system}$ leads to angles upon which they have been validated. A certain consistency is noticeable when the Perez transposition model is applied. In the tracked system, the discrepancy between models employing Perez is marginal, with only a difference of 1.09% between the highest and lowest MAD (i.e., all fall within the 3.38% to 4.37% margin). However, the FT system does not exhibit a similar pattern, having a more significant percentage difference; i.e., 4.10% between 4.99% and 9.09%. This may suggest that the Perez model functions well under intermediate conditions and that with accurate DHI estimation, it may yield smaller percentage differences. Its coefficients seem better suited due to two primary factors: the selected coefficients align better with the average intermediate sky, and the SZA parameter may inadvertently contribute to intermediate conditions being aligned with brightness coefficients.

Moreover, during intermediate conditions, which account for the majority of the experiment's duration with an average K_t of 0.48, the roles of the decomposition and transposition models become equivalent as both B_T and D_T contribute similarly to the POA. For the tracked system, employing an isotropic transposition model (LJ) leads to an overestimation of 7.20% if BRL is the decomposition basis or 5.62% if Erbs is chosen. By assuming an isotropic sky, models can effectively capture scattering. However, FT portrayed a two-fold increase in MAD from measurement with BRL-LJ and Erbs-LJ compared to its tracking counterpart as the tracker observes sky variations under different cloud accumulations owing to its $\beta - \psi_{system}$ combinations. The decomposition models used for LJ (i.e., Erbs and BRL) may require adjustments in intermediate conditions due to their inverse sigmoid function, elucidating the estimation sign change when transitioning to a tracking system. The DISC-SO pair indicates the most suitable performance across both systems.

4.3.4 Analysis of Decomposition Against Transposition

Identifying appropriate irradiance models is critical, whether for transposition or decomposition purposes. It is particularly important to validate these models from various angles (i.e., through the use of a tracker). Feasibility software programs integrate diverse methods that incorporate decomposition models to forecast DHI and then DNI (or the other way around), followed by transposing them. The examination underway investigates which factor plays a stronger role in percentage discrepancies: the decomposition or the transposition model. Figure 27 presents the overall percentage error of the 15 model pairs on the tracker system, and Figure 28 on the FT setup. Notably, the variations display distinct percentage discrepancies. The decomposition model employed will contribute to this difference, but the transposition model implementation after the prediction of DHI (and DNI) proves to be crucial.

Decomposition \ Transposition	LJ	Perez	Hay	SO	Bugler	TC	Willmot
BRL	6.24	-	-	-	-	-	-
Erbs	5.28	13.95	6.74	6.63	7.63	23.11	16.14
DIRINT	-	14.85	-	-	-	-	-
Disc	-	14.68	5.86	3.17	-	-	-
Reindl	-	12.25	7.33	7.34	-	-	-

Figure 27: Across the 15 different optical models, the overall percentage error due to the effects of decomposition and transposition is presented for the Tracker.

A closer analysis of various combinations indicates that the main variation stems from the choice of the transposition model, irrespective of the foundation of the decomposition model. For example, considering the Erbs, DISC, and Reindl models and pairing them with Perez, Hay, or SO

reveals more apparent differences in the choice of transposition model than in the choice of decomposition model. Taking Erbs-Perez as a reference point: Altering the decomposition model leads to a maximum variation of 2.43% for the tracked system and 2.17% for the FT system among the previously mentioned models. To further corroborate this, analyzing the DISC decomposition model combined with Hay, Perez, or SO shows a variation of 6.29% for the FT system and 7.32% for the tracker system across these three configurations. Moreover, using Hay for transposition while varying the decomposition models (such as DISC, Erbs, and Reindl) results in a 5.34% variation for the FT system and 1.47% for the tracker system yet again changing the transposition yields to a maximum difference of 11.51% for the tracker system and 8.53% for the FT system. In essence, while there is a discernible difference in selecting the decomposition model, it is not as pronounced as when choosing the transposition model. This can be attributed to the varied mathematical approaches used by the transposition model to estimate the diffuse component based on DHI data.

		Transposition						
		LJ	Perez	Hay	SO	Bugler	TC	Willmot
Decomposition	BRL	9.58	-	-	-	-	-	-
	Erbs	8.77	13.54	7.25	11.47	10.92	24.95	15.63
	DIRINT	-	12.73	-	-	-	-	-
	Disc	-	11.37	6.35	2.84	-	-	-
	Reindl	-	13.20	11.69	9.33	-	-	-

Figure 28: Across the 15 different optical models, the overall percentage error due to the effects of decomposition and transposition is presented for the FT system.

4.3.5 Efficacy of the Optimal Optical Model

An important aspect of this study is to examine how well an optimal model combination performs. As noted in prior literature, it is imperative to examine the scalability of model pairs at different $\beta - \psi_{system}$ system combinations, thus this section's focus will be solely on the actuator-based tracker. Figure 25 provides a comprehensive analysis, showing that the pairing of the DISC decomposition model with the SO transposition model results in the smallest percentage errors. The DISC model incorporates SZA, and the SO model, devised empirically at ϕ =60°, includes SZA in its equation in conjunction with the AOI. Figure 29 illustrates the comparison between measured and modelled data (DISC-SO), for varying sky conditions.

Figures 29a and 29b demonstrate a close alignment between the modelled and measured POA irradiance, mirroring similar fluctuations. This alignment suggests that while the model generally captures the irradiance profile, it occasionally diverges by overestimating or underestimating the POA. The coefficients of determination (R^2), 0.5034 for clear conditions and 0.5379 for

intermediate suggest a scatter in the data points due to the high temporal resolution of the input data and hourly basis of the SO model's creation, particularly evident in Figure 29e, which shows dense clustering of data points from 0 to 200 W/m^2. In overcast conditions, as depicted in Figure 29f, there is an initial strong alignment in low irradiance readings, but less so at higher levels, explaining the low R^2 and variability.

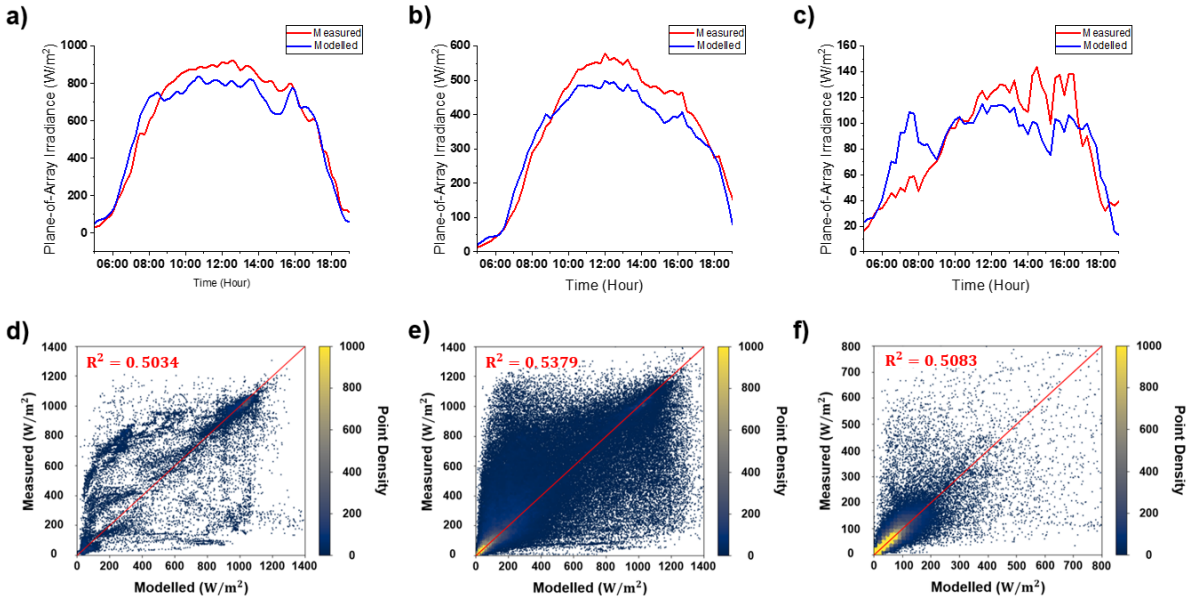

Figure 29: The given illustration shows a side-by-side comparison of POA irradiance recorded every minute but displayed in 15-minute slots against the time of day. This includes both measured and the DISC-SO model for the tracked system under clear **(a)**, intermediate **(b)**, and overcast **(c)** conditions. Additionally, a scatter plot provides a comparison of per-minute irradiance over the selected period between the measured and modelled POA for clear **(d)**, intermediate **(e)**, and overcast **(f)** conditions.

Solar radiation data is often required at intervals shorter than the typical hourly break. This demand becomes even more pressing in light of the volatile weather typical of temperate regions. Accurate irradiance estimation is crucial, especially in areas with significant variations in SZA. Using an hourly timeframe can compromise the reliability of these estimates. However, most decomposition and transposition models have been empirically developed using hourly data inputs. Hence, this study investigates the effectiveness of the DISC-SO when utilizing both hourly and minute-by-minute input data.

Across all the sky conditions, as evident in Figure 30, feeding hourly data into the decomposition and transposition contexts results in a lower MAD of the DISC-SO compared to feeding in minute-by-minute data. The most significant difference occurs during intermediate conditions, where switching from hourly to minute data shows increases of 1.68% to 3.19%. Additionally, in overcast and clear conditions, similar trends are observed. Specifically, under clear conditions, hourly data exhibit MAD of 2.35%, while minute data show 3.31%. Moreover, during overcast

conditions, minute data results in an MAD of 3.23%, whereas hourly data has an MAD of 2.15%. These variations may be due to the overprediction of DHI at the minute scale, leading to underestimations in POA when transposed, and the reverse occurring under clear conditions with minute data.

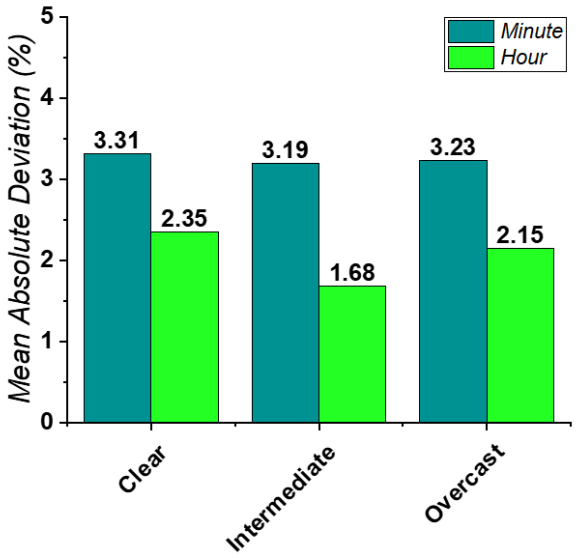

Figure 30: The MAD (%) of the DISC-SO model pair for the tracked system, using solar irradiance inputs in both hourly and minute intervals, across different sky conditions.

4.4 Sub-Hourly Validation of Transposition Models

4.4.1 Assessing Cloud Coverage Effects

Transposition Model	CAELUS Cloud Condition					
	Cloud Enhancement	Cloudless	Thin Clouds	Scatter Clouds	Thick Clouds	Overcast
Badescu	8.64	7.90	12.28	14.69	11.13	12.35
Bugler	6.76	7.19	11.10	12.67	10.56	11.48
Hay	7.32	7.60	11.23	12.85	10.58	11.49
Hay 1993	7.32	7.57	11.27	12.14	10.46	11.49
HDKR	7.54	7.73	11.48	12.18	10.97	11.03
Jimenez	15.80	11.77	17.23	27.66	38.44	39.19
Klucher	7.51	7.67	11.25	12.32	10.60	11.50
Koronakis	7.07	7.15	11.36	12.51	11.95	12.63
LJ	7.54	7.35	11.62	13.08	10.56	11.48
MI	16.18	11.27	16.38	24.60	38.61	41.91
Perez	7.42	7.46	14.37	15.66	18.12	17.42
Reindl	7.88	7.69	11.75	12.67	10.64	11.53
SO	2.69	2.84	4.44	5.03	4.23	4.59
TC	7.91	7.44	12.69	16.43	28.40	27.41
Tian	8.55	7.82	12.11	14.43	10.20	11.54
Willmot	13.21	12.64	10.04	13.83	25.75	24.81

Figure 31: The MAD (%) of 16 different transposition models over six distinct cloud coverage scenarios utilizing the CAELUS algorithm, incorporating inputs of measured GHI, DNI and DHI.

Figure 31 clearly illustrates that among the 16 transposition models evaluated, the SO model consistently performs the best under varying cloud conditions as recorded by CAELUS. The SO

model shows the smallest deviation from measured DAT POA irradiance, with discrepancies ranging from 2.7% under cloud enhancement conditions to 5.0% in scattered cloud conditions. Specifically, the lowest MAD of 2.7% occurs under the cloud enhancement condition, attributed to the SO model, while the highest MAD, reaching 41.9%, is observed in the Ma-Iqbal (MI) model during overcast conditions.

Regarding discrepancies, the Jiminez and MI models consistently exhibit the highest MAD. This pattern arises because both models employ a similar approach to calculating the transposition factor, incorporating functions of the AOI and SZA along with their tilt inputs. Delving into the specifics, the MI model incorporates both K_t and K_t^2 within its calculations. This approach might introduce exacerbating effects when squared, particularly under conditions of low K_t moments which are typical in overcast and thick cloud scenarios. In such weather, a low K_t value does not directly correspond to a specific, singular higher K_d value; instead, K_d exhibits significant variability across a range of K_t values as discussed in the earlier chapter. For the Jiminez model, it operates under the assumption that 20% of the cloud cover is diffused. This assumption proves problematic, particularly in the contexts of overcast and thick cloud formations, where such a simplification can lead to significant inaccuracies in model outputs.

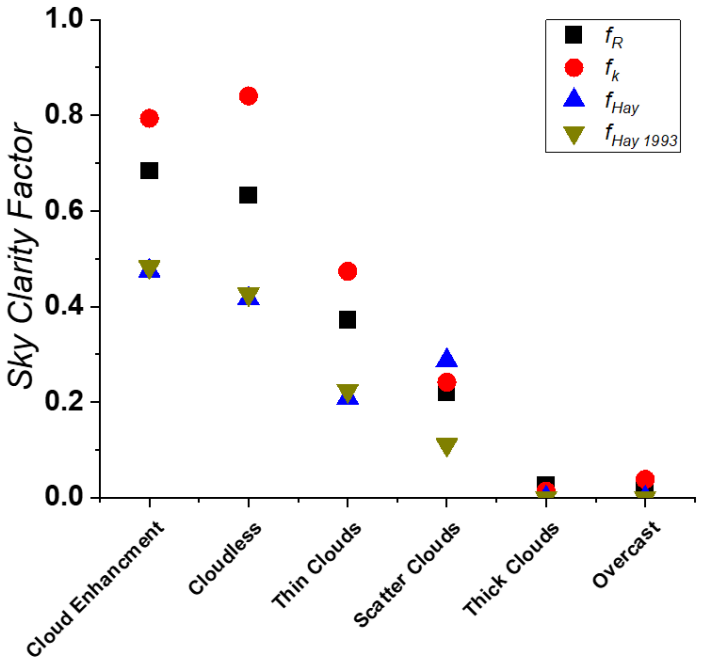

Figure 32: Four distinct factors are utilized within transposition models, each exhibiting average values across six unique cloud coverage scenarios from the CAELUS algorithm.

In contrast, the Hay and Hay1993 models demonstrate remarkably similar performances, with a maximum deviation of only 0.39% under scattered cloud conditions. The Hay1993 model, an updated version of the Hay model, modifies the original sky factor. However, this alteration

seems ineffective in temperate regions, particularly when observing minute-by-minute variations as per Figure 32 which shows the different factors. Specifically, the original Hay model calculates a sky clarity factor using the ratio of DNI to Extraterrestrial Direct Normal Solar Irradiance (named f_{Hay}), whereas the Hay1993 model adjusts this ratio to DNI divided by the solar constant, thereby normalizing to the peak values of solar irradiance (named $f_{Hay\ 1993}$). Nonetheless, it is observed that during periods of scattered clouds, the average value f_{Hay} is 0.29, in contrast to $f_{Hay\ 1993}$, which averages at 0.11 (nearly three times less). This difference could account for why the Hay 1993 model exhibits a MAD of less than 0.71% in scatter cloud conditions. Furthermore, Figure 32 shows that f_{Hay} is not showing the inversely proportion trend of a lower factor as moving toward overcast conditions, unlike its counterparts.

Moreover, isotropic models such as those by Badescu, Koronakis, LJ, and Tian demonstrate minor discrepancies across various cloud conditions. The differences are modest, ranging from 1.57% in cloud-enhanced scenarios to 0.75% in cloudless conditions, 0.92% in thin clouds, 2.18% in scattered clouds, 1.75% in thick clouds, and 1.15% in overcast conditions. These models assume that the intensity of diffuse irradiance is uniformly distributed across the sky. However, this isotropic assumption does not entirely hold as the models apply different numerical splits to the sky conditions; for instance, LJ uses a division factor of 50%, Badescu uses 75%, and Koronakis applies two-thirds. This variation underscores the limitations of the isotropic approach in accurately modelling sky conditions across different cloud types.

The Reindl model seeks to quantify the diffuse irradiance emanating from near-horizon regions by introducing a modulation factor (f_R). This model posits that the intensity of diffuse irradiance decreases with increasing cloud cover, specifically from the horizon. Its performance is nearly identical to that of its successor, the Klucher model, with only minor discrepancies, peaking at a difference of 0.5% during thin cloud conditions. The Klucher model builds on this by attempting to refine cloud coverage estimations to better capture horizon effects, aiming to enhance sky clarity through deploying its own factor named (f_K). Klucher outperforms its Reindl counterpart primarily due to the effectiveness of its applied factor. Notably, the values of f_K exceed those of f_R in various conditions; by over 0.11 during cloud enhancement, more than 0.21 in cloudless conditions, and exceeding 0.10 during thin cloud coverage. This differential in factor values may account for Klucher's slight edge over the Reindl model. Consequently, the Klucher model achieves modest improvements, noting a 0.40% increase in accuracy during cloud-enhanced conditions, a 0.02% improvement under cloudless skies, and a 0.50% enhancement during thin cloud periods, when compared to the Reindl benchmark. Figure 32 illustrates only minor discrepancies between f_R and f_K in overcast and thick cloud scenarios (less than 0.02%),

corresponding to minimal MAD differences of 0.03% and 0.04% for overcast and thick cloud conditions, respectively.

The HDKR model, derived from the Hay model, incorporates a horizon brightening mechanism akin to the Klucher model (f_K) but still delivers similar performance. This similarity suggests that its empirical mathematical equation does not significantly enhance irradiance predictions in temperate climates on a minute-by-minute basis. Consistent with previous findings, the TC and Willmot models also display comparable outcomes, indicating that their empirical approaches to quantifying solar disc proximity and sky irradiance from the horizon region fall short, particularly under thick cloud and overcast conditions, where their MAD exceeds 24%.

Delving deeper into the empirical foundations of the SO model, which utilized solar irradiance measurements from Norway at a specific ϕ (60.2º), it appears that diffuse radiation primarily emanates from parts of the sky near the SZA under overcast conditions. This effect diminishes with the absence of cloud cover, as demonstrated by its optimal performances with the lowest MAD of 2.68% in cloud enhancement conditions and 2.84% in cloudless conditions. The SO model advances the Hay model by integrating a correction factor that accounts for barriers that obscure part of the diffuse irradiance from the horizon. This inclusion is distinctive, as such barriers are often overlooked in other transposition models.

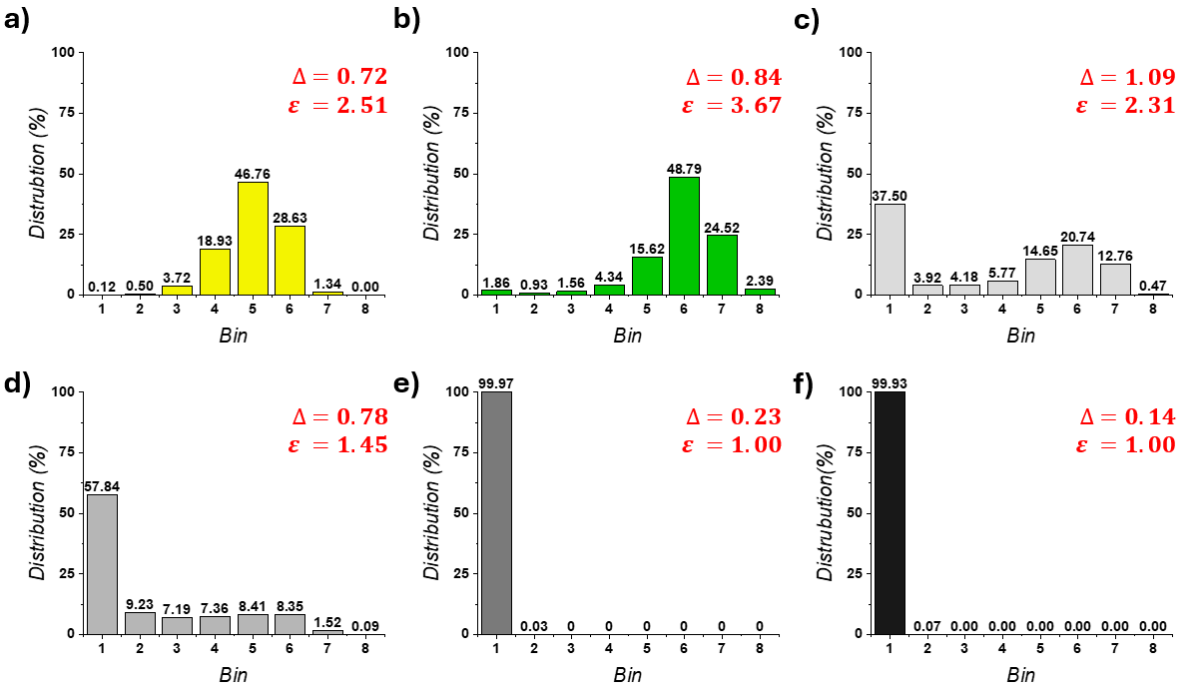

Figure 33: Bar chart series designed to illustrate the distribution of bins utilized by the Perez model in its mathematical computations across various cloud conditions: **a)** cloud enhancement moments, **b)** cloudless moments, **c)** thin cloud moments, **d)** scattered cloud moments, **e)** thick cloud moments, and **f)** overcast moments. The average sky clearness (ε) and brightness (Δ) coefficients are shown for each cloud condition.

Most feasibility software opts for either a simple isotropic model, such as LJ, or a more complex transposition model like the Perez Model. It would be insightful to compare the performance of these models more closely with the superior SO model. According to Figure 31, the performance of the Perez model declines as cloud cover increases. The MAD reaches its highest at 18.12% under thick cloud conditions and 17.42% during overcast scenarios. Additionally, in scattered clouds and thin cloud conditions, the MAD registers at 15.66% and 14.37%, respectively. This observation confirms earlier findings that the coefficients deployed within the Perez model's lookup tables may not be well-suited for temperate climates like that of the United Kingdom, despite including DHI and DNI measurements. The Perez model incorporates two principal parameters within its empirical framework: the brightness coefficient (Δ) and the clearness coefficient (ε). These coefficients are integral to the empirical functions utilized in the model. However, the primary challenge may not stem from Δ but from ε, which are pivotal for ensuring model accuracy across varying sky conditions. According to Figure 33, it presents the average Δ and ε specified under the CAELUS cloud conditions. Furthermore, it delineates the distribution of bins that the Perez model employs in its mathematical computations across different cloud scenarios. The Perez model utilizes eight bins to determine the coefficients for its mathematical function. Notably, in conditions such as thin, scattered, thick, and overcast clouds, the majority of counts (i.e., the computed ε condition) are predominantly found in bin number 1, accounting for 37.50% in thin clouds, 57.84% in scattered clouds, 99.97% in thick clouds, and 99.93% in overcast conditions. This suggests that the coefficients associated with bin 1 in the Perez model, designed to adapt to various sky conditions, may not be optimal for temperate regions.

Different transposition models handle anisotropic cloud brightening effects through varying approaches. Cloud brightening refers to the phenomenon where thin or fragmented clouds increase diffuse irradiance near the solar disk, within the circumsolar region [40]. This leads to a non-uniform, or anisotropic, distribution of diffuse radiation with a greater concentration near the sun’s position rather than being evenly scatted across the sky. The Perez example, as previously discussed, explicitly incorporates anisotropic sky conditions by separating the diffuse irradiance into three distinct components: circumsolar brightening, horizon brightening and isotropic diffuse radiation [185]. It adjusts the transposition of the diffuse irradiance through dynamically weighing these components based on the clearness index and SZA. The SO model, through its mathematical formulation, introduces a correction mechanism based on the parameter f_{Hay}. When f_{Hay} is elevated, which is typical under clear skies or conditions with pronounced circumsolar enhancement, the model applies a correction factor to account for increased anisotropy. This adjustment helps reduce the overestimation of irradiance near the solar disk, particularly during periods of thin cloud cover or high cloud concentration. By scaling the

circumsolar contribution appropriately, the SO model improves its accuracy under varying cloud conditions as depicted in Figure 31.

4.4.2 Investigating Solar Position Dynamics

Figure 31 illustrates that the SO model consistently surpasses the performance of both the LJ and Perez models under various atmospheric conditions. This superiority is primarily due to the different methods these models use to manage anisotropy and circumsolar effects in dynamic cloud scenarios. Specifically, the LJ model, a traditional approach to diffuse irradiance modelling, assumes a uniform distribution of diffuse light across the sky dome. This isotropic assumption falters under conditions such as thin or scattered clouds, which can intensify brightness in specific sections of the sky, leading to significant deviations in its predictions, as evidenced by its MAD of 11.62% for thin clouds and 13.08% for scattered clouds. This limitation results in broader scatter and systematic errors in the predicted POA irradiance. In contrast, the Perez model introduces adjustments for the anisotropic distribution of diffuse irradiance, incorporating factors that account for circumsolar and horizon brightening along with other directional influences. However, in environments characterized by complex cloud movements (such as thin clouds traversing the solar disk or scattered clouds causing intermittent bright spots) Perez's mathematical model may still fall short. The model occasionally fails to capture the high spatial and temporal variability brought on by fluctuating cloud cover. The consistently superior performance of the SO model is attributed to its refined approach in modelling the sky's diffuse component, which effectively adapts to evolving atmospheric dynamics. This model integrates angular distribution functions sensitive to the direct beam’s position and the heterogeneous nature of cloud layers. For instance, under thin clouds, the SO model records MAD of 4.44%, significantly lower than Perez's 14.37% and LJ's 11.62%. Under scattered clouds and thick cloud instances, the SO model maintains MAD rates of 5.03% and 4.23%, respectively, while LJ and Perez exhibit markedly higher errors. This trend highlights the SO model's capability to maintain lower error rates in highly variable and challenging sky conditions, showcasing its advanced handling of anisotropic diffuse radiation and dynamic cloud interactions.

Figure 34 presents scatter graphs that illustrate the point density for six specified cloud conditions, also showing the distribution of altitude and azimuth (i.e., the sun path) as a function of K_t, using measured DAT POA as the benchmark. In scenarios of cloud enhancement, the SO model registers the lowest MAD at 2.69%, followed by the Perez model at 7.42%, and the LJ model trailing slightly with an additional 0.12%. Notably, during cloud enhancement, the majority of K_t values exceed 0.68, with lower values observed at times of low altitude (high SZA). Furthermore,

Figure 35 delves into the interplay between solar position and the MAD for each model. The SO model displays fewer instances where MAD exceeds 20%, especially when compared to the LJ and Perez models, which both show a broader distribution of MAD instances above 20% during periods of low altitude. In conditions characterized by bright cloud edges that amplify local irradiance, the measured POA irradiance frequently surpasses predictions by the LJ and Perez models. This discrepancy is addressed by the SO model, which incorporates elements (such as the AOI and SZA) that account for transient increases in light due to forward scattering at cloud edges, thereby enhancing accuracy and consistency in matching observed data.

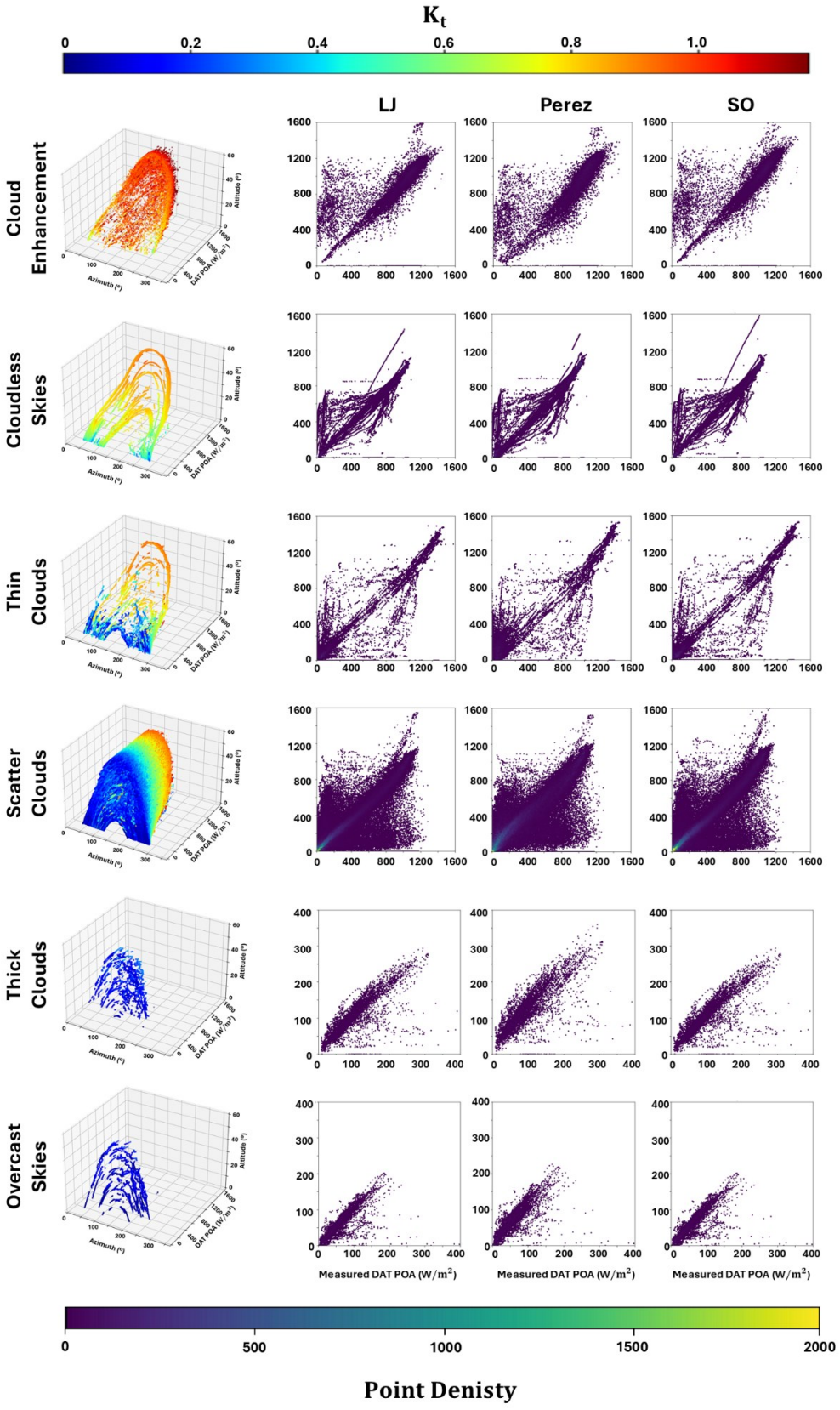

Figure 34: In an analysis of six distinct cloud formation instances, the scatter plots for the Liu-Jordan (LJ), Perez, and Skartveit-Olseth (SO) models are displayed, emphasizing point density variations. Additionally, the measured DAT POA values are presented across various solar position coordinates, serving as a benchmark relative to the clearness index (K_t).

During cloudless moments, the LJ and Perez models exhibit closely matched performances, with only a 0.11% difference in MAD; however, the SO model achieves the lowest MAD at just 2.84%. Even under clear skies, slight variations in atmospheric clarity, aerosol content, and solar geometry (as depicted in Figure 35) can introduce significant anisotropy in diffuse irradiance. The SO model's advanced angular distributions enable it to more accurately align with measured POA values, evident by the denser clustering of data points along the one-to-one line. Even in scenarios typically considered straightforward for modelling, the SO model demonstrates superior performance with MAD nearly one-third that of the LJ (7.35%) and Perez (7.46%) models. Figure 35 also highlights the rarity of instances where the SO model's MAD exceeds 20%, contrasting sharply with the Perez and LJ models under thin and scattered cloud conditions. When said clouds intermittently block the sun or drift through the circumsolar region, the direct-to-diffuse irradiance ratio shifts abruptly. The SO model efficiently accommodates these rapid changes through a function that manages the effects of obstacles blocking the horizon and partially obscuring diffuse irradiance. This approach results in a more consistent alignment of modelled points with measured data, avoiding the broad spread or systematic deviations that are more apparent in the LJ and Perez models.

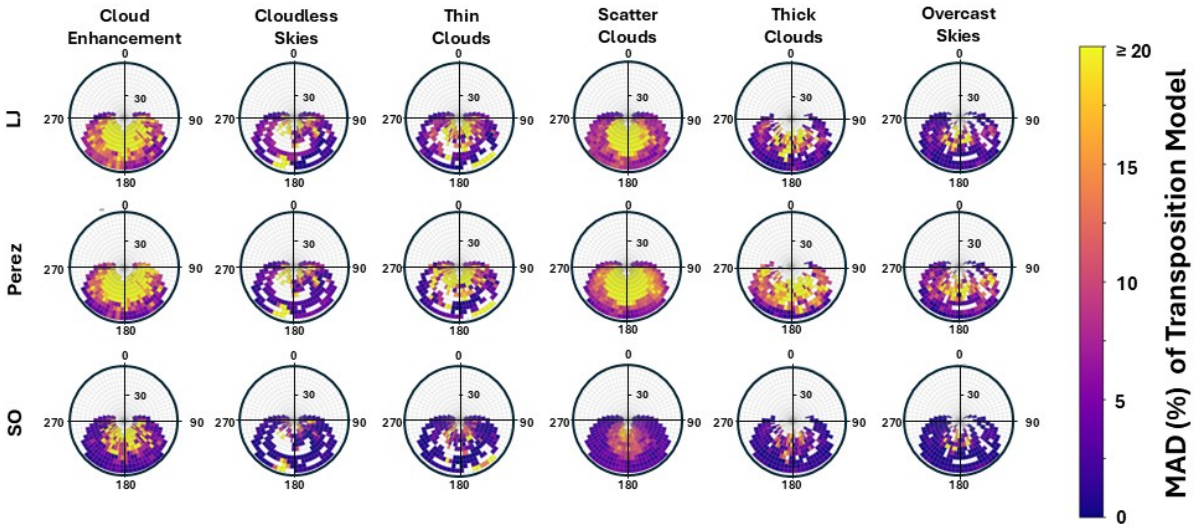

Figure 35: The altitude-azimuth coordinate system illustrates the MAD as a function of cloud formation, utilizing the CAELUS algorithm across three transposition models: Liu-Jordan (LJ), Perez, and Skartveit-Olseth (SO). In such plots, sections are demarcated at 10 degrees azimuth and 5 degrees altitude.

Under uniformly cloudy conditions (i.e., overcast conditions), where irradiance is predominantly diffuse yet directionally influenced (e.g., minimal horizon brightening but increased illumination from the cloud base), the SO model demonstrates greater adaptability compared to the LJ model, which tends to underperform because of its reliance on isotropic assumptions. It also consistently surpasses the Perez model, which struggles with inaccuracies due to poorly

calibrated parameters for thick, homogeneous clouds, particularly due to the incorrect coefficients from bin 1 as discussed previously. These differences highlight the advanced capabilities of the SO model in handling diverse atmospheric conditions more effectively. Figure 35 demonstrates that in scenarios with dense clouds and overcast skies, the SO model maintains a more stable distribution of MAD values across azimuthal-altitude coordinates, indicating its effectiveness not only in complex weather conditions but also in improving overall measurement accuracy. Numerically, as per Figure 31, when diffuse irradiance predominates (i.e., Overcast conditions), the SO model achieves a notably lower MAD of 4.59% compared to LJ (11.48%) and Perez (17.42%). This significant advantage underscores the SO model's superior performance in modelling diffuse irradiance, even in environments with uniformly low light levels.

4.5 Conclusion

In conclusion, this chapter involved analysing 15 different optical model combinations within feasibility software, comparing them against measured POA for both a tracking and a south-facing tilted system set at 55° in a sub-hourly context. The error of the model-derived POA from that derived from measurement (i.e., the error of the model) ranged drastically, from 2.67% to 51.07%, influenced by factors such as K_t and the type of system used. Evaluating the precision of these models, particularly when MAD exceeded 5%, revealed inconsistencies across different sky conditions. Specifically, the number of model pairs meeting the threshold decreased with diminishing sky clarity: 10 pairs in clear skies (ranging from 2.78% to 4.97%), five pairs in intermediate conditions (from 3.12% to 4.37%), and only two pairs under overcast conditions (4.81% and 3.23%) for the tracking system. For the fixed tilt system, the numbers were five in clear conditions (from 3.21% to 4.96%) and two in intermediate conditions, dropping to just one, DISC-SO, in overcast conditions with an MAD of 2.67%. Furthermore, the impact of decomposition versus transposition was examined. While changes in decomposition resulted in a maximum percentage discrepancy of 2.43% for tracking systems and 5.34% for fixed-tilt systems, altering the transposition model led to a percentage error of 11.51% for tracking systems and 8.53% for fixed-tilt systems. Additionally, the DISC-SO pair was analyzed to assess the effect of temporal resolution in input solar irradiance data. It was found that using hourly input data resulted in lower MAD, with values of 1.44% under intermediate conditions, 2.15% in overcast conditions, and 2.35% in clear conditions, performing better than minute data. This may be due to the empirical definition of the model combination, as the models were developed using hourly data rather than minute data. This chapter examines the integration of measurement data into transposition models, eliminating the necessity for decomposition models. The analysis covered 16

transposition models, eight of which are utilized in feasibility software, across six different cloud conditions. Discrepancies in model outputs ranged from 2.69% to 41.91%. Notably, the SO model demonstrated the smallest deviations from measured DAT POA irradiance, with discrepancies as low as 2.69% under cloud enhancement conditions and up to 5.03% under scattered cloud conditions. Further mathematical exploration of these models revealed that the specific implementations of some models significantly influence their performance under varying cloud scenarios. Both the original Hay model and its refined version, Hay1993, displayed similar performance, with maximum discrepancies of just 0.71%, attributed to the updated factor in Hay1993. Moreover, the analysis highlighted the Perez model's poor performance in cloudy conditions, which is primarily due to the unsuitability of the clearness coefficient used within its 1st bin for temperate climates at minute-level irradiance measurement. Further investigations into the Perez model, alongside the LJ and SO models, delved into the dynamics of cloud concentration and azimuth-altitude movements. Among these, the SO model was found to be the most effective, showing the lowest MAD values of 2.69%, 2.84%, 4.44%, 5.03%, 4.23%, and 4.59% under various cloud conditions including cloud enhancement, cloudless, thin clouds, scattered clouds, thick clouds, and overcast, respectively. Future research can progress by adjusting the thresholds of the clearness coefficient for various bins to better align with temperate climates and minute-level data. Additionally, the findings presented in this chapter establish a foundation for BOA irradiance estimations, utilizing the identified transposition factor, specifically the SO model.

Chapter 5 Evaluation of Clear-Sky Irradiance Prediction with Varying Atmospheric Data Inputs

5.1 Introduction

Accurate solar resource assessments are vital for the effective design and performance modelling of PV systems throughout their operational lifespan, significantly influencing economic planning based on anticipated energy outputs. These evaluations typically depend on precise solar radiation data, ideally obtained from direct irradiance measurements, which underpin feasibility studies. Yet, the acquisition of such data often faces challenges due to the substantial upfront investment required for radiometers, their maintenance costs, and the demands of continuous operation. Comprehensive data collection necessitates monitoring across all seasonal cycles with different sun paths to capture the dynamic nature of solar conditions and varied sunlight exposure. In many areas, especially those without direct irradiance measurements, the complexity of solar irradiance estimations increases due to atmospheric interference such as gas absorption, particle scattering, and cloud coverage, all of which vary by geography and climate, complicating site-specific assessments. Consequently, forecasters frequently resort to using modelled data. These models primarily employ clear sky irradiance estimates, which predict the solar irradiance that reaches the Earth's surface under clear sky conditions, proving essential not only for projections but also for assessing solar potential in optimal conditions. Previous studies have recommended using specific measurement inputs like AOD550, AE, and PW for these models, although such detailed measurements often remain unrecorded. This chapter will delve into the critical role of precise clear-sky irradiance data across various applications and evaluate the impact of atmospheric conditions derived from satellite data on solar irradiance modelling. It will scrutinize six clear-sky models, including the accessible McClear and ERA5 model alongside four REST2 variants that integrate data from MERRA2 (with and without an elevation adjustment mechanism), CAMS, and benchmark measurements from AERONET. By merging irradiance modelling with assorted satellite datasets from 67 global stations, totaling over 18 million data points, this analysis will offer a comprehensive insight into how different atmospheric inputs influence the errors in modelled irradiance, shaped by the specific configurations of radiation models and the diverse satellite data utilized.

5.2 Research Approach

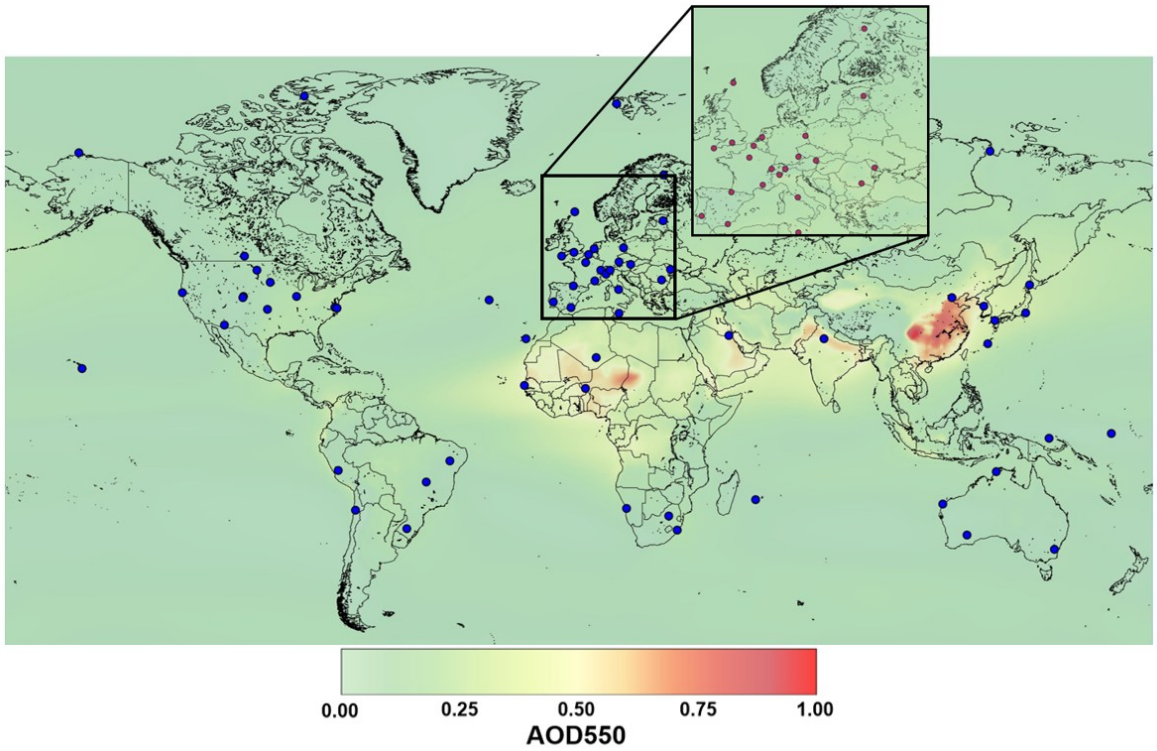

Figure 36: Global map showing the mean annual aerosol optical depth (AOD) from MERRA2 for regions within ±60° latitude [72][274], featuring pairs of radiometric and sunphotometric stations marked by blue circular dots. The inset focuses on European stations, which are highlighted with dark pink dots.

Prior studies have demonstrated that clear-sky models incorporating atmospheric inputs like AOD550, AE, and PW yield more accurate predictions. These parameters significantly influence irradiance, as previously detailed in this thesis. The focus here is on two readily accessible models that employ these specific inputs, beginning with the McClear model. It is a fully physical model, that not only surpasses many empirical models but which also operates as a web service. This model is based on radiative transfer principles, it uses atmospheric properties provided by the EU-funded MACC project to estimate solar irradiance during cloud-free instances. It incorporates AE and AOD values synonymous with CAMS. McClear's design utilizes lookup tables established with the libRadTran radiative transfer model, allowing rapid execution and the capability to run as a web service using satellite data sets. The service delivers GHI_{Clear} and DNI_{Clear} at one-minute intervals. The physical nature and user-friendly accessibility of McClear make it an attractive option for solar forecasters. The other easily accessible irradiance model is ERA5, the fifth-generation satellite dataset from the European Centre for Medium-Range Weather Forecasts (ECMWF), offers significant improvements in spatial and temporal resolution compared to its predecessors, providing data from 1950 to nearly real-time. It supports satellite-

derived parameters with a spatial resolution of 31 km and hourly temporal updates. Furthermore, This research also employs the REST2 model in four distinct iterations, including one from AERONET that serves as the benchmark. The other three iterations of REST2 utilize satellite data from CAMS and MERRA-2, the latter of which is analysed both with and without elevation correction procedures. Thus, this chapter compares the integration of REST2 with various satellite datasets against DNI_{Clear} and GHI_{Clear} estimates derived from McClear and ERA5. This comparison aims to illuminate the variances between predicted and actual measured GHI and DNI under clear-sky conditions, potentially providing new perspectives on solar irradiance predictions.

To develop a dependable approach for estimating solar irradiance, this chapter merges irradiance modelling with diverse satellite datasets. It evaluates the influence of different modelling challenges on solar radiation estimates, utilizing data from 67 high-quality stations worldwide, as illustrated in Figure 36 (and see Appendix D). With over 18 million valid data points gathered from these stations, this extensive dataset enables a thorough exploration of how errors in modelled irradiance propagate from varied atmospheric inputs, influenced by the architectural complexities of the radiation models and the heterogeneous application of satellite data.

In the process of estimating clear sky irradiance, several data manipulation and handling steps are required. The initial phase involves preparing data to ensure that the measured irradiance at the target station coincides with both AERONET readings and the temporal scope of satellite data from MERRA2, CAMS, and ERA5. This comprehensive analysis spans five distinct datasets (three from satellite sources, one from measured readings, and one from AERONET), focusing on the period from 2003 to 2022. It is crucial that AERONET and measured irradiance data overlap within this 19-year window.

After addressing the data preparation aspect, the measured GHI and DNI data are applied to two distinct clear-sky methodologies, specifically BrightSun [43] and CAELUS [40] models. For BrightSun, inputs include computed values of GHI and DNI, while CAELUS additionally requires the insertion of cloudless, clean, and dry global horizontal irradiance, denoted as GHI_{cda} in the Figure 37. Both approaches require data on solar positioning along with reference values for GHI_{Clear} and DNI_{Clear}. A moment recognized as clear, despite stringent criteria, is best identified when BrightSun and CAELUS criteria are concurrently satisfied (i.e., showing mutual inclusivity), ensuring precise delineation of clear conditions. This method enables accurate identification and analysis of clear-sky conditions, as detailed within this chapter. After identifying the clear-sky periods, four distinct iterations of the REST2 model were implemented. In parallel, irradiance estimates from the ERA5 and McClear models were obtained. The required input parameters for

these models were gathered by matching them to their respective sources: for example, aerosol optical properties were retrieved from the AERONET site corresponding to each location (67 sites in total), while MERRA-2 data were used for meteorological parameters, and CAMS data were used for atmospheric composition inputs. Only three parameters (AOD550, AE and PW) varied across the four datasets, as illustrated in Figure 37. The remaining input parameters for the proprietary REST2 model were standardized: near-infrared and visible albedo values were sourced from ERA5; NO2 concentrations were taken from CAMS; ozone levels were retrieved from MERRA-2; and surface pressure data were obtained from on-site meteorological measurements. The entire workflow was programmed in Python at a minute-by-minute resolution. The MAD metric was calculated using the scikit-learn library. Model performance was evaluated by comparing the estimated irradiance values to ground-based measurements obtained from the corresponding AERONET radiometer site. Further details regarding the AERONET configuration and associated radiometric instrumentation are provided in Appendix D.

***Table 9*:** Sources of input data used with REST2, with their spatial resolution. The elevation correction procedure modifies both Precipitable water and AOD550 to take the difference in elevation between the station and the MERRA-2 pixel into consideration, resulting in a particular form of interpolation.

Quantity	Source	Spatial resolution
Solar constant	[58]	Point
Solar position	[53]	Point
Station pressure	Site observation (AERONET if missing)	Point
Ozone column	MERRA2	0.5 x 0.625°
Aerosol single-scattering albedo	MERRA2	0.5 x 0.625°
Surface albedo, UV-VIS	ERA5	0.25 x 0.25°
Surface albedo, NIR	ERA5	0.25 x 0.25°
Nitrogen dioxide	CAMS	0.5 x 0.5°
Precipitable water	MERRA2 (reference)	0.5 x 0.625°
	MERRA2 (elevation corrected)	0.5 x 0.625° (interp.)
AOD550 & AE	AERONET (reference)	Point
	CAMS	0.5 x 0.5°
	MERRA2	0.5 x 0.625°
	MERRA2 (elevation corrected)	0.5 x 0.625° (interp.)

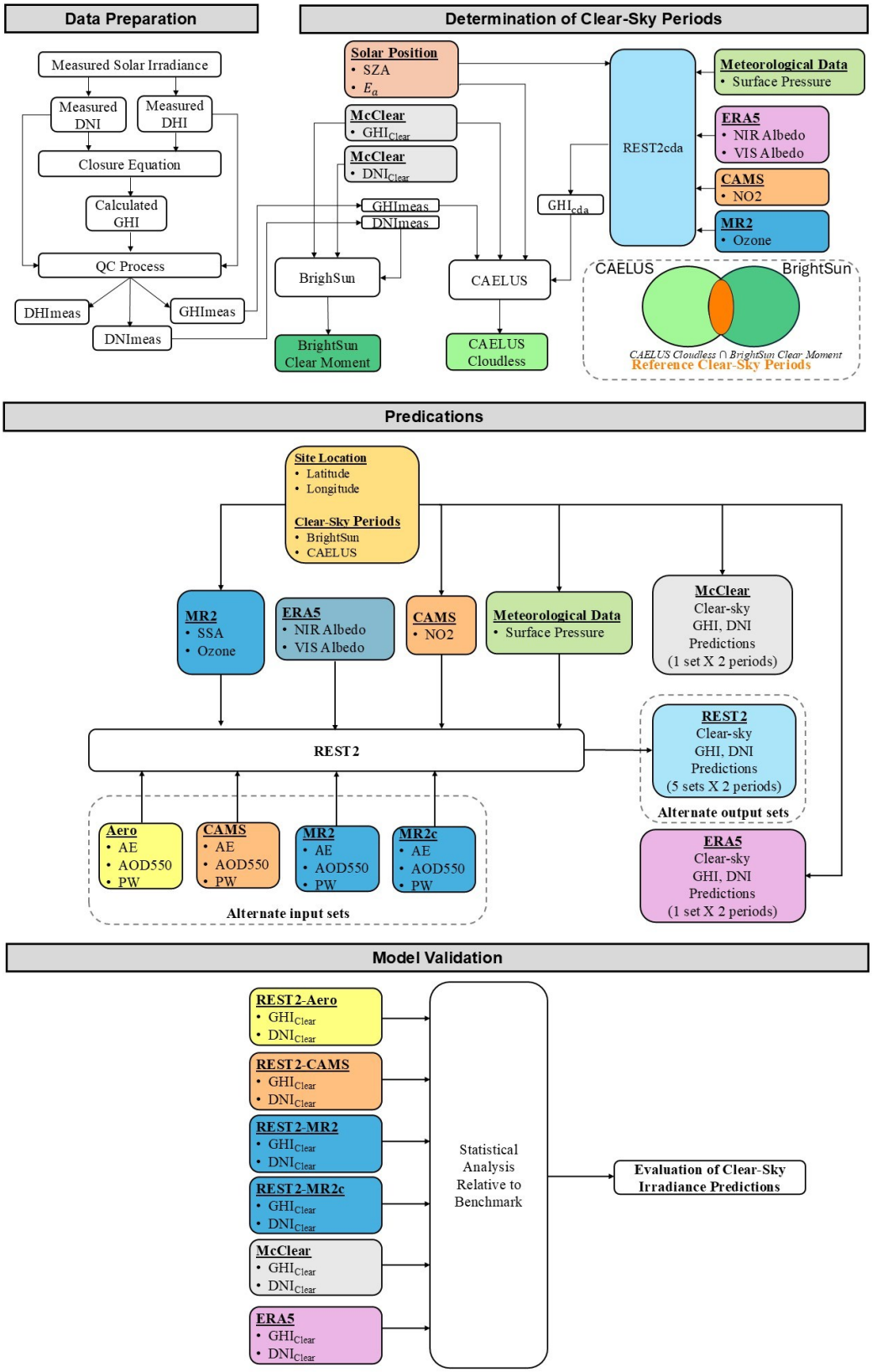

Figure 37: Flowchart illustrating the parallel computation of clear-sky irradiance using four alternative methods in addition to the precalculated results from McClear and ERA5. The process is divided into several stages: data preparation, determination of clear-sky periods, predictions made using the REST2 model, and subsequent model validation.

The computation of AE involves various methodologies across different data sources as per Table 9. MERRA2 uses a preset default value for this calculation. In contrast, AERONET and CAMS determine AE through a least-squares fit applied to a logarithmic equation [67]. Since McClear is derived from CAMS data, it adopts the same AE as CAMS. Regarding the calculation of AOD550, both CAMS and MERRA2 utilize their respective default values. For AERONET, AOD550 is calculated using a linear fit, which is derived from the linearization of the Ångström law [68]. McClear, on the other hand, employs the sum of eight Different AOD550 values for its computations.

The REST2 model is utilized with four distinct alternate input sets. The baseline inputs include the computed AE and AOD550 from AERONET, alongside data from CAMS and MERRA2. Additionally, the MERRA2 AOD and PW inputs are both alternatively adjusted for elevation, hence the named *MERRA2c* which connotes to MERRA2 with elevation correction. Therefore, the CAMS and MERRA2 atmospheric data are all compared to AERONET for further insight.

The various satellite datasets used in this study feature different temporal resolutions, whereas the measured irradiance data is recorded in 1-minute increments. To achieve temporal homogeneity, a two-step process is employed. Firstly, for the satellite data, a 1-minute interpolation is performed using the piecewise cubic Hermite polynomial to align with the measured irradiance data as per [68]. Secondly, since AERONET operates on a different (and variable) time increment compared to the other datasets, a matching process is implemented. The midpoint of each 1-minute period is aligned with the exact AERONET observation time within a 10-minute window, i.e., ±5 minutes around the specific time point. If multiple AERONET observations fall within this window, each corresponding radiation data point is included to ensure comprehensive temporal alignment and to decrease possible errors [68].

5.3 Comparison of Atmospheric Data Inputs

It is essential to recognize the significance of aerosol measurements, particularly AOD550 and AE. These elements are critical for clear-sky modelling. AE indicates an inverse relationship with particle size within aerosols - the smaller the particles, the higher the exponent. Large particles, like cloud droplets, result in a minimal Angstrom exponent. AOD550 measures how much light aerosols absorb or scatter through an atmospheric column. The choice of 550 nm as a standard measurement wavelength is due to its position at the peak of the solar irradiance spectrum, which captures a significant amount of solar energy. Standardizing this measurement across

various times and locations using instruments or satellite data is vital for consistent aerosol monitoring and atmospheric model validation.

Table 10: The MAD values for the AE, AOD550, and PW across all 67 sites are presented with bold highlighting on the reanalysis data (either CAMS or MERRA2) that shows the least discrepancy between the two.

Statistical Value	AE	AOD550	PW
MAD(%)			
MERRA2	**17.24**	**50.48**	**33.92**
CAMS	29.12	85.44	36.46

A comprehensive assessment of satellite data sources for both AOD550 and *AE* remains essential. Examination of 67 sites indicates that MERRA2 demonstrates superior performance compared to CAMS for these aerosol parameters. As shown in Table 10, MERRA2 attains an MAD reduction of approximately 11.88% for AE and 34.96% for AOD550 relative to CAMS. This discrepancy can be partially attributed to MERRA2's direct assimilation of MODIS observations, which undergo bias correction to ensure closer agreement with AERONET measurements. In contrast, CAMS calculates *AE* from only four reported AOD wavelengths (469 nm, 550 nm, 670 nm, and 865 nm) using the Ångström exponent, whereas MERRA2 applies a comparable methodology but incorporates a different aerosol modelling framework. Such distinctions may reflect differences in aerosol chemistry and transport modelling and the varying impacts of assimilating diverse remotely sensed data sources. These factors may also explain why, despite both datasets showing relatively high AOD550, MERRA2 generally outperforms CAMS. This advantage likely arises from MERRA2's broader inclusion of spaceborne retrievals, bias-corrected MODIS data, and assimilation of extensive AERONET observations. However, it is acknowledged that this approach somewhat favors MERRA2 by design, given that its validation is not fully independent from AERONET. In addition, MERRA2 may also be validated through other sunphotometer networks that do not have publicly accessible data, limiting the availability of truly independent ground-truth information. The current difficulty in establishing the exact uncertainty in AOD550 predictions from these reanalyses is further compounded by differences between gridded data products (such as MERRA2 or CAMS) and actual ground-based measurements. Nevertheless, the results in Table 10 strongly indicate that MERRA2 generally surpasses CAMS. Both datasets, however, offer distinct advantages over more traditional satellite-only observations, including improved spatial and temporal continuity, reduced cloud interference, and enhanced temporal resolution (3-hourly for CAMS and hourly for MERRA2). Yet both still rely critically on satellite observations. The biases observed here suggest that further refinements are needed in the chemical transport models underlying these satellite products, as

their effectiveness may depend on correctly representing the composition and temporal variability of local aerosol populations.

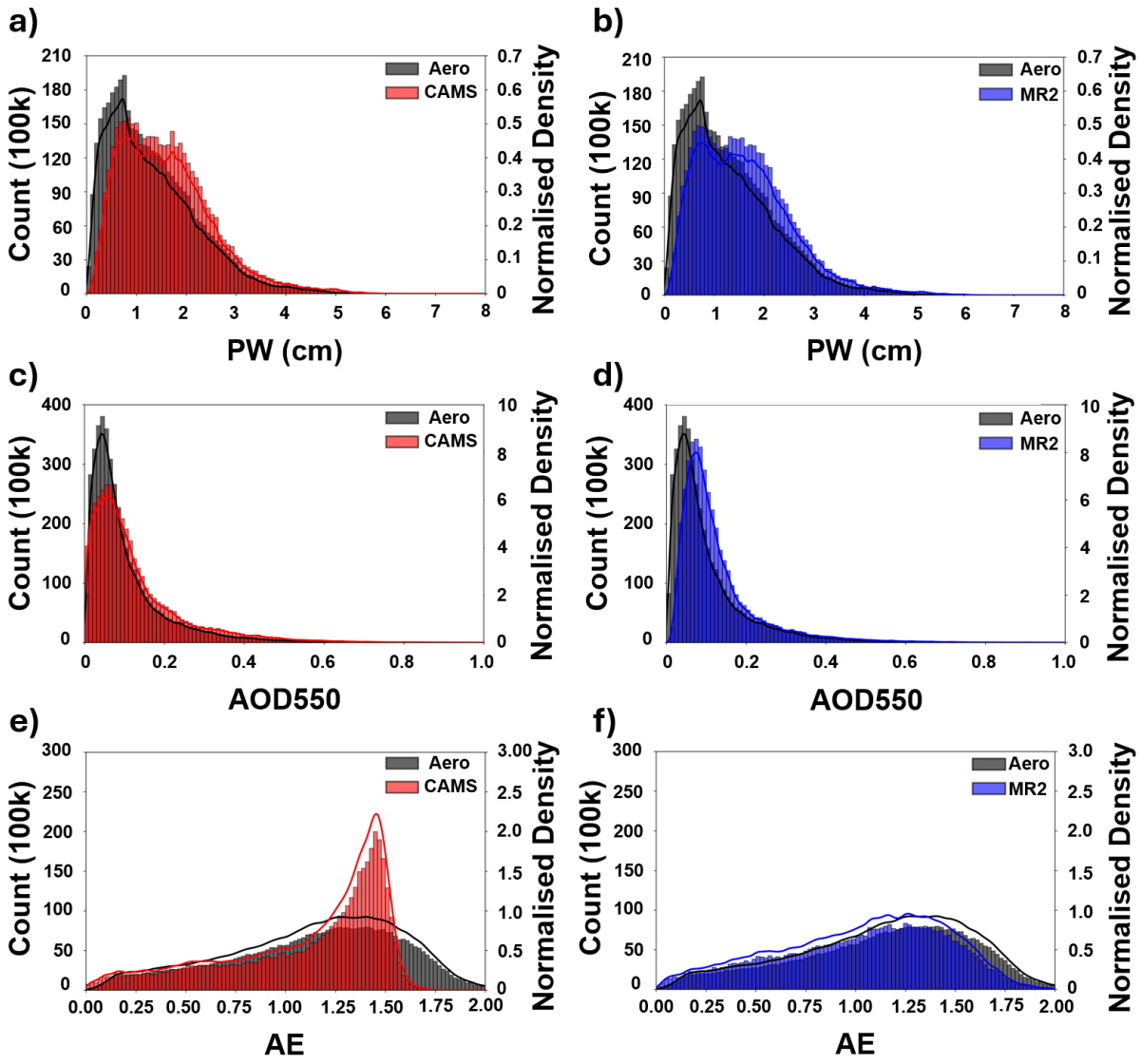

Figure 38: The histograms present the distributions across 100 bins for: **a)** and **b)** PW, **c)** and **d)** AOD550, and **e)** and **f)** AE, highlighting comparisons between CAMS (red) and MERRA2 (blue), against AERONET (black) across all 67 sites.

Figure 38 offers a significant visualization through histograms, which reveal critical data about the counts of AE across 67 sites, displaying notable similarities between MERRA2 and AERONET measurements. Upon closer inspection, CAMS demonstrates an overestimation in the range of AE from 1.25 to 1.60 (as per Figure 38e), where there is an evident peak. This indicates that in this specific range, CAMS records a higher concentration of data points, thus exaggerating AE compared to the more moderate peak seen in AERONET, which serves as the reference standard. In contrast, Figure 38f conveys that MERRA2 demonstrates a close alignment with AERONET by maintaining counts near 100,000, unlike CAMS, which shows counts exceeding that by an

additional 100,000. This indicates that CAMS's distribution may be inaccurately represented, and its central tendency does not effectively depict the scenario as accurately as MERRA2. For AOD550, Figure 38d shows that MERRA2 demonstrates distributions that closely mirror that of AERONET, although MERRA2 notably does not account for AOD550 values near zero, unlike CAMS and AERONET as in Figure 38c. However, the number of counts for CAMS is significantly lower at approximately 280,000, while AERONET's is higher than 400,000, and MERRA2's is just under it. This discrepancy highlights a weaker performance by CAMS, with MERRA2 presenting a more accurate alignment but still not perfectly matching AERONET. This variation in counts indicates the degree to which MERRA2 and CAMS differ in terms of data accuracy and consistency when compared to AERONET. This supports the inference that the discrepancies in AOD550 values for MERRA2 and CAMS, which are pronounced in their MAD values, are due to the temporal resolution of MERRA2, which is higher than that of CAMS. Furthermore, MERRA2's use of diverse data sources such as MODIS, MISR, AVHRR, and AERONET, compared to CAMS's limited use of MODIS and AATSR, provides a more robust data assimilation framework, enhancing its overall performance in modelling aerosol measurements.

A closer examination of Figure 39 reveals that nine locations were selected for analysis due to their low irradiance levels, making them suitable for evaluating the effects of AOD550 and AE. These criteria provide a solid benchmark to compare the operational effectiveness of CAMS and MERRA2. In terms of AOD550, eight of these nine locations displayed lower MAD values when comparing MERRA2 with CAMS. MERRA2 typically showing denser concentrations of data points, particularly noticeable in sites such as SHA, ROC, and CAH. The MAD values exhibit variability, yet the overall pattern indicates that MERRA2 frequently achieves lower values than CAMS. Even when CAMS surpasses MERRA2 in performance, the margin of superiority remains narrow (i.e., in CAH, a difference of 2.23%). Conversely, MERRA2 shows a significant reduction in the MAD by up to 33.06% at the BAR location compared to CAMS. Furthermore, in analyzing AE, it is observed that in six out of nine selected locations, MERRA2 demonstrates lower MAD values. For example, at the SMS site, CAMS records an MAD of 41.34%, whereas MERRA2 shows a lower MAD at 30.87%. This analysis highlights MERRA2's superior precision and dependability in assessing aerosol properties, especially in areas where solar irradiance is subdued.

PW measures the depth of water vapor in a column of atmosphere and it significantly influences infrared opacity, playing a crucial role in the attenuation of radiation, making it a key factor in clear-sky modelling. Accurate simulation of PW in satellite data, which may mirror actual measurements, is vital. These reanalyses data often rely on raw satellite sensor estimates, which help define the atmospheric models' boundary conditions. Understanding the precision of these

initial satellite estimates is essential to identify any potential climatological biases. PW also impacts cloud formation and alters the size and optical properties of aerosols, thus affecting atmospheric optical transparency. The reliance on uncertain PW data, especially data from satellite data with limited spatiotemporal resolution or data interpolated from adjacent stations, can lead to significant errors in DNI estimates, particularly in regions with high ϕ or during periods of low solar elevation.

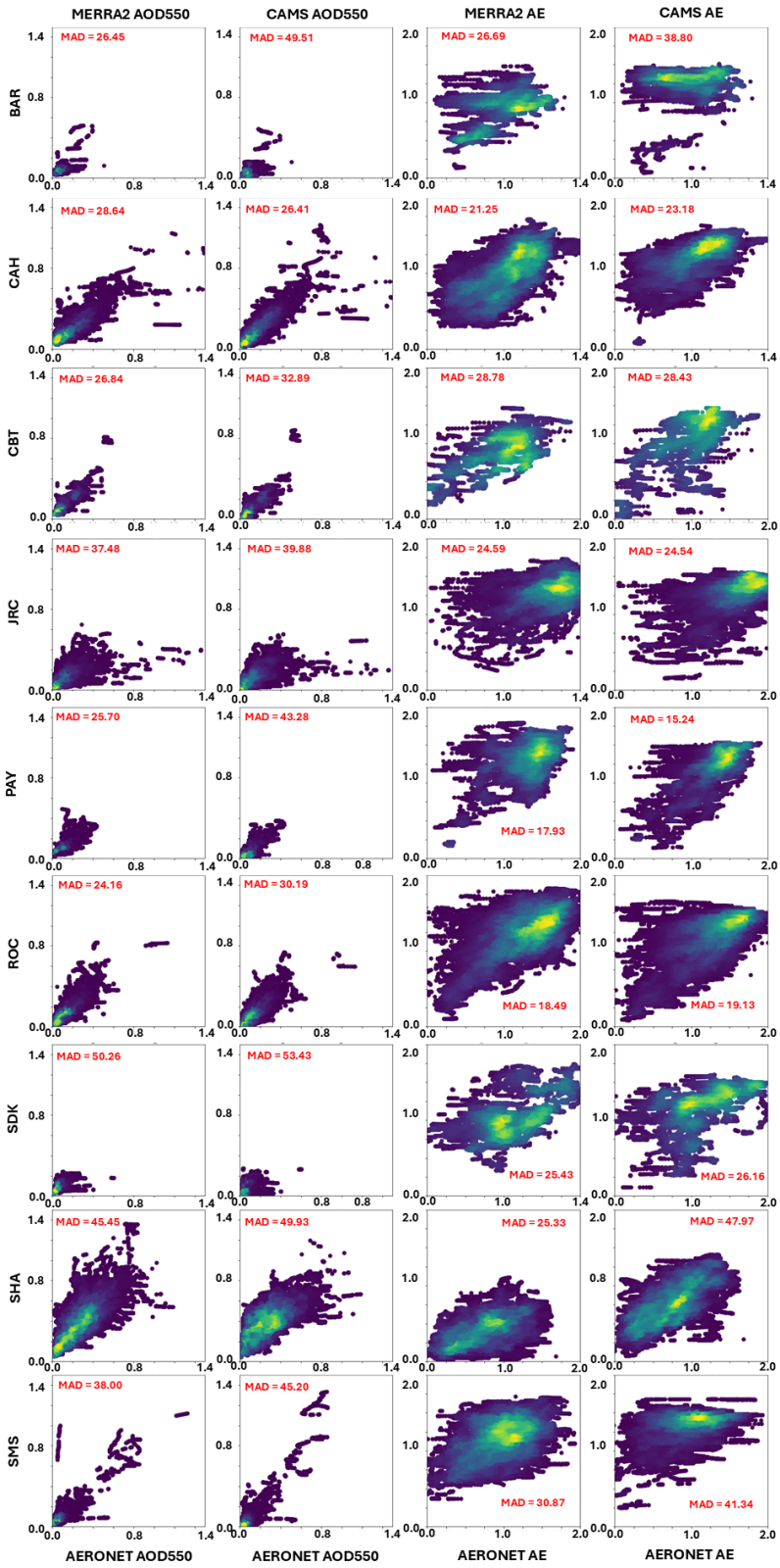

Figure 39: Scatter plots display the comparative analysis of MERRA2 and CAMS AOD550 (first two columns) alongside the AE (last two columns) as measured by sun photometers as part of AERONET. Each row represents one of the nine locations, with each chart detailing the MAD value.

According to Table 10, PW sourced from MERRA2 demonstrates a lower MAD of 33.92% compared to CAMS' 36.46%, and thus the difference is small. An analysis of Figure 38a and 38b reveals that both CAMS and MERRA2 display similar counts, both around 150,000 counts at their peak, in contrast to AERONET's exceeding 180,000 counts at its peak, highlighting the reason behind the large MAD values for both models. For PW measurements greater than 3 cm, both MERRA2 and CAMS exhibit trends that closely align with AERONET data, with MERRA2 showing a particularly close correlation.

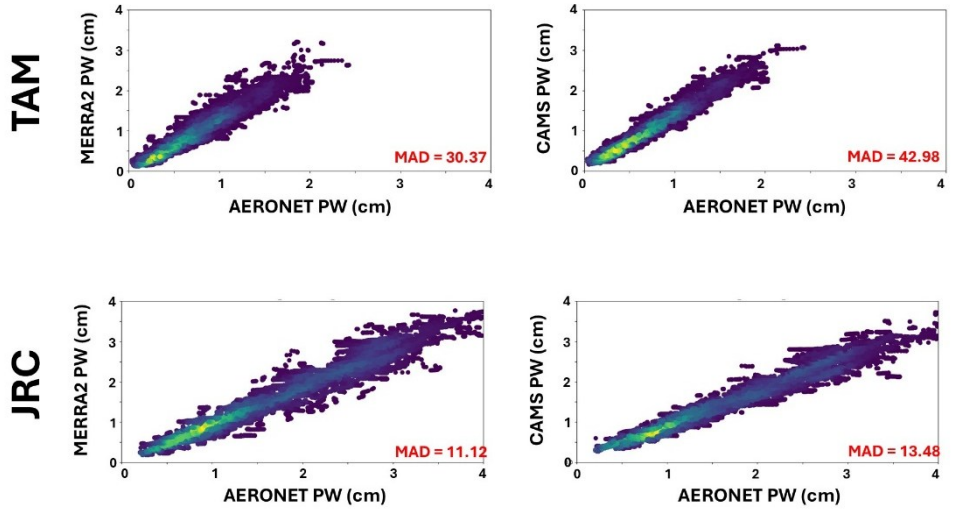

Figure 40: The scatter diagrams present a comparative evaluation of MERRA2 and CAMS PW data in relation to AERONET observations at two different sites.

One potential reason for the observed differences in performance between MERRA-2 and CAMS could be the frequency of data output. MERRA-2 uniquely offers hourly outputs for PW, which is particularly advantageous for solar-related research and other applications requiring high temporal resolution. In contrast, CAMS provides data at coarser three-hour intervals. In areas where PW can fluctuate significantly throughout the day, affecting both atmospheric opacity and incoming irradiance, a higher resolution of data is crucial. Moreover, a notable discrepancy exists in the calculation of water vapor between the two. For instance, at the JRC station, which is situated at an elevation of 800 meters, the mean PW value recorded by AERONET is 1.625 cm. In comparison, MERRA-2 reports a slightly lower figure at 1.522 cm, while CAMS records 1.434 cm. This positioning highlights the inferior performance of CAMS at higher altitudes, with MERRA-2 displaying an MAD of 11.12%, illustrating how inaccurate PW estimates can degrade performance. In TAM, known for its dry and arid climate, the levels of PW are relatively low. Analysis shows that the MERRA-2 model estimates an average PW of 0.900 cm, while the CAMS model estimates it slightly higher at 0.998 cm. Both of these are high compared to the AERONET measurements, which report a lower average of 0.698 cm. This discrepancy highlights a tendency

for both MERRA2 and CAMS to overestimate PW in regions with minimal rainfall. The MAD further illustrate these overestimations and their implications for model accuracy and reliability.

5.4 Model Validation

5.4.1 Individual Matrix Combination

Figure 41 reveals that GHI MAD values fluctuate significantly across various models. McClear shows a variation from 0.81% to 8.31%, ERA5 from 3.09% to 55.95%, and REST2 (independent of input data) from 0.71% to 17.25%. Notably, REST2-Aero frequently exhibits the most favorable for 38 out of the 67 sites. ERA5, in particular, records substantial MAD at specific locations, such as FUA with an MAD of 44.31%, which is higher than those of other REST2 model combinations and McClear. Similarly, for GUR, ERA5 records a MAD of 55.95%. These substantial deviations might be attributed to high pollution levels and aerosol concentrations in urban areas, which could interfere with the model's ability to accurately predict irradiance and cloud cover variability. Additionally, high humidity levels could also affect model accuracy by absorbing and scattering solar radiation. For GUR, the data station instruments were not cleaned as frequently as they should have been due to the frequent soiling of the region, thus affecting all 6 models; with REST2 coupled with AERONET measurements having a MAD of 13.49%.

SHA, characterized by a desert-like climate with prevalent sand storms and high concentrations of airborne dust and sand particles, presents a challenging environment for solar irradiance measurement. These aerosols, common in desert settings, significantly scatter and absorb sunlight, reducing the solar radiation that reaches the ground. Additionally, fine airborne dust creates haze, further diminishing visibility and solar irradiance. For GHI, analysis shows using McClear and various REST2 models, regardless of the satellite data employed, indicates MAD values ranging from 2.65% to 3.40%. However, data from ERA5 exhibit a significantly higher MAD of 15.37%. In Figure 42, REST2-AERO data show greater alignment and closer one-to-one estimates of GHI under clear conditions compared to other models. This closer approximation is attributed to the similarity of AOD550 measurements and *AE* to those recorded by AERONET.

Furthermore, Figure 43 illustrates that all clear-sky models, except for REST2-Aero produce less accurate plots, where REST2-AERO almost achieves a one-to-one line correlation. DNI estimations for SHA, as shown in Figure 44, exhibit MAD values ranging from 2.69% to 17.03% when using any of the REST2 iterations. McClear and ERA5 report MAD values of 14.53% and 25.84%, respectively, suggesting that ERA5 may not yield reliable predictions in desert-like

climates, potentially due to satellite imaging techniques or the application of AOD550 predictions. The performance of CAMS and McClear is comparably close, with only a 0.96% difference in MAD, underlining the nuanced impacts of aerosol modelling in arid environments. Conversely, REST2-AERO achieves the lowest MAD value at 2.69%, highlighting the effectiveness of AOD550 estimates in satellite data. In fact, 62 of the 67 sites show that REST2-Aero combination results with the lowest MAD value; between 0.46% and 4.49%.

In locations such as PRE, seasonal biomass burning from agricultural activities and regional wildfires during the dry season significantly enhances aerosol concentrations. The smoke and particulate matter from this vegetation burning considerably diminish solar irradiance by scattering and absorbing sunlight. Analysis of GHI across various clear-sky models, as depicted in Figure 42, demonstrates consistent scatter plot patterns regardless of the model used. Delving further, for GHI, ERA5 registers the highest MAD value at 15.46%, suggesting a potential shortfall in accurately capturing events of seasonal biomass burning. Conversely, the integration of REST2 with CAMS and MERRA2 demonstrates enhanced accuracy, yielding deviations of 3.66% and 3.94% respectively, which markedly surpass those obtained using ERA5 and approach the precision of sunphotometer readings by a narrow margin of less than 0.64%. In terms of DNI predictions, as depicted in Figure 44, both McClear and REST2-CAMS present closely comparable MAD values of 8.35% and 6.56% respectively. Furthermore, the disparity in GHI estimations between REST2-CAMS and McClear is minimal, at 0.95% compared to 1.79%. This variation underscores the necessity for model refinement, particularly in areas impacted by significant biomass burning. This leads to an inquiry into the extent of deviation between REST2-CAMS and McClear in terms of GHI and DNI estimations.

At EUR, the difference in GHI between McClear and REST2-CAMS is relatively minor at 0.40%, whereas for DNI, the disparity escalates to approximately 10 times this amount. The notable discrepancy at MLO raises concerns about potential underestimations by McClear, with similar trends observed at FUA and IZA, which reported differences of 32.86% and 24.79% respectively. These locations are geographically distinct, contributing to the variations observed. MLO, characterized by its high elevation and remote oceanic setting, should theoretically show minimal discrepancy with REST2-CAMS measurements. However, CAMS might face challenges in accurately capturing the low aerosol environment of such an isolated site. Furthermore, volcanic activity in the area could sporadically introduce aerosols from eruptions or transported volcanic plumes, which might not be fully represented in global models or could differ in timing from CAMS's assumptions. At MLO, the average AOD550 measured by AERONET is 0.240, while CAMS significantly overestimates it at 2.312.

For FUA, positioned near a coastal area with substantial human activity, the site experiences a mix of aerosols from pollution and regionally transported dust. The variability and complexity of local sources, such as urban emissions and industrial aerosol sources, can cause rapid fluctuations in AOD550. Despite this, CAMS and sunphotometer measurements align closely, with CAMS recording an average AOD of 1.730 compared to 1.695 by the sunphotometer, suggesting that operational differences in McClear's modelling approach or its variable inputs could affect its accuracy. At IZA, known for its pristine atmospheric conditions typically above the marine boundary layer, the site measures free-tropospheric conditions different from those at ground-level coastal sites. IZA lies in a transitional zone between marine and continental air masses and is subject to Saharan dust intrusions. CAMS may not accurately resolve these episodic events and their vertical distributions, leading to significant overestimations of AOD550 compared to AERONET sunphotometer measurements, with actual averages at 0.450 versus CAMS's modelled 1.897.

XIA is recognized as a site with very high AOD550 levels due to urban smog, industrial emissions, and significant particulate matter from industries, vehicle exhaust, and construction activities. As anticipated, REST2-Aero demonstrates the densest plot on scatter graphs for both GHI and DNI, as evidenced in Figures 41 and 44 respectively, with MAD values of 2.99% for GHI and 2.44% for DNI. REST2-CAMS and McClear display nearly identical performances; the differences are less than 0.63% for GHI estimates and near identical (difference of 0.06%) for DNI estimates. The average AOD550 values at XIA, as measured by CAMS, stand at 0.696, while MERRA2 records a lower average of 0.407, compared to AERONET's actual measurements of 0.623. This variation partly explains the higher MAD values observed when using MERRA2 for both GHI and DNI estimations. Moreover, ERA5 struggles with accuracy in GHI_{Clear} estimations, showing the highest MAD among the models evaluated at 45.72% for DNI_{Clear}, indicating substantial challenges in modelling under these specific environmental conditions.

	Clear Model					
	McClear	ERA5	REST2-Aero	REST2-CAMS	REST2-MER2	REST2-MER2c
ARG	4.10	15.72	2.35	3.16	2.30	2.49
BAR	3.89	10.00	7.61	6.33	8.09	8.06
BIL	2.21	14.52	0.81	1.66	1.21	1.22
BIS	2.49	10.88	1.75	1.91	1.65	1.68
BMT	2.83	12.84	1.44	1.55	1.26	1.04
BON	2.42	14.22	1.20	1.88	2.12	2.10
BOU	1.67	14.06	1.42	2.60	2.21	3.02
BRB	5.86	15.30	3.60	5.08	4.04	4.41
CAB	2.12	16.94	0.91	1.81	1.07	1.07
CAH	2.12	13.48	1.79	2.07	2.31	2.23
CAM	2.35	16.98	1.08	1.51	1.38	1.35
CAR	3.17	13.41	1.56	1.77	1.56	1.42
CBT	2.56	16.00	1.93	2.46	2.69	2.59
CHI	2.15	13.12	1.98	3.16	4.40	4.51
CLH	1.87	13.21	1.26	1.30	1.38	1.35
CNR	2.61	13.57	1.08	1.57	1.38	1.36
DAR	3.00	20.52	2.34	4.21	4.69	4.72
DAV	1.44	11.87	2.16	3.27	3.11	4.27
ENA	1.85	14.69	1.68	2.19	1.81	1.82
EUR	5.07	6.83	5.70	5.47	6.36	6.64
EVO	2.78	15.40	2.80	3.66	3.69	3.46
FUA	5.02	44.31	1.58	15.35	4.06	6.81
GOB	2.72	12.39	2.12	1.75	1.58	1.54
GOL	2.31	12.03	0.93	1.72	1.98	2.29
GUR	7.03	55.95	13.49	9.95	15.31	15.75
INO	4.96	14.99	3.26	3.93	2.92	2.98
IZA	2.24	15.79	1.00	9.57	9.71	2.47
JRC	6.19	14.46	2.88	4.24	4.33	2.86
KAL	3.39	13.07	0.81	1.04	1.11	1.02
KZH	4.72	5.11	4.18	3.26	3.58	4.19
LEA	3.62	12.90	2.00	2.20	1.70	1.67
LER	0.81	12.66	1.31	1.33	2.77	2.40
LIL	1.89	15.16	1.03	1.89	1.78	1.73
LIN	2.16	15.17	0.97	1.78	1.55	1.47
LPU	2.26	5.32	2.67	2.15	2.35	2.49
LRC	1.75	13.35	0.90	1.21	1.31	1.31
MAN	1.46	12.05	1.79	1.33	1.20	1.20
MBO	3.38	13.91	2.55	2.81	2.96	2.98
MLO	4.28	19.11	0.95	17.25	11.46	3.45
NAU	1.79	20.66	1.43	1.84	1.76	1.75
NIA	2.10	19.01	1.91	2.12	2.55	2.60
NYA	0.97	10.02	0.87	1.10	2.04	4.01
OHY	4.03	11.42	1.83	2.26	2.60	2.99
PAL	1.66	14.91	0.71	1.60	1.89	1.68
PAY	2.63	12.37	0.75	1.19	1.21	2.32
PRE	4.22	15.46	3.27	3.66	3.94	3.39
PSA	2.34	14.06	1.53	1.49	1.60	1.46
PSD	4.54	5.40	4.06	2.43	2.13	1.67
PTR	5.24	16.74	3.49	4.63	3.50	3.32
REG	2.21	12.94	1.73	2.39	2.09	2.21
ROC	4.44	14.11	3.23	3.50	3.21	3.04
RTV	5.03	18.08	3.91	3.75	4.20	3.86
RUN	1.52	14.97	0.98	1.29	1.28	2.13
SAP	2.43	13.82	1.65	2.14	2.09	2.23
SDK	2.11	11.05	2.61	3.56	4.26	4.43
SEO	6.04	24.75	8.09	6.11	7.70	9.46
SHA	3.40	15.37	3.05	3.03	2.65	2.65
SMS	6.52	17.88	5.33	4.49	3.61	4.51
SPO	8.31	3.09	6.62	6.59	6.83	7.43
SXF	2.74	13.42	1.88	2.33	2.22	2.18
TAM	4.15	24.61	3.57	3.05	3.60	3.17
THD	1.84	4.17	1.47	1.55	1.55	1.53
TIK	6.23	11.69	3.49	4.54	3.81	3.66
TOR	2.45	14.61	1.66	1.95	2.01	2.00
TUC	2.70	5.01	1.79	1.72	1.76	1.77
WHW	3.23	14.89	1.65	2.58	2.46	2.18
XIA	3.74	20.81	2.99	4.37	5.49	5.32

Figure 41: A heatmap generated illustrating GHI_{Clear} alongside comparative data from McClear, ERA5, and REST2. The REST2 variations include Aeronet inputs (REST2-Aero), CAMS inputs (REST2-CAMS), MERRA2 inputs (REST2-MER2), and MERRA2 with elevation correction inputs (REST2-MERc). MAD (%) is used as the of merit, with white signifying MAD values close to zero and darker red indicating increasing MAD levels, across all 67 individual sites.

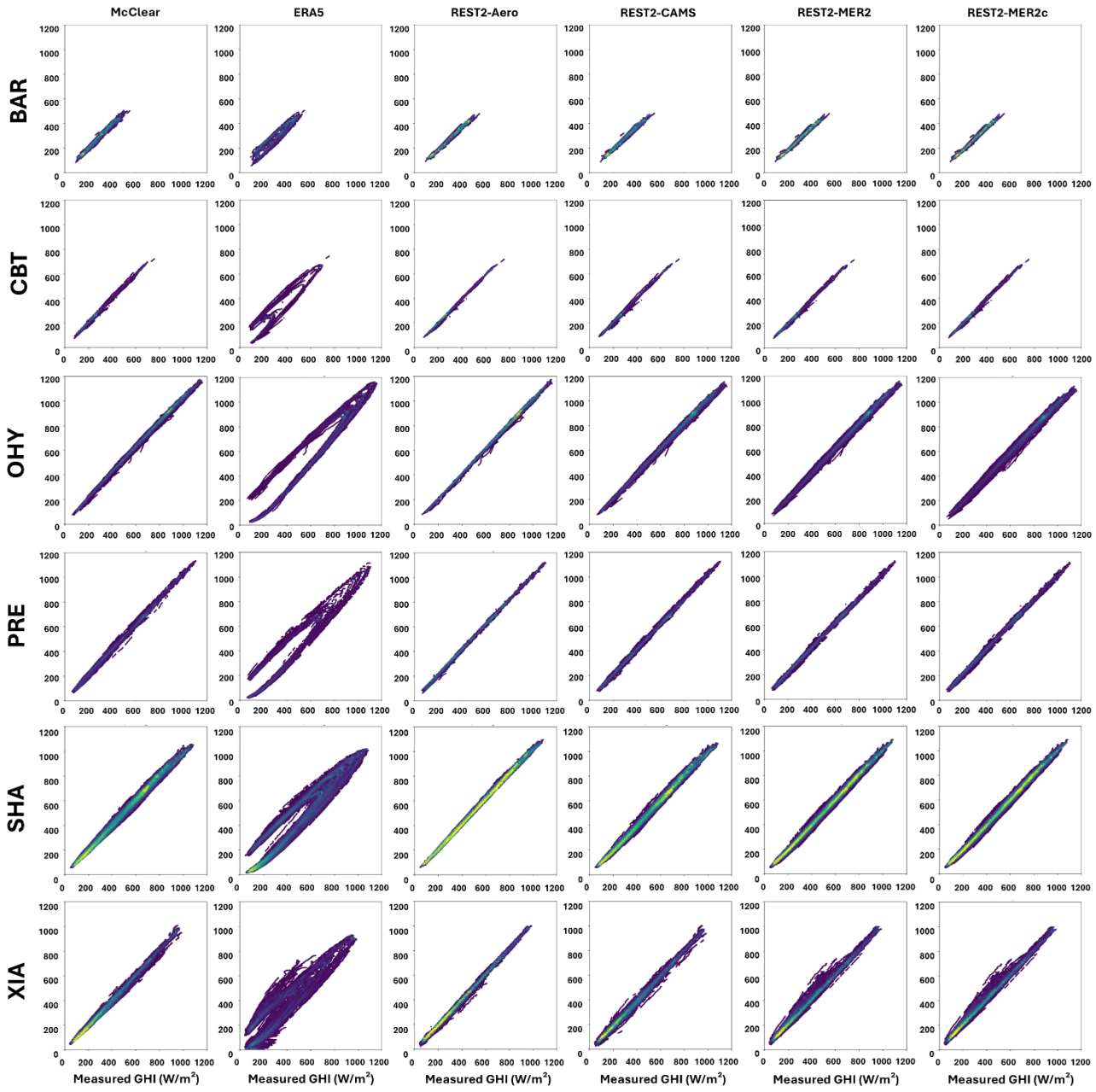

Figure 42: Scatter plots comparing the outputs from McClear, ERA5, and REST2, which use four unique inputs from reanalysis data and AERONET measurements, to GHI measurements. These comparisons are made across six sites that vary in climate, site elevation, and weather patterns.

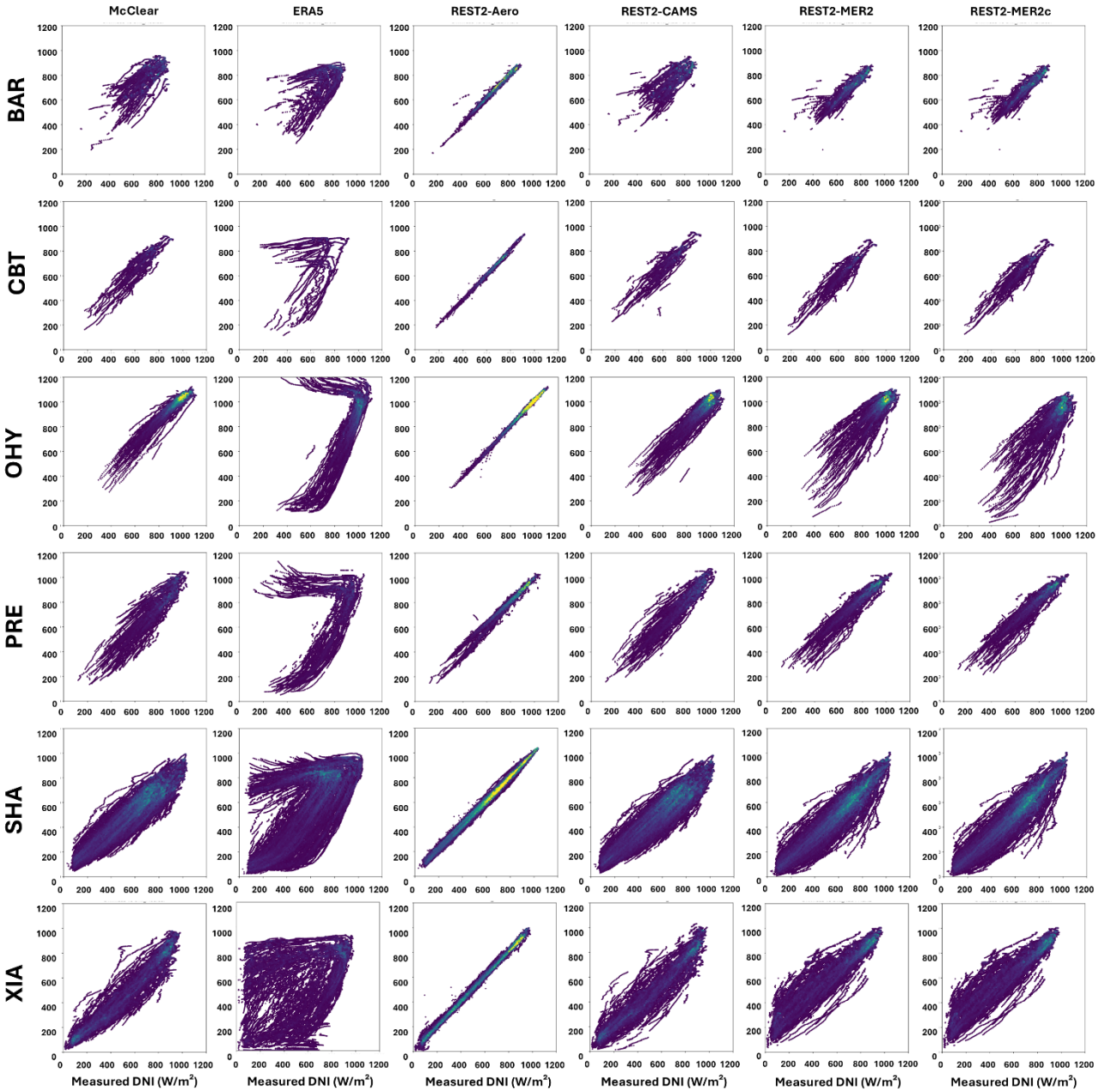

Figure 43: Scatter plots comparing the outputs from McClear, ERA5, and REST2, which use four unique inputs from reanalysis data and AERONET measurements, to DNI measurements. These comparisons are made across six sites that vary in climate, site elevation, and weather patterns.

	Clear Model					
	McClear	ERA5	REST2-Aero	REST2-CAMS	REST2-MER2	REST2-MER2c
ARG	7.56	25.09	1.51	7.45	5.71	5.40
BAR	12.08	13.41	1.72	10.55	4.74	4.71
BIL	4.66	22.33	0.65	6.48	3.99	4.05
BIS	6.00	18.00	2.14	5.83	4.89	5.39
BMT	3.95	20.04	1.33	3.71	3.08	4.33
BON	5.28	20.47	0.75	4.80	5.61	5.57
BOU	3.89	21.75	1.03	5.43	3.15	4.30
BRB	10.70	24.98	1.99	12.20	7.01	7.87
CAB	8.07	27.40	1.22	6.74	4.89	4.89
CAH	5.95	25.53	0.93	5.17	6.21	5.83
CAM	6.05	26.01	1.40	5.85	4.75	4.91
CAR	5.78	21.98	0.83	5.70	4.64	5.76
CBT	9.09	26.28	1.73	9.59	6.26	6.11
CHI	7.57	22.78	7.30	6.82	7.00	7.12
CLH	5.31	21.12	3.34	4.72	3.83	3.55
CNR	5.74	21.96	2.33	5.31	4.62	4.84
DAR	6.14	32.46	1.70	7.73	14.58	14.49
DAV	3.87	17.38	1.17	5.06	4.30	6.62
ENA	5.06	26.46	1.72	5.16	4.17	4.19
EUR	24.52	15.85	4.45	20.08	15.75	15.69
EVO	7.64	21.09	1.62	6.90	6.11	5.30
FUA	15.29	43.94	2.23	48.15	16.47	23.75
GOB	5.19	19.85	1.30	5.70	6.35	6.74
GOL	3.66	19.46	0.46	4.59	5.23	6.20
GUR	19.84	194.38	27.81	22.08	37.43	38.62
INO	5.88	23.27	1.94	9.34	5.72	5.71
IZA	5.53	24.70	0.82	19.26	20.56	4.96
JRC	8.94	21.57	1.84	6.71	7.03	8.42
KAL	5.09	21.50	1.73	3.64	3.68	3.30
KZH	5.68	7.53	2.71	4.24	3.70	4.29
LEA	5.27	22.21	1.27	4.74	3.22	3.25
LER	2.34	17.56	1.61	2.44	5.39	4.72
LIL	6.72	23.38	2.23	6.70	6.24	6.14
LIN	7.70	23.57	1.37	6.76	6.07	5.61
LPU	6.67	13.74	0.82	5.42	4.67	4.33
LRC	5.05	20.12	0.72	4.06	5.56	5.60
MAN	3.76	19.39	2.86	3.68	2.54	2.54
MBO	11.22	35.85	3.73	9.33	11.16	11.11
MLO	8.18	27.42	0.57	37.03	18.44	3.94
NAU	4.24	32.84	2.05	4.63	4.35	4.30
NIA	8.94	35.53	1.76	8.80	12.03	12.46
NYA	3.60	16.69	1.59	4.43	5.88	10.28
OHY	5.07	17.48	1.23	4.56	6.26	9.74
PAL	6.11	23.17	1.37	5.24	6.09	5.55
PAY	3.74	19.45	1.61	4.80	4.00	6.66
PRE	8.35	25.87	2.53	6.56	6.33	5.65
PSA	5.28	24.38	0.76	5.59	5.12	6.36
PSD	3.78	11.03	4.18	3.25	3.12	4.91
PTR	6.41	28.01	2.16	9.38	4.03	3.91
REG	7.15	20.01	1.30	6.86	4.43	4.93
ROC	6.33	23.41	4.00	5.51	5.08	5.27
RTV	11.60	28.52	4.49	11.64	11.31	11.88
RUN	6.26	22.19	1.02	5.29	4.40	8.00
SAP	6.63	23.08	1.53	6.62	6.63	9.91
SDK	5.74	16.49	2.95	5.96	8.15	8.59
SEO	12.09	33.57	4.04	13.33	8.93	10.67
SHA	14.53	25.84	2.69	15.49	16.51	17.03
SMS	5.80	28.11	3.45	6.19	4.15	4.10
SPO	4.62	4.34	1.26	1.72	1.05	1.73
SXF	6.46	21.46	2.14	6.88	5.29	5.11
TAM	11.24	37.16	3.04	13.68	10.85	13.91
THD	3.57	5.51	1.70	3.09	3.24	3.04
TIK	8.90	18.38	2.06	6.57	3.91	4.33
TOR	6.18	22.79	3.81	5.78	6.18	6.12
TUC	3.54	6.73	2.32	3.26	2.98	3.78
WHW	8.29	22.72	1.97	7.49	6.17	6.30
XIA	12.84	45.72	2.44	12.78	17.00	16.62

Figure 44: A heatmap generated illustrating DNI_{Clear} alongside comparative data from McClear, ERA5, and REST2. The REST2 variations include Aeronet inputs (REST2-Aero), CAMS inputs (REST2-CAMS), MERRA2 inputs (REST2-MER2), and MERRA2 with elevation correction inputs (REST2-MERc). MAD (%) is used as the of merit, with white signifying MAD values close to zero and darker red indicating increasing MAD levels, across all 67 individual sites.

5.4.2 Latitude and Altitude Effects

MERRA-2 generally outperforms CAMS in terms of AOD accuracy and demonstrates similar precision in statistical evaluations as depicted in Figure 39. However, the influence of altitude is critical in clear-sky modelling, particularly at higher elevations. Standard atmospheric data used in clear-sky models are typically derived from sea-level conditions, which may not be representative of conditions at elevated terrains, leading to potential discrepancies in model accuracy.

To address this, elevation corrections for key atmospheric parameters such as PW and AOD550 were assessed to determine their impact on enhancing solar irradiance estimations using MERRA-2 data at high-altitude locations. Atmospheric conditions affect solar irradiance in two primary ways: absorption and scattering. Absorption, mainly by atmospheric gases, significantly reduces direct solar radiation reaching the ground. Scattering, influenced by aerosols and atmospheric molecules, redirects solar radiation, thereby increasing the diffuse component of sunlight. At higher elevations, the thinner atmosphere contains less water vapor, which diminishes both absorption and scattering effects. This alteration directly affects the measurements of DNI and GHI. Moreover, it is crucial to recognize the distinct sensitivity of DNI to elevation corrections compared to GHI, largely due to DNI's reliance on the unobstructed clarity of the atmospheric path between the sun and the measurement sensor. DNI experiences more direct impact from factors like aerosol scattering and water vapor absorption as outlined earlier in the thesis. Consequently, precise adjustments to AOD550 and PW are essential at high-altitude locations to ensure accurate readings. In contrast, GHI, which is affected by both direct and diffuse components of solar radiation, exhibits a reduced sensitivity to these adjustments. This is attributed to the balancing effect of increased diffuse radiation, which mitigates the impact of higher aerosol scattering typically less pronounced at elevated altitudes. This phenomenon underpins why MERRA-2 corrections result in substantial improvements in both MAD across three sites, OHY, IZA and SPO independent of the clear-sky detection mechanism used.

Analysis of two high-altitude stations, each above 2250 meters, reveals significant variances in the correction factors needed. At IZA (2373 m), corrections led to notable improvements in MAD by 7.24% for GHI and 15.59% for DNI, indicating a substantial underestimation of irradiance in the original MERRA-2 outputs. These results highlight DNI's increased sensitivity compared to GHI. This is further confirmed in Figure 44, where it can be seen that MERRA2 corrections show more overlap. At MLO (3397 m), improvements utilizing REST2-MER2c show a decrease of 8.00 in MAD differences compared to its MERRA2 counterpart for GHI, and 14.50% for DNI. In high-altitude climates that do not have an elevation correction close to 0, such as OHY (3314m with

an elevation correction of 1.766) and DAV (1589m with an elevation correction of 1.227), have resulted in diminished performances for GHI but even more so for DNI. This could indicate that the initial model predictions were already well-suited to the actual atmospheric conditions at higher elevations, potentially accounting for factors like snow.

The impact of inclined solar paths, particularly in high- ϕ or snowy locations, is significant due to the high margin of error in clear-sky irradiance estimations in these areas. Figure 41 demonstrates that sites like CAM, CBT, and TOR exhibit consistent performance in estimating clear-sky GHI, regardless of the chosen model, whether McClear, or REST2 iterations. For these models, the MAD values remain between 1.08% and 2.69%, indicating close alignment with zero. McClear and REST2-CAMS also perform relatively well, with McClear and CAMS displaying near identical performance. However, in the case of DNI estimations, illustrated in Figure 44, the situation is more nuanced. ERA5 still demonstrates weaker performance, with MAD values reaching 26.01% for CAM, 26.28% for CBT and 22.79% for TOR. A comparison between CAMS and MERRA2 reveals CAMS's notably higher error, likely influenced by the climatology of stations like CBT, CAM, and TOR, where MAD values for CAMS are nearly twice those of MERRA2, regardless of elevation-corrections.

5.4.3 Global Results

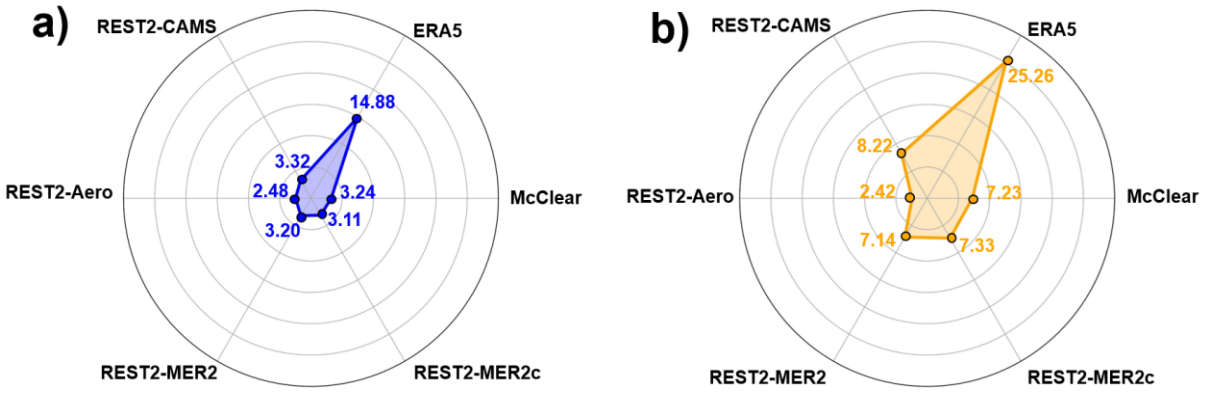

Figure 45: A radar chart that displays the global MAD (%) outcomes for McClear, ERA5, and REST2 models, utilizing various data sources: AERONET (REST2-Aero), CAMS (REST2-CAMS), MERRA2 (REST2-MER2), and MERRA2 with elevation adjustment (REST2-MER2c). The segments of the chart are categorized as follows: **(Left)** GHI **(Right)** DNI.

Figure 45 illustrates that whether estimating GHI or DNI, the integration of AERONET data into the REST2 model consistently yields the lowest MAD values, registering 2.48% for GHI and 2.42% for DNI. Given that AERONET measurements are not always accessible, determining the most suitable satellite data becomes crucial. As per earlier findings noted in Table 10, MERRA2 surpasses CAMS in AE, AOD550, and PW estimations, suggesting that REST2-MER2 is preferable.

The difference in deploying REST2-MER2 for GHI estimations is minute, only 0.74% if it is not corrected, and 0.63% if corrected for elevation. While MERRA2 with elevation correction demonstrates a slight variance in performance, its use should be considered selectively. Elevation correction is particularly beneficial at notably high elevations; otherwise, it might not be essential However, for DNI estimations, there is a larger difference moving away from AERONET to MERRA2 parameters, by 3 folds.

In contrast, McClear and REST2-CAMS show nearly identical performances, with only a 0.08% difference in GHI but a tenfold difference in DNI. ERA5 is the least effective model for both GHI and DNI, exhibiting MAD values that are more than five folds those of other models, 14.88% for GHI and 25.26% for DNI. This significant disparity underscores its ineffectiveness. Considering REST2's proprietary nature, McClear consistently offers superior performance both individually and globally compared to ERA5. Moreover, when selecting parameters from satellite datasets, MERRA2 is preferable to CAMS, as previously noted.

5.5 Conclusion

In conclusion, this chapter examined six clear-sky models, including readily accessible McClear and ERA5 models, alongside four combinations involving REST2 with data sources from satellite data such as CAMS, MERRA2 (including elevation correction), and actual AERONET measurements at 67 stations globally. Among these, the combination of REST2 combined with AERONET data emerged as the most precise for GHI and DNI estimations, showing a global MAD of 2.48% for GHI and 2.42% for DNI. In light of the frequent absence of AERONET data, determining the most suitable satellite dataset for incorporation becomes a critical consideration. MERRA2 data surpasses CAMS in performance across all evaluated parameters, including AOD550, AE and PW. Specifically, on a global scale, MERRA2 exhibits superior performance by 11.88% for AE, 34.96% for AOD550 and 2.54% for PW. Thus, on a global scale for GHI estimations, REST2-MER2 had an MAD of 3.20%; a 0.12% improvement than REST2-CAMS. For DNI, REST2-CAMS records an MAD of 8.22%, 1.08% shy of REST2-MER2. Comparatively, REST2-CAMS and McClear demonstrate similar overall performances in GHI estimation, with negligible MAD discrepancy of 0.08% for GHI but almost twelve-folds for DNI. ERA5 reported MAD values of 14.88% for GHI and a peak of 25.26% for DNI. This could be attributed to inadequate AOD550 estimations, particularly at sites with high aerosol density, where ERA5 performed notably poorly. In environments of high altitudes, McClear and CAMS display divergent results, suggesting there may be potential inaccuracies in McClear’s underlying equation, coefficients it deploys, or perhaps how it gathers other parameters, especially at elevated altitudes, despite

both models utilizing AE and AOD550 from CAMS data. While, REST2-MER2 requires elevation corrections, as it can improve performances by up to 7.24% for GHI and 15.59% for DNI. Globally, the optimal approach is to combine REST2 with AERONET measurements. However, due to the limited availability of sunphotometers, it is advisable to use REST2 with MERRA2, applying elevation correction only at high elevations. Moreover, given the proprietary nature of REST2, the alternatives are McClear or ERA5. Among these, McClear is recommended as it delivers performance comparable to REST2 iterations (when not incorporating AERONET data).

Chapter 6 Predictive Models for Photosynthetic Active Radiation Irradiance

6.1 Introduction

The expansion of AgriPV is gaining momentum, yet challenges such as limited land availability pose significant obstacles to its broader adoption. In assessing the viability of AgriPV systems, it is crucial to accurately predict irradiance levels for both photovoltaic and agricultural needs. Photosynthetically Active Radiation (PAR) irradiance, in particular, is critical yet rarely measured, leading to a notable knowledge gap in predicting PAR levels, especially within the variable conditions of temperate climates. The scarcity of PAR measurements complicates the assessment and optimization of AgriPV systems. Addressing this, the forthcoming chapter delves into both established and innovative methodologies for estimating PAR irradiance. This includes an analysis of 10 contemporary empirical models, assessing their effectiveness in predicting PAR in locations beyond their initial calibration settings - specifically in European temperate regions. Moreover, this chapter introduces a new model for predicting PAR irradiance that surpasses traditional approaches. This model utilizes readily accessible inputs such as clear sky irradiance, AOD550, and ozone concentrations, which are available through satellite data, thus circumventing the dependency on conventional data such as DHI or Perez coefficients. The chapter first evaluates these ten empirical models and the novel approach across 9 temperate European climates, where the new PAR model is also formulated. Comprehensive statistical analysis is conducted to examine the precision and scalability of all models across six additional, unseen, temperate locations. This rigorous evaluation highlights their capacity to deliver reliable predictions across diverse settings, thereby enhancing the accessibility and integration of PAR data into economic assessments like LCOE or LER figures of merit, facilitating the growth of the AgriPV market.

6.2 Interplay of Different Parameters

6.2.1 Data Sources

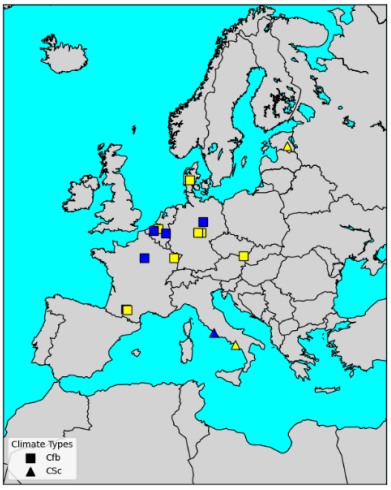

Figure 46: The spatial layout of the 15 chosen locations includes 9 sites marked in yellow for the purpose of model training and validation, and 6 sites indicated in blue dedicated to evaluating the models against new data. Among these, 12 sites are classified under Temperate Oceanic Climates (Cfb), while 3 sites fall within the Cool Summer Mediterranean Climate category (Csc) as per the Köppen–Geiger climate classification [18].

Table 11: Details on the 15 sites selected for assessing PAR, with the first nine sites selected for the training and validation of models, whereas the remaining 5 sites serve the purpose of model testing. The provided average values of PAR and GHI pertain solely to data points deemed valid.

Code	Radiometric site	Lat. (°)	Long. (°)	Site Elev. (m)	Period	Climate Classification	Mean PAR (W/m^2)	Mean GHI (W/m^2)
BHT	Brasschaat	51.307	4.520	16.0	2019 - 2023	Cfb	139.83	324.29
GEB	Gebesee	51.100	10.915	161.5	2020 - 2023	Cfb	134.24	312.41
HAI	Hainich	51.079	10.452	438.7	2019 - 2023	Cfb	137.75	317.46
HES	Hesse	48.674	7.065	310.0	2021 - 2023	Cfb	190.16	410.28
LQE	Lamasquere	43.496	1.238	181.0	2020 - 2023	Cfb	213.13	449.92
LZT	Lanzhot	48.682	16.946	150.0	2022 - 2023	Cfb	157.19	362.31
VAD	Voulundgaard	56.038	9.161	67.7	2020 - 2023	Cfb	117.8	286.99
BCI	Borgo Cioffi	40.524	14.957	10.0	2023	Csa	227.76	535.14
TOR	Tõravere	58.264	26.462	70.0	2016 - 2019	Csa	115.92	279.47
ADE	Aurade	43.550	1.106	250.0	2019 - 2023	Cfb	197.16	427.11
FBU	Fontainebleau-Barbeau	48.476	2.781	103.0	2023	Cfb	178.77	368.97
HHH	Hohes Holz	52.086	11.222	193.0	2019 - 2023	Cfb	123.19	299.17
LOH	Lochristi	51.112	3.850	6.3	2019 - 2022	Cfb	152.92	340.86
MMN	Maasmechelen	50.980	5.631	87.0	2020 - 2023	Cfb	166.61	352.02
CIO	Castelporziano	41.704	12.357	19.0	2021 - 2023	Csa	244.28	481.57

The Integrated Carbon Observation System (ICOS) network [276], a European research infrastructure, encompasses multiple stations across Europe, each adhering to strict protocols and standards for data measurement. For GHI measurements, these stations employ Spectrally Flat Class A pyranometers, in accordance with the International Organization for Standardization (ISO) 9060:1990 [271]. PAR measurements are conducted using photodetectors to measure PPF, adhering to specific requirements as outlined in Carra et al [277]. The measurement of PAR utilizes a conversion factor of 4.57 μmol/m^2/s to translate these measurements into watts per square meter (W/m^2), aligning with methodologies established in previous studies [33][139]. A total of 14 locations from ICOS were selected. One additional location from the Baseline Surface Radiation Network (BSRN) in Tõravere is included [54], resulting in 15 locations altogether as per Figure 46 and Table 11. Given the scarcity of simultaneous measurements of PAR and GHI, these specific weather stations that record both parameters concurrently and adhere to the aforementioned standards were chosen. The open-source dataset was selected for its reliability and relevance to the study of PAR. All data were recorded on a minute-basis but averaged over a 30-minute period by their respective radiometric stations. For model training and validation, 9 of the 15 locations are highlighted, with the remaining 6 reserved exclusively for model testing. This distinction ensures a thorough evaluation of model performance on unseen data, particularly focusing on their applicability and scalability within European climates. Such an approach underscores the importance of a rigorous evaluation process, considering the models' robustness, which is critical [177]. However, the independence of some locations was limited due to proximity, potentially introducing bias in the development of the new and mathematical regression analyses. Therefore, the dataset was partitioned based on randomly sampled days, with an 80-20 percentage split for training and validation, respectively, following practices as recommended in the literature [278].

In this thesis, a quality control mechanism is implemented for solar irradiance. However, distinct quality control protocols for PAR irradiance are yet to be established. Drawing on insights from the operation of the BSRN, a detailed set of guidelines has been developed to screen for unreliable irradiance; these guidelines build on existing protocols for GHI and DHI. Thus, using that as motivation, this chapter includes several key criteria for evaluating PAR data before it is used in analysis or model development. Key parameters for PAR data quality include ensuring that PAR values are greater than zero and that GHI must always exceed PAR. Additionally, the SZA is scrutinized, particularly filtering out values greater than 85º where uncertainty peaks. These criteria form the core of a robust framework designed to enhance the reliability of PAR irradiance data in scientific research. PAR, GHI, and DHI datasets were sourced from the ICOS platform, initially provided in .txt format. These files were converted into .csv format to facilitate more

efficient data handling and processing. Time standardization was performed to align all ICOS data to UTC ensuring consistency with the Tõravere dataset obtained from the BSRN. Subsequently, ten PAR estimation models were individually developed and implemented using Python, given the absence of publicly available libraries addressing PAR or AgriPV-specific calculations. In line with the statistical procedures adopted in previous chapters

6.2.2 Present Models

Recent advancements in PAR estimation models have introduced a variety of approaches and parameters, as detailed in Table 12. A consistent feature across these models is their reliance on GHI, K_t, and, frequently, SZA. These elements are typically derived from Solar Position Algorithm (SPA) through calculations including GHI measurements; hence are easily attainable.

Table 12: Details on the parameters used across the 10 PAR models under evaluation. The following variables: the Global Horizontal Irradiance (GHI) in W/m^2, sky clearness index (K_t), Pressure in millibars (P), the Solar Zenith Angle (SZA), the Perez brightness coefficient (**Δ**), the Perez clearness coefficient (ε) and the dew point temperature (T_d). Alados refers to Model 1 in [280].

Model	GHI	K_t	P	SZA	Δ	ε	T_d
Tan-Ismail	✓						
Escobedo	✓	✓					
Akitsu 1	✓	✓					
Akitsu 2	✓	✓	✓				
Peng	✓	✓		✓			
Wang	✓	✓		✓			
Hu	✓			✓	✓		
Jacovides		✓			✓	✓	
Garcia-Rodriguez	✓	✓		✓	✓	✓	
Alados	✓			✓	✓	✓	✓

Among the 10 models evaluated, the Tan-Ismail model stands out for its simplicity [279]. It proposes a straightforward conversion ratio over a one-year period in Singapore. Escobedo et al. crafted a model that categorizes K_t into distinct segments [255][262]. This technique draws inspiration from the segmentation of DHI from GHI in numerous decomposition models, but it uniquely applies this strategy to extract PAR from GHI based on varied sky conditions over 4 years in Botucatu, Brazil. Akitsu et al. have contributed two models to the field [263]. The first, Akitsu1,

integrates only GHI and pressure, while the second, Akitsu2, also incorporates K_t. Similarly, Peng and Wang have developed models that utilize a piecewise mathematical function, with coefficients as functions of K_t [256][257]. These models also account for SZA, observing an exponential increase in hourly PAR for specific K_t intervals. Despite sharing a common equation, said models diverge in their coefficient weighting systems, showcasing a tailored approach to PAR estimation based on varying K_t values.

Table 12 reveals that the latter four models utilize DHI or Perez equations that compute ε and Δ, with the former utilizing DNI. Such irradiance value can be directly measured via the use of a pyrheliometer or estimated through the closure equation (see equation 4). The estimated dew point temperature (T_d) integrates relative humidity as a percentage and air temperature in ˚C. T_d is calculated based on the adopted methodology identified through a comprehensive review of the literature [266].

6.2.3 Model Development

Previous studies have highlighted the multifaceted influences on PAR, suggesting no single factor can solely affect it. However, Figures 47 and 48 demonstrate how individual parameter values can be linked to a range of PAR outcomes. Both figures present a detailed visualization of how various parameters interact with measured PAR, offering a nuanced understanding of their relationships and dependencies. Figures 47a and 47b show a logistic growth concerning the cosine of SZA and K_t relative to measured PAR, illustrating an initial swift escalation that tapers off due to a limiting factor, embodying a sigmoidal curve that nears an asymptote. Conversely, Figure 47c introduces a weighted function depicting dew point temperatures starting from 0 to 35◦C, where the data points exhibit a positive linear growth. Additionally, Figure 47d suggests that lower Δ may inversely correlates with higher PAR values, evidenced by a denser concentration of points, indicating a potential inverse relationship between these variables.

A clear objective of this research is to identify new parameters that directly influence PAR, with a focus on variables that are readily accessible and not derived empirically through decomposition models, such is the case if DHI measurements are missing. An integral part of this research involves leveraging clear sky irradiances, specifically DNI, under clear conditions. The sensitivity of DNI to aerosols necessitates careful parameter selection. This study has evaluated six clear sky irradiance models, identifying REST2-Aero as a strong performer. However, considering the practical applications and the fact that REST2 is proprietary, the choice was between ERA5 and McClear. McClear was selected for its enhanced performance compared to ERA5. Additionally, McClear is preferred for its ease of access, requiring only the geographical coordinates and

elevation for input, making it highly user-friendly for various applications. Additionally, to explore further variables potentially affecting PAR estimations, this work incorporates satellite data from MERRA-2. Firstly, MERRA-2 consistently demonstrates superior performance on a global scale, as highlighted in a previous chapter, and it offers easy accessibility. This data source is crucial for upholding the standards of integrity and analytical rigor in this work. The chosen data, featuring an hourly temporal resolution and a recent update with a delay of less than two months, is meticulously aligned with the temporal resolution and the time frame of the measured PAR data.

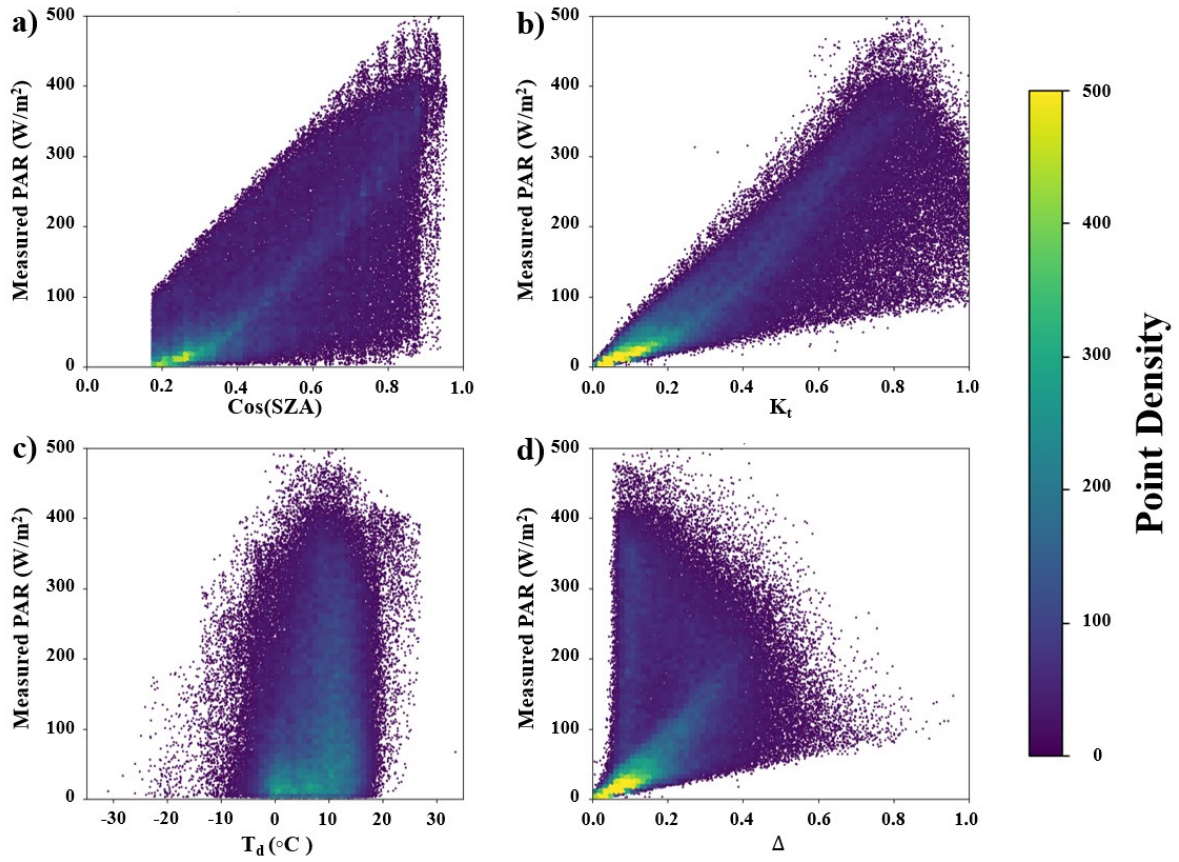

Figure 47: The relationship of different parameters with regards to the measured PAR using data from both the training and testing segments across the 9 aforementioned sites. The concept of point density is employed to gauge the frequency of data point convergence within a scatter plot, specifically concerning the parameter and PAR, across a grid formation in increments of 0.01.

Incorporating new variables into a new PAR model, alongside variables outlined in Figures 47a-47c, becomes essential due to the identified robust correlation among DNI_{Clear}, AOD550, and Ozone levels as per Figure 48. These parameters are crucial for PAR modelling because they influence the sunlight's path through the Earth's atmosphere, affecting its absorption and scattering potential. This, in turn, is influenced by molecular and aerosol interactions, as captured by AOD and ozone concentration metrics.

Table 13: The summary of Variables with Sources and Methods to be used in PAR prediction.

Variable	Source	Method
DNI_{Clear} (W/m^2)	McClear	Data for the half-hour was computed by averaging the lead and lag hour
AOD 550nm	Collection "*M21TNXAER*" with Parameter Code "*TOTEXTTAU*"	Data for the half-hour was computed by averaging the lead and lag hour.
Total Ozone Amount (atm-cm)	Collection "*M2T1NXSLV*" with Parameter Code "*TO3*"	Data for the half-hour was computed by averaging the lead and lag hour. Raw data divided by 1000 to get in atm-cm

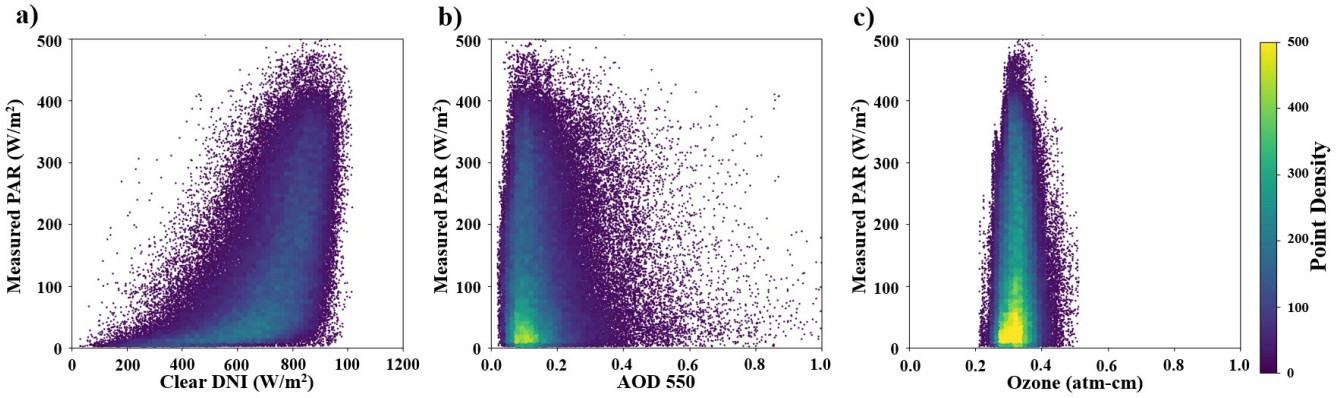

Figure 48: Data from both the training and testing segments of the 9 aforementioned sites were used to investigate the relationship between the new parameters and the measured PAR. Data points in a scatter plot can be gauged by their density in increments of 0.01 using the point density concept, specifically concerning the parameter and PAR.

Analysis beginning with Figure 48a reveals densification of data points at elevated DNI values, suggesting a potential exponential relationship where PAR escalates with rising DNI. This correlation is logical, given that increased solar irradiance directly translates to enhanced irradiance within PAR wavelengths. Furthermore, DNI is influenced by solar geometry, encompassing SZA and the Earth-sun distance. Higher solar positions correlate with increased DNI due to the reduced atmospheric path, minimizing scattering and absorption phenomena.

Contrastingly, Figure 48b illustrates a dense vertical aggregation, indicating a significant concentration of data points around a specific AOD 550 value. AOD 550, quantifying solar radiation extinction by atmospheric aerosols, is a unitless measure indicating the extent to which

aerosols hinder sunlight from reaching the ground. Elevated AOD values suggest increased aerosol presence, which can scatter and absorb sunlight, diminishing the PAR reaching the Earth's surface. Since AOD measurements at 550 nm align with the PAR spectrum, it directly affects the light available for photosynthesis. The impact of AOD on PAR is further modulated by solar geometry; for instance, lower solar positions result in sunlight traversing more of the atmosphere, thereby encountering more aerosols and amplifying AOD's effect on PAR. Moreover, Figure 48c displays a concentrated vertical distribution of PAR measurements around specific ozone concentrations, ranging between 0.2 and 0.3. Ozone predominantly absorbs sunlight in the UV spectrum, having a less immediate impact on PAR. Nonetheless, ozone can indirectly influence PAR through its effects on atmospheric thermal structure and composition, which can alter cloud formation and other atmospheric conditions affecting PAR levels at the surface. In this context, the relevance of Fraunhofer lines emerges, given the potential overlap of ozone absorption with these lines. However, the primary consideration for PAR remains the broader absorption characteristics of ozone, rather than the specific Fraunhofer lines.

In response to these findings, this work proposes shifting away from DHI towards a new set of variables outlined in Figure 48. These are integrated with K_t, GHI, SZA, and T_d based on their demonstrated correlation with PAR in literature and observations. The resulting Musleh-Rahman (MR) model incorporates the new variables in a weighted exponential formula. The model's coefficients, as per equation 16, are determined through nonlinear regression using least squares fit [53], a method chosen for its statistical consistency and relevance to reducing MAD. This iterative fitting process starts with initial values derived from the Garcia-Rodriguez model for K_t, GHI, and SZA while for T_d and the new variables are initially set to 0.1, ensuring a robust foundation for accurate PAR estimation.

$$PAR = \mathrm{GHI} \cdot \left(\frac{1.386 + \ln \mathrm{K_t}^{-0.059} + 1.06\times10^{-3}\cdot \mathrm{T}_d + 0.185\cdot\cos(\mathrm{SZA})}{\mathrm{e}^{(6.60\times10^{-5}\cdot \mathrm{DNI}_{Clear} + 2.384\cdot \mathrm{Ozone} + 0.135\cdot \mathrm{AOD550})}}\right) \quad (16)$$

6.3 Evaluation and Testing Against Present Models

The analysis of 10 models for estimating PAR reveals a broad spectrum of MAD values, spanning from 2.12% to 41.31%, as illustrated in Figure 49. The Akitus1 and Tan-Ismail models, which rely on fewer variables, show enhanced accuracy. This underscores the importance of GHI and K_t in estimating PAR across the nine evaluated sites, with MADs of 10.73% and 9.38% respectively. However, the Akitsu2 model, which includes atmospheric pressure, might be prone to overfitting, as indicated by its elevated MAD values ranging from 14.61% to 28.70%. The Escobedo models, designed to adapt strategies based on K_t values, fail to consistently correlate with the Cfb or Cfc

Köppen-Geiger climate classifications, as evidenced by all nine sites reporting MAD values above 10%, culminating in an average of 18.47%. The Peng and Wang models, which are structurally similar, exhibit similar performances and, while validated in Chinese temperate climates, do not adapt well to European temperate climates with varying SZA and GHI (and consequently, K_t values). This misalignment results in high MAD values for Peng and Wang at 31.76% and 28.05%, respectively, as per Figure 50. Models that incorporate DHI or Perez coefficients, like those by Jacovides and Garcia-Rodriguez, should better align with European temperate climates. Notably, the Alados model, also validated in Spain - a climate akin to Garcia-Rodriguez's - shows a marked increase in MAD by 18.85% when replacing K_t with T_d, highlighting the pivotal role of K_t in PAR estimation and the challenges of using a weighted T_d coefficient in diverse European climates.

	PAR Model										
Location	Tan-Ismail	Escobedo	Akitsu 1	Akitsu 2	Peng	Wang	Hu	Jacovides	Garcia-Rodriguez	Alados	Musleh-Rahman
BHT	11.66	19.92	11.57	23.79	34.25	30.25	16.32	10.95	3.45	23.78	3.16
GEB	12.15	20.75	12.05	24.78	35.68	31.51	17.00	11.40	3.59	24.77	3.29
HAI	11.84	20.22	11.75	24.15	34.77	30.71	16.56	11.11	3.50	24.14	3.21
HES	8.58	14.65	8.51	17.50	25.18	22.25	12.00	8.05	2.54	17.49	2.32
LQE	7.65	13.07	7.59	15.61	22.47	19.85	10.71	7.18	2.26	15.60	2.07
LZT	10.37	17.72	10.29	21.17	30.47	26.91	14.52	9.74	3.07	21.15	2.81
VAD	8.06	23.64	13.74	28.24	40.65	35.91	19.37	12.99	4.09	28.23	3.75
BCI	7.39	12.23	7.10	14.61	21.03	18.57	10.02	6.72	2.12	14.60	1.94
TOR	6.73	24.03	13.96	28.70	41.31	36.49	19.68	13.20	4.16	28.68	3.81

Figure 49: The effectiveness of ten empirical PAR models, featuring the recently introduced Musleh-Rahman model, was assessed using the MAD (%) values at nine different locations.

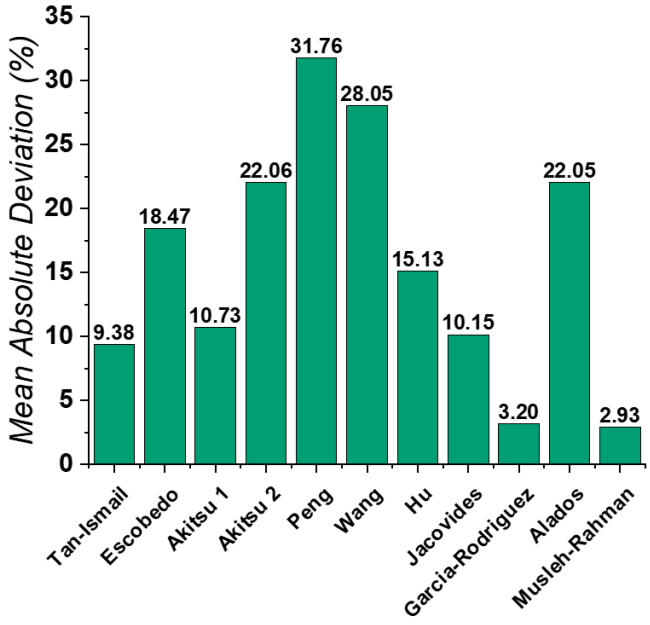

Figure 50: The overall MAD (%) values of the 10 models and the newly introduced MR model across 9 distinct locations.

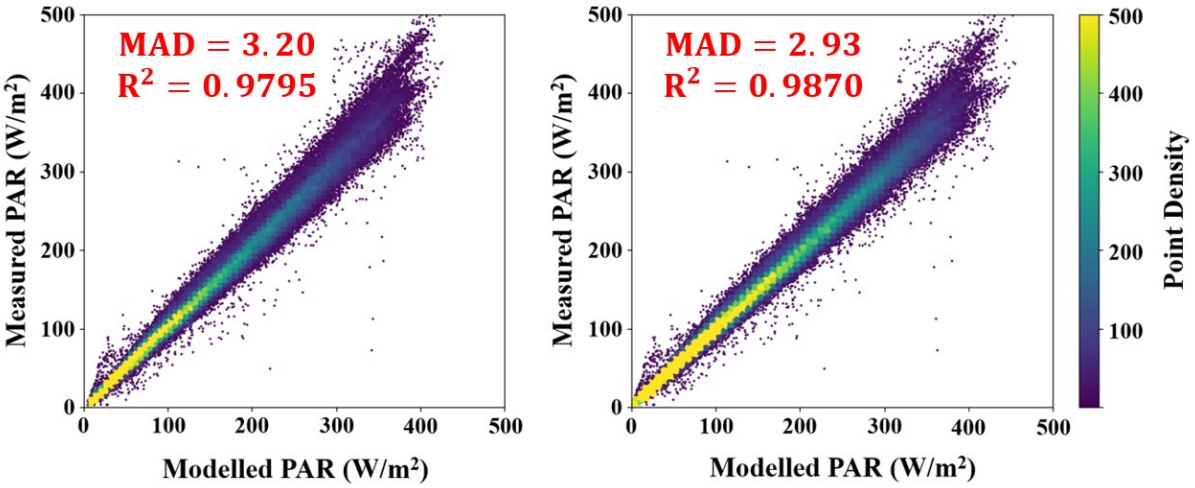

Figure 51: A side-by-side comparison of measured versus modelled PAR using two distinct models: the Garcia-Rodriguez model is depicted on the **left**, while the MR model is featured on the **right**. The comparison aims to illustrate the accuracy of each model in replicating observed PAR data across 9 validation sites.

The MR model demonstrates enhanced performance in predicting PAR values for European temperate climates, as evidenced in Figure 50. It achieves a decrease in MAD by 0.27% when compared to the best performing PAR estimations (i.e., the Garcia-Rodriguez model). This improvement is expected, given that the MR model is specifically calibrated using data from European climates, tailoring its coefficients to this particular environmental context. Figure 51 reveals that, unlike its counterpart, the MR model exhibits a more diverse point density across the spectrum of irradiance levels, noted by its improved R^2 approaching one. It not only maintains accuracy at the initial irradiance levels but also extends this accuracy to higher levels of irradiance. This characteristic is crucial for enabling more precise estimations of PAR during critical periods, such as the harvesting season for certain crops, by providing insights into the required irradiance levels under different sky conditions. Consequently, the MR model's applicability extends beyond the limitations of data availability from stations measuring DHI, promoting its broader use in various applications. Additionally, Figure 51 highlights a denser overlap between modelled and measured PAR across the entire range of PAR values, indicating a more robust and versatile performance compared to the DHI-dependent Garcia-Rodriguez model.

Location	PAR Model										
	Tan-Ismail	Escobedo	Akitsu 1	Akitsu 2	Peng	Wang	Hu	Jacovides	Garcia-Rodriguez	Alados	Musleh-Rahman
ADE	18.74	18.54	18.63	31.45	42.32	38.06	19.61	17.71	4.39	25.94	3.98
FBU	13.29	13.15	13.21	22.31	30.01	26.99	13.91	12.56	3.11	18.40	2.82
HHH	14.66	14.50	14.57	24.60	33.10	29.77	15.34	13.85	3.43	20.29	3.11
LOH	21.28	21.04	21.15	35.70	48.03	43.20	22.26	20.10	4.98	29.44	4.51
MMN	17.14	16.95	17.04	28.76	38.69	34.80	17.93	16.19	4.01	23.72	3.64
CIO	15.73	15.56	15.64	26.40	35.51	31.94	16.46	14.86	3.68	21.77	3.34

Figure 52: The performance of the ten distinct empirical PAR models, including the Musleh-Rahman model, was evaluated based on MAD (%) values across six untested locations.

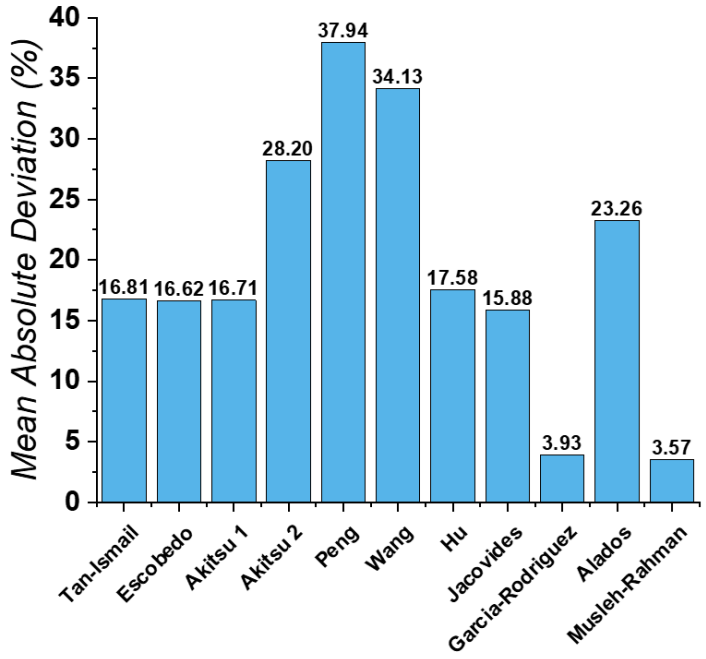

Figure 53: The overall MAD (%) values of the 10 models and the newly introduced MR model across six unseen locations.

To assess the robustness of the MR model, it is crucial to evaluate its performance across untested sites. Figure 52 displays a significant range of MAD values among 11 models, spanning from 2.82% to 48.03%. The MR model exhibits outstanding performance with an overall MAD of 3.57%, slightly outperforming the Garcia-Rodriguez model by 0.37% as per Figure 53. Again, the Peng and Wang models do not adequately address the substantial SZA experienced at higher ϕ, which explains their comparable and less favorable MAD values. Additionally, the simple ratio conversion used in the Tan-Ismail method results in an MAD ranging from 13.29% to 21.28%. This variation may stem from the complexities introduced by the dynamics of GHI distribution, which includes various influencing factors and variables, thus impacting PAR irradiance. This effect is particularly evident at the location LOH, situated near the sea, where increased humidity and variable weather conditions such as precipitation and temperature variations can lead to differing PW levels. As previously discussed in this thesis, these PW values can significantly influence GHI.

This analysis suggests that a straightforward arithmetic transformation may lack the necessary precision for accurate PAR estimation. Although segmenting the analysis based on sky clarity at LOH resulted in a modest MAD improvement of 0.16%, the overall performance using the Escobedo model remains unsatisfactory. However, enhancements in model accuracy are noted when incorporating DHI through Perez coefficients. Among the models evaluated, the Garcia-Rodriguez model continues to perform better, particularly at LOH where it shows a superior MAD of 3.93% against the highest observed value of 4.98%, underscoring the complex influence of PW on GHI and consequently on PAR.

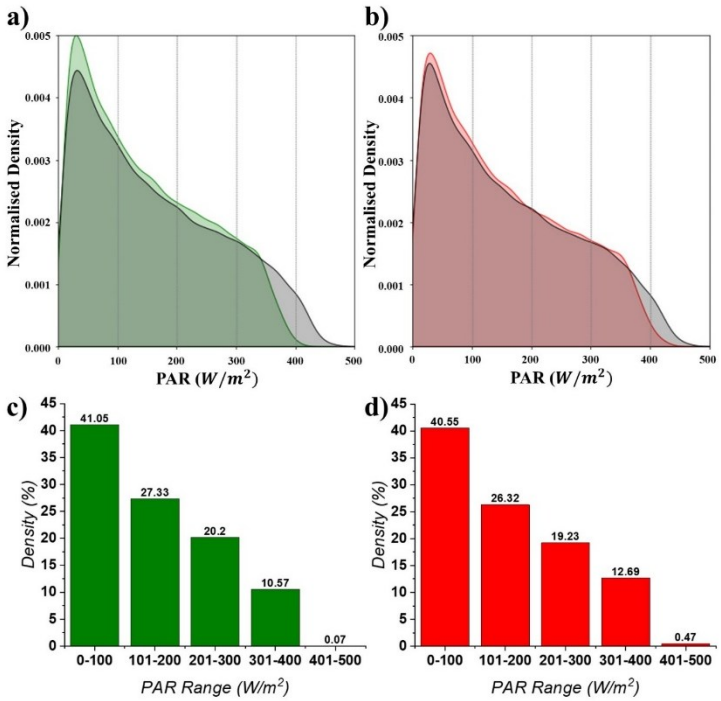

Figure 54: Comparative performance of the best-performing models with the normalised density distributions (**a** and **b**) and the associated data density percentages within specific PAR intervals (**c** and **d**) for the Garcia-Rodriguez model (in green) and the MR model (in red).

Exploring the performance nuances of the Garcia-Rodriguez and the MR, against different PAR irradiance levels, Figure 54 shows kernel density estimations shed light on their performance. These estimations reveal a heavily-skewed bell-shaped distribution for PAR values, highlighting a peak around 50 W/m^2. The Garcia-Rodriguez model aligns well with observed PAR levels but tends to slightly overestimate at the peak as per Figure 54a, predominantly covering lower irradiance values below 200 W/m^2, reflective of most dataset observations. From Figure 54d, the MR model, through its integration of McClear DNI_{Clear}, avoids the peak overestimation seen in Garcia-Rodriguez, providing a more consistent density across the 0 to 100 W/m^2 range. It exhibits a broader and more even distribution of predicted PAR values, particularly reducing bias towards higher or lower extremes as seen in Figure 54b. This refined strategy enhances the alignment of

the MR model with the actual distribution of PAR values in the dataset, boosting its precision across a variety of conditions. This subtle adjustment in prediction density could afford the MR model a slight edge in accuracy, particularly for datasets characterized by a moderate prevalence of PAR values. Additionally, its consistent performance throughout the entire PAR range demonstrates its robust ability to deliver accurate predictions across various irradiance levels. The nuanced distribution of the MR model suggests it could provide the most thorough and balanced performance among all the empirical models reviewed, particularly valuable in scenarios that demand accurate predictions across a wide spectrum of PAR irradiance.

Through examining Figure 55, it becomes evident that the Garcia-Rodriguez model's point density is predominantly concentrated within the initial 100 PAR irradiance values. This observation aligns with previous discussions, highlighting a decrease in modelling performance, in terms of point density, as PAR values escalate. Specifically, the density of grid interactions diminishes. Such model elucidates the variance observed in measured PAR data, as reflected by an R^2 value of 0.9463. This indicates that although the model exhibits a consistent bias towards higher estimates, its predictions align closely with the trends observed in actual measurements, reinforcing insights presented in Figure 55. In contrast, the MR model exhibits a reduction in performance at unseen sites, resulting in an overall MAD of 3.57% yielding an R^2 value of 0.9709. This similar performance in MAD suggests a narrower average error margin compared to the findings in Figure 54a. Furthermore, an enhanced R^2 value signifies a superior model fit to the measured data, implying not only an accurate trend prediction but also greater precision on average. The density of points near the 1:1 line is notably high for lower PAR values, with no distinct peak value as indicated in Figure 54b, pointing towards numerous accurate predictions.

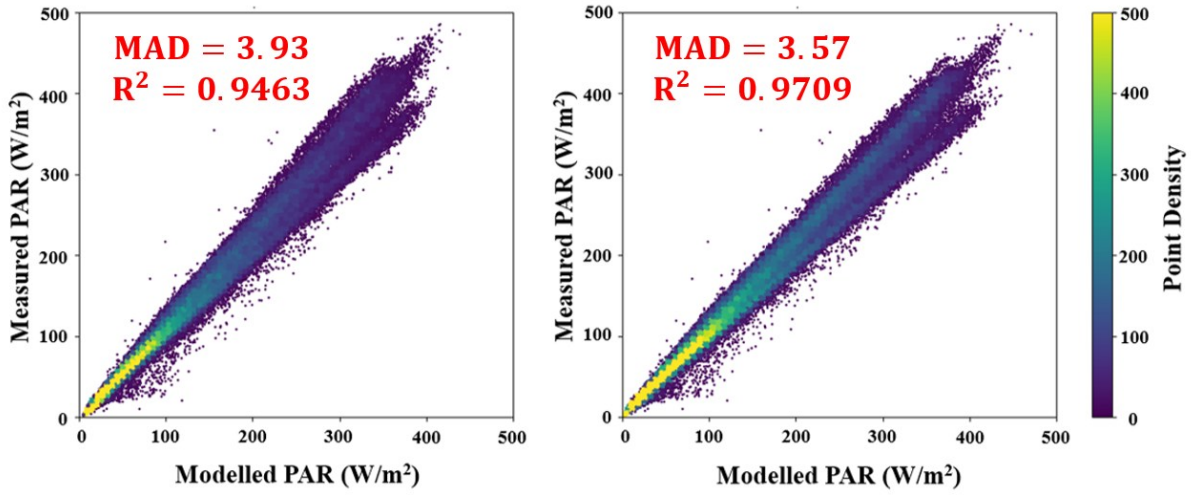

Figure 55: Comparative scatter plots of measured PAR against the best-performing models with Garcia-Rodriguez (**Left**), and MR (**Right**), at 6 unseen European Temperate Locations.

It becomes apparent that eliminating DHI and incorporating McClear DNI_{Clear}, Ozone, and AOD550 not only reduces MAD (albeit by a small margin of 0.36%) and improves the R^2 value but also enhances the model's robustness, making it applicable beyond sites equipped to measure DHI. Specifically, the inclusion of McClear DNI_{Clear} addresses the issue of early PAR values, while Ozone and AOD550 adjustments rectify overestimations beyond 200 W/m^2, facilitating a more accurate representation of fluctuations.

6.4 Conclusion

This chapter presents an analysis of ten empirical models for predicting PAR irradiance, with four models that incorporate DHI (or its derivatives such as Perez coefficients) across 15 temperate European environments. The evaluation highlights their performance under diverse solar, atmospheric, and cloud cover conditions at higher ϕ, leading to the development of the Musleh-Rahman (MR) model. This new model cedes the use of DHI in favor of DNI_{Clear}, as well as Ozone and AOD 550 data sourced from satellite observations using MERRA-2. The substitution of DHI with these readily available variables supports advancements in AgriPV by providing essential, accessible data. The MR model performance was extensively tested, showing a notable improvement in accuracy, particularly across nine European climates where it achieved a MAD of 2.93%, a reduction from the 3.20% observed in best empirical model (i.e, the Garcia-Rodriguez model). Further validation across six additional, unseen European sites showed MAD values ranging from 2.82% to 4.51% for the newly developed MR model. The MR model demonstrated exceptional precision in predicting lower PAR values, as evidenced by kernel density and scatter plot analyses, achieving a robust R^2 value of 0.9709. Such advancements aim to enhance accurate PAR irradiance predictions in temperate European climates, where the MR model surpasses other models. Its accuracy could be integrated into feasibility software and other metrics to assess potential crop yields and, when combined with other models, to predict diffuse PAR values. This integration is intended to promote the adoption of AgriPV, offering a robust foundation for optimizing agricultural productivity under varying solar conditions.

Chapter 7 Conclusions and Future Work

7.1 Summary of Research Findings

The swift expansion of the PV industry, along with other renewable energy sources, has been propelled by several critical factors. Central to these considerations is the dual imperative to meet escalating global energy demands and address climate change concerns due to fossil fuel emissions. Nations worldwide strive to achieve their carbon neutrality targets, underscoring the necessity for innovative solutions in the energy sector. To challenge the supremacy of non-renewable energy, a diverse array of PV technologies must be investigated. This exploration is conducted through sophisticated modelling to assess the viability of various systems. Traditional monofacial, fixed-tilt solar setups are giving way to more advanced configurations, such as bifacial modules with tracking systems and the integration of photovoltaics with agriculture, known as AgriPV. Validating these empirical mathematical models is crucial to gaining public trust. As the PV sector continues to expand, the demand for more precise feasibility assessments and financial projections is becoming increasingly critical. A key approach to achieving this accuracy involved thoroughly evaluating and analysing the irradiance models embedded within current feasibility software. Equally concerning is the shortage of dedicated feasibility software for AgriPV, which is essential for addressing land scarcity and enabling the harmonious integration of agricultural activities and PV systems on shared land. This involved testing the models against minutely resolved irradiance data, a shift from the previous hourly-based models, and examining their performance in temperate climates like the UK, where conditions differ significantly from the regions where these models were originally conceptualized. This thesis aimed to validate and, where necessary, refine various optical models, examining the methodologies used, and the limitations of current feasibility software, and proposing potential enhancements.

The core goal of this research was to facilitate the growth of solar energy in the market by integrating accurate evaluations of PV system performance into mainstream feasibility software. This approach will attract potential investors by offering reliable, validated methodologies for calculating irradiance components essential for solar resource assessment and various irradiance parameters. The focus extends to systems ranging from tilted installations to tracking solutions in temperate climates such as the UK, thereby enhancing confidence in the rapidly advancing PV technologies. This thesis undertook a comprehensive investigation of bifacial, tracking, and AgriPV systems, amalgamating insights from diverse studies and geographical ϕ to

demonstrate the viability of these varied systems. Given solar investors' critical dependence on irradiance data to calculate incident irradiance on inclined surfaces, it is essential to understand the models employed by feasibility software. This research delineated the breakdown of GHI into its constituent fractions by establishing a foundation in solar irradiance through the analysis of solar resources and the use of satellite data, grounded in the mathematical principles of solar irradiance modelling. Firstly, this thesis established a benchmarking framework, employing the UK as a case study, to conduct detailed examinations of decomposition models that breakdown GHI into its constituent fractions of DHI (and subsequently DNI). Moreover, it highlighted the significance of transposition modelling in various systems for estimating POA irradiance (and thus, lays the foundation for BOA estimations). This involves scrutinizing the limitations of feasibility software and conducting sub-hourly validations, with the former focusing on sky clearness and the latter on assessing the effects of cloud coverage. Additionally, this research evaluated the accuracy of clear sky modelling on a global scale, factoring in diverse atmospheric conditions, as clear sky modelling is essential for all irradiance modelling endeavours. Lastly, the thesis offered insights into PAR irradiance modelling by exploring its constraints and developing a tailored optical model to predict PAR in temperate settings.

The necessity for reliable solar irradiance estimations is paramount, particularly in locations lacking direct measurements, which is the overwhelming majority. Researchers are increasingly turning to decomposition models designed to estimate DHI, a critical component for determining titled irradiance calculations for solar panels. Given the abundance of models present, this thesis introduced a clear and structured benchmarking framework tailored for regions devoid of solar irradiance data. Focusing on precision and robustness, the framework established a cap for the MAD at 15%, and incorporated explanations from statistical, mathematical, and physical aspects of 104 models using the UK as a case study. The first examination assessed the effects of temporal resolution on the accuracy of the models. In Camborne, hourly-to-minute analysis narrowed 18 models to 6, with only 2 consistent across both periods. Chilbolton's count reduced from 32 to 5, with 2 models meeting both thresholds. Lerwick saw a drop from 13 to 9, with 5 models effective in both time resolutions. Furthermore, this chapter identified models effective in multiple locations in both time domains. The Paulescu model excelled in all locations (MADs of 12.37% to 13.05%). In Camborne and Lerwick, Starke1 were found to be in common, particularly due to the empirical nature such model has with respect to its coastal contexts. A spatial homogeneity assessment across the three locations found only five models meeting the threshold, with Paulescu having the lowest average MAD (12.76%). Paulescu, Yang5, SM, Starke3, and Yang4 adhered to the threshold across varying datasets and hence, were confirmed as the most robust with MADs of 12.57%, 13.24%, 13.42%, 14.12% and 14.22%, respectively.

Finally, a comprehensive approach was implemented by integrating 10 distinct GHI_{Clear} models, each with unique number of input parameters. These models were systematically combined in a matrix format across 15 decomposition models that use clear-sky models. This strategy successfully expanded the number of models meeting the MAD threshold from 5 to 20. Furthermore, by integrating REST2 or McClear as the basis for GHI_{Clear} models, 15 models were found to be within MAD < 15%. Modifying clear-sky models to enhance the robustness of these systems underscores the need to evaluate clear sky irradiance predictions using varied atmospheric inputs. Analysing the leading decomposition models by adapting the GHI_{Clear} model results in the Engerer2a model combined with McClear yielding the lowest MAD value of 12.77%, demonstrating substantial room for optimization.

Feasibility software for photovoltaic systems primarily uses decomposition-transposition model pairs to estimate POA irradiance. Additionally, said software is capable of incorporating measured GHI, DHI, and DNI to calculate POA irradiance, although this is less common. Hence, it is imperative to look into both aspects, using optical pairs and also using measured inputs to assess the viability of transposition models. Firstly, this thesis analysed the accuracy of 15 optical model pairs, using minute input irradiance, to assess POA predictions in a temperate setting by comparing to measured POA for both an actuator-based tracker and a 55° south-facing tilted system. Using the MAD of <5% as the benchmark, significant variations were revealed across diverse sky conditions. Model estimates portrayed a broad range of errors from the measured data, from 2.67% to 51.07%, influenced by variables such as K_t and system type. For the tracking system, the evaluation showed that in clear conditions, ten model pairs maintained errors within the range. However, this success diminished under intermediate skies, with only five models remaining within range, and further reduced to two models in overcast conditions. The fixed tilt system demonstrated similar trends but with fewer models meeting the required thresholds; four models in clear conditions, and only two in intermediate conditions. Remarkably, only the DISC-SO model pair met the threshold in overcast conditions, exhibiting an MAD of 2.67%. Thus, the DISC-SO model pair consistently met the threshold for both systems under all conditions, making it a preferred choice for transposing horizontal irradiance. However, R^2 values (0.5034, 0.5379, 0.5083 for clear, intermediate, and overcast conditions, respectively) highlighted challenges due to the high temporal resolution of input data and the hourly data-based SO transposition model. Moreover, the study also examined the impact of decomposition and transposition models on percentage errors. Decomposition changes caused discrepancies of up to 2.43% for tracking systems and 5.34% for fixed-tilt systems. In contrast, transposition model changes resulted in errors of 8.53% and 11.51%, respectively. Additionally, using hourly solar irradiance data yielded lower errors compared to minute data, with 1.51% in intermediate

conditions, 1.08%, and 0.96% in overcast and clear conditions, likely due to the models being developed empirically with hourly data.

This thesis also investigated the integration of measurement data into transposition models, a move that renders decomposition models obsolete. The research involved an analysis of 16 transposition models, eight of which are frequently utilized in feasibility software, across six distinct cloud conditions. The results revealed MAD in model outputs ranging from 2.69% to 41.91%. The SO model, in particular, demonstrated the most accurate performance, with the smallest deviations from measured POA irradiance; with discrepancies being minimal at 2.69% under cloud enhancement conditions and up to 5.03% under scattered cloud scenarios. A deeper mathematical evaluation showed that the specific implementations of these models play a critical role in their effectiveness under various cloud conditions. Both the original and the revised versions of the Hay model, known as Hay1993, displayed robust performances with maximum discrepancies of just 0.71%, a testament to the updated factor in Hay1993. Additionally, this thesis investigated the decline in the Perez model's performance in the presence of clouds, which deteriorates significantly, reaching a MAD of 18.12%. The analysis identified a critical flaw in the Perez model: the unsuitability of the clearness coefficient in its first bin, especially when applied to temperate climates with minute-level irradiance data. To enhance the Perez model's applicability, a revision of the coefficients, particularly those in the first bin of its lookup table, is essential. Additional scrutiny of the Perez model, along with the LJ and SO models, delved into the influence of cloud concentration and azimuth-altitude adjustments on model accuracy. Of these, the SO model emerged as the most consistent, registering the lowest MAD values of 2.69%, 2.84%, 4.44%, 5.03%, 4.23%, and 4.59% across different cloud conditions, namely cloud enhancement, cloudless, thin clouds, scattered clouds, thick clouds, and overcast, respectively. This translated to that, regardless of using measured inputs or using a robust decomposition model, the SO model is superior.

Accurate clear-sky irradiance data plays a crucial role in various applications, such as estimating all-sky irradiance components with an attenuation factor or serving as a fundamental parameter in decomposition models. Henceforward, content within this thesis assessed the impact of atmospheric data inputs sourced from satellite data on the accuracy of solar irradiance modelling. It evaluated six clear-sky models, specifically the widely-used McClear and ERA5, alongside four REST2 variants that utilize data from MERRA2 (with and without elevation adjustments), CAMS, and AERONET measurements at 67 international locations. The analysis revealed that the REST2 model, when combined with AERONET data, consistently achieves the most accurate predictions for GHI and DNI on a global scale, with MAD of 2.48% and 2.42%,

respectively. In scenarios lacking sunphotometer data, which are common, choosing the right satellite dataset is crucial for model accuracy. Findings showed that that MERRA2 data provides superior performance over CAMS in terms of *AE*, AOD550 and PW, showing improvements of 11.88%, 34.96%, and 2.54% respectively. For global GHI estimates, the REST2 variant using MERRA2 data recorded an MAD of 3.20%, and for DNI, an MAD of 7.14%, ranking second after the AERONET-integrated model. McClear, which relies on CAMS data, was evaluated to understand how its internal formulas differ. The performance of McClear and REST2-CAMS was incomparable in estimating GHI, with a minimal MAD difference of 0.08%. However, for DNI predictions, the discrepancy was significantly larger, nearly twelvefold. At higher altitudes, McClear and REST2-CAMS showed differing results, indicating potential inaccuracies in McClear's formulas or its data integration process, particularly with elevation data and AOD550 from CAMS. Conversely, ERA5 reported higher MAD values of 14.88% for GHI and 25.26% for DNI globally, but showed improved accuracy at high-altitude sites with MADs of 3.09% for GHI, outperforming McClear by 5.22%. Therefore, for high-altitude locations, ERA5 was preferred over McClear. However, the REST2 model using MERRA2 data, particularly with elevation correction, is recommended for broader applications. Given the proprietary nature of REST2, viable alternatives include McClear or ERA5, with McClear being advisable due to its performance closely matching that of REST2 iterations, except when integrating AERONET data.

The rise of AgriPV underscores the necessity for precise PAR irradiance predictions, particularly in higher ϕ where standard models may falter due to atmospheric discrepancies. This thesis concluded that through critically evaluating ten empirical models and introducing the Musleh-Rahman (MR) model, which optimizes input selection by excluding DHI. Based on findings within this thesis, these inputs were selected to simplify the application process and enhance data accessibility, thus why DNI_{Clear} (from McClear) alongside AOD550 and Ozone concentrations (from MERRA2) were selected. Utilizing sub-hourly data from nine temperate climates, the MR model demonstrated an MAD of 2.93%, surpassing the 3.20% MAD of the best performing empirical model (which did utilize DHI measurements as an input). Further validation of the MR model across six unseen temperate sites revealed MAD values ranging from 2.82% to 4.51%. The model's accuracy in predicting lower PAR values was substantiated through kernel density and scatter plot analyses, achieving a robust R^2 value of 0.9709. This precision not only establishes the MR model's superiority over its competitors but also underscores its utility in feasibility software for predicting potential crop yields and diffuse PAR values. The ultimate goal was to facilitate the widespread adoption of AgriPV by providing reliable and easily accessible data to optimize agricultural productivity under varied solar conditions.

This research made several contributions in the realm of solar resource assessment. Firstly, it introduced a benchmarking framework featuring a series of four tests designed to evaluate the robustness of decomposition models. This transparent framework can be universally applied and considers all relevant factors influencing the model selection process. Secondly, the thesis examined the dynamics of transposition models, addressing both the constraints of feasibility software in deploying optical model pairs (decomposition coupled with transposition) and the evaluation of transposition models based on measured inputs. These analyses are conducted in a temperate climate context and under minute-to-minute irradiance variations. Thirdly, the thesis assessed the accuracy of clear-sky irradiance models across global settings, comparing both proprietary and open-access models using varied atmospheric data inputs. Lastly, the thesis presented the development of a mathematical model formulated with readily available inputs to predict PAR irradiance, a critical factor for AgriPV applications. This model supports both standalone agricultural applications and the combined use of PV and agriculture.

7.2 Suggestions for Future Research Directions

This research laid the groundwork for enhancing PV modelling and opens up possibilities for further exploration in various fields. By delving into innovative structures, it aimed to pave the way for the development of more precise models across different PV technologies. The findings presented offer numerous opportunities for extension, yet it would be beneficial to concentrate on specific areas where this thesis could significantly impact the advancement of accurate solar resource assessment.

ML research is rapidly gaining momentum, with significant attention directed towards enhancing model performance through optimal input parameter selection. This thesis highlighted key features that could significantly impact ML models. Although AERONET measurements are ideal for atmospheric inputs, they are often unavailable. Thus, incorporating parameters such as AE, AOD550, and PW from MERRA2 into ML models is recommended over CAMS. Additionally, considering clear-sky irradiance, regardless of access to proprietary models, could improve both irradiance predictions and decomposition models, potentially leading to the creation of a new model variant that optimizes decomposition processes. To advance this field, employing ML to replace traditional decomposition models presents a promising avenue. Future research should not only integrate the new features identified but also engage in reverse engineering existing methods. It is crucial to examine the robust framework developed and ensure the ML model's robustness through spatial homogeneity. This can be achieved by analyzing a wide range of global sites with varying solar irradiance and positions. Additionally, addressing temporal resolution

through minute-by-minute input handling and assessing dataset viability could further refine model accuracy and reliability.

In the transposition segment, a shift toward spatial uniformity is essential, encompassing multiple sites rather than concentrating on a single location to give an accurate representation of POA. It is crucial to validate transposition techniques across various system configurations, including different elevation heights, azimuths, and tilts. However, for high tilt angles, it may be beneficial to obstruct part of a pyranometer to mitigate the influence of reflective contributions, focusing solely on the diffuse aspect of the transposition model. Research presented in this thesis indicates that the coefficients employed in the Perez Model's lookup function are inadequate, particularly under varying cloud conditions. This suggests the potential for developing new coefficients.

Exploring measured albedo inputs is also beneficial as this can significantly influence POA measurements. Given the established standards for BOA measurements, evaluating ground reflective models using the transposition models discussed in this thesis is warranted. This involves implementing a 180-degree tilt shift and moving beyond traditional transposition model evaluations to assess reflective models. Moving away from stand-alone systems for BOA modelling is imperative. Configuring the setup in an array format (minimally three rows and columns with measurement devices in the center of the second row and column) is required, as this configuration represents the most challenging scenario for BOA measurement due to shading. Further investigations are necessary to determine the overall irradiance spectrum, acknowledging that the spectral component of BOA differs from POA due to the PAR range. Comprehensive spectral measurements, encompassing not only albedo but also BOA, are crucial. These measurements are vital for understanding the inhomogeneity of rear irradiance and its effects, which remain largely unquantified. Such variability can significantly affect the performance and predictive accuracy of bifacial PV performance. Therefore, further exploration and evaluation of the non-uniformity on the rear-side irradiance through integrated optical and electrical models are necessary.

For AgriPV systems, employing specialized equipment such as quantum sensors beneath PV installations (particularly in differing tilt scenarios) facilitates the calculation of the diffuse component of PAR. As research on PAR irradiance increasingly adopts minute-to-minute analysis, similar to its spectrally flat counterparts like GHI, this approach enables detailed studies, either empirical or ML based. By analyzing the separation of PAR into its diffuse and direct components, these insights can be integrated into feasibility software. Integrating this methodology is pivotal for assessing crop yields beneath PV installations, moving beyond the

unshaded PAR estimations explored earlier in this thesis. Such integration will facilitate a comprehensive evaluation of performance metrics, deepening the understanding of AgriPV's effects. Building upon the results discussed in this thesis, it becomes imperative to develop models that are not only accessible but also broadly applicable across various domains such as PAR, decomposition, and transposition.

Appendix A

The follow table presents a thorough review of 104 decomposition models, highlighting those developed specifically in temperate climates or successfully validated in the same region. It details the latitude where the model originated, the year of development, the data range used during its creation, and the temporal resolution of the dataset involved. Additionally, the table includes relevant references and remarks to provide further context and insights.

Table A.1: Comprehensive Literature Review of 104 Decomposition Models for Estimating Diffuse Horizontal Irradiance (DHI).

Model	Latitude	Year	Range	Data Resolution	Reference	Comments
Boland1	38.1	-	67 days	Hourly	[A1]	Equation 1
Boland2	38.1	-	-	-	[A1]	Equation 2
Bakhsh	26.2	Jan 1984 - Apr 1985	15 months	Hourly	[A10]	
Kuo1	23	Jan 2011 - Dec 2012	24 months	Hourly	[A11]	Model 1 (with fitting dataset of 2011)
Kuo2	23	Jan 2011 - Dec 2012	24 months	Hourly	[A11]	Model 2 (with fitting dataset of 2012)
Kuo3	23	Jan 2011 - Dec 2012	24 months	Hourly	[A11]	Model 3 (with fitting dataset of 2011)
Kuo4	23	Jan 2011 - Dec 2012	25 months	Hourly	[A11]	Model 4 (with fitting dataset of 2012)
Yao1	31.1	Jun 2012 - Nov 2012	5 months	Hourly	[A12]	HMDF model 1
Yao2	31.1	Jun 2012 - Nov 2012	5 months	Hourly	[A12]	HMDF model 2
Yao3	31.1	Jun 2012 - Nov 2012	5 months	Hourly	[A12]	HMDF model 3
Yao4	31.1	Jun 2012 - Nov 2012	5 months	Hourly	[A12]	HMDF model 5
Bourges	(37 locations) 37.4 - 55.8	-	48 months	Hourly	[A13]	
CK	13	Jan 1983 - Dec 1987	60 months	Hourly	[A14]	Equation 6
CM1	6.6	Jan 1991 - Dec 1992	24 months	Hourly	[A15]	Model 1
CM2	6.6	Jan 1990 - Jun 1991	17 months	Hourly	[A16]	Model I
chikh1	31.6	Aug 1990 - Dec 1992	29 months	Hourly	[A17]	Bechar Site

chikh2	22.8	Jan 1990 - Aug 1992	32 months	Hourly	[A17]	Tamanrasseet Site
chikh3	36.4	Jan 1992 - Dec 1992	12 months	Hourly	[A17]	Alger Site
FO	23.3	Jan 2002 - Dec 2002	12 months	Hourly	[A18]	
Hawlader	1.2	Mar 1932 - Aug 1962	5 months	Hourly	[A19]	
Boland3	51.4	-	-	-	[A2]	Bracknell Coefficients
Boland4	12.5	-	-	-	[A2]	Darwin Coefficients
Boland5	38.7	-	-	-	[A2]	Lisbon Coefficients
Boland6	22.2	-	-	-	[A2]	Macau Coefficients
Boland7	50.8	-	-	-	[A2]	Uccle Coefficients
Hollands	43.7	Jan 1967 - Dec 1971	60 months	Hourly	[A20]	
Jacovides	37	Jan 2000 - Dec 2002	36 months	Hourly	[A21]	
Lam and Li	22.3	Jan 1991 - Jun 1994	41 months	Hourly	[A22]	Model 1
LAM2	22.3	Jan 1991 - June 1994	48 months	Hourly	[A22]	Model 2
Li And Lam	22.3	Jan 1991 - June 1994	48 months	Hourly	[A23]	
Louche	41.6	Oct 1983 - Jun 1985	20 months	Hourly	[A24]	
Moreno	37.4	Jan 2000 - Dec 2008	108 months	Hourly	[A25]	
Muneer3	(2 locations) (51.3 - 54.7)	Jan 1990 - Dec 1995	72 months	Hourly	[A26]	
Oliveira	23.3	May 1994 - Jun 1999	61 months	Hourly	[A27]	
Pagola1	(3 locations) 38.0 - 40.4	Oct 2005 - Sep 2008	36 months	Hourly	[A28]	Model 1
Pagola2	(3 locations) 38.0 - 40.4	Oct 2005 - Sep 2008	36 months	Hourly	[A28]	Model 2
Perez-Burgos	(4 locations) 48.0 - 43.5	Jan 2002 - Jun 2012	120 months	Hourly	[A29]	
SM	32	Nov 1985 - Nov 986	12 months	Hourly	[A3]	Equation 4 with Equation 1, Equation 2, Equation 3
PLL1	37.5	Jan 1993 - Dec 2002	120 months	Hourly	[A30]	Model 1
PLL2	37.5	Jan 1993 - Dec 2002	120 months	Hourly	[A30]	Model 2
Karatasou	38	Jan 1996 - Dec 1998	36 months	Hourly	[A31]	

Rerhrhaye	33.1	Oct 1991 - Sep 1993	24 months	Hourly	[A31]	
Ruiz-Arias1	39	Jan 2002 - Dec 2006	60 months	Hourly	[A32]	Albacete (Spain) Model G0
Ruiz-Arias2	40	Jan 1961 - Dec 1990	360 months	Hourly	[A32]	Boulder (Western USA) Model G0
Ruiz-Arias3	51.1	Jan 1981 - Dec 1990	120 months	Hourly	[A32]	Dresden (Germ.) Model G0
Ruiz-Arias4	40.4	Jan 1961 - Dec 1990	360 months	Hourly	[A32]	Pittsburgh (NE USA) Model G0
Ruiz-Arias5	32.1	Jan 1961 - Dec 1990	360 months	Hourly	[A32]	Tuscon (SW USA) Model G0
Ruiz-Arias6	62.3	Jan 1961 - Dec 1990	360 months	Hourly	[A32]	Talkeetna (Alaska) Model G0
Sanchez	38.5	Nov 2009 - Oct 2010	12 months	Hourly	[A33]	
Skartveit	60.5	Jan 1965 - Dec 1979	180 months	Hourly	[A34]	
Soares	23.6	Jan 1998 - Sep 2001	44 months	Hourly	[A35]	
Spencer	(12 locations) 20.0 - 45.0	Aug 1971 - Jul 1977	71 months	Hourly	[A36]	
Tapakis1	31.5	Jan 2001 - Dec 2010	120 months	Hourly	[A37]	Table 4
Tapakis2	31.5	Jan 2001 - Dec 2010	120 months	Hourly	[A37]	Corrected Table 5 (reverse order of p6 to p1)
Tapakis3	31.5	Jan 2001 - Dec 2010	120 months	Hourly	[A37]	Table 8
Torres1	42.8	Oct 2006 - May 2008	19 months	Hourly	[A38]	Model 1 Pamplona (Table 1), a8 = 0.1923
Torres2	42.8	Oct 2006 - May 2008	19 months	Hourly	[A38]	Model 2 Pamplona (Table 1)
Torres3	42.8	Oct 2006 - May 2008	19 months	Hourly	[A38]	Model 3 Pamplona (Table 1)
Torres4	42.8	Oct 2006 - May 2008	19 months	Hourly	[A38]	Model 4 Pamplona (Table 1)
Tuomiranta1	(8 locations) 23.6 - 24.5	Jun 2007 - Jun 2013	72 months	Hourly	[A39]	UAE general (U1): all sites apart from East of Jebel Hafeet
Tuomiranta2	(8 locations) 23.6 - 24.5	Jun 2007 - Jun 2013	72 months	Hourly	[A39]	UAE inland (U2): all inland sites apart from East of Jebel Hafeet
Tuomiranta3	(8 locations) 23.6 - 24.5	Jun 2007 - Jun 2013	72 months	Hourly	[A39]	UAE east: sites close to East of Jebel Hafeet
De Jong	52.1	Jan 1961 - Dec 1977	204 months	Hourly	[A4]	
UH1	38.2	Jan 1994 - Dec 1998	60 months	Hourly	[A40]	Equation 9
UH2	38.2	Jan 1994 - Dec 1998	60 months	Hourly	[A41]	Equation 10

De Miguel	(11 locations) 37.0 - 44.1	Jan 1978 - Dec 1996	216 months	Hourly	[A42]	
Orgill-Hollands	43.7	Sep 1967 - Aug 1971	47 months	Hourly	[A43]	
Erbs	(4 locations) 31.1 - 42.4	Aug 1974 - Dec 1976	28 months	Hourly	[A44]	
Reindl	(6 locations) 28.4 - 59.6	Jan 1979 - Dec 1980	24 months	Hourly	[A45]	
Reindl2	(6 locations) 28.4 - 59.6	Jan 1979 - Dec 1980	24 months	Hourly	[A45]	Equation3a, 3b, 3c
BRL	(7 locations) 12.5 - 51.4	-	-	-	[A46]	Equation 10
Engerer1	(6 locations) 34.2 - 40.7	Jan 2001 - Dec 2011	132 months	Minute	[A47]	
Engerer2a	(6 locations) 34.2 - 40.7	Jan 2001 - Dec 2011	132 months	Minute	[A47]	Referred to Engerer2
Engerer3	(6 locations) 34.2 - 40.7	Jan 2001 - Dec 2011	132 months	Minute	[A47]	
Abreu	(48 locations) 8.53 - 75.1	1995 - 2017	Multiple	Minute	[A48]	
Energer2b	(70 locations) 96.6 - 0.52	Jan 2013 - Aug 2018	Multiple	Minute	[A49]	Referred to New 1-min Engerer2
Energer2c	(70 locations) 96.6 - 0.52	Jan 2013 - Aug 2018	Multiple	Minute	[A49]	Referred to New 5-min Engerer2
Energer2d	(70 locations) 96.6 - 0.52	Jan 2013 - Aug 2018	Multiple	Minute	[A49]	Referred to New 10-min Engerer2
Energer2e	(70 locations) 96.6 - 0.52	Jan 2013 - Aug 2018	Multiple	Minute	[A49]	Referred to New 15-min Engerer2
Energer2f	(70 locations) 96.6 - 0.52	Jan 2013 - Aug 2018	Multiple	Minute	[A49]	Referred to New 30-min Engerer2
Energer2g	(70 locations) 96.6 - 0.52	Jan 2013 - Aug 2018	Multiple	Minute	[A49]	Referred to New 1-h Engerer2
Energer2h	(70 locations) 96.6 - 0.52	Jan 2013 - Aug 2018	Multiple	Minute	[A49]	Referred to New 1-day Engerer2
Mondol 2	54.6	Jan 1989 - Dec 1998	120 months	Hourly	[A5]	
Starke1	(4 locations) 12.5 - 37.8	1999 - 2013	Multiple	Minute	[A50]	Australian Data (Table 3)
Starke2	(3 locations) 9.1 - 27.6	2004 - 2016	Multiple	Minute	[A50]	Brazilian Data (Table 5)
Paulescu	(37 locations) 60.1 - 0.52	2002 - 2013	Multiple	Minute	[A51]	
Boland 8	38.1	-	67 days	-	[A52]	Corrected Equation 4
Every1	(19 locations) 12.4 - 41.0	-	24 months	Minute	[A53]	Using Worldwide coefficients
Every2	(2 locations) 37.8 - 41.0	-	24 months	Minute	[A53]	Using coefficients from 'Cfb'

Starke3	24 locations (24.3 - 60.1)	-	-	Minute	[A53]	Using coefficients from 'C'
Yang4	(126 locations) 60.1 - 0.52	2016 - 2020	48 months	Minute	[A54]	
Yang5	(126 locations) 60.1 - 0.52	2016 - 2020	48 months	Minute	[A55]	
Gonzalez1	(2 locations) 41.2 - 41.4	Jan 1994 - Dec 1996	36 months	5 Minute	[A56]	T1
Gonzalez2	(2 locations) 41.2 - 41.4	Jan 1994 - Dec 1996	36 months	5 Minute	[A56]	T2
Gonzalez3	(2 locations) 41.2 - 41.4	Jan 1994 - Dec 1996	36 months	5 Minute	[A56]	T3
Gonzalez4	(2 locations) 41.2 - 41.4	Jan 1994 - Dec 1996	36 months	5 Minute	[A56]	T4
Gonzalez6	(2 locations) 41.2 - 41.4	Jan 1994 - Dec 1996	36 months	5 Minute	[A56]	T6
Gonzalez7	(2 locations) 41.2 - 41.4	Jan 1994 - Dec 1996	36 months	5 Minute	[A56]	T7
Muneer2	(5 locations) 51.2 - 60.1	Jan 1981 - Dec 1983	36 months	Hourly	[A6]	
Ineichen1	46.2	Jun 1979 - Jun 1983	48 months	Hourly	[A7]	Model 1
Ineichen2	46.2	Jun 1979 - Jun 1983	48 months	Hourly	[A7]	Model 2
Ineichen3	46.2	Jun 1979 - Jun 1983	48 months	Hourly	[A7]	Model 3
Mondol 1	54.6	Jan 1989 - Dec 1998	120 months	Hourly	[A8]	
Muneer1	28.6	Jan 1974 - Jun 1995	24 months	Hourly	[A9]	

[A1] J. Boland, L. Scott, and M. Luther, “Modelling the diffuse fraction of global solar radiation on a horizontal surface,” Environmetrics, vol. 12, no. 2. Wiley, pp. 103–116, 2001. doi: 10.1002/1099-095x(200103)12:2<103::aid-env447>3.0.co;2-2.

[A2] J. Boland, B. Ridley, and B. Brown, “Models of diffuse solar radiation,” Renewable Energy, vol. 33, no. 4. Elsevier BV, pp. 575–584, Apr. 2008. doi: 10.1016/j.renene.2007.04.012.

[A3] H. Suehrcke and P. G. McCormick, “The diffuse fraction of instantaneous solar radiation,” Solar Energy, vol. 40, no. 5. Elsevier BV, pp. 423–430, 1988. doi: 10.1016/0038-092x(88)90097-7

[A4] C. J. T. Spitters, H. A. J. M. Toussaint, and J. Goudriaan, “Separating the diffuse and direct component of global radiation and its implications for modeling canopy photosynthesis Part I. Components of incoming radiation,” Agricultural and Forest Meteorology, vol. 38, no. 1–3. Elsevier BV, pp. 217–229, Oct. 1986. doi: 10.1016/0168-1923(86)90060-2.

[A5] J. D. Mondol, Y. G. Yohanis, and B. Norton, “Solar radiation modelling for the simulation of photovoltaic systems,” Renewable Energy, vol. 33, no. 5. Elsevier BV, pp. 1109–1120, May 2008. doi:10.1016/j.renene.2007.06.005.

[A6] T. Muneer and G. S. Saluja, “Correlation between hourly diffuse and global solar irradiation for the UK,” Building Services Engineering Research and Technology, vol. 7, no. 1. SAGE Publications, pp. 37–43, Feb. 1986. doi: 10.1177/014362448600700106

[A7] Ineichen, P., Guisan, O., & Razafindraibe, A. (1984). Indice de clarté. Available from http://www.cuepe.ch/html/biblio/pdf/ineichen1984-indicedeclarte(9).pdf, University of Geneva, Switzerland.

[A8] J. D. Mondol, Y. G. Yohanis, M. Smyth, and B. Norton, “Long-term validated simulation of a building integrated photovoltaic system,” Solar Energy, vol. 78, no. 2. Elsevier BV, pp. 163–176, Feb. 2005. doi: 10.1016/j.solener.2004.04.021.

[A9] T. Muneer, M. M. Hawas, and K. Sahili, “Correlation between hourly diffuse and global radiation for New Delhi,” Energy Conversion and Management, vol. 24, no. 4. Elsevier BV, pp. 265–267, Jan. 1984. doi: 10.1016/0196-8904(84)90004-9.

[A10] H. Bakhsh, R. Srinivasan, and V. Bahel, “Correlation between hourly diffuse and global radiation for Dhahran, Saudi Arabia,” Solar & Wind Technology, vol. 2, no. 1. Elsevier BV, pp. 59–61, Jan. 1985. doi: 10.1016/0741-983x(85)90027-x.

[A11] C.-W. Kuo, W.-C. Chang, and K.-C. Chang, “Modeling the hourly solar diffuse fraction in Taiwan,” Renewable Energy, vol. 66. Elsevier BV, pp. 56–61, Jun. 2014. doi: 10.1016/j.renene.2013.11.072.

[A12] Yao, Wanxiang & Li, Zhengrong & Lu, Yuan & Jiang, Fujian & Li, Cui. (2014). New Models for Separating Hourly Diffuse and Direct Components of Global Solar Radiation. Lecture Notes in Electrical Engineering. 261. 653-663. 10.1007/978-3-642-39584-0-72.

[A13] Bourges, B. (1990). Climatic data handbook for Europe. Netherlands

[A14] J. Chandrasekaran and S. Kumar, “Hourly diffuse fraction correlation at a tropical location,” Solar Energy, vol. 53, no. 6. Elsevier BV, pp. 505–510, Dec. 1994. doi: 10.1016/0038-092x(94)90130-t.

[A15] M. A. C. Chendo and A. A. L. MAEuekwe, “Hourly global and diffuse radiation of Lagos, Nigeria—Correlation with some atmospheric parameters,” Solar Energy, vol. 52, no. 3. Elsevier BV, pp. 247– 251, Mar. 1994. doi: 10.1016/0038-092x(94)90491-x.

[A16] A. A. L. MAEuekwe and M. A. C. Chendo, “Atmospheric turbidity and the diffuse irradiance in Lagos, Nigeria,” Solar Energy, vol. 61, no. 4. Elsevier BV, pp. 241–249, Oct. 1997. doi: 10.1016/s0038-092x(97)00020-0.

[A17] M. Chikh, A. Mahrane, and M. Haddadi, “Modeling the Diffuse Part of the Global Solar Radiation in Algeria,” Energy Procedia, vol. 18. Elsevier BV, pp. 1068–1075, 2012. doi: 10.1016/j.egypro.2012.05.121

[A18] Furlan, C., & de Oliveira, A. P. (2008). Hourly diffuse solar radiation in the presence of clouds and other environmental parameters: the city of São Paulo. Working Paper Series, Instituto de Astronomia, Geofísica e Ciências Atmosféricas, Universidade de São Paulo, Padua.

[A19] M. N. A. Hawlader, “Diffuse, global and extra-terrestrial solar radiation for Singapore,” International Journal of Ambient Energy, vol. 5, no. 1. Informa UK Limited, pp. 31–38, Jan. 1984. doi: 10.1080/01430750.1984.9675406.

[A20] K. G. T. Hollands, “A derivation of the diffuse fraction’s dependence on the clearness index,” Solar Energy, vol. 35, no. 2. Elsevier BV, pp. 131–136, 1985. doi: 10.1016/0038-092x(85)90003-9.

[A21] C. P. Jacovides, J. Boland, D. N. Asimakopoulos, and N. A. Kaltsounides, “Comparing diffuse radiation models with one predictor for partitioning incident PAR radiation into its diffuse component in the eastern Mediterranean basin,” Renewable Energy, vol. 35, no. 8. Elsevier BV, pp. 1820–1827, Aug. 2010. doi: 10.1016/j.renene.2009.11.015.

[A22] S. Karatasou, M. Santamouris, and V. Geros, “Analysis of experimental data on diffuse solar radiation in Athens, Greece, for building applications,” International Journal of Sustainable Energy, vol. 23, no. 1–2. Informa UK Limited, pp. 1–11, Mar. 2003. doi: 10.1080/0142591031000148597.

[A23] J. C. Lam and D. H. W. Li, “Correlation between global solar radiation and its direct and diffuse components,” Building and Environment, vol. 31, no. 6. Elsevier BV, pp. 527–535, Nov. 1996. doi: 10.1016/0360-1323(96)00026-1.

[A24] D. H. W. Li and J. C. Lam, “Analysis of solar heat gain factors using sky clearness index and energy implications,” Energy Conversion and Management, vol. 42, no. 5. Elsevier BV, pp. 555–571, Mar. 2001. doi: 10.1016/s0196-8904(00)00082-0.

[A25] A. Louche, G. Notton, P. Poggi, and G. Simonnot, “Correlations for direct normal and global horizontal irradiation on a French Mediterranean site,” Solar Energy, vol. 46, no. 4. Elsevier BV, pp. 261–266, 1991. doi: 10.1016/0038-092x(91)90072-5.

[A26] Moreno, S., Silva, M., Fernández-Peruchena, C. M., & Pagola, Í. (2009). Comparison of Methodologies to Estimate Direct Normal Irradiation From Daily Values of Global Horizontal Irradiation.

[A27] T. Muneer, S. Younes, and S. Munawwar, “Discourses on solar radiation modeling,” Renewable and Sustainable Energy Reviews, vol. 11, no. 4. Elsevier BV, pp. 551–602, May 2007. doi: 10.1016/j.rser.2005.05.006

[A28] A. P. Oliveira, J. F. Escobedo, A. J. Machado, and J. Soares, “Correlation models of diffuse solarradiation applied to the city of São Paulo, Brazil,” Applied Energy, vol. 71, no. 1. Elsevier BV, pp. 59–73, Jan. 2002. doi: 10.1016/s0306-2619(01)00040-x.

[A29] Pagola, Íñigo & Gastón, Martín & Fernández-Peruchena, Carlos M & Torres, José & Silva, Manuel & Santigosa, L.. (2009). Comparison and fitting of several Global-to_beam irradiance models in Spain.

[A30] A. Pérez-Burgos, J. Bilbao, A. de Miguel, and R. Román, “Analysis of Solar Direct Irradiance in Spain,” Energy Procedia, vol. 57. Elsevier BV, pp. 1070–1076, 2014. doi: 10.1016/j.egypro.2014.10.070.

[A31] R. Posadillo and R. López Luque, “Hourly distributions of the diffuse fraction of global solar irradiation in Córdoba (Spain),” Energy Conversion and Management, vol. 50, no. 2. Elsevier BV, pp. 223–231, Feb. 2009. doi: 10.1016/j.enconman.2008.09.042.

[A32] A. Rerhrhaye, M. Zehaf, and J. Flechon, “Estimation of the direct beam from seasonal correlations,” Renewable Energy, vol. 6, no. 7. Elsevier BV, pp. 779–785, Oct. 1995. doi: 10.1016/0960- 1481(95)00006-6.

[A33] J. A. Ruiz-Arias, H. Alsamamra, J. Tovar-Pescador, and D. Pozo-Vázquez, “Proposal of a regressive model for the hourly diffuse solar radiation under all sky conditions,” Energy Conversion and Management, vol. 51, no. 5. Elsevier BV, pp. 881–893, May 2010. doi: 10.1016/j.enconman.2009.11.024.

[A34] G. Sanchez, “Adapting the Spencer model for diffuse solar radiation in Badajoz (Spain),” Optica Pura y Aplicada, vol. 45, no. 1. Sociedad Espanola de Optica, pp. 5–9, Mar. 15, 2012. doi: 10.7149/opa.45.1.5.

[A35] A. Skartveit and J. A. Olseth, “A model for the diffuse fraction of hourly global radiation,” Solar Energy, vol. 38, no. 4. Elsevier BV, pp. 271–274, 1987. doi: 10.1016/0038-092x(87)90049-1.

[A36] J. Soares, A. P. Oliveira, M. Z. Božnar, P. Mlakar, J. F. Escobedo, and A. J. Machado, “Modeling hourly diffuse solar-radiation in the city of São Paulo using a neural-network technique,” Applied Energy, vol. 79, no. 2. Elsevier BV, pp. 201–214, Oct. 2004. doi: 10.1016/j.apenergy.2003.11.004.

[A37] J. W. Spencer, “A comparison of methods for estimating hourly diffuse solar radiation from global solar radiation,” Solar Energy, vol. 29, no. 1. Elsevier BV, pp. 19–32, 1982. doi: 10.1016/0038-092x(82)90277-8.

[A38] R. Tapakis, S. Michaelides, and A. G. Charalambides, “Computations of diffuse fraction of global irradiance: Part 1 – Analytical modelling,” Solar Energy, vol. 139. Elsevier BV, pp. 711–722, Dec. 2016. doi: 10.1016/j.solener.2014.10.005.

[A39] J. L. Torres, M. De Blas, A. García, and A. de Francisco, “Comparative study of various models in estimating hourly diffuse solar irradiance,” Renewable Energy, vol. 35, no. 6. Elsevier BV, pp. 1325– 1332, Jun. 2010. doi: 10.1016/j.renene.2009.11.025.

[A40] Arttu Tuomiranta and H. Ghedira, “Evaluation of Decomposition and Transposition Models for Irradiance Data Conversion under a Hot Desert Climate,” Unpublished, 2015, doi: 10.13140/RG.2.2.34482.89288.

[A41] K. Ulgen and A. Hepbasli, “Prediction of Solar Radiation Parameters Through Clearness Index for Izmir, Turkey,” Energy Sources, vol. 24, no. 8. Informa UK Limited, pp. 773–785, Aug. 2002. doi: 10.1080/00908310290086680.

[A42] A. de Miguel, J. Bilbao, R. Aguiar, H. Kambezidis, and E. Negro, “Diffuse solar irradiation model evaluation in the North Mediterranean Belt area,” Solar Energy, vol. 70, no. 2. Elsevier BV, pp. 143–153, 2001. doi: 10.1016/s0038-092x(00)00135-3.

[A43] J. F. Orgill and K. G. T. Hollands, “Correlation equation for hourly diffuse radiation on a horizontal surface,” Solar Energy, vol. 19, no. 4. Elsevier BV, pp. 357–359, 1977. doi: 10.1016/0038-092x(77)90006-8.

[A44] D. G. Erbs, S. A. Klein, and J. A. Duffie, “Estimation of the diffuse radiation fraction for hourly, daily and monthly-average global radiation,” Solar Energy, vol. 28, no. 4. Elsevier BV, pp. 293–302, 1982. doi: 10.1016/0038-092x(82)90302-4.

[A45] T. Reindl, W. A. Beckman, and J. A. Duffie, “Diffuse fraction correlations,” Solar Energy, vol. 45, no. 1. Elsevier BV, pp. 1–7, 1990. doi: 10.1016/0038-092x(90)90060-p.

[A46] B. Ridley, J. Boland, and P. Lauret, “Modelling of diffuse solar fraction with multiple predictors,” Renewable Energy, vol. 35, no. 2. Elsevier BV, pp. 478–483, Feb. 2010. doi: 10.1016/j.renene.2009.07.018.

[A47] N. A. Engerer, “Minute resolution estimates of the diffuse fraction of global irradiance for southeastern Australia,” Solar Energy, vol. 116. Elsevier BV, pp. 215–237, Jun. 2015. doi:10.1016/j.solener.2015.04.012.

[A48] E. F. M. Abreu, P. Canhoto, and M. J. Costa, “Prediction of diffuse horizontal irradiance using a new climate zone model,” Renewable and Sustainable Energy Reviews, vol. 110. Elsevier BV, pp. 28–42, Aug. 2019. doi: 10.1016/j.rser.2019.04.055.

[A49] J. M. Bright and N. A. Engerer, “Engerer2: Global re-parameterisation, update, and validation of an irradiance separation model at different temporal resolutions,” Journal of Renewable and Sustainable Energy, vol. 11, no. 3. AIP Publishing, May 01, 2019. doi: 10.1063/1.5097014.

[A50] A. R. Starke, L. F. L. Lemos, J. Boland, J. M. Cardemil, and S. Colle, “Resolution of the cloud enhancement problem for one-minute diffuse radiation prediction,” Renewable Energy, vol. 125. Elsevier BV, pp. 472–484, Sep. 2018. doi: 10.1016/j.renene.2018.02.107.

[A51] E. Paulescu and R. Blaga, “A simple and reliable empirical model with two predictors for estimating 1-minute diffuse fraction,” Solar Energy, vol. 180. Elsevier BV, pp. 75–84, Mar. 2019. doi: 10.1016/j.solener.2019.01.029.

[A52] J. Boland, J. Huang, and B. Ridley, “Decomposing global solar radiation into its direct and diffuse components,” Renewable and Sustainable Energy Reviews, vol. 28. Elsevier BV, pp. 749–756, Dec. 2013. doi: 10.1016/j.rser.2013.08.023.

[A53] J. P. Every, L. Li, and D. G. Dorrell, “Köppen-Geiger climate classification adjustment of the BRL diffuse irradiation model for Australian locations,” Renewable Energy, vol. 147. Elsevier BV, pp. 2453–2469, Mar. 2020. doi: 10.1016/j.renene.2019.09.114.

[A54] D. Yang, “Estimating 1-min beam and diffuse irradiance from the global irradiance: A review and an extensive worldwide comparison of latest separation models at 126 stations,” Renewable and Sustainable Energy Reviews, vol. 159. Elsevier BV, p. 112195, May 2022. doi: 10.1016/j.rser.2022.112195.

[A55] D. Yang et al., “Regime-dependent 1-min irradiance separation model with climatology clustering,” Renewable and Sustainable Energy Reviews, vol. 189. Elsevier BV, p. 113992, Jan. 2024. doi: 10.1016/j.rser.2023.113992.

[A56] J. González and J. Calbó, “INFLUENCE OF THE GLOBAL RADIATION VARIABILITY ON THE HOURLY DIFFUSE FRACTION CORRELATIONS,” Solar Energy, vol. 65, no. 2. Elsevier BV, pp. 119–131, Feb. 1999. doi: 10.1016/s0038-092x(98)00121-2.

The table below presents the outcomes of 104 decomposition models, incorporating both minute-by-minute and hourly input data. It highlights key factors, including temporal resolution, spatial homogeneity, and dataset influence. The numerical values provided represent the Mean Absolute Deviation (MAD) expressed as a percentage (%).

Table A.2: Results of 104 Decomposition Models Highlighting Temporal Resolution, Spatial Homogeneity, and Dataset Influence - A Foundational Framework for Estimating Diffuse Horizontal Irradiance (DHI).

Model	Chilbolton	Camborne	Lerwick	Chilbolton	Camborne	Lerwick
	Minute			Hour Data		
	2022 Dataset			2016 Dataset		
Abreu	15.30	17.49	15.50	14.98	15.20	14.84	15.02
Bakhsh	19.67	23.42	21.27	19.56	16.36	16.53	16.30
Boland 8	21.53	21.25	19.19	18.39	16.83	16.52	16.42
Boland1	19.24	21.58	18.81	17.75	16.06	15.29	15.14
Boland2	20.85	22.24	19.94	19.06	16.00	15.68	15.89
Boland3	19.77	25.25	22.13	18.97	19.09	18.39	15.92
Boland4	23.05	23.00	21.08	20.36	16.86	16.81	17.18
Boland5	19.82	22.07	19.53	18.45	15.88	15.37	15.35
Boland6	19.92	21.95	19.43	18.42	15.88	15.36	15.39
Boland7	22.56	22.29	20.28	19.59	16.67	16.43	16.74
Bourges	18.73	19.03	16.98	16.79	14.71	14.46	15.47

BRL	19.23	19.05	17.17	16.83	14.07	14.02	14.05
chikh1	18.10	19.39	17.67	16.96	14.71	14.76	15.33
chikh2	16.82	21.80	18.98	16.81	16.60	15.86	15.02
chikh3	16.33	21.67	18.88	16.68	16.82	16.04	15.09
CK	21.81	26.66	24.33	21.99	18.37	18.69	17.89
CM1	23.76	29.44	27.25	24.54	20.82	21.42	20.35
CM2	22.94	25.35	23.38	22.29	17.68	18.20	18.78
De Jong	20.73	22.74	18.58	18.39	15.37	14.10	15.55
De Miguel	18.96	19.49	17.76	17.21	14.82	14.91	15.51
Energer2b	14.91	20.28	19.09	15.75	20.26	19.42	15.30
Energer2c	17.26	20.41	15.46	18.52	19.53	15.98	16.83
Energer2d	16.24	16.76	15.21	14.86	14.11	13.81	14.30
Energer2e	16.43	16.91	15.40	14.98	14.17	13.82	14.22
Energer2f	16.73	17.09	15.63	15.13	14.07	13.74	14.10
Energer2g	16.99	17.18	15.66	15.19	14.39	14.00	14.26
Energer2h	17.49	17.38	15.82	15.25	14.36	13.93	14.14
Engerer1	18.18	17.91	16.07	15.42	14.42	13.90	14.10
Engerer2a	23.20	30.31	25.14	24.49	22.27	20.75	22.14
Engerer3	71.89	72.35	72.19	74.97	66.79	70.47	75.13
Erbs	19.06	18.88	17.20	16.76	14.94	14.91	15.58
Every1	22.02	20.06	18.38	18.01	16.11	15.69	15.72
Every2	20.84	19.28	17.51	17.46	16.20	15.38	15.49
FO	34.21	31.96	30.55	29.26	23.56	23.96	23.36
Gonzalez1	19.57	19.38	17.68	17.68	15.02	15.14	16.49
Gonzalez2	85.23	86.13	84.47	83.07	80.06	82.07	82.63
Gonzalez3	16.40	23.50	20.77	17.88	18.97	18.36	16.40
Gonzalez4	19.41	27.20	24.07	20.49	20.85	20.15	17.97
Gonzalez6	15.00	21.84	19.83	17.15	18.91	18.30	16.05
Gonzalez7	16.62	24.09	21.73	18.80	19.78	19.14	16.99
Hawlader	36.65	42.07	42.65	43.84	34.89	38.32	41.87
Hollands	109.95	120.37	123.87	148.07	112.30	121.69	153.11
Ineichen1	17.82	20.21	18.60	17.62	15.11	15.39	15.67
Ineichen2	19.10	21.09	18.51	17.99	14.93	14.51	15.56
Ineichen3	46.02	45.24	42.74	43.95	37.49	38.12	40.68
Jacovides	21.12	22.55	20.81	20.05	16.07	16.57	17.24
Karatasou	22.61	24.64	22.94	22.07	17.61	18.32	18.99
Kuo1	38.30	48.34	45.81	27.86	47.63	46.79	30.43
Kuo2	41.79	52.43	49.18	30.17	50.51	49.43	32.30
Kuo3	19.81	19.59	17.94	17.69	16.02	16.12	16.70

Kuo4	17.46	19.33	17.97	17.18	16.24	16.54	16.46
Lam and Li	19.75	23.12	21.66	20.49	16.98	17.79	17.88
LAM2	30.47	35.11	35.68	36.31	28.61	32.28	34.99
Li And Lam	19.57	21.22	19.88	18.95	15.97	16.37	16.66
Louche	70.53	71.13	55.80	87.69	73.41	50.67	68.04
Mondol 1	16.84	19.71	17.86	16.70	14.90	14.90	14.89
Mondol 2	15.95	20.58	18.64	16.68	15.65	15.71	14.71
Moreno	29.47	27.45	25.68	23.98	21.45	20.80	20.95
Muneer1	19.40	23.33	21.63	19.97	16.87	17.37	17.04
Muneer2	16.10	20.53	18.39	16.38	15.65	15.49	14.57
Muneer3	28.31	37.34	34.18	27.37	31.50	30.57	24.31
Oliveira	21.20	21.12	19.41	19.25	15.84	16.27	17.42
Orgill-Hollands	18.89	19.91	18.01	17.16	15.30	15.27	15.47
Pagola1	22.53	25.40	24.30	23.17	18.97	20.21	20.49
Pagola2	21.58	24.83	23.67	22.64	19.20	20.32	20.59
Paulescu	12.00	14.05	12.87	12.37	13.57	13.63	13.86
Perez-Burgos	101.72	105.98	90.74	129.03	116.94	83.13	101.69
PLL1	54.54	68.20	65.77	61.34	56.38	58.22	57.06
PLL2	510.60	547.20	501.40	403.67	455.07	403.31	306.32
Reindl	20.23	20.81	18.72	18.12	15.30	15.25	15.99
Reindl2	16.52	20.87	19.56	18.51	18.87	18.48	17.67
Rerhrhaye	64.62	77.26	67.79	49.50	71.79	64.70	48.44
Ruiz-Arias1	220.11	246.45	226.95	206.76	184.54	164.89	136.19
Ruiz-Arias2	223.38	267.80	274.72	291.09	248.81	265.50	293.63
Ruiz-Arias3	294.12	321.05	293.35	240.49	260.90	231.37	177.34
Ruiz-Arias4	65.15	78.06	69.09	50.09	72.19	65.56	48.55
Ruiz-Arias5	64.11	77.07	68.26	49.36	70.85	64.45	47.65
Ruiz-Arias6	63.70	76.60	67.78	48.97	70.50	64.08	47.32
Sanchez	31.16	30.86	29.96	29.58	23.73	25.43	26.69
Skartveit	85.05	86.48	84.92	84.88	80.08	82.24	84.30
SM	22.09	22.63	21.50	21.57	17.73	18.72	19.23
Soares	21.62	20.18	18.76	18.22	15.79	16.05	16.61
Spencer	16.29	16.26	14.52	14.60	15.30	14.80	13.93
Starke1	20.28	18.32	16.75	16.86	14.12	14.06	14.01
Starke2	15.24	15.00	13.28	13.97	17.34	15.96	15.20
Starke3	14.44	14.72	12.74	12.79	19.55	17.69	15.81
Tapakis1	20.60	21.87	19.58	19.56	17.06	16.69	17.14
Tapakis2	85.19	86.26	84.73	83.27	80.00	82.13	82.77
Tapakis3	86.44	87.47	85.88	84.98	82.35	84.32	85.06

Torres1	20.90	21.60	20.04	19.43	15.84	16.39	17.09
Torres2	21.59	21.84	20.20	19.71	16.01	16.46	17.17
Torres3	21.63	21.89	20.22	19.73	16.03	16.46	17.18
Torres4	21.47	21.81	20.17	19.67	15.99	16.43	17.15
Tuomiranta1	73.22	86.29	77.43	54.04	80.92	74.41	53.06
Tuomiranta2	71.07	84.01	74.94	52.62	78.53	71.89	51.60
Tuomiranta3	70.57	83.47	74.35	52.23	77.96	71.28	51.22
UH1	30.83	36.53	36.08	35.02	28.89	31.72	32.59
UH2	31.53	37.18	36.81	35.65	29.69	32.74	33.48
Yang4	17.01	14.60	13.75	12.51	26.38	23.87	20.89
Yang5	14.17	14.04	13.23	12.51	23.89	21.79	19.20
Yao1	17.34	23.06	20.28	16.84	19.38	18.70	16.08
Yao2	17.78	23.66	20.60	17.43	19.36	18.55	16.19
Yao3	17.09	23.17	20.00	17.37	20.34	19.15	16.20
Yao4	17.44	23.36	20.43	16.96	20.79	19.93	16.77

Appendix B

The full python script to implement the 104 decomposition models is seen below:

```
# -*- coding: utf-8 -*-

"""

==============================

104 DECOMPOSITION MODEL SCRIPT

==============================

It would be helpful to install the following libraries using pip install:

pip install pandas numpy openpyxl tqdm

"""

import math, os

from pathlib import Path

import numpy as np, pandas as pd

from tqdm import tqdm


DATA_PATH = Path(r"INSERT/YOUR/PATH/HERE")


def phi_series(kt):

    return (kt.shift(1).fillna(method="bfill") + kt.shift(-1).fillna(method="ffill")) / 2


def Energer2a(Kt, altitude, GHI, GHI_clear, ea, AST, zenith_angle):

    kde = max(0,1-(GHI_clear/GHI)); delta_ktc=(GHI_clear/ea)-Kt if ea else 0

    cc,bb0,bb1,bb2,bb3,bb4,bb5=0.042336,-3.7912,7.5479,-0.010036,0.003148,-5.3146,1.7073

    f=cc+(1-cc)/(1+np.exp(bb0+bb1*Kt+bb2*AST+bb3*zenith_angle/180*math.pi+bb4*delta_ktc))+bb5*kde

    return f*GHI


def Energer2b(Kt, altitude, GHI, GHI_clear, ea, AST, zenith_angle):

    kde=max(0,1-(GHI_clear/GHI));delta_ktc=(GHI_clear/ea)-Kt if ea else 0

    c,b0,b1,b2,b3,b4,b5=0.10562,-4.1332,8.2578,0.010087,0.00088801,-4.9302,0.44378

    f=c+(1-c)/(1+np.exp(b0+b1*Kt+b2*AST+b3*zenith_angle/180*math.pi+b4*delta_ktc))+b5*kde

    return f*GHI


def Energer2c(Kt, altitude, GHI, GHI_clear, ea, AST, zenith_angle):

    kde=max(0,1-(GHI_clear/GHI));delta_ktc=(GHI_clear/ea)-Kt if ea else 0

    c,b0,b1,b2,b3,b4,b5=0.093936,-4.5771,8.4641,0.010012,0.003975,-4.3921,0.39331

    f=c+(1-c)/(1+np.exp(b0+b1*Kt+b2*AST+b3*zenith_angle/180*math.pi+b4*delta_ktc))+b5*kde

    return f*GHI
```

```
def Energer2d(Kt, altitude, GHI, GHI_clear, ea, AST, zenith_angle):
    kde=max(0,1-(GHI_clear/GHI));delta_ktc=(GHI_clear/ea)-Kt if ea else 0
    c,b0,b1,b2,b3,b4,b5=0.079965,-4.8539,8.4764,0.018849,0.0051497,-4.1457,0.37466
    f=c+(1-c)/(1+np.exp(b0+b1*Kt+b2*AST+b3*zenith_angle/180*math.pi+b4*delta_ktc))+b5*kde
    return f*GHI

def Energer2e(Kt, altitude, GHI, GHI_clear, ea, AST, zenith_angle):
    kde=max(0,1-(GHI_clear/GHI));delta_ktc=(GHI_clear/ea)-Kt if ea else 0
    c,b0,b1,b2,b3,b4,b5=0.065972,-4.7211,8.3294,0.0095444,0.0053493,-4.169,0.39526
    f=c+(1-c)/(1+np.exp(b0+b1*Kt+b2*AST+b3*zenith_angle/180*math.pi+b4*delta_ktc))+b5*kde
    return f*GHI

def Energer2f(Kt, altitude, GHI, GHI_clear, ea, AST, zenith_angle):
    kde=max(0,1-(GHI_clear/GHI));delta_ktc=(GHI_clear/ea)-Kt if ea else 0
    c,b0,b1,b2,b3,b4,b5=0.032675,-4.8681,8.1867,0.015829,0.0059922,-4.0304,0.47371
    f=c+(1-c)/(1+np.exp(b0+b1*Kt+b2*AST+b3*zenith_angle/180*math.pi+b4*delta_ktc))+b5*kde
    return f*GHI

def Energer2g(Kt, altitude, GHI, GHI_clear, ea, AST, zenith_angle):
    kde=max(0,1-(GHI_clear/GHI));delta_ktc=(GHI_clear/ea)-Kt if ea else 0
    c,b0,b1,b2,b3,b4,b5=-0.0097539,-5.3169,8.5084,0.013241,0.0074356,-3.0329,0.56403
    f=c+(1-c)/(1+np.exp(b0+b1*Kt+b2*AST+b3*zenith_angle/180*math.pi+b4*delta_ktc))+b5*kde
    return f*GHI

def Energer2h(Kt, altitude, GHI, GHI_clear, ea, AST, zenith_angle):
    kde=max(0,1-(GHI_clear/GHI));delta_ktc=(GHI_clear/ea)-Kt if ea else 0
    c,b0,b1,b2,b3,b4,b5=0.32726,-9.4391,17.113,0.13752,-0.024099,6.6257,0.31419
    f=c+(1-c)/(1+np.exp(b0+b1*Kt+b2*AST+b3*zenith_angle/180*math.pi+b4*delta_ktc))+b5*kde
    return f*GHI

def Starke1(Kt, AST, altitude, phi_val, daily_kt, GHI_clear, GHI):
    b=[-6.70407,6.99137,-0.00048,0.03839,3.36003,1.97891,-0.96758,0.15623,-4.21938,-0.00207,-0.06604,2.12613,2.56515,1.62075]
    p1=math.exp(b[0]+b[1]*Kt+b[2]*AST+b[3]*altitude+b[4]*daily_kt+b[5]*phi_val+b[6]*(GHI_clear/277.28))
    p2=math.exp(b[7]+b[8]*Kt+b[9]*AST+b[10]*altitude+b[11]*daily_kt+b[12]*phi_val+b[13]*(GHI_clear/277.28))
    return GHI/(1+p2) if (Kt>0.65 and Kt/GHI_clear>=1.05) else GHI/(1+p1)

def Starke2(Kt, AST, altitude, phi_val, daily_kt, GHI_clear, GHI):
    b=[-6.37505,6.68399,0.01667,0.02552,3.32837,1.97935,-0.74116,0.19486,-3.52376,-0.00325,-0.03737,2.68761,1.60666,1.07129]
    p1=math.exp(b[0]+b[1]*Kt+b[2]*AST+b[3]*altitude+b[4]*daily_kt+b[5]*phi_val+b[6]*(GHI_clear/277.28))
    p2=math.exp(b[7]+b[8]*Kt+b[9]*AST+b[10]*altitude+b[11]*daily_kt+b[12]*phi_val+b[13]*(GHI_clear/277.28))
    return GHI/(1+p2) if (Kt>0.65 and Kt/GHI_clear>=1.05) else GHI/(1+p1)
```

```
def Starke3(Kt, AST, altitude, phi_val, daily_kt, hourly_kt, GHI_clear, GHI):

    b=[-0.083,-3.14711,0.00176,-0.03354,1.40264,0.81353,0.00343,1.95109,-7.28853,7.15225,0.00384,0.02535,2.35926,0.83439,-
0.00327,3.19723]

    p1=math.exp(b[0]+b[1]*Kt+b[2]*AST+b[3]*altitude+b[4]*daily_kt+b[5]*phi_val+b[6]*GHI_clear+b[7]*hourly_kt)

    p2=math.exp(b[8]+b[9]*Kt+b[10]*AST+b[11]*altitude+b[12]*daily_kt+b[13]*phi_val+b[14]*GHI_clear+b[15]*hourly_kt)

    return GHI/(1+p1) if (Kt>=0.75 and Kt/GHI_clear>=1.05) else GHI/(1+p2)



def yang4(Kt, altitude, GHI, GHI_clear, ea, AST, zenith_angle):

    kde=max(0,1-(GHI_clear/GHI));delta_ktc=(GHI_clear/ea)-Kt if ea else 0

    cc,b0,b1,b2,b3,b4,b5,b6=0.042336,-3.7912,7.5479,-0.010036,0.003148,-5.3146,1.7073,0.0361

    d=cc+(1-cc)/(1+np.exp(b0+b1*Kt+b2*AST+b3*zenith_angle/180*math.pi+b4*delta_ktc))+b5*kde

    z=[-0.5744,4.3184,-0.0011,0.004,-4.7952,1.4414,-2.8396]

    f=b6+(1-b6)/(1+np.exp(z[0]+z[1]*Kt+z[2]*AST+z[3]*zenith_angle/180*math.pi+z[4]*delta_ktc+z[6]*d))+z[5]*kde

    return f*GHI



def yang5(Kt, altitude, GHI, GHI_clear, ea, AST, zenith_angle):

    kde=max(0,1-(GHI_clear/GHI));delta_ktc=(GHI_clear/ea)-Kt if ea else 0

    cc,b0,b1,b2,b3,b4,b5=0.042336,-3.7912,7.5479,-0.010036,0.003148,-5.3146,1.7073

    d=cc+(1-cc)/(1+np.exp(b0+b1*Kt+b2*AST+b3*zenith_angle/180*math.pi+b4*delta_ktc))+b5*kde

    z=[0.04294,-1.64437,4.71808,0.01462,0.00745,-3.35223,1.25192,-2.36477]

    f=z[0]+(1-z[0])/(1+np.exp(z[1]+z[2]*Kt+z[3]*AST+z[4]*zenith_angle/180*math.pi+z[5]*delta_ktc+z[7]*d))+z[6]*kde

    return f*GHI



def every_1(Kt, altitude, GHI, AST, phi_val, daily_kt):

    x=-6.862+9.068*Kt+0.01468*AST-0.00472*altitude+1.703*daily_kt+1.084*phi_val

    return GHI/(1+math.exp(x))



def every_2(Kt, altitude, GHI, AST, phi_val, daily_kt):

    x=-6.764+9.958*Kt+0.01271*AST-0.01249*altitude+0.928*daily_kt+1.142*phi_val

    return GHI/(1+math.exp(x))



def Arbeu(Kt,GHI):

    A,B,N=10.79,-5.87,2.24

    y=(A*(Kt-0.5)**2+B*(Kt-0.5)+1)**(-N)

    return GHI*(1+y)**(-1/N)



def paulescu(Kt,daily_kt,GHI):

    b=[1.0119,-0.0316,-0.0294,-1.6567,0.367,1.8982,0.734,-0.8548,0.462]

    i1=1 if Kt>=b[4] else 0;i2=1 if Kt>=b[6] else 0;i3=1 if Kt>=b[8] else 0

    return GHI*(b[0]+b[1]*Kt+b[2]*daily_kt+b[3]*(Kt-b[4])*i1+b[5]*(Kt-b[6])*i2+b[7]*(daily_kt-b[8])*i3)
```

```
def brl(Kt, altitude, GHI, AST, phi_val, mean_Kt):
    x=-5.38+6.63*Kt+0.006*AST-0.007*altitude+1.75*mean_Kt+1.31*phi_val
    return abs(GHI/(1+math.exp(x)))


def _kuo_exp(a):
    try: return math.exp(a)
    except OverflowError: return 0


def Kuo1(Kt_list, altitude, GHI, AST, zenith_angle):
    mean_Kt=sum(Kt_list)/len(Kt_list)
    def _phi(i): return Kt_list[i] if i in (0,len(Kt_list)-1) else (Kt_list[i-1]+Kt_list[i+1])/2
    e=_kuo_exp(-4.5274+5.6956*Kt_list[0]-0.0814*altitude-0.0464*AST+2.4162*mean_Kt+1.0125*_phi(0))
    return GHI/(1+e)


def Kuo2(Kt_list, altitude,GHI,AST,zenith_angle):
    mean_Kt=sum(Kt_list)/len(Kt_list);phi=(Kt_list[0]+Kt_list[min(1,len(Kt_list)-1)])/2
    return GHI/(1+_kuo_exp(-4.5312+5.7627*Kt_list[0]-0.0882*altitude-0.0391*AST+1.9998*mean_Kt+1.1521*phi))


def Kuo3(Kt_list, altitude,GHI,AST,zenith_angle):
    mean_Kt=sum(Kt_list)/len(Kt_list)
    phi=(Kt_list[0]+Kt_list[min(1,len(Kt_list)-1)])/2
    if mean_Kt<0.2: return 0.9885*GHI
    if mean_Kt<=0.3:return (1.0981-0.3769*mean_Kt+0.0233*math.sin(altitude)+0.002*AST-0.1451*mean_Kt-0.1727*phi)*GHI
    if mean_Kt<=0.75:return (1.4185-1.1897*mean_Kt+0.01*math.sin(altitude)+0.0071*AST-0.3891*mean_Kt-0.2181*phi)*GHI
    return 0.1922*GHI


def Kuo4(Kt_list, altitude,GHI,AST,zenith_angle):
    mean_Kt=sum(Kt_list)/len(Kt_list);phi=(Kt_list[0]+Kt_list[min(1,len(Kt_list)-1)])/2
    if mean_Kt<0.2:return 0.9896*GHI
    if mean_Kt<=0.3:return (1.0874-0.3936*mean_Kt+0.0359*math.sin(altitude)+0.0035*AST-0.1899*mean_Kt-0.1253*phi)*GHI
    if mean_Kt<=0.75:return (1.4188-1.2191*mean_Kt+0.015*math.sin(altitude)+0.0063*AST-0.3403*mean_Kt-0.2125*phi)*GHI
    return 0.2775*GHI


def Boland8(Kt_list, altitude,GHI,AST,zenith_angle):
    mean_Kt=sum(Kt_list)/len(Kt_list);phi=(Kt_list[0]+Kt_list[min(1,len(Kt_list)-1)])/2
    e=_kuo_exp(-7.75*Kt_list[0]-1.185*mean_Kt-1.05*phi-0.004*AST+0.003*altitude)
    dni=(0.02628/(0.006+4.374*e))*1000/3.6
    return abs(dni*math.cos(math.radians(zenith_angle))-GHI)


def baksh(Kt,GHI):
    return (1-0.22*Kt)*GHI if Kt<=0.23 else (1.235-1.26*Kt)*GHI if Kt<0.80 else 0.225*GHI
```

```
def chikh1(Kt, GHI):
    if Kt <= 0.175:
        return (1-0.3*Kt)*GHI
    elif Kt > 0.175 and Kt < 0.87:
        return (1.137 - 1.077*Kt) * GHI
    else:
        return (0.2043) * GHI


def chikh2(Kt, GHI):
    if Kt <= 0.175:
        return (1-0.64*Kt)*GHI
    elif Kt > 0.175 and Kt < 0.87:
        return (1.052 - 0.935*Kt) * GHI
    else:
        return (0.24) * GHI


def chikh3(Kt, GHI):
    if Kt <= 0.175:
        return (1-0.232*Kt)*GHI
    elif Kt > 0.175 and Kt < 0.87:
        return (1.17 - 1.23*Kt) * GHI
    else:
        return (0.203) * GHI


def LAM2(Kt, GHI):
    if Kt <= 0.15:
        return (0.974*Kt)*GHI
    elif Kt > 0.15 and Kt < 0.70:
        return (1.192 - 1.394*Kt) * GHI
    else:
        return (0.259) * GHI


def Mondol1(Kt, GHI):
    if Kt <= 0.20:
        return (0.98)*GHI
    else:
        return (0.5836 + 3.6259*Kt - 10.171*Kt*Kt+6.338*Kt*Kt*Kt) * GHI


def Mondol2(Kt, GHI, zenith_angle):
    if Kt <= 0.20:
        return(GHI*0.98)
    elif Kt > 0.20 and Kt <= 0.70:
```

```
        return(GHI * (0.61092 + 3.6259*Kt - 10.171*Kt*Kt + 6.338*Kt*Kt*Kt))
    else:
        return(GHI * (0.672 - 0.474*Kt))


def Muneer1(Kt, GHI):
    if Kt <= 0.175:
        return 0.95 * GHI
    elif Kt <= 0.755:
        return (0.9698 + 0.4353 * Kt - 3.4499 * Kt**2 + 2.1888 * Kt**3) * GHI
    else:
        return 0.26 * GHI


def Muneer2(Kt, GHI):
    if Kt <= 0.20:
        return (0.98)*GHI
    else:
        return (0.687+2.932*Kt-8.546*Kt*Kt + 5.277*Kt*Kt*Kt) * GHI


def PerezBurgos(Kt, GHI, zenith_angle):
    k = 0.0909 + 594.67*Kt - 3796.1*Kt*Kt + 5837.3*Kt*Kt*Kt
    return (GHI - k)


def Rerhrhaye(Kt, GHI, zenith_angle):
    k = 1/math.cos(math.radians(zenith_angle))
    if Kt <0.12:
        return GHI
    else:
        return GHI -k*(0.16 - 1.19*Kt + 2.25*Kt*Kt)


def DeJong(Kt, GHI, altitude):
    r = 0.847 - 1.61*math.sin(math.radians(altitude))
    x = ((1.47 - r)/1.66)
    if Kt <= 0.22:
        return GHI
    elif Kt > 0.22 and Kt <= 0.35:
        return GHI*(1-6.4*(Kt-0.22)**2)
    elif Kt > 0.35 and Kt <=x:
        return GHI*(1.47-1.66*Kt)
    else:
        return GHI*r
```

```
def Tuomiranta3(Kt, GHI, zenith_angle):
    m = 1.0 / (math.cos(math.radians(zenith_angle)) + 0.50572*((96.07995 - zenith_angle)**-1.6364))
    kt_mod = Kt / (1.031 * math.exp(-1.4/0.9 + (9.4/m)) + 0.1)
    if kt_mod <= 0.46:
        return GHI*(1.055 - 0.241*kt_mod)
    elif kt_mod > 0.46 and kt_mod <= 0.77:
        return (0.866+1.598*kt_mod - 3.102 *kt_mod*kt_mod) * GHI
    else:
        return 0.257*GHI


def Tuomiranta1(Kt, GHI, zenith_angle):
    m = 1.0 / (math.cos(math.radians(zenith_angle)) + 0.50572*((96.07995 - zenith_angle)**-1.6364))
    kt_mod = Kt / (1.031 * math.exp(-1.4/0.9 + (9.4/m)) + 0.1)
    if kt_mod <= 0.49:
        return GHI*(1.08 - 0.367*kt_mod)
    elif kt_mod > 0.49 and kt_mod <= 0.76:
        return (2.162-2.717*kt_mod + 0.288 *kt_mod*kt_mod) * GHI
    else:
        return 0.264*GHI


def Tuomiranta2(Kt, GHI, zenith_angle):
    m = 1.0 / (math.cos(math.radians(zenith_angle)) + 0.50572*((96.07995 - zenith_angle)**-1.6364))
    kt_mod = Kt / (1.031 * math.exp(-1.4/0.9 + (9.4/m)) + 0.1)
    if kt_mod <= 0.48:
        return GHI*(1.06 - 0.271*kt_mod)
    elif kt_mod > 0.48 and kt_mod <= 0.77:
        return (1.072+0.989*kt_mod - 2.674 *kt_mod*kt_mod) * GHI
    else:
        return 0.247*GHI


def chandraskaran_kumar(Kt, GHI):
    if Kt <= 0.24:
        return (1.0086 - 0.178*Kt)*GHI
    elif Kt > 0.24 and Kt < 0.80:
        return (0.9686 + 0.1325*Kt + 1.4183*Kt*Kt - 10.1862*Kt*Kt*Kt + 8.3733*Kt*Kt*Kt*Kt) * GHI
    else:
        return (0.197) * GHI


def erbs(Kt, GHI):
    if Kt <= 0.22:
        return (1 - 0.09*Kt) * GHI
    elif Kt > 0.22 and Kt <= 0.80:
```

```
        return (0.9511 - 0.1604*Kt + 4.388*Kt*Kt - 16.638*Kt*Kt*Kt + 12.336*Kt*Kt*Kt*Kt) * GHI

    else:

        return 0.165 * GHI


def hawlader(Kt, GHI):

    if Kt < 0.225:

        return 0.915 * GHI * Kt

    elif Kt >= 0.225 and Kt < 0.775:

        return (1.1389 - 0.9422*Kt - 0.3878*Kt*Kt) * GHI

    else:

        return 0.215 * GHI


def jacovides(Kt, GHI):

    if Kt <= 0.1:

        return 0.987 * GHI

    elif Kt > 0.1 and Kt <= 0.8:

        return (0.94 + 0.937*Kt - 5.01*Kt*Kt + 3.32*Kt*Kt*Kt) * GHI

    else:

        return 0.177 * GHI


def karatasou(Kt, GHI):

    if Kt <= 0.78:

        return (0.9995 - 0.05*Kt - 2.4156*Kt*Kt + 1.4926*Kt*Kt*Kt) * GHI

    else:

        return 0.2 * GHI


def lam_and_li(Kt, GHI):

    if Kt <= 0.15:

        return 0.977 * GHI

    elif Kt > 0.15 and Kt <= 0.70:

        return (1.237 - 1.361*Kt) * GHI

    else:

        return 0.273 * GHI

def louche(Kt, GHI, zenith_angle):

    return GHI - (((-10.7676*Kt**5 + 15.307*Kt**4 - 5.205*Kt**3 + 0.99*Kt**2 - 0.059*Kt + 0.02) * GHI) /
math.cos(math.radians(zenith_angle)))
```

```
def orgill_and_hollands(Kt, GHI):
    if Kt <= 0.35:
        return (1 - 0.249*Kt) * GHI
    elif Kt <= 0.75:
        return (1.577 - 1.84*Kt) * GHI
    else:
        return 0.177 * GHI


def Hollands(Kt, GHI):
    a_holl = 1.115
    b_holl = 0.491
    if Kt >= 0 and GHI > 0:
        expr = (1-b_holl)**2 - 4*a_holl*b_holl*Kt*(1-a_holl*Kt)
        if expr >= 0:
            return GHI*(1 - b_holl - math.sqrt(expr)/(2*a_holl*b_holl*Kt))
        else:
            return 0
    else:
        return 0


def Bourges(Kt, GHI):
    if Kt <= 0.20:
        return GHI
    elif Kt > 0.20 and Kt <= 0.35:
        return (1.116 - 0.580*Kt) * GHI
    elif Kt > 0.35 and Kt <= 0.75:
        return (1.557 - 1.840*Kt) * GHI
    else:
        return 0.177 * GHI


def boland1(Kt, GHI):
    return GHI / (1 + np.exp(8.645 * (Kt - 0.613)))


def boland2(Kt, GHI):
    return GHI / (1 + np.exp(7.997 * (Kt - 0.586)))


def boland3(Kt, GHI):
    return GHI / (1 + np.exp(-4.38  + 6.62*Kt))


def boland4(Kt, GHI):
    return GHI / (1 + np.exp(-4.53  + 8.05*Kt))
```

```
def boland5(Kt, GHI):
    return GHI / (1 + np.exp(-4.80  + 7.98*Kt))


def boland6(Kt, GHI):
    return GHI / (1 + np.exp(-4.87  + 8.12*Kt))


def boland7(Kt, GHI):
    return GHI / (1 + np.exp(-4.94 + 8.66*Kt))


def reindl(Kt, GHI):
    if Kt <= 0.3:
        return (1.02 - 0.248 * Kt) * GHI
    elif Kt > 0.3 and Kt <=0.78:
        return (1.45 - 1.67 * Kt) * GHI
    else:
        return 0.147 * GHI


def De_Miguel(Kt, GHI):
    if Kt <= 0.21:
        return (0.995 - 0.081*Kt)* GHI
    elif Kt > 0.21 and Kt <= 0.76:
        return (0.724 + 2.738*Kt - 8.320*Kt*Kt + 4.967*Kt*Kt*Kt) * GHI
    else:
        return 0.180 * GHI


def Li_And_Lam(Kt, GHI):
    if Kt <= 0.15:
        return (0.976)* GHI
    elif Kt > 0.15 and Kt <= 0.70:
        return (0.996 + 0.036*Kt - 1.589*Kt*Kt) * GHI
    else:
        return 0.230 * GHI


def Spencer(Kt, GHI):
    if Kt < 0.3:
        return 0.97975 * GHI
    elif Kt >= 0.3 and Kt <= 0.75:
        return (1.5418 - 1.8735*Kt) * GHI
    else:
        return 0.136675 * GHI
```

```
def Ineichen1(Kt, GHI):
    if Kt < 0.15:
        return 0.98 * GHI
    else:
        return (0.8 + 2.25*Kt - 7.93*Kt*Kt + 5.26*Kt*Kt*Kt)*GHI


def Ineichen2(Kt, GHI):
    if Kt < 0.25:
        return GHI
    elif Kt >= 0.25 and Kt <= 0.80:
        return (1.38 - 1.52*Kt) * GHI
    else:
        return (0.16)*GHI


def Ineichen3(Kt, GHI):
    if Kt < 0.25:
        return GHI
    else:
        return (1.28*Kt - 1.40*Kt*Kt)*GHI


def reindl2(Kt, GHI, altitude):
    if Kt <= 0.3:
        return (1.02 - 0.254 * Kt + 0.0123 * math.sin(math.radians(altitude))) * GHI
    elif Kt > 0.3 and Kt <=0.78:
        return (1.4 - 1.749 * Kt + 0.177 * math.sin(math.radians(altitude))) * GHI
    else:
        return (0.486 * GHI - 0.182 * math.sin(math.radians(altitude)))


def oliveira(Kt, GHI):
    if Kt <= 0.17:
        return GHI
    elif Kt > 0.17 and Kt < 0.75:
        return (0.97 + 0.8 * Kt - 3 * Kt**2 - 3.1 * Kt**3 + 5.2 * Kt**4) * GHI
    else:
        return 0.17 * GHI
```

```
def Ulgen_And_Hepbasli1(Kt, GHI):
    if Kt <= 0.32:
        return 0.68*GHI
    elif Kt > 0.32 and Kt < 0.62:
        return (1.0609 - 1.2138*Kt) * GHI
    else:
        return 0.30 * GHI


def Ulgen_And_Hepbasli2(Kt, GHI):
    if Kt <= 0.32:
        return 0.68*GHI
    elif Kt > 0.32 and Kt < 0.62:
        return (0.0743 - 19.3430*Kt + 206.91*Kt*Kt - 719.72*Kt*Kt*Kt + 1053.4 *Kt*Kt*Kt*Kt- 562.69*Kt*Kt*Kt*Kt*Kt) * GHI
    else:
        return 0.30 * GHI


def soares(Kt,GHI):
        return (0.9 + 1.1 * Kt - 4.5 * Kt**2 + 0.01 * Kt**3 + 3.14 * Kt**4) * GHI


def chendo_and_maduekwe1(Kt, GHI):
     if Kt <= 0.30:
         return (1.022 -0.156*Kt)*GHI
     elif Kt > 0.30 and Kt < 0.80:
         return (1.385 - 1.396*Kt) * GHI
     else:
         return (0.264) * GHI


def chendo_and_maduekwe2(Kt, GHI):
     if Kt <= 0.30:
         return (1.021 -0.151*Kt)*GHI
     elif Kt > 0.30 and Kt < 0.80:
         return (1.385 - 1.396*Kt) * GHI
     else:
         return (0.295) * GHI


def Furlan_and_Oliveira(Kt, GHI):
     if Kt <= 0.228:
         return (0.961)*GHI
     else:
         return (1.337 - 1.650*Kt) * GHI
```

```
def Moreno(Kt, GHI):
     if Kt <= 0.20:
         return (0.9930)*GHI
     elif Kt > 0.20 and Kt < 0.70:
         return (1.4946 - 1.7899*Kt)*GHI
     else:
         return (0.045) * GHI


def Pagola1(Kt, GHI):
     if Kt <= 0.35:
         return (0.9818 - 0.5870*Kt)*GHI
     elif Kt > 0.35 and Kt < 0.75:
         return (1.2056 - 1.3240*Kt)*GHI
     else:
         return (0.2552) * GHI


def Pagola2(Kt, GHI):
      if Kt <= 0.22:
          return (0.9522 - 0.3119*Kt)*GHI
      elif Kt > 0.22 and Kt < 0.80:
          return (0.6059 + 2.987*Kt - 10.5675*Kt**2 +10.1833*Kt**3 - 3.0475*Kt**4)*GHI
      else:
          return (0.3209) * GHI


def Posadillo_Lopez1(Kt, GHI):
    return (Kt*1.77 - 1.381*Kt*Kt) * GHI


def Posadillo_Lopez2(Kt, GHI):
    return (-0.00829 + 1.163*Kt + 0.433*Kt*Kt + 5.839*Kt*Kt*Kt + 4.6488*Kt*Kt*Kt*Kt)*GHI


def Ruiz_Arias1(Kt, GHI):
    return (0.086 + 0.88*math.exp(-3.877 + 6.138*Kt))*GHI


def Ruiz_Arias2(Kt, GHI):
    return (0.967 - 1.024*math.exp(2.473 - 5.324*Kt))*GHI


def Ruiz_Arias3(Kt, GHI):
    return (0.140 + 0.962*math.exp(-1.976 + 4.067*Kt))*GHI


def Ruiz_Arias4(Kt, GHI):
    return (1.001 - 1*math.exp(-2.45 -5.048*Kt))*GHI
```

```
def Ruiz_Arias5(Kt, GHI):

    return (0.988 - 1*math.exp(-2.456 -5.172*Kt))*GHI


def Ruiz_Arias6(Kt, GHI):

          return (0.985 - 0.962*math.exp(-2.655 - 6.003*Kt))*GHI


def Torres1(Kt, GHI):

      if Kt <= 0.24:

          return (1.0058 - 0.2195*Kt)*GHI

      elif Kt > 0.24 and Kt < 0.75:

          return (1.3264 - 1.5120*Kt)*GHI

      else:

          return (0.1923) * GHI


def Torres2(Kt, GHI):

      if Kt <= 0.22:

          return (0.9920 - 0.0980*Kt)*GHI

      elif Kt > 0.22 and Kt < 0.75:

          return (1.2158 - 1.0467*Kt - 0.448*Kt*Kt)*GHI

      else:

          return 0.1787*GHI


def Torres3(Kt, GHI):

      if Kt <= 0.225:

          return (0.9923 - 0.0980*Kt)*GHI

      elif Kt > 0.225 and Kt < 0.755:

          return (1.1459 - 0.5612*Kt - 1.4952*Kt*Kt + 0.7103*Kt*Kt*Kt)*GHI

      else:

          return 0.1755*GHI


def Torres4(Kt, GHI):

      if Kt <= 0.225:

          return (0.9943 - 0.1165*Kt)*GHI

      elif Kt > 0.225 and Kt < 0.755:

          return (1.4101 - 2.9918*Kt + 6.4599*Kt*Kt -10.329*Kt*Kt*Kt + 5.5140*Kt*Kt*Kt*Kt)*GHI

      else:

          return 0.18*GHI
```

```
def Sanchez(Kt, GHI):
      if Kt < 0.3:
          return (0.78)*GHI
      elif Kt >= 0.30 and Kt <= 0.75:
          return (1.23 - 1.43*Kt)*GHI
      else:
          return 0.13*GHI
def Tapakis1(Kt, GHI):
      if Kt < 0.10:
          return (0.91 + 2.4993*Kt - 18.858*Kt*Kt)*GHI
      elif Kt >= 0.10 and Kt <= 0.78:
          return (0.9605 + 0.4482*Kt - 2.0011*Kt*Kt - 1.5581*Kt*Kt*Kt + 2.008*Kt*Kt*Kt*Kt)*GHI
      else:
          return (-2.4518 + 3.3014*Kt)*GHI
def Tapakis2(Kt, altitude, GHI):
    if altitude >= 5 and altitude < 10:
        return GHI*(-246.06*Kt**5 + 412.05*Kt**4 -236.59*Kt**3 +53.9*Kt**2 -4.72*Kt +1.10)
    elif altitude >= 10 and altitude < 15:
        return GHI*(-94.4*Kt**5 + 189.87*Kt**4 -127.29*Kt**3 +32.63*Kt**2 -3.29*Kt +1.08)
    elif altitude >= 15 and altitude < 20:
        return GHI*(-36.9*Kt**5 + 94.73*Kt**4 -75.34*Kt**3 +21.23*Kt**2 -2.24*Kt +1.05)
    elif altitude >= 20 and altitude < 25:
        return GHI*(84.95*Kt**5 -114.34*Kt**4 +49.34*Kt**3 -9.50*Kt**2 +0.66*Kt +0.98)
    elif altitude >= 25 and altitude < 30:
        return GHI*(40.61*Kt**5 -52.24*Kt**4 + 18.70*Kt**3 -2.99*Kt**2 +0.10*Kt +0.99)
    elif altitude >= 30 and altitude < 35:
        return GHI*(63.53*Kt**5 -104.96*Kt**4 +59.07*Kt**3 -15.34*Kt**2 +1.52*Kt +0.95)
    elif altitude >= 35 and altitude < 40:
        return GHI*(56.06*Kt**5 + -100.60*Kt**4 +64.47*Kt**3 -20.02*Kt**2 +2.51*Kt +0.89)
    elif altitude >= 40 and altitude < 45:
        return GHI*(28.16*Kt**5 -43.96*Kt**4 +22.34*Kt**3 -6.29*Kt**2 +0.71*Kt +0.96)
    elif altitude >= 45 and altitude < 50:
        return GHI*(39.69*Kt**5 -72.72*Kt**4 +47.24*Kt**3 -15.05*Kt**2 +1.77*Kt +0.93)
    elif altitude >= 50 and altitude < 55:
        return GHI*(15.59*Kt**5 -33.36*Kt**4 +28.09*Kt**3 -12.80*Kt**2 +1.92*Kt +0.91)
    elif altitude >= 55 and altitude < 60:
        return GHI*(26.66*Kt**5 -46.68*Kt**4 +29.02*Kt**3 -9.99*Kt**2 +1.36*Kt +0.93)
    elif altitude >= 60 and altitude < 65:
        return GHI*(69.77*Kt**5 -163.83*Kt**4 +142.13*Kt**3 -56.08*Kt**2 +8.58*Kt +0.57)
    elif altitude >= 65 and altitude < 70:
        return GHI*(19.27*Kt**5 -37.50*Kt**4 +26.92*Kt**3 -10.47*Kt**2 +1.38*Kt +0.93)
    else:
```

```
        return GHI*(43.02*Kt**5 -93.20*Kt**4 +72.92*Kt**3 -25.81*Kt*Kt +3.06*Kt +0.88)


def Tapakis3(Kt, altitude, GHI):

      if Kt < 0.32:

          return (7.37/(7.52 + math.exp(-13.57 + 64.94*Kt + -22.06*Kt**2 -71.73*altitude*math.pi/180 +6.97*Kt*altitude*math.pi/180)))*GHI

      elif Kt >= 0.32 and Kt <= 0.63:

          return (5.11/(3.91 + math.exp(-0.07 + 1.67*Kt +0.94*Kt**2 + 2.90*altitude*math.pi/180 -0.50*Kt*altitude*math.pi/180)))*GHI

      else:

          return (11.7 / (29.85 + math.exp(-83.28 + 241.32*Kt +21.06*Kt**2 -168.56*altitude*math.pi/180 -
14.84*Kt*altitude*math.pi/180))) * GHI



def Suehrcke_McCormick(Kt, GHI, zenith_angle):

    m = 1/((math.cos(math.radians(zenith_angle)) + 0.50572*(96.07995 - zenith_angle)**-1.6364))

    kc = 0.877*math.exp(-0.0933*m)

    dc = 0.0366 + 0.0477*m

    if Kt <= kc:

        return (1-(1-dc)*(Kt/kc)**4.4)*GHI

    else:

        return ((kc*dc + (Kt-kc))/Kt)*GHI



def Skartveit1(Kt, altitude, GHI):

    k1 = 0.87 - 0.56 * math.exp(-0.06 * altitude)

    alpha = 1.09

    d1 = 0.15 + 0.43 * math.exp(-0.06 * altitude)

    a = 0.27

    b = 0

    inside = (Kt - 0.2) / (k1 - 0.2)

    K = 0.5 * (1 + math.sin(math.radians(math.pi * (inside - 0.5))))

    if Kt <= 0.2:

        return GHI

    elif Kt > 0.3 and Kt <= 1.09 * k1:

        return GHI * ((1 - (1 - d1) * (a * math.sqrt(K) + b * K + (1 - a - b) * (K) * (K))))

    else:

        return 1 - (alpha * k1 * (1 - (1 - d1) * (a * math.sqrt(K) + b * K + (1 - a - b) * (K) * (K)))) / Kt
```

```
def Engerer1(Kt, altitude, GHI, GHI_clear, ea, AST, zenith_angle):
    kde = max(0, 1 - (GHI_clear / GHI))
    if ea != 0:
        delta_ktc = (GHI_clear / ea) - Kt
    else:
        # Handle the case when ea is zero
        # Return 0 as the default value
        return 0
    C = 0.1527
    b0 = -4.1092
    b1 = 6.1661
    b2 = -0.0022304
    b3 = 0.011026
    b4 = -4.3314
    b5 = 0
    return (C + ((1 + C) / (1 + math.exp(b0 + b1 * Kt + b2 * AST + b3 * zenith_angle + b4 * delta_ktc))) + b5 * kde) * GHI
def Engerer2(Kt, altitude, GHI, GHI_clear,ea, AST, zenith_angle):
    kde = max(0,1-(GHI_clear/GHI))
    if ea != 0:
        delta_ktc = (GHI_clear / ea) - Kt
    else:
        # Handle the case when ea is zero
        # Return 0 as the default value
        return 0
    C = 0.042336
    b0 = -3.7912
    b1 = 7.5479
    b2 = -0.010036
    b3 = 0.003148
    b4 = -5.3146
    b5 = 1.7073
    return (C+((1+C)/(1 + math.exp(b0 + b1*Kt+ b2*AST + b3*zenith_angle + b4*delta_ktc))) + b5*kde)*GHI
def Engerer3(Kt, altitude, GHI, GHI_clear,ea, AST, zenith_angle):
    kde = max(0,1-(GHI_clear/GHI))
    if ea != 0:
        delta_ktc = (GHI_clear / ea) - Kt
    else:
        # Handle the case when ea is zero
        # Return 0 as the default value
        return 0
    C = 0.1090
    b0 = -0.020506
```

```
    b1 = 8.1249
    b2 = -0.036234
    b3 = 0.041397
    b4 = -5.1045
    b5 = 0
    return (C+((1+C)/(1 + math.exp(b0 + b1*Kt+ b2*AST + b3*zenith_angle + b4*delta_ktc))) + b5*kde)*GHI


def Gonzalez4(GHI, Kt, zenith_angle):
    m = 1/((math.cos(math.radians(zenith_angle)) + 0.50572*(96.07995 - zenith_angle)**-1.6364))
    zeta = 0.124 - 0.0285*math.log(m)
    fm = 0.229 + 0.957*math.exp(-1.74*zeta*m)
    if fm <= 0.0001:
        return GHI
    kt_dash = Kt/fm
    if kt_dash <= 0:
        return GHI
    delta2 = math.log(kt_dash)/kt_dash
    if Kt <= 0.25:
        return GHI
    elif Kt > 0.25 and Kt < 0.75:
        return GHI * (1.409 - 1.431*Kt + 0.0382*delta2)
    else:
        return GHI * (0.49 -0.065*Kt - 0.0562*delta2)


def Gonzalez7(Kt, altitude, GHI, zenith_angle):
    m = 1/((math.cos(math.radians(zenith_angle)) + 0.50572*(96.07995 - zenith_angle)**-1.6364))
    zeta = 0.124 - 0.0285*math.log(m)
    fm = 0.229 + 0.957*math.exp(-1.74*zeta*m)
    kt_dash = Kt/fm
    if kt_dash <= 0:
        return GHI
    delta2 = math.log(kt_dash)/kt_dash
    if Kt <= 0.25:
        return GHI
    elif Kt > 0.25 and Kt < 0.75:
        return GHI * (1.386 -1.586*Kt + 0.181*math.sin(math.radians(altitude)) + 0.032*delta2)
    else:
        return GHI * (0.528 - 0.087*Kt - 0.019*math.sin(math.radians(altitude)) + 0.0557*delta2)


def Gonzalez1(Kt, GHI):
    if Kt <= 0.25:
        return GHI
```

```
    elif Kt > 0.25 and Kt < 0.75:
        return GHI * (1.421 - 1.670*Kt)
    else:
        return GHI * (-0.043 + 0.290*Kt)


def Gonzalez2(Kt, GHI, altitude):
    if Kt <= 0.25:
        return GHI
    elif Kt > 0.25 and Kt < 0.75:
        return GHI * (1.391 - 1.812*Kt + 0.219*math.sin(math.radians(altitude)))
    else:
        return GHI * (0.123 +0.164*Kt - 0.094*math.sin(math.radians(altitude)))


def Gonzalez3(Kt, altitude, GHI, zenith_angle):
    m = 1/((math.cos(math.radians(zenith_angle)) + 0.50572*(96.07995 - zenith_angle)**-1.6364))
    zeta = 0.124 - 0.0285*math.log(m)
    fm = 0.229 + 0.957*math.exp(-1.74*zeta*m)
    if fm == 0:
        return GHI
    kt_dash = abs(Kt/fm)
    if kt_dash == 0:
        return GHI
    std = math.sqrt(kt_dash)
    delta1 = math.log(std/kt_dash)
    if Kt <= 0.25:
        return GHI
    elif Kt > 0.25 and Kt < 0.75:
        return GHI * (1.381 - 1.432*Kt + 0.0352*delta1)
    else:
        return GHI * (0.607 - 0.242*Kt + 0.0549*delta1)


def Gonzalez6(Kt, altitude, GHI, zenith_angle):
    m = 1/((math.cos(math.radians(zenith_angle)) + 0.50572*(96.07995 - zenith_angle)**-1.6364))
    zeta = 0.124 - 0.0285*math.log(m)
    fm = 0.229 + 0.957*math.exp(-1.74*zeta*m)
    if abs(fm) <= 0.0001:
        return GHI
    kt_dash = abs(Kt/fm)
    std = math.sqrt(kt_dash)
    if kt_dash <= 0:
        return GHI
    delta1 = math.log(std/kt_dash)
```

```
    if Kt <= 0.25:
        return GHI
    elif Kt > 0.25 and Kt < 0.75:
        return GHI * (1.361 - 1.593*Kt + 0.193*math.sin(math.radians(altitude)) + 0.02985*delta1)
    else:
        return GHI * (0.598 - 0.235*Kt +0.007*math.sin(math.radians(altitude)) + 0.0551*delta1)


# Yao 3 --> MBD -0.37%
def Yao3(Kt, GHI, zenith_angle):
    if Kt <= 0.20:
        return(GHI*(0.8775 + 1.3991*Kt - 4.9285*Kt*Kt))
    else:
        return(GHI*(1.1209 - 2.1699*Kt + 11.06*Kt*Kt - 22.355*Kt*Kt*Kt + 12.863*Kt*Kt*Kt*Kt))


# Yao 4 --> MBD 2.73%
def Yao4(Kt, GHI, zenith_angle):
    dhi_4 = (0.2421 + 0.7202/(1+math.exp((Kt-0.6203)/0.0749))) * GHI
    return dhi_4


# Yao 2 --> MBD 3.84%
def Yao2(Kt, GHI, zenith_angle):
    dhi_2 = (0.8142 + 2.0792*Kt - 6.1439*Kt**2 + 3.4707*Kt**3) * GHI
    return dhi_2


# Yao 1 --> MBD 4.58%
def Yao1(Kt, GHI, zenith_angle):
    dhi1 = (0.9381 + 0.1481*Kt)*GHI
    dhi2 = (1.5197 - 1.534*Kt)*GHI
    dhi3 = (0.27*GHI)
    if Kt <= 0.30:
        return dhi1
    elif Kt > 0.30 and Kt < 0.80:
        return dhi2
    else:
        return dhi3


def muneer3(Kt, GHI, zenith_angle, declination):
    m = 1 / (math.cos(math.radians(zenith_angle)) + 0.50572 * (96.07995 - zenith_angle) ** -1.6364)
    sf = (2 / 15) * math.acos(-math.tan(math.radians(51.145101)) * math.tan(math.radians(declination)))
    return GHI * ((0.899 - 0.683 * sf + 0.648 * sf ** 2 + 0.028 * m - 0.002 * m * m) +
                  (0.88 - 0.666 * sf - 0.314 * sf ** 2 - 0.158 * m + 0.003 * m * m) * Kt +
                  (-1.751 + 2.786 * sf - 1.924 * sf ** 2 + 0.044 * m + 0.012*m*m) * Kt * Kt)
```

```
MODELS={

"Energer2a":Energer2a,"Energer2b":Energer2b,"Energer2c":Energer2c,"Energer2d":Energer2d,

"Energer2e":Energer2e,"Energer2f":Energer2f,"Energer2g":Energer2g,"Energer2h":Energer2h,

"Starke1":Starke1,"Starke2":Starke2,"Starke3":Starke3,

"Yang4":yang4,"Yang5":yang5,

"Every1":every_1,"Every2":every_2,"Arbeu":Arbeu,"Paulescu":paulescu,

"BRL":lambda **r: brl(r['Kt'],r['altitude'],r['GHI'],r['AST'],r['Phi'],r['mean_Kt']),

"Kuo1"                    :lambda **r: Kuo1([r['Kt']],r['altitude'],r['GHI'],r['AST'],r['zenith_angle']),

"Kuo2"                    :lambda **r: Kuo2([r['Kt']],r['altitude'],r['GHI'],r['AST'],r['zenith_angle']),

"Kuo3"                    :lambda **r: Kuo3([r['Kt']],r['altitude'],r['GHI'],r['AST'],r['zenith_angle']),

"Kuo4"                    :lambda **r: Kuo4([r['Kt']],r['altitude'],r['GHI'],r['AST'],r['zenith_angle']),

"Boland8"                 :lambda **r: Boland8([r['Kt']],r['altitude'],r['GHI'],r['AST'],r['zenith_angle']),

"baksh"                   :lambda **r: baksh(r['Kt'],r['GHI']),

"chikh1"         : lambda **r: chikh1(r["Kt"], r["GHI"]),

"chikh2"         : lambda **r: chikh2(r["Kt"], r["GHI"]),

"chikh3"                  : lambda **r: chikh3(r["Kt"], r["GHI"]),

"LAM2"                    : lambda **r: LAM2(r["Kt"], r["GHI"]),

"Mondol1"                 : lambda **r: Mondol1(r["Kt"], r["GHI"]),

"Muneer1"                 : lambda **r: Muneer1(r["Kt"], r["GHI"]),

"Muneer2"                 : lambda **r: Muneer2(r["Kt"], r["GHI"]),

"chandraskaran_kumar"     : lambda **r: chandraskaran_kumar(r["Kt"], r["GHI"]),

"erbs"                    : lambda **r: erbs(r["Kt"], r["GHI"]),

"hawlader"                : lambda **r: hawlader(r["Kt"], r["GHI"]),

"jacovides"               : lambda **r: jacovides(r["Kt"], r["GHI"]),

"karatasou"               : lambda **r: karatasou(r["Kt"], r["GHI"]),

"lam_and_li"              : lambda **r: lam_and_li(r["Kt"], r["GHI"]),

"orgill_and_hollands"     : lambda **r: orgill_and_hollands(r["Kt"], r["GHI"]),

"Hollands"                : lambda **r: Hollands(r["Kt"], r["GHI"]),

"Bourges"                 : lambda **r: Bourges(r["Kt"], r["GHI"]),

"boland1"                 : lambda **r: boland1(r["Kt"], r["GHI"]),

"boland2"                 : lambda **r: boland2(r["Kt"], r["GHI"]),

"boland3"                 : lambda **r: boland3(r["Kt"], r["GHI"]),

"boland4"                 : lambda **r: boland4(r["Kt"], r["GHI"]),

"boland5"                 : lambda **r: boland5(r["Kt"], r["GHI"]),

"boland6"                 : lambda **r: boland6(r["Kt"], r["GHI"]),

"boland7"                 : lambda **r: boland7(r["Kt"], r["GHI"]),

"reindl"                  : lambda **r: reindl(r["Kt"], r["GHI"]),

"De_Miguel"               : lambda **r: De_Miguel(r["Kt"], r["GHI"]),

"Li_And_Lam"              : lambda **r: Li_And_Lam(r["Kt"], r["GHI"]),

"Spencer"                 : lambda **r: Spencer(r["Kt"], r["GHI"]),

"Ineichen1"               : lambda **r: Ineichen1(r["Kt"], r["GHI"]),

"Ineichen2"               : lambda **r: Ineichen2(r["Kt"], r["GHI"]),
```

```
"Ineichen3"              : lambda **r: Ineichen3(r["Kt"], r["GHI"]),

"oliveira"               : lambda **r: oliveira(r["Kt"], r["GHI"]),

"Ulgen_Hepbasli1"        : lambda **r: Ulgen_And_Hepbasli1(r["Kt"], r["GHI"]),

"Ulgen_Hepbasli2"        : lambda **r: Ulgen_And_Hepbasli2(r["Kt"], r["GHI"]),

"soares"                 : lambda **r: soares(r["Kt"], r["GHI"]),

"chendo_maduekwe1"       : lambda **r: chendo_and_maduekwe1(r["Kt"], r["GHI"]),

"chendo_maduekwe2"       : lambda **r: chendo_and_maduekwe2(r["Kt"], r["GHI"]),

"Furlan_Oliveira"        : lambda **r: Furlan_and_Oliveira(r["Kt"], r["GHI"]),

"Moreno"                 : lambda **r: Moreno(r["Kt"], r["GHI"]),

"Pagola1"                : lambda **r: Pagola1(r["Kt"], r["GHI"]),

"Pagola2"                : lambda **r: Pagola2(r["Kt"], r["GHI"]),

"Posadillo_Lopez1"       : lambda **r: Posadillo_Lopez1(r["Kt"], r["GHI"]),

"Posadillo_Lopez2"       : lambda **r: Posadillo_Lopez2(r["Kt"], r["GHI"]),

"Ruiz_Arias1"           : lambda **r: Ruiz_Arias1(r["Kt"], r["GHI"]),

"Ruiz_Arias2"            : lambda **r: Ruiz_Arias2(r["Kt"], r["GHI"]),

"Ruiz_Arias3"            : lambda **r: Ruiz_Arias3(r["Kt"], r["GHI"]),

"Ruiz_Arias4"            : lambda **r: Ruiz_Arias4(r["Kt"], r["GHI"]),

"Ruiz_Arias5"            : lambda **r: Ruiz_Arias5(r["Kt"], r["GHI"]),

"Ruiz_Arias6"            : lambda **r: Ruiz_Arias6(r["Kt"], r["GHI"]),

"Torres1"                : lambda **r: Torres1(r["Kt"], r["GHI"]),

"Torres2"                : lambda **r: Torres2(r["Kt"], r["GHI"]),

"Torres3"                : lambda **r: Torres3(r["Kt"], r["GHI"]),

"Torres4"                : lambda **r: Torres4(r["Kt"], r["GHI"]),

"Sanchez"                : lambda **r: Sanchez(r["Kt"], r["GHI"]),

"Tapakis1"               : lambda **r: Tapakis1(r["Kt"], r["GHI"]),

"Yao1"                   : lambda **r: Yao1(r["Kt"], r["GHI"], r["zenith_angle"]),

"Yao2"                   : lambda **r: Yao2(r["Kt"], r["GHI"], r["zenith_angle"]),

"Yao3"                   : lambda **r: Yao3(r["Kt"], r["GHI"], r["zenith_angle"]),

"Yao4"                   : lambda **r: Yao4(r["Kt"], r["GHI"], r["zenith_angle"]),

"muneer3"                : lambda **r: muneer3(r["Kt"], r["GHI"], r["zenith_angle"], r["declination"]),

"Mondol2"                : lambda **r: Mondol2(r["Kt"], r["GHI"], r["zenith_angle"]),

"PerezBurgos"            : lambda **r: PerezBurgos(r["Kt"], r["GHI"], r["zenith_angle"]),

"Rerhrhaye"              : lambda **r: Rerhrhaye(r["Kt"], r["GHI"], r["zenith_angle"]),

"Tuomiranta1"            : lambda **r: Tuomiranta1(r["Kt"], r["GHI"], r["zenith_angle"]),

"Tuomiranta2"            : lambda **r: Tuomiranta2(r["Kt"], r["GHI"], r["zenith_angle"]),

"Tuomiranta3"            : lambda **r: Tuomiranta3(r["Kt"], r["GHI"], r["zenith_angle"]),

"louche"                 : lambda **r: louche(r["Kt"], r["GHI"], r["zenith_angle"]),

"Suehrcke_McCormick"     : lambda **r: Suehrcke_McCormick(r["Kt"], r["GHI"], r["zenith_angle"]),

"Gonzalez4"              : lambda **r: Gonzalez4(r["GHI"], r["Kt"], r["zenith_angle"]),

"DeJong"                 : lambda **r: DeJong(r["Kt"], r["GHI"], r["altitude"]),

"reindl2"                : lambda **r: reindl2(r["Kt"], r["GHI"], r["altitude"]),

"Tapakis2"               : lambda **r: Tapakis2(r["Kt"], r["altitude"], r["GHI"]),
```

```
"Tapakis3"                : lambda **r: Tapakis3(r["Kt"], r["altitude"], r["GHI"]),

"Skartveit1"              : lambda **r: Skartveit1(r["Kt"], r["altitude"], r["GHI"]),

"Gonzalez2"               : lambda **r: Gonzalez2(r["Kt"], r["GHI"], r["altitude"]),

"Gonzalez6"               : lambda **r: Gonzalez6(r["Kt"], r["altitude"], r["GHI"], r["zenith_angle"]),

"Gonzalez7"               : lambda **r: Gonzalez7(r["Kt"], r["altitude"], r["GHI"], r["zenith_angle"]),

}


files=list(sorted(DATA_PATH.glob("*.xlsx")))

for f in tqdm(files,desc="Workbooks",unit="file"):

    try: df=pd.read_excel(f,engine="openpyxl")

    except Exception as e: print("read",f.name,e);continue

    df['mean_Kt']=df['Kt'].mean();df['Phi']=phi_series(df['Kt'])

    for name,func in MODELS.items():

        if name in df.columns:continue

        try: df[name]=df.apply(lambda r: func(**r.to_dict()),axis=1)

        except Exception as e: print(name,f.name,e)

    df.to_excel(f,engine="openpyxl",index=False)

print("done",len(files),"files,",len(MODELS),"models")
```

Appendix C

The figure below presents the distribution of the sky clearness index (K_t) for three locations in the UK, comparing two temporal resolutions: hourly and one-minute intervals. The histogram reveal that one minute data retains short term fluctuations more effectively, leading to more distinct and sharper peaks.

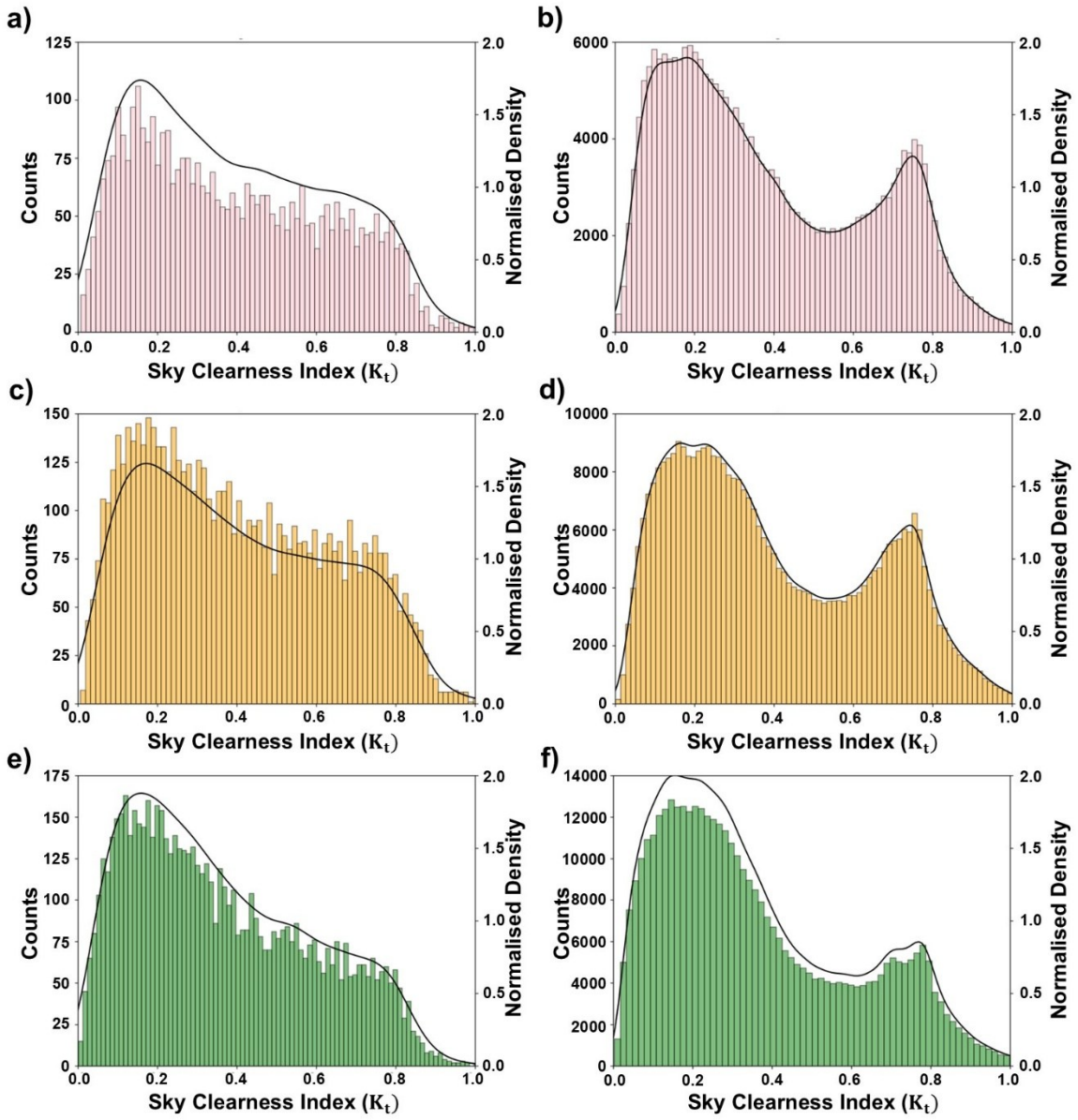

Figure C.1: The sky clearness index distributions for three UK locations : Lerwick **(a, b)**, Chilbolton **(c, d),** and Camborne **(e, f)**. They are illustrated across two temporal resolutions: hourly data is shown in panels **a**, **c**, and **e**, while one-minute data appears in panels **b**, **d**, and **f**.

Appendix D

The table below represents the 67 sites used for the clear-sky irradiance study.

Table D.1: Information on radiometric sites, and the source of their data. The corresponding AERONET site name is indicated in the last column. The 3-letter BSRN code name is used wherever available.

Code	Radiometric site	Lat. (°)	Long. (°)	Site Elev. (m)	MERRA2 Elev. (m)	Elev. Corr.	Source	AERONET Site
ARG	Kishinev	47.001	28.816	205	150.2	0.964	H	Moldova
BAR	Barrow	71.323	-156.607	8	0.5	0.995	A	Barrow
BIL	Billings	36.605	-97.516	317	325.3	1.006	A	ARM_SGP
BIS	Bismarck	46.772	-100.76	503	571.7	1.047	K	NEON_NOGP
BMT	Black Mountain	-35.275	149.114	595	792.8	1.141	D	Canberra
BON	Bondville	40.067	-88.367	213	208.8	0.997	A	Bondville
BOU	Boulder	40.05	-105.007	1577	1801.8	1.162	A	BSRN_BAO_Boulder
BRB	Brasilia	-15.601	-47.713	1023	948	0.951	A	Brasilia_SONDA
CAB	Cabauw	51.971	4.927	0	3.5	1.002	A	Cabauw
CAH	Cape Hedo	26.867	128.248	65	14.9	0.967	P	Okinawa_Hedo
CAM	Camborne	50.217	-5.317	88	22.5	0.957	A	Camborne_MO
CAR	Carpentras	44.083	5.059	100	266.2	1.117	A	Carpentras
CBT	Chilbolton	51.144	-1.437	81	62.1	0.987	T	Chilbolton
CHI	Chiba	35.625	140.104	21	38.7	1.012	P	Chiba_University
CLH	Chesapeake Light	36.905	-75.713	37	0.2	0.976	A	COVE_SEAPRISM
CNR	CENER	42.816	-1.601	471	516.7	1.031	A	CENER
DAR	Darwin	-12.425	130.891	30	9.5	0.986	A	ARM_Darwin
DAV	Davos	46.813	9.844	1589	1896.3	1.227	M	Davos
ENA	Eastern North Atlantic	39.091	-28.029	15	20.1	1.003	A	ARM_Graciosa
EUR	Eureka	79.989	-85.94	85	160.4	1.052	A	OPAL
EVO	Evora	38.568	-7.911	293	173.2	0.923	Q	Evora
FUA	Fukuoka	33.582	130.376	3	185.4	1.129	A	Fukuoka
GOB	Gobabeb	-23.561	15.042	407	443	1.024	A	Gobabeb

GOL	Golden	39.742	-105.18	1829	2095.7	1.195	L	NREL-Golden
GUR	Gurgaon	28.425	77.156	259	230.4	0.981	A	Amity_Univ_Gurgaon
INO	Magurele MARS	44.348	26.031	90	76.7	0.991	A	Magurele_Inoe
IZA	Izana	28.309	-16.499	2373	178.8	0.232	A	Izana
JRC	Ispra	45.812	8.627	220	800	1.472	I	Ispra
KAL	Kalgoorlie	-30.785	121.453	365	307.8	0.962	C	Lake_Lefroy
KZH	Durban	-29.871	30.977	150	15.2	0.914	O	Durban_UKZN
LEA	Learmonth	-22.241	114.097	5	17.3	1.008	C	Learmonth
LER	Lerwick	60.139	-1.185	80	3.7	0.95	A	Lerwick_MO
LIL	Lille	50.611	3.14	63	41.9	0.986	R	Lille
LIN	Lindenberg	52.21	14.122	125	71.3	0.965	A	MetObs_Lindenberg
LPU	Lampedusa	35.517	12.632	45	0.2	0.971	F	Lampedusa
LRC	Langley Research Center	37.104	-76.387	3	6.6	1.002	A	NASA_LaRC
MAN	Momote	-2.058	147.425	6	4.7	0.999	A	Manus
MBO	M'Bour	14.394	-16.958	21	16.7	0.997	R	Dakar
MLO	Mauna_Loa	19.539	-155.578	3397	1145	0.223	K	Mauna_Loa
NAU	Nauru	-0.521	166.917	7	0.1	0.995	A	Nauru
NIA	Niamey	13.477	2.176	223	241.7	1.013	B	Niamey
NYA	Ny-Ålesund	78.925	11.93	11	294	1.208	A	Ny_Alesund_AWI
OHY	Observatory of Huancayo	-12.05	-75.32	3314	4167.5	1.766	A	Huancayo-IGP
PAL	Palaiseau	48.713	2.208	156	103.9	0.966	A	Palaiseau
PAY	Payerne	46.815	6.944	491	782.3	1.214	A	Payerne
PRE	Pretoria	-25.753	28.229	1410	1538.7	1.09	O	Pretoria_CSIR-DPSS
PSA	PSA-DLR	37.091	-2.358	500	666.1	1.117	E	Tabernas_PSA-DLR
PSD	PSDA	-24.09	-69.929	965	1261.4	1.218	N	PSDA_Chile
PTR	Petrolina	-9.068	-40.319	387	428.8	1.028	A	Petrolina_SONDA
REG	Regina	50.205	-104.713	578	638.8	1.041	A	Bratts_Lake
ROC	Rome-Casaccia	42.042	12.307	150	198.5	1.033	F	Rome_La_Sapienza

RTV	Rome Tor Vergata	48.84	12.647	331	451.7	1.084	S	Rome_Tor_Vergata
RUN	Reunion Island, University	-20.901	55.484	116	533.1	1.321	C	Reunion_St_Denis
SAP	Sapporo	43.06	141.329	17	279.2	1.191	A	Hokkaido_University
SDK	Sodankyla	67.367	26.628	195	227.9	1.022	G	Sodankyla
SEO	Seoul	37.46	126.95	300	73.3	0.86	P	Seoul_SNU
SHA	Shagaya	29.209	47.061	242	264.1	1.015	J	Shagaya_Park
SMS	Sao Martinho da Serra	-29.443	-53.823	489	286.7	0.874	A	Sao_Martinho_SONDA
SPO	South Pole	-89.983	-24.799	2800	3078	1.204	A	South_Pole_Obs_NOAA
SXF	Sioux_Falls	43.73	-96.62	473	442.9	0.98	A	Sioux_Falls
TAM	Tamanrasset	22.79	5.529	1385	1681.9	1.219	A	Tamanrasset_INM
THD	Trinidad Head	41.054	-124.151	107	66.9	0.974	K	Trinidad_Head
TIK	Tiksi	71.586	128.919	48	116.5	1.047	A	Tiksi
TOR	Toravere	58.254	26.462	70	63.7	0.996	A	Toravere
TUC	Tucson	32.23	-110.955	786	962.3	1.125	L	Tucson
WHW	Vienna	48.249	16.356	198	372.9	1.124	U	Vienna_BOKU
XIA	XiangHe	39.754	116.962	32	59	1.018	A	XiangHe

[A] BSRN: Baseline Surface Radiation Network

[B] ARM: Atmospheric Radiation Measurement, U.S. Department of Energy

[C] BoM: Bureau of Meteorology

[D] CSIRO: Commonwealth Scientific and Industrial Research Organisation

[E] DLR: Deutsches Zentrum für Luft- und Raumfahrt

[F] ENEA: Agenzia nazionale per le nuove tecnologie, l'energia e lo sviluppo economico sostenible

[G] FMI: Finnish Meteorological Institute

[H] IAP: Institute of Applied Physics, Moldova

[I] JRC: The European Commission's Joint Research Centre

[J] KISR: Kuwait Institute for Scientific Research

[K] NOAA: National Oceanic and Atmospheric Administration, Global Monitoring Laboratory

[L] NREL: National Renewable Energy Laboratory, Measurement and Instrumentation Data Center

[M] PMOD: Physikalisch-Meteorologisches Observatorium Davos / World Radiation Data Center

[N] PSDA: Plataforma Solar del Desierto de Atacama

[O] SAURAN: Southern African Universities Radiometric Network

[P] SKYNET: International Skynet Data Center

[Q] UoE: University of Evora

[R] UoL: University of Lille

[S] UoR: University of Rome Tor Vergata

[T] CEDA: Centre for Environmental Data Analysis

[U] ZAMG-ARAD: Zentralanstalt für Meteorologie und Geodynamik

Bibliography

[1]: United Nations, “Paris agreement to the United Nations framework convention on climate change,” T.I.A.S. No. 16-1104, Dec. 2015

[2]: IPCC, Climate Change 2022: Impacts, Adaptation and Vulnerability: Working Group II Contribution to the Sixth Assessment Report of the Intergovernmental Panel on Climate Change, H.-O. Pörtner, et al., Cambridge, U.K.: Cambridge Univ. Press, 2022, doi: 10.1017/9781009325844.

[3]: Energy Agency, I. (2021). World Energy Outlook 2021. Retrieved from www.iea.org/weo

[4]: IEA. (2020). Projected Costs of Generating Electricity 2020. Paris: IEA. Retrieved from https://www.iea.org/reports/projected-costs-of-generating-electricity-2020

[5]: IRENA. (2024). Renewable Energy Statistics 2024. Abu Dhabi: The International Renewable Energy Agency.

[6]: M. Lennan and E. Morgera, “The glasgow climate conference (COP26),” Int. J. Marine Coastal Law, vol. 37, no. 1, pp. 137–151, Feb. 2022, doi: 10.1163/15718085-bja10083.

[7]: C. D. Rodríguez-Gallegos et al., “Global techno-economic performance of bifacial and tracking photovoltaic systems,” Joule, vol. 4, no. 7, pp. 1514–1541, Jul. 2020, doi: 10.1016/j.joule.2020.05.005.

[8]: International Technology Roadmap for Photovoltaic (ITRPV), “15th Edition 2024.” Accessed: May 20, 2024. [Online]

[9]: Y. J. K. Musleh, W. Herring, C. D. Rodríguez-Gallegos, S. A. Boden and T. Rahman, "Subhourly Error Analysis of Decomposition–Transposition Model Pairs for Temperate Climates," in IEEE Journal of Photovoltaics, vol. 15, no. 1, pp. 164-172, Jan. 2025, doi: 10.1109/JPHOTOV.2024.3483262

[10]: Y. Peng et al., “Energy performance assessment of photovoltaic greenhouses in summer based on coupled optical-electrical-thermal models and plant growth requirements,” Energy Conversion and Management, vol. 287. Elsevier BV, p. 117086, Jul. 2023. doi: 10.1016/j.enconman.2023.117086.

[11]: C. A. Gueymard, “A review of validation methodologies and statistical performance indicators for modeled solar radiation data: Towards a better bankability of solar projects,”

Renewable and Sustainable Energy Reviews, vol. 39. Elsevier BV, pp. 1024–1034, Nov. 2014. doi: 10.1016/j.rser.2014.07.117.

[12]: C. A. Gueymard and J. A. Ruiz-Arias, “Extensive worldwide validation and climate sensitivity analysis of direct irradiance predictions from 1-min global irradiance,” Solar Energy, vol. 128. Elsevier BV, pp. 1–30, Apr. 2016. doi: 10.1016/j.solener.2015.10.010

[13]: J. A. Ruiz-Arias and C. A. Gueymard, “Solar irradiance component separation benchmarking: The critical role of dynamically-constrained sky conditions,” Renewable and Sustainable Energy Reviews, vol. 202. Elsevier BV, p. 114678, Sep. 2024. doi: 10.1016/j.rser.2024.114678.

[14]: J. A. Ruiz-Arias and C. A. Gueymard, “GISPLIT: High-performance global solar irradiance component-separation model dynamically constrained by 1-min sky conditions,” Solar Energy, vol. 269. Elsevier BV, p. 112363, Feb. 2024. doi: 10.1016/j.solener.2024.112363.

[15]: A. Forstinger et al., “Worldwide solar radiation benchmark of modelled surface irradiance.” Copernicus GmbH, Jun. 28, 2022. doi: 10.5194/ems2022-547.

[16]: O. Gandhi et al., “The value of solar forecasts and the cost of their errors: A review,” Renewable and Sustainable Energy Reviews, vol. 189. Elsevier BV, p. 113915, Jan. 2024. doi: 10.1016/j.rser.2023.113915.

[17]: M. J. Mayer and D. Yang, “Probabilistic photovoltaic power forecasting using a calibrated ensemble of model chains,” Renewable and Sustainable Energy Reviews, vol. 168. Elsevier BV, p. 112821, Oct. 2022. doi: 10.1016/j.rser.2022.112821.

[18]: H. E. Beck, N. E. Zimmermann, T. R. McVicar, N. Vergopolan, A. Berg, and E. F. Wood, “Present and future Köppen-Geiger climate classification maps at 1-km resolution,” Scientific Data, vol. 5, no. 1. Springer Science and Business Media LLC, Oct. 30, 2018. doi: 10.1038/sdata.2018.214.

[19]: J.A. Duffie and W.A. Beckman, Solar Engineering of Thermal Processes, Wiley, Hoboken, 1991

[20]: M. Iqbal, "Chapter 1 - SUN–EARTH ASTRONOMICAL RELATIONSHIPS," in M. Iqbal (Ed.), An Introduction to Solar Radiation, Academic Press, 1983, pp. 1-28, ISBN 9780123737502, doi: 10.1016/B978-0-12-373750-2.50006-9

[21]: V. Khavrus and I. Shelevytsky, “Geometry and the physics of seasons,” Physics Education, vol. 47, no. 6. IOP Publishing, pp. 680–692, Oct. 22, 2012. doi: 10.1088/0031-9120/47/6/680.

[22]: ASTM, " G173 - 03 Standard tables for reference solar spectral irradiances: direct normal and hemispherical on 37°tilted surface," 2012

[23]: United States Committee on Extension to the Standard Atmosphere. (1962). U.S. Standard Atmosphere, 1962: ICAO Extension to 32 Kilometers. Committee on Extension to the Standard Atmosphere. Washington, D.C.: U.S. Government Printing Office

[24]: A. I. Shapiro, S. K. Solanki, N. A. Krivova, R. V. Tagirov, and W. K. Schmutz, “The role of the Fraunhofer lines in solar brightness variability,” Astronomy & Astrophysics, vol. 581. EDP Sciences, p. A116, Sep. 2015. doi: 10.1051/0004-6361/201526483.

[25]: C. A. Gueymard, “The sun’s total and spectral irradiance for solar energy applications and solar radiation models,” Solar Energy, vol. 76, no. 4. Elsevier BV, pp. 423–453, Apr. 2004. doi: 10.1016/j.solener.2003.08.039

[26]: R. Perez, R. Seals, and A. Zelenka, “Comparing satellite remote sensing and ground network measurements for the production of site/time specific irradiance data,” Solar Energy, vol. 60, no. 2. Elsevier BV, pp. 89–96, Feb. 1997. doi: 10.1016/s0038-092x(96)00162-4

[27]: Stackhouse, P. W., Westberg, D. J., Hoell, J. M., Chandler, W. S., & Zhang, T. (2015). Surface Meteorology and Solar Energy (SSE) Release 6.0 Methodology Version 3.1.2. Hampton, VA, USA: National Aeronautics and Space Administration (NASA) Langley Research Center

[28]: D. Palmer, I. Cole, T. Betts, and R. Gottschalg, “Interpolating and Estimating Horizontal Diffuse Solar Irradiation to Provide UK-Wide Coverage: Selection of the Best Performing Models,” Energies, vol. 10, no. 2. MDPI AG, p. 181, Feb. 05, 2017. doi: 10.3390/en10020181

[29]: D. R. Myers, “Solar Radiation Resource Assessment for Renewable Energy Conversion,” Comprehensive Renewable Energy. Elsevier, pp. 213–237, 2012. doi: 10.1016/b978-0-08-087872-0.00112-8

[30]: J. S. Stein and C. W. Hansen, “Irradiance on the Plane of the Array,” Photovoltaic Solar Energy. Wiley, pp. 25–38, Jun. 21, 2024. doi: 10.1002/9781119578826.ch4.

[31]: P. Campana et al., “Solar irradiance distribution under vertically mounted agrivoltaic systems – Model development, validation, and applications for microclimate assessment.” California Digital Library (CDL), Nov. 23, 2022. doi: 10.31223/x5g07d.

[32]: S. Ma Lu et al., “Photosynthetically active radiation decomposition models for agrivoltaic systems applications,” Solar Energy, vol. 244. Elsevier BV, pp. 536–549, Sep. 2022. doi: 10.1016/j.solener.2022.05.046.

[33]: S. Ma Lu et al., “Photosynthetically active radiation separation model for high-latitude regions in agrivoltaic systems modeling,” Journal of Renewable and Sustainable Energy, vol. 16, no. 1. AIP Publishing, Jan. 01, 2024. doi: 10.1063/5.0181311.

[34]: E. F. M. Abreu, P. Canhoto, and M. J. Costa, “Prediction of diffuse horizontal irradiance using a new climate zone model,” Renewable and Sustainable Energy Reviews, vol. 110. Elsevier BV, pp. 28–42, Aug. 2019. doi: 10.1016/j.rser.2019.04.055.

[35]: M. de C. Alves, L. Sanches, J. de S. Nogueira, and V. A. M. Silva, “Effects of Sky Conditions Measured by the Clearness Index on the Estimation of Solar Radiation Using a Digital Elevation Model,” Atmospheric and Climate Sciences, vol. 03, no. 04. Scientific Research Publishing, Inc., pp. 618–626, 2013. doi: 10.4236/acs.2013.34064.

[36]: P. Lauret, R. Alonso-Suárez, J. Le Gal La Salle, and M. David, “Solar Forecasts Based on the Clear Sky Index or the Clearness Index: Which Is Better?,” Solar, vol. 2, no. 4. MDPI AG, pp. 432–444, Oct. 11, 2022. doi: 10.3390/solar2040026.

[37]: J. Page, “Chapter II-1-A—The role of solar-radiation climatology in the design of photovoltaic systems,” in McEvoy’s Handbook of Photovoltaics, S. A. Kalogirou, Ed., 3rd ed. New York, NY, USA: Academic, 2018, pp. 601–670, doi: 10.1016/B978-0-12-809921-6.00016-1.

[38]: M. Perry and A. Troccoli, “An approach for generating synthetic fine temporal resolution solar radiation time series from hourly gridded datasets,” Meteorologische Zeitschrift, vol. 26, no. 3. Schweizerbart, pp. 265–276, Jun. 14, 2017. doi: 10.1127/metz/2016/0746.

[39]: T. M. Mercier, A. Sabet, and T. Rahman, “Vision transformer models to measure solar irradiance using sky images in temperate climates,” Applied Energy, vol. 362. Elsevier BV, p. 122967, May 2024. doi: 10.1016/j.apenergy.2024.122967.

[40]: J. A. Ruiz-Arias and C. A. Gueymard, “CAELUS: Classification of sky conditions from 1-min time series of global solar irradiance using variability indices and dynamic thresholds,” Solar Energy, vol. 263. Elsevier BV, p. 111895, Oct. 2023. doi: 10.1016/j.solener.2023.111895.

[41]: C. A. Gueymard, J. M. Bright, D. Lingfors, A. Habte, and M. Sengupta, “A posteriori clear-sky identification methods in solar irradiance time series: Review and preliminary validation using sky

imagers," Renewable and Sustainable Energy Reviews, vol. 109. Elsevier BV, pp. 412–427, Jul. 2019. doi: 10.1016/j.rser.2019.04.027.

[42]: M. J. Reno and C. W. Hansen, "Identification of periods of clear sky irradiance in time series of GHI measurements," Renewable Energy, vol. 90. Elsevier BV, pp. 520–531, May 2016. doi: 10.1016/j.renene.2015.12.031.

[43]: J. M. Bright, X. Sun, C. A. Gueymard, B. Acord, P. Wang, and N. A. Engerer, "Bright-Sun: A globally applicable 1-min irradiance clear-sky detection model," Renewable and Sustainable Energy Reviews, vol. 121. Elsevier BV, p. 109706, Apr. 2020. doi: 10.1016/j.rser.2020.109706.

[44]: M. Sengupta, A. Habte, S. Wilbert, C. Gueymard, and J. Remund, "Best Practices Handbook for the Collection and Use of Solar Resource Data for Solar Energy Applications: Third Edition," Office of Scientific and Technical Information (OSTI), Apr. 2021. doi: 10.2172/1778700

[45]: J. Freeman, D. Freestate, W. Hobbs, and C. Riley, "Using measured plane-of-array data directly in photovoltaic modeling: Methodology and validation," 2016 IEEE 43rd Photovoltaic Specialists Conference (PVSC). IEEE, Jun. 2016. doi: 10.1109/pvsc.2016.7750130.

[46]: M. Gostein et al., "Measuring Irradiance for Bifacial PV Systems," 2021 IEEE 48th Photovoltaic Specialists Conference (PVSC). IEEE, Jun. 20, 2021. doi: 10.1109/pvsc43889.2021.9518601.

[47]: L. Dunn, M. Gostein and K. Emery, "Comparison of pyranometers vs. PV reference cells for evaluation of PV array performance," 2012 38th IEEE Photovoltaic Specialists Conference, Austin, TX, USA, 2012, pp. 002899-002904, doi: 10.1109/PVSC.2012.6318193.

[48]: International Electrotechnical Commission. (2021). IEC 61724-1: Photovoltaic system performance - Part 1: Monitoring

[49]: W.G.J.H.M. Van Sark, N.H. Reich, B. Müller, A. Armbruster, K. Kiefer, and Ch. Reise, "Review of PV performance ratio development," Unpublished, 2012, doi: 10.13140/2.1.2138.7204

[50]: International Electrotechnical Commission. (1998). IEC 61724. Photovoltaic system performance monitoring— guidelines for measurement, data exchange and analysis. Edition 1.0

[51]: N. H. Reich, B. Mueller, A. Armbruster, W. G. J. H. M. van Sark, K. Kiefer, and C. Reise, "Performance ratio revisited: is PR > 90% realistic?," Progress in Photovoltaics: Research and Applications, vol. 20, no. 6. Wiley, pp. 717–726, Jan. 18, 2012. doi: 10.1002/pip.1219.

[52]: M. Sengupta et al., “Best Practices Handbook for the Collection and Use of Solar Resource Data for Solar Energy Applications: Fourth Edition,” Office of Scientific and Technical Information (OSTI), Sep. 2024. doi: 10.2172/2448063.

[53]: I. Reda and A. Andreas, “Solar position algorithm for solar radiation applications,” Solar Energy, vol. 76, no. 5. Elsevier BV, pp. 577–589, 2004. doi: 10.1016/j.solener.2003.12.003.

[54]: A. Ohmura et al., “Baseline Surface Radiation Network (BSRN/WCRP): New Precision Radiometry for Climate Research,” Bulletin of the American Meteorological Society, vol. 79, no. 10. American Meteorological Society, pp. 2115–2136, Oct. 1998. doi: 10.1175/1520-0477(1998)079<2115:bsrnbw>2.0.co;2.

[55]: D. Perez-Astudillo, D. Bachour, and L. Martin-Pomares, “Improved quality control protocols on solar radiation measurements,” Solar Energy, vol. 169. Elsevier BV, pp. 425–433, Jul. 2018. doi: 10.1016/j.solener.2018.05.028.

[56]: A. Roesch, M. Wild, A. Ohmura, E. G. Dutton, C. N. Long, and T. Zhang, “Assessment of BSRN radiation records for the computation of monthly means,” Atmospheric Measurement Techniques, vol. 4, no. 2. Copernicus GmbH, pp. 339–354, Feb. 23, 2011. doi: 10.5194/amt-4-339-2011.

[57]: F. M. Nollas, G. A. Salazar, and C. A. Gueymard, “Quality control procedure for 1-minute pyranometric measurements of global and shadowband-based diffuse solar irradiance,” Renewable Energy, vol. 202. Elsevier BV, pp. 40–55, Jan. 2023. doi: 10.1016/j.renene.2022.11.056

[58]: C. A. Gueymard, ‘A reevaluation of the solar constant based on a 42-year total solar irradiance time series and a reconciliation of spaceborne observations’, Sol. Energy, vol. 168, pp. 2–9, Jul. 2018, doi: 10.1016/j.solener.2018.04.001

[59]: Standard Solar Constant and Zero Air Mass Solar Spectral Irradiance Tables. doi: 10.1520/e0490-22

[60]: R. Urraca, T. Huld, A. Gracia-Amillo, F. J. Martinez-de-Pison, F. Kaspar, and A. Sanz-Garcia, “Evaluation of global horizontal irradiance estimates from ERA5 and COSMO-REA6 reanalyses using ground and satellite-based data,” Solar Energy, vol. 164. Elsevier BV, pp. 339–354, Apr. 2018. doi: 10.1016/j.solener.2018.02.059

[61]: A. Sinyuk et al., “The AERONET Version 3 aerosol retrieval algorithm, associated uncertainties and comparisons to Version 2,” Atmospheric Measurement Techniques, vol. 13, no. 6. Copernicus GmbH, pp. 3375–3411, Jun. 26, 2020. doi: 10.5194/amt-13-3375-2020.

[62]: B. Schmid et al., “Comparison of columnar water-vapor measurements from solar transmittance methods,” Applied Optics, vol. 40, no. 12. Optica Publishing Group, p. 1886, Apr. 20, 2001. doi: 10.1364/ao.40.001886.

[63]: O. Thomas and J. Causse, “From spectra to qualitative and quantitative results,” UV-Visible Spectrophotometry of Waters and Soils. Elsevier, pp. 59–94, 2022. doi: 10.1016/b978-0-323-90994-5.00011-3.

[64]: C. Toledano et al., “Sun photometers,” Field Measurements for Passive Environmental Remote Sensing. Elsevier, pp. 121–138, 2023. doi: 10.1016/b978-0-12-823953-7.00005-8.

[65]: J. A. Lee, C. A. Gueymard, and P. A. Jiménez, “Performance of aerosol optical depth forecasts over the Middle East: Multi-model analysis and validation.” Wiley, Mar. 18, 2021. doi: 10.1002/essoar.10506487.1

[66]: B. N. Holben et al., “AERONET—A Federated Instrument Network and Data Archive for Aerosol Characterization,” Remote Sensing of Environment, vol. 66, no. 1. Elsevier BV, pp. 1–16, Oct. 1998. doi: 10.1016/s0034-4257(98)00031-5.

[67]: C. A. Gueymard and D. Yang, “Worldwide validation of CAMS and MERRA-2 reanalysis aerosol optical depth products using 15 years of AERONET observations,” Atmospheric Environment, vol. 225. Elsevier BV, p. 117216, Mar. 2020. doi: 10.1016/j.atmosenv.2019.117216

[68]: E. F. M. Abreu, C. A. Gueymard, P. Canhoto, and M. J. Costa, “Performance assessment of clear-sky solar irradiance predictions using state-of-the-art radiation models and input atmospheric data from reanalysis or ground measurements,” Solar Energy, vol. 252. Elsevier BV, pp. 309–321, Mar. 2023. doi: 10.1016/j.solener.2023.01.051.

[69]: A. Ångström, “On the Atmospheric Transmission of Sun Radiation and on Dust in the Air,” Geografiska Annaler, vol. 11, no. 2. Informa UK Limited, pp. 156–166, Aug. 1929. doi: 10.1080/20014422.1929.11880498.

[70]: A. Salmon et al., “Advances in aerosol optical depth evaluation from broadband direct normal irradiance measurements,” Solar Energy, vol. 221. Elsevier BV, pp. 206–217, Jun. 2021. doi: 10.1016/j.solener.2021.04.039

[71]: V. Buchard et al., “The MERRA-2 Aerosol Reanalysis, 1980 Onward. Part II: Evaluation and Case Studies,” Journal of Climate, vol. 30, no. 17. American Meteorological Society, pp. 6851–6872, Sep. 2017. doi: 10.1175/jcli-d-16-0613.1.

[72]: R. Gelaro et al., “The Modern-Era Retrospective Analysis for Research and Applications, Version 2 (MERRA-2),” Journal of Climate, vol. 30, no. 14. American Meteorological Society, pp. 5419–5454, Jul. 2017. doi: 10.1175/jcli-d-16-0758.1.

[73]: A. Molod, L. Takacs, M. Suarez, and J. Bacmeister, “Development of the GEOS-5 atmospheric general circulation model: evolution from MERRA to MERRA2,” Geoscientific Model Development, vol. 8, no. 5. Copernicus GmbH, pp. 1339–1356, May 12, 2015. doi: 10.5194/gmd-8-1339-2015.

[74]: A. Benedetti et al., “Aerosol analysis and forecast in the European Centre for Medium-Range Weather Forecasts Integrated Forecast System: 2. Data assimilation,” Journal of Geophysical Research: Atmospheres, vol. 114, no. D13. American Geophysical Union (AGU), Jul. 11, 2009. doi: 10.1029/2008jd011115.

[75]: J. Flemming et al., “Tropospheric chemistry in the Integrated Forecasting System of ECMWF,” Geoscientific Model Development, vol. 8, no. 4. Copernicus GmbH, pp. 975–1003, Apr. 07, 2015. doi: 10.5194/gmd-8-975-2015.

[76]: A. Inness et al., “The CAMS reanalysis of atmospheric composition,” Atmospheric Chemistry and Physics, vol. 19, no. 6. Copernicus GmbH, pp. 3515–3556, Mar. 20, 2019. doi: 10.5194/acp-19-3515-2019.

[77]: J. -J. Morcrette et al., “Aerosol analysis and forecast in the European Centre for Medium-Range Weather Forecasts Integrated Forecast System: Forward modelling,” Journal of Geophysical Research: Atmospheres, vol. 114, no. D6. American Geophysical Union (AGU), Mar. 25, 2009. doi: 10.1029/2008jd011235.

[78]: Reanalyses.org, 2017. Advancing in Reanalysis. [Accessed 17/09/2024]

[79]: M. Lave, W. Hayes, A. Pohl, and C. W. Hansen, “Evaluation of global horizontal irradiance to plane-of-array irradiance models at locations across the United States,” IEEE J. Photovolt., vol. 5, no. 2, pp. 597–606, Mar. 2015, doi: 10.1109/JPHOTOV.2015.2392938.

[80]: T. Mahachi and A. J. Rix, “Evaluation of irradiance decomposition and transposition models for a region in South Africa investigating the sensitivity of various diffuse radiation models,” in Proc. IEEE 42nd Annu. Conf. Ind. Electron. Soc., Florence, Italy, 2016, pp. 3064–3069, doi: 10.1109/IECON.2016.7793897

[81]: B. G. Pierce, J. L. Braid, J. S. Stein, J. Augustyn, and D. Riley, “Solar transposition modeling via deep neural networks with sky images,” IEEE J. Photovolt., vol. 12, no. 1, pp. 145–151, Jan. 2022, doi: 10.1109/JPHOTOV.2021.3120508

[82]: International Technology Roadmap for Photovoltaic (ITRPV), “13th Edition 2022.” Accessed: May 15, 2024. [Online]. Available: https://archive.org/details/2022-itrpv-edition-13/mode/2up

[83]: J. Stein and G. Maugeri, “Fact Sheet: Bifacial Tracking,” International Energy Agency Photovoltaic Power Systems Programme, 2024. doi: 10.69766/ulmk1464.

[84]: PVPS Task 1, Trends in photovoltaic applications 2022 task 1 strategic PV analysis and outreach PVPS, 2022. [Online]. Available: www.iea-pvps.org

[85]: R. Kopecek and J. Libal, “Bifacial photovoltaics 2021: Status, opportunities and challenges,” Energies, vol. 14, no. 8, Apr. 2021, Art. no. 2076, doi: 10.3390/en14082076.

[86]: Adnot J, Bourges B, Campana D, Gicquel R. Utilisation de courbes de fréquences cumulées d’irradiation solaire globale pour le calcul des installations solaires. In: Lestienne R, editor. Analyse statistique des processus météorologiques appliquée à l'énergie solaire. Paris: CNRS; 1979.

[87]: D. S. Kumar, G. M. Yagli, M. Kashyap, and D. Srinivasan, “Solar irradiance resource and forecasting: a comprehensive review,” IET Renewable Power Generation, vol. 14, no. 10. Institution of Engineering and Technology (IET), pp. 1641–1656, Jul. 2020. doi: 10.1049/iet-rpg.2019.1227.

[88]: J. Leloux, E. Lorenzo, B. García-Domingo, J. Aguilera, and C. A. Gueymard, “A bankable method of assessing the performance of a CPV plant,” Applied Energy, vol. 118. Elsevier BV, pp. 1–11, Apr. 2014. doi: 10.1016/j.apenergy.2013.12.014

[89]: S. A. Pelaez, C. Deline, S. M. MacAlpine, B. Marion, J. S. Stein, and R. K. Kostuk, “Comparison of Bifacial Solar Irradiance Model Predictions With Field Validation,” IEEE Journal of Photovoltaics, vol. 9, no. 1. Institute of Electrical and Electronics Engineers (IEEE), pp. 82–88, Jan. 2019. doi: 10.1109/jphotov.2018.2877000.

[90]: Pelaez, S. A. (2019). Bifacial solar panels system design, modeling, and performance. PhD thesis, The University of Arizona.

[91]: Kopecek, R., & Libal, J. (2018). Towards large-scale deployment of bifacial photovoltaics. Nature Energy, 3(6), 443.

[92]: I. Shoukry, J. Libal, R. Kopecek, E. Wefringhaus, and J. Werner, “Modelling of Bifacial Gain for Stand-alone and in-field Installed Bifacial PV Modules,” Energy Procedia, vol. 92. Elsevier BV, pp. 600–608, Aug. 2016. doi: 10.1016/j.egypro.2016.07.025.

[93]: International Electrotechnical Commission. (2019). IEC TS 60904-1-2: Photovoltaic devices - Part 1-2: Measurement of current-voltage characteristics of bifacial photovoltaic (PV) devices.

[94]: International Electrotechnical Commission. IEC 60904-7: Photovoltaic devices; part 7: Computation of the spectral mismatch correction for measurements of photovoltaic devices.

[95]: J. Padilla, C. Toledo, and J. Abad, “Enovoltaics: Symbiotic integration of photovoltaics in vineyards,” Frontiers in Energy Research, vol. 10. Frontiers Media SA, Sep. 29, 2022. doi: 10.3389/fenrg.2022.1007383.

[96]: E. Sng, S. W. Chua, S. Roy and I. Lim, "Solar Energy Simulation of Bifacial Panels for Performance Optimisation," 2020 47th IEEE Photovoltaic Specialists Conference (PVSC), Calgary, AB, Canada, 2020, pp. 2590-2595, doi: 10.1109/PVSC45281.2020.9300749.

[97]: T. M. Mahim, A. H. M. A. Rahim and M. M. Rahman, "Review of Mono- and Bifacial Photovoltaic Technologies: A Comparative Study," in IEEE Journal of Photovoltaics, vol. 14, no. 3, pp. 375-396, May 2024, doi: 10.1109/JPHOTOV.2024.3366698.

[98]: T. Dullweber and J. Schmidt, “Industrial Silicon Solar Cells Applying the Passivated Emitter and Rear Cell (PERC) Concept—A Review,” IEEE Journal of Photovoltaics, vol. 6, no. 5. Institute of Electrical and Electronics Engineers (IEEE), pp. 1366–1381, Sep. 2016. doi: 10.1109/jphotov.2016.2571627.

[99]: C. Deline, S. A. Peláez, B. Marion, B. Sekulic, M. Woodhouse, and J. Stein, “Bifacial PV System Performance: Separating Fact from Fiction,” Unpublished, 2019, doi: 10.13140/RG.2.2.23189.27365.

[100]: A. Hubner, A. Aberle and R. Hezel, "Temperature behavior of monofacial and bifacial silicon solar cells," Conference Record of the Twenty Sixth IEEE Photovoltaic Specialists Conference - 1997, Anaheim, CA, USA, 1997, pp. 223-226, doi: 10.1109/PVSC.1997.654069

[101]: Sánchez, H., Meza, C., Dittmann, S., & Gottschalg, R. (2020). The effect of clearance height, albedo, tilt and azimuth angle in bifacial PV energy estimation using different existing algorithms.

[102]: PVPS Task 13. (2021). Bifacial Photovoltaic Modules and Systems: Experience and Results from International Research and Pilot Applications 2021 Task 13 Performance, Operation and Reliability of Photovoltaic Systems PVPS. Retrieved from www.iea-pvps.org

[103]: L. Kreinin, N. Bordin, A. Karsenty, A. Drori, D. Grobgeld, and N. Eisenberg, “PV module power gain due to bifacial design. Preliminary experimental and simulation data,” 2010 35th IEEE Photovoltaic Specialists Conference. IEEE, Jun. 2010. doi: 10.1109/pvsc.2010.5615874.

[104]: D. Berrian, J. Libal, M. Klenk, H. Nussbaumer, and R. Kopecek, “Performance of Bifacial PV Arrays With Fixed Tilt and Horizontal Single-Axis Tracking: Comparison of Simulated and Measured Data,” IEEE Journal of Photovoltaics, vol. 9, no. 6. Institute of Electrical and Electronics Engineers (IEEE), pp. 1583–1589, Nov. 2019. doi: 10.1109/jphotov.2019.2924394.

[105]: B. Marion, “Albedo Data Sets for Bifacial PV Systems,” 2020 47th IEEE Photovoltaic Specialists Conference (PVSC). IEEE, Jun. 14, 2020. doi: 10.1109/pvsc45281.2020.9300470.

[106]: N. Riedel-Lyngskar et al., “Spectral Albedo in Bifacial Photovoltaic Modeling: What can be learned from Onsite Measurements?,” 2021 IEEE 48th Photovoltaic Specialists Conference (PVSC). IEEE, Jun. 20, 2021. doi: 10.1109/pvsc43889.2021.9519085.

[107]: R. W. Andrews and J. M. Pearce, “The effect of spectral albedo on amorphous silicon and crystalline silicon solar photovoltaic device performance,” Solar Energy, vol. 91. Elsevier BV, pp. 233–241, May 2013. doi: 10.1016/j.solener.2013.01.030.

[108]: T. J. B. Carruthers, B. J. Longstaff, W. C. Dennison, E. G. Abal, and K. Aioi, “Measurement of light penetration in relation to seagrass,” Global Seagrass Research Methods. Elsevier, pp. 369–392, 2001. doi: 10.1016/b978-044450891-1/50020-7

[109]: D. Palmer, R. Gottschalg, and T. Betts, “The future scope of large-scale solar in the UK: Site suitability and target analysis,” Renewable Energy, vol. 133. Elsevier BV, pp. 1136–1146, Apr. 2019. doi: 10.1016/j.renene.2018.08.109

[110]: M. A. Green, “Self-consistent optical parameters of intrinsic silicon at 300K including temperature coefficients,” Solar Energy Materials and Solar Cells, vol. 92, no. 11. Elsevier BV, pp. 1305–1310, Nov. 2008. doi: 10.1016/j.solmat.2008.06.009

[111]: T. C. R. Russell, R. Saive and H. A. Atwater, "Thermodynamic Efficiency Limit of Bifacial Solar Cells for Various Spectral Albedos," 2017 IEEE 44th Photovoltaic Specialist Conference (PVSC), Washington, DC, USA, 2017, pp. 1531-1536, doi: 10.1109/PVSC.2017.8366261

[112]: J. C. Blakesley et al., “Effective Spectral Albedo from Satellite Data for Bifacial Gain Calculations of PV Systems,” 37th European Photovoltaic Solar Energy Conference and Exhibition; 1292-1297, 2020, doi: 10.4229/EUPVSEC20202020-5CO.9.3

[113]: N. Riedel-Lyngskær et al., “The effect of spectral albedo in bifacial photovoltaic performance,” Solar Energy, vol. 231. Elsevier BV, pp. 921–935, Jan. 2022. doi: 10.1016/j.solener.2021.12.023

[114]: HIS Markit. (2021). PV Module Supply Chain Tracker 2021.

[115]: S. A. Pelaez, C. Deline, J. S. Stein, B. Marion, K. Anderson, and M. Muller, “Effect of torque-tube parameters on rear-irradiance and rear-shading loss for bifacial PV performance on single-axis tracking systems,” 2019 IEEE 46th Photovoltaic Specialists Conference (PVSC). IEEE, Jun. 16, 2019. doi: 10.1109/pvsc40753.2019.9198975.

[116]: Guerrero-Perez, J., & Berbel, J. N. (2019). BiTEC: How to simulate bifacial projects.

[117]: A. Di Stefano, G. Leotta, and F. Bizzarri, “La Silla PV Plant as a Utility-Scale Side-by-Side Test for Innovative Modules Technologies,” 33rd European Photovoltaic Solar Energy Conference and Exhibition; 1978-1982, 2017, doi: 10.4229/EUPVSEC20172017-6CO.14.1.

[118]: M. T. Patel, M. S. Ahmed, H. Imran, N. Z. Butt, M. R. Khan, and M. A. Alam, “Global analysis of next-generation utility-scale PV: Tracking bifacial solar farms,” Applied Energy, vol. 290. Elsevier BV, p. 116478, May 2021. doi: 10.1016/j.apenergy.2021.116478.

[119]: N. A. Kelly and T. L. Gibson, “Improved photovoltaic energy output for cloudy conditions with a solar tracking system,” Solar Energy, vol. 83, no. 11. Elsevier BV, pp. 2092–2102, Nov. 2009. doi: 10.1016/j.solener.2009.08.009

[120]: L. Burnham, D. Riley, B. Walker, and J. M. Pearce, “Performance of Bifacial Photovoltaic Modules on a Dual-Axis Tracker in a High-Latitude, High-Albedo Environment,” 2019 IEEE 46th Photovoltaic Specialists Conference (PVSC). IEEE, Jun. 2019. doi: 10.1109/pvsc40753.2019.8980964.

[121]: C. A. Gueymard, D. Myers, and K. Emery, “Proposed reference irradiance spectra for solar energy systems testing,” Solar Energy, vol. 73, no. 6. Elsevier BV, pp. 443–467, Dec. 2002. doi: 10.1016/s0038-092x(03)00005-7

[122]: Rodríguez-Gallegos, C. D., Gandhi, O., Panda, S. K., & Reindl, T. (2020). On the PV Tracker Performance: Tracking the Sun Versus Tracking the Best Orientation. IEEE Journal of Photovoltaics, 10(5), 1474-1480. doi:10.1109/JPHOTOV.2020.3006994.

[123]: H. Mousazadeh, A. Keyhani, A. Javadi, H. Mobli, K. Abrinia, and A. Sharifi, "A review of principle and sun-tracking methods for maximizing solar systems output," Renewable and Sustainable Energy Reviews, vol. 13, no. 8. Elsevier BV, pp. 1800–1818, Oct. 2009. doi: 10.1016/j.rser.2009.01.022.

[124]: E. Lorenzo, L. Narvarte, and J. Muñoz, "Tracking and back-tracking," Progress in Photovoltaics: Research and Applications, vol. 19, no. 6. Wiley, pp. 747–753, Feb. 23, 2011. doi: 10.1002/pip.1085.

[125]: O. Ayadi, M. Jamra, A. Jaber, L. Ahmad, and M. Alnaqep, "An Experimental Comparison of Bifacial and Monofacial PV Modules," 2021 12th International Renewable Engineering Conference (IREC). IEEE, Apr. 14, 2021. doi: 10.1109/irec51415.2021.9427864.

[126]: M. Chiodetti, J. Kang, C. Reise, and A. Lindsay, "Predicting Yields of Bifacial PV Power Plants – What Accuracy Is Possible?," 35th European Photovoltaic Solar Energy Conference and Exhibition; 1623-1629, 2018, doi: 10.4229/35THEUPVSEC20182018-6CO.3.4.

[127]: N. Riedel-Lyngskær et al., "Validation of Bifacial Photovoltaic Simulation Software against Monitoring Data from Large-Scale Single-Axis Trackers and Fixed Tilt Systems in Denmark," Applied Sciences, vol. 10, no. 23. MDPI AG, p. 8487, Nov. 27, 2020. doi: 10.3390/app10238487.

[128]: C. Pike, E. Whitney, M. Wilber, and J. S. Stein, "Field Performance of South-Facing and East-West Facing Bifacial Modules in the Arctic," Energies, vol. 14, no. 4. MDPI AG, p. 1210, Feb. 23, 2021. doi: 10.3390/en14041210.

[129]: J. S. Stein, D. Riley, M. Lave, C. Hansen, C. Deline, and F. Toor, "Outdoor Field Performance from Bifacial Photovoltaic Modules and Systems," 2017 IEEE 44th Photovoltaic Specialist Conference (PVSC). IEEE, Jun. 2017. doi: 10.1109/pvsc.2017.8366042.

[130]: A. Asgharzadeh et al., "A Benchmark and Validation of Bifacial PV Irradiance Models," 2019 IEEE 46th Photovoltaic Specialists Conference (PVSC). IEEE, Jun. 2019. doi: 10.1109/pvsc40753.2019.8981272.

[131]: Y. Seo et al., "Effect of Front Irradiance and Albedo on Bifacial Gain in 1.8kW Bifacial Silicon Photovoltaic System," 2019 IEEE 46th Photovoltaic Specialists Conference (PVSC). IEEE, Jun. 2019. doi: 10.1109/pvsc40753.2019.8980585.

[132]: M. Bahiraei, N. Mazaheri, and M. Hanooni, “Employing a novel crimped-spiral rib inside a triple-tube heat exchanger working with a nanofluid for solar thermal applications: Irreversibility characteristics,” Sustainable Energy Technologies and Assessments, vol. 52. Elsevier BV, p. 102080, Aug. 2022. doi: 10.1016/j.seta.2022.102080.

[133]: H. Akbari Variani, A. Afshar, M. Vahabzadeh, A. Molajou, and M. M. Akbari Varyani, “Development of a novel framework for agriculture simulation model for food-energy-water nexus analysis in watershed-scale,” Journal of Cleaner Production, vol. 429. Elsevier BV, p. 139492, Dec. 2023. doi: 10.1016/j.jclepro.2023.139492.

[134]: R. F. Ferreira, R. A. Marques Lameirinhas, C. P. Correia V. Bernardo, J. P. N. Torres, and M. Santos, “Agri-PV in Portugal: How to combine agriculture and photovoltaic production,” Energy for Sustainable Development, vol. 79. Elsevier BV, p. 101408, Apr. 2024. doi: 10.1016/j.esd.2024.101408.

[135]: M. Trommsdorff, M. Hopf, O. Hörnle, M. Berwind, S. Schindele, and K. Wydra, “Can synergies in agriculture through an integration of solar energy reduce the cost of agrivoltaics? An economic analysis in apple farming,” Applied Energy, vol. 350. Elsevier BV, p. 121619, Nov. 2023. doi: 10.1016/j.apenergy.2023.121619.

[136]: S. Schindele et al., “Implementation of agrophotovoltaics: Techno-economic analysis of the price-performance ratio and its policy implications,” Applied Energy, vol. 265. Elsevier BV, p. 114737, May 2020. doi: 10.1016/j.apenergy.2020.114737.

[137]: M. Sojib Ahmed, M. Rezwan Khan, A. Haque, and M. Ryyan Khan, “Agrivoltaics analysis in a techno-economic framework: Understanding why agrivoltaics on rice will always be profitable,” Applied Energy, vol. 323. Elsevier BV, p. 119560, Oct. 2022. doi: 10.1016/j.apenergy.2022.119560.

[138]: B. Willockx, C. Lavaert, and J. Cappelle, “Performance evaluation of vertical bifacial and single-axis tracked agrivoltaic systems on arable land,” Renewable Energy, vol. 217. Elsevier BV, p. 119181, Nov. 2023. doi: 10.1016/j.renene.2023.119181.

[139]: P. E. Campana, B. Stridh, S. Amaducci, and M. Colauzzi, “Optimisation of vertically mounted agrivoltaic systems,” Journal of Cleaner Production, vol. 325. Elsevier BV, p. 129091, Nov. 2021. doi: 10.1016/j.jclepro.2021.129091.

[140]: S. Edouard, D. Combes, M. Van Iseghem, M. Ng Wing Tin, and A. J. Escobar-Gutiérrez, “Increasing land productivity with agriphotovoltaics: Application to an alfalfa field,” Applied Energy, vol. 329. Elsevier BV, p. 120207, Jan. 2023. doi: 10.1016/j.apenergy.2022.120207.

[141]: P. E. Campana et al., “Experimental results, integrated model validation, and economic aspects of agrivoltaic systems at northern latitudes,” Journal of Cleaner Production, vol. 437. Elsevier BV, p. 140235, Jan. 2024. doi: 10.1016/j.jclepro.2023.140235.

[142]: Y. J. K. Musleh and T. Rahman, “Predictive models for photosynthetic active radiation irradiance in temperate climates,” Renewable and Sustainable Energy Reviews, vol. 200. Elsevier BV, p. 114599, Aug. 2024. doi: 10.1016/j.rser.2024.114599.

[143]: E. Mouhib et al., “Enhancing land use: Integrating bifacial PV and olive trees in agrivoltaic systems,” Applied Energy, vol. 359. Elsevier BV, p. 122660, Apr. 2024. doi: 10.1016/j.apenergy.2024.122660.

[144]: K. J. McCree, “Test of current definitions of photosynthetically active radiation against leaf photosynthesis data,” Agricultural Meteorology, vol. 10. Elsevier BV, pp. 443–453, Jan. 1972. doi: 10.1016/0002-1571(72)90045-3.

[145]: J. Widmer, B. Christ, J. Grenz, and L. Norgrove, “Agrivoltaics, a promising new tool for electricity and food production: A systematic review,” Renewable and Sustainable Energy Reviews, vol. 192. Elsevier BV, p. 114277, Mar. 2024. doi: 10.1016/j.rser.2023.114277.

[146]: R. Jegan, Walter D. Leon-Salas, Miguel A. Vizcardo, and Mauricio Postigo-Malaga, “Photosynthetically Active Radiation (PAR): A Review of Sensing Solutions,” 淡江理工學刊, vol. 26, no. 3, Mar. 2023, doi: 10.6180/jase.202303_26(3).0010.

[147]: I. L. Lozano, G. Sánchez-Hernández, J. L. Guerrero-Rascado, I. Alados, and I. Foyo-Moreno, “Analysis of cloud effects on long-term global and diffuse photosynthetically active radiation at a Mediterranean site,” Atmospheric Research, vol. 268. Elsevier BV, p. 106010, Apr. 2022. doi: 10.1016/j.atmosres.2021.106010.

[148]: C. A. Gueymard, “Direct solar transmittance and irradiance predictions with broadband models. Part I: detailed theoretical performance assessment,” Solar Energy, vol. 74, no. 5. Elsevier BV, pp. 355–379, May 2003. doi: 10.1016/s0038-092x(03)00195-6

[149]: C. A. Gueymard, “A review of validation methodologies and statistical performance indicators for modeled solar radiation data: Towards a better bankability of solar projects,”

Renewable and Sustainable Energy Reviews, vol. 39. Elsevier BV, pp. 1024–1034, Nov. 2014. doi: 10.1016/j.rser.2014.07.117.

[150]: L. T. Wong and W. K. Chow, “Solar radiation model,” Applied Energy, vol. 69, no. 3. Elsevier BV, pp. 191–224, Jul. 2001. doi: 10.1016/s0306-2619(01)00012-5.

[151]: R. Yacef, A. Mellit, S. Belaid, and Z. Şen, “New combined models for estimating daily global solar radiation from measured air temperature in semi-arid climates: Application in Ghardaïa, Algeria,” Energy Conversion and Management, vol. 79. Elsevier BV, pp. 606–615, Mar. 2014. doi: 10.1016/j.enconman.2013.12.057.

[152]: M. R. Yaiche, A. Bouhanik, S. M. A. Bekkouche, A. Malek, and T. Benouaz, “Revised solar maps of Algeria based on sunshine duration,” Energy Conversion and Management, vol. 82. Elsevier BV, pp. 114–123, Jun. 2014. doi: 10.1016/j.enconman.2014.02.063.

[153]: B. Y. H. Liu and R. C. Jordan, “The interrelationship and characteristic distribution of direct, diffuse and total solar radiation,” Solar Energy, vol. 4, no. 3. Elsevier BV, pp. 1–19, Jul. 1960. doi:10.1016/0038-092x(60)90062-1.

[154]: J. A. Ruiz-Arias, H. Alsamamra, J. Tovar-Pescador, and D. Pozo-Vázquez, “Proposal of a regressive model for the hourly diffuse solar radiation under all sky conditions,” Energy Conversion and Management, vol. 51, no. 5. Elsevier BV, pp. 881–893, May 2010. doi: 10.1016/j.enconman.2009.11.024.

[155]: J. F. Orgill and K. G. T. Hollands, “Correlation equation for hourly diffuse radiation on a horizontal surface,” Solar Energy, vol. 19, no. 4. Elsevier BV, pp. 357–359, 1977. doi: 10.1016/0038-092x(77)90006-8.

[156]: D. G. Erbs, S. A. Klein, and J. A. Duffie, “Estimation of the diffuse radiation fraction for hourly, daily and monthly-average global radiation,” Solar Energy, vol. 28, no. 4. Elsevier BV, pp. 293–302, 1982. doi: 10.1016/0038-092x(82)90302-4.

[157]. T. Reindl, W. A. Beckman, and J. A. Duffie, “Diffuse fraction correlations,” Solar Energy, vol. 45, no. 1. Elsevier BV, pp. 1–7, 1990. doi: 10.1016/0038-092x(90)90060-p.

[158]: B. Ridley, J. Boland, and P. Lauret, “Modelling of diffuse solar fraction with multiple predictors,” Renewable Energy, vol. 35, no. 2. Elsevier BV, pp. 478–483, Feb. 2010. doi: 10.1016/j.renene.2009.07.018.

[159]: N. A. Engerer, “Minute resolution estimates of the diffuse fraction of global irradiance for southeastern Australia,” Solar Energy, vol. 116. Elsevier BV, pp. 215–237, Jun. 2015. doi:10.1016/j.solener.2015.04.012.

[160]: W. Yao, Z. Li, Y. Wang, F. Jiang, and L. Hu, “Evaluation of global solar radiation models for Shanghai, China,” Energy Conversion and Management, vol. 84. Elsevier BV, pp. 597–612, Aug. 2014. doi: 10.1016/j.enconman.2014.04.017.

[161]: O. Behar, A. Khellaf, and K. Mohammedi, “Comparison of solar radiation models and their validation under Algerian climate – The case of direct irradiance,” Energy Conversion and Management, vol. 98. Elsevier BV, pp. 236–251, Jul. 2015. doi: 10.1016/j.enconman.2015.03.067.

[162]: Y. Zhou, D. Wang, Y. Liu, and J. Liu, “Diffuse solar radiation models for different climate zones in China: Model evaluation and general model development,” Energy Conversion and Management, vol. 185. Elsevier BV, pp. 518–536, Apr. 2019. doi: 10.1016/j.enconman.2019.02.013.

[163]: J. Stein, C. Hansen, and M. Reno, “Global horizontal irradiance clear sky models : implementation and analysis.,” Office of Scientific and Technical Information (OSTI), Mar. 2012. doi: 10.2172/1039404.

[164]: K. Yin, X. Zhang, J. Xie, Z. Hao, G. Xiao, and J. Liu, “Modeling hourly solar diffuse fraction on a horizontal surface based on sky conditions clustering,” Energy, vol. 272. Elsevier BV, p. 127008, Jun. 2023. doi: 10.1016/j.energy.2023.127008.

[165]: J. M. Bright and N. A. Engerer, “Engerer2: Global re-parameterisation, update, and validation of an irradiance separation model at different temporal resolutions,” Journal of Renewable and Sustainable Energy, vol. 11, no. 3. AIP Publishing, May 01, 2019. doi: 10.1063/1.5097014.

[166]: K. Bakirci, “Prediction of diffuse radiation in solar energy applications: Turkey case study and compare with satellite data,” Energy, vol. 237. Elsevier BV, p. 121527, Dec. 2021. doi: 10.1016/j.energy.2021.121527.

[167]: A. R. Starke, L. F. L. Lemos, J. Boland, J. M. Cardemil, and S. Colle, “Resolution of the cloud enhancement problem for one-minute diffuse radiation prediction,” Renewable Energy, vol. 125. Elsevier BV, pp. 472–484, Sep. 2018. doi: 10.1016/j.renene.2018.02.107.

[168]: P. Ineichen, “A broadband simplified version of the Solis clear sky model,” Solar Energy, vol. 82, no. 8. Elsevier BV, pp. 758–762, Aug. 2008. doi: 10.1016/j.solener.2008.02.009.

[169]: E. Paulescu and R. Blaga, “A simple and reliable empirical model with two predictors for estimating 1-minute diffuse fraction,” Solar Energy, vol. 180. Elsevier BV, pp. 75–84, Mar. 2019. doi: 10.1016/j.solener.2019.01.029.

[170]: A. R. Starke et al., “Assessing one-minute diffuse fraction models based on worldwide climate features,” Renewable Energy, vol. 177. Elsevier BV, pp. 700–714, Nov. 2021. doi: 10.1016/j.renene.2021.05.108.

[171]: J. Boland, J. Huang, and B. Ridley, “Decomposing global solar radiation into its direct and diffuse components,” Renewable and Sustainable Energy Reviews, vol. 28. Elsevier BV, pp. 749–756, Dec. 2013. doi: 10.1016/j.rser.2013.08.023.

[172]: J. P. Every, L. Li, and D. G. Dorrell, “Köppen-Geiger climate classification adjustment of the BRL diffuse irradiation model for Australian locations,” Renewable Energy, vol. 147. Elsevier BV, pp. 2453–2469, Mar. 2020. doi: 10.1016/j.renene.2019.09.114.

[173]: D. Yang, “Estimating 1-min beam and diffuse irradiance from the global irradiance: A review and an extensive worldwide comparison of latest separation models at 126 stations,” Renewable and Sustainable Energy Reviews, vol. 159. Elsevier BV, p. 112195, May 2022. doi: 10.1016/j.rser.2022.112195.

[174]: Lefèvre M, Oumbe A, Blanc P, Espinar B, Gschwind B, Qu Z, Wald L, Homscheidt MS, Hoyer-Klick C, Arola A, et al. McClear: a new model estimating downwelling solar radiation at ground level in clear-sky conditions. Atmos Meas Tech 2013;6:2403–18.

[175]: D. Yang and J. Boland, “Satellite-augmented diffuse solar radiation separation models,” Journal of Renewable and Sustainable Energy, vol. 11, no. 2. AIP Publishing, Mar. 01, 2019. doi: 10.1063/1.5087463.

[176]: Y. Chu, D. Yang, H. Yu, X. Zhao, and M. Li, “Can end-to-end data-driven models outperform traditional semi-physical models in separating 1-min irradiance?,” Applied Energy, vol. 356. Elsevier BV, p. 122434, Feb. 2024. doi: 10.1016/j.apenergy.2023.122434.

[177]: D. Yang et al., “Regime-dependent 1-min irradiance separation model with climatology clustering,” Renewable and Sustainable Energy Reviews, vol. 189. Elsevier BV, p. 113992, Jan. 2024. doi: 10.1016/j.rser.2023.113992.

[178]: D. Palmer, I. Cole, T. Betts, and R. Gottschalg, “Interpolating and Estimating Horizontal Diffuse Solar Irradiation to Provide UK-Wide Coverage: Selection of the Best Performing Models,” Energies, vol. 10, no. 2. MDPI AG, p. 181, Feb. 05, 2017. doi: 10.3390/en10020181.

[179]: A. de Miguel, J. Bilbao, R. Aguiar, H. Kambezidis, and E. Negro, “Diffuse solar irradiation model evaluation in the North Mediterranean Belt area,” Solar Energy, vol. 70, no. 2. Elsevier BV, pp. 143–153, 2001. doi: 10.1016/s0038-092x(00)00135-3.

[180]: M. Nunez Munoz, E. E. F. Ballantyne, and D. A. Stone, “Development and evaluation of empirical models for the estimation of hourly horizontal diffuse solar irradiance in the United Kingdom,” Energy, vol. 241. Elsevier BV, p. 122820, Feb. 2022. doi: 10.1016/j.energy.2021.122820

[181]: Y. F. Nassar, S. Y. Alsadi, H. J. El-Khozondar, and S. S. Refaat, “Determination of the most accurate horizontal to tilted sky-diffuse solar irradiation transposition model for the capital cities in MENA region,” in Proc. IEEE 3rd Int. Conf. Smart Grid Renewable Energy, Doha, Qatar, 2022, pp. 1–6, doi: 10.1109/SGRE53517.2022.9774146.

[182]: J. Freeman, J. Whitmore, N. Blair, and A. P. Dobos, “Validation of multiple tools for flat plate photovoltaic modeling against measured data,” in Proc. IEEE 40th Photovolt. Specialist Conf., Denver, CO, USA, 2014, pp. 1932–1937, doi: 10.1109/PVSC.2014.6925304

[183]: E. L. Maxwell, “A quasi-physical model for converting hourly global horizontal to direct normal insolation,” Solar Energy Research Institute, Golden, CO, USA, Tech. Rep. SERI/TR-215-3087, 1987.

[184]: R. R. Perez, P. Ineichen, E. L. Maxwell, R. D. Seals, and A. Zelenka, “Dynamic global-to-direct irradiance conversion models,” ASHRAE Trans., vol. 98, pp. 354–369, 1992

[185]: R. Perez, P. Ineichen, R. Seals, J. Michalsky, and R. Stewart, “Modeling daylight availability and irradiance components from direct and global irradiance,” Sol. Energy, vol. 44, no. 5, pp. 271–289, 1990, doi: 10.1016/0038-092x(90)90055-h.

[186]: B. Y. H. Liu and R. C. Jordan, “The long-term average performance of flat-plate solar-energy collectors,” Sol. Energy, vol. 7, no. 2, pp. 53–74, Apr. 1963, doi: 10.1016/0038- 092x(63)90006-9.

[187]: A. Skartveit and J. A. Olseth, “Modelling slope irradiance at high latitudes,” Sol. Energy, vol. 36, no. 4, pp. 333–344, 1986, doi: 10.1016/0038-092x(86)90151-9.

[188]: R. C. Temps and K. L. Coulson, “Solar radiation incident upon slopes of different orientations,” Sol. Energy, vol. 19, no. 2, pp. 179–184, 1977, doi: 10.1016/0038-092x(77)90056-1.

[189]: C. J. Willmott, “On the climatic optimization of the tilt and azimuth of flat-plate solar collectors,” Sol. Energy, vol. 28, no. 3, pp. 205–216, 1982, doi: 10.1016/0038-092x(82)90159-1.

[190]: J. W. Bugler, “The determination of hourly insolation on an inclined plane using a diffuse irradiance model based on hourly measured global horizontal insolation,” Sol. Energy, vol. 19, no. 5, pp. 477–491, 1977, doi: 10.1016/0038-092x(77)90103-7.

[191]: J. E. Hay, “Study of shortwave radiation on non-horizontal surfaces,” Canadian Climate Centre Report, Downs View, 1979.

[192]: Logiciel Photovoltaïque, Pvsyst, 2013. [Online]. Available: https://www. pvsyst.com/

[193]: Insel Group AG, 2021. [Online]. Available: https://insel.eu/en/home_en. html

[194]: Natural Resources Canada, RETScreen, 2016. [Online]. Available: https://naturalresources.Canada.ca/maps-tools-and-publications/tools/ modelling-tools/retscreen/7465

[195]: M. M. D. Ross, D. Turcotte, and M. A. Fry, “PVToolbox simulation output compared with monitored data from PV hybrid test bench,” in Proc. 30th Annu. Conf. Sol. Energy Soc., Canada, 2005, pp. 8–16.

[196]: TRNSYS, 2017. [Online]. Available: https://www.trnsys.com/

[197]: SolarAnywhere, 2023. [Online]. Available: https://www.solaranywhere. com/

[198]: Solargis, 2022. [Online]. Available: https://solargis.com/

[199]: Meteonorm, 2016. [Online]. Available: https://meteonorm.com/en/

[200]: S. Summa, G. Remia, A. Sebastianelli, G. Coccia, and C. Di Perna, “Impact on thermal energy needs caused by the use of different solar irradiance decomposition and transposition models: Application of EN ISO 52016-1 and EN ISO 52010-1 standards for five European cities,” Energies, vol. 15, no. 23, Nov. 2022, Art. no. 8904, doi: 10.3390/en15238904.

[201]: PVSOL Software, 2022. [Online]. Available: https://pvsol.software/en/

[202]: J. M. Bright, “The impact of globally diverse GHI training data: Evaluation through application of a simple Markov chain downscaling methodology,” Journal of Renewable and Sustainable Energy, vol. 11, no. 2. AIP Publishing, Mar. 01, 2019. doi: 10.1063/1.5085236.

[203]: J. E. Castillo-Aguilella and P. S. Hauser, "Multi-Variable Bifacial Photovoltaic Module Test Results and Best-Fit Annual Bifacial Energy Yield Model," in IEEE Access, vol. 4, pp. 498-506, 2016, doi: 10.1109/ACCESS.2016.2518399.

[204]: S. Ayala Pelaez, C. A. Deline, W. F. Marion, W. R. Sekulic, and J. S. Stein, "Understanding Bifacial PV Modeling: Raytracing and View Factor Models," [Online]. Available: https://www.osti.gov/servlets/purl/1597241.

[205]: McMillan, J. E. (1995). The Optics of Particle Detection: Note 1 Geometrical Configuration Factors in the Design and Utilization of Particle Detectors. CERN Libraries, Geneva

[206]: J. Manuel Longares, A. García-Jiménez, and N. García-Polanco, “Multiphysics simulation of bifacial photovoltaic modules and software comparison,” Solar Energy, vol. 257. Elsevier BV, pp. 155–163, Jun. 2023. doi: 10.1016/j.solener.2023.04.005.

[207]: M. S. Lave, “Albedo and Diffuse POA Measurements to Evaluate Transposition Model Uncertainty,” Office of Scientific and Technical Information (OSTI), Oct. 2015. doi: 10.2172/1529054

[208]: Asgharzadeh, Amir, Toor, Fatima, Riley, Daniel, Stein, Joshua, Hansen, Clifford, Marion, William F, MacAlpine, Sara M, and Deline, Christopher A. A Practical Irradiance Model for Bifacial PV Modules. United States: N. p., 2018. Web. doi:10.1109/PVSC.2017.8366263.

[209]: C.-W. Kuo, W.-C. Chang, and K.-C. Chang, “Modeling the hourly solar diffuse fraction in Taiwan,” Renewable Energy, vol. 66. Elsevier BV, pp. 56–61, Jun. 2014. doi: 10.1016/j.renene.2013.11.072.

[210]: J. E. Hay, “Calculating solar radiation for inclined surfaces: Practical approaches,” Renewable Energy, vol. 3, no. 4–5. Elsevier BV, pp. 373–380, Jun. 1993. doi: 10.1016/0960-1481(93)90104-o.

[211]: D. T. Reindl, W. A. Beckman, and J. A. Duffie, “Evaluation of hourly tilted surface radiation models,” Solar Energy, vol. 45, no. 1. Elsevier BV, pp. 9–17, 1990. doi: 10.1016/0038-092x(90)90061-g.

[212]: T. M. Klucher, “Evaluation of models to predict insolation on tilted surfaces,” Solar Energy, vol. 23, no. 2. Elsevier BV, pp. 111–114, 1979. doi: 10.1016/0038-092x(79)90110-5.

[213]: J. E. Hay, “Calculation of solar irradiances for inclined surfaces: Validation of selected hourly and daily models,” Atmosphere-Ocean, vol. 24, no. 1. Informa UK Limited, pp. 16–41, Mar. 1986. doi: 10.1080/07055900.1986.9649238.

[214]: P. S. Koronakis, “On the choice of the angle of tilt for south facing solar collectors in the Athens basin area,” Solar Energy, vol. 36, no. 3. Elsevier BV, pp. 217–225, 1986. doi: 10.1016/0038-092x(86)90137-4.

[215]: Jimenez, J., & Castro, Y. (1986). National Assembly of Geophysics and Geodesy, Vol. II.

[216]: Y. Q. Tian, R. J. Davies-Colley, P. Gong, and B. W. Thorrold, “Estimating solar radiation on slopes of arbitrary aspect,” Agricultural and Forest Meteorology, vol. 109, no. 1. Elsevier BV, pp. 67–74, Aug. 2001. doi: 10.1016/s0168-1923(01)00245-3.

[217]: V. Badescu, “3D isotropic approximation for solar diffuse irradiance on tilted surfaces,” Renewable Energy, vol. 26, no. 2. Elsevier BV, pp. 221–233, Jun. 2002. doi: 10.1016/s0960-1481(01)00123-9.

[218]: Arttu Tuomiranta and H. Ghedira, “Evaluation of Decomposition and Transposition Models for Irradiance Data Conversion under a Hot Desert Climate,” Unpublished, 2015, doi: 10.13140/RG.2.2.34482.89288.

[219]: M. S. Okundamiya, J. O. Emagbetere, and E. A. Ogujor, “Evaluation of various global solar radiation models for Nigeria,” International Journal of Green Energy, vol. 13, no. 5. Informa UK Limited, pp. 505–512, Jan. 06, 2015. doi: 10.1080/15435075.2014.968921.

[220]: R. Moretón, E. Lorenzo, A. Pinto, J. Muñoz, and L. Narvarte, “From broadband horizontal to effective in-plane irradiation: A review of modelling and derived uncertainty for PV yield prediction,” Renewable and Sustainable Energy Reviews, vol. 78. Elsevier BV, pp. 886–903, Oct. 2017. doi: 10.1016/j.rser.2017.05.020.

[221]: P. I. Raptis, S. Kazadzis, B. Psiloglou, N. Kouremeti, P. Kosmopoulos, and A. Kazantzidis, “Measurements and model simulations of solar radiation at tilted planes, towards the maximization of energy capture,” Energy, vol. 130. Elsevier BV, pp. 570–580, Jul. 2017. doi: 10.1016/j.energy.2017.04.122.

[222]: R. Mubarak, M. Hofmann, S. Riechelmann, and G. Seckmeyer, “Comparison of Modelled and Measured Tilted Solar Irradiance for Photovoltaic Applications,” Energies, vol. 10, no. 11. MDPI AG, p. 1688, Oct. 25, 2017. doi: 10.3390/en10111688.

[223]: D. Yang, “Solar radiation on inclined surfaces: Corrections and benchmarks,” Solar Energy, vol. 136. Elsevier BV, pp. 288–302, Oct. 2016. doi: 10.1016/j.solener.2016.06.062.

[224]: Wlodarczyk and H. Nowak, “Statistical analysis of solar radiation models onto inclined planes for climatic conditions of Lower Silesia in Poland,” Archives of Civil and Mechanical Engineering, vol. 9, no. 2. Springer Science and Business Media LLC, pp. 127–144, Jan. 2009. doi: 10.1016/s1644-9665(12)60064-8.

[225]: U. A. Yusufoglu, T. M. Pletzer, L. J. Koduvelikulathu, C. Comparotto, R. Kopecek, and H. Kurz, “Analysis of the Annual Performance of Bifacial Modules and Optimization Methods,” IEEE Journal of Photovoltaics, vol. 5, no. 1. Institute of Electrical and Electronics Engineers (IEEE), pp. 320–328, Jan. 2015. doi: 10.1109/jphotov.2014.2364406.

[226]: C. D. Rodríguez-Gallegos, M. Bieri, O. Gandhi, J. P. Singh, T. Reindl, and S. K. Panda, “Monofacial vs bifacial Si-based PV modules: Which one is more cost-effective?,” Solar Energy, vol. 176. Elsevier BV, pp. 412–438, Dec. 2018. doi: 10.1016/j.solener.2018.10.012.

[227]: X. Sun, M. R. Khan, C. Deline, and M. A. Alam, “Optimization and performance of bifacial solar modules: A global perspective,” Applied Energy, vol. 212. Elsevier BV, pp. 1601–1610, Feb. 2018. doi: 10.1016/j.apenergy.2017.12.041.

[228]: D. Yang, Z. Dong, A. Nobre, Y. S. Khoo, P. Jirutitijaroen, and W. M. Walsh, “Evaluation of transposition and decomposition models for converting global solar irradiance from tilted surface to horizontal in tropical regions,” Solar Energy, vol. 97. Elsevier BV, pp. 369–387, Nov. 2013. doi: 10.1016/j.solener.2013.08.033.

[229]: M. Manni, A. Nocente, M. Bellmann, and G. Lobaccaro, “Multi-Stage Validation of a Solar Irradiance Model Chain: An Application at High Latitudes,” Sustainability, vol. 15, no. 4. MDPI AG, p. 2938, Feb. 06, 2023. doi: 10.3390/su15042938.

[230]: J. J. Roberts, A. A. Mendiburu Zevallos, and A. M. Cassula, “Assessment of photovoltaic performance models for system simulation,” Renewable and Sustainable Energy Reviews, vol. 72. Elsevier BV, pp. 1104–1123, May 2017. doi: 10.1016/j.rser.2016.10.022.

[231]: C. A. Gueymard, “Direct and indirect uncertainties in the prediction of tilted irradiance for solar engineering applications,” Solar Energy, vol. 83, no. 3. Elsevier BV, pp. 432–444, Mar. 2009. doi: 10.1016/j.solener.2008.11.004.

[232]: M. Hofmann and G. Seckmeyer, “Influence of Various Irradiance Models and Their Combination on Simulation Results of Photovoltaic Systems,” Energies, vol. 10, no. 10. MDPI AG, p. 1495, Sep. 26, 2017. doi: 10.3390/en10101495.

[233]: D. Yang, “Choice of clear-sky model in solar forecasting,” Journal of Renewable and Sustainable Energy, vol. 12, no. 2. AIP Publishing, Mar. 01, 2020. doi: 10.1063/5.0003495.

[234]: Threlkeld J, Jordan R. Direct solar radiation available on clear days. Heat, Piping Air Cond. 1957;29(12).

[235]: Y. El Mghouchi, A. El Bouardi, Z. Choulli, and T. Ajzoul, “New model to estimate and evaluate the solar radiation,” International Journal of Sustainable Built Environment, vol. 3, no. 2. Elsevier BV, pp. 225–234, Dec. 2014. doi: 10.1016/j.ijsbe.2014.11.001.

[236]: L. Kumar, A. L. Skidmore, and E. Knowles, “Modelling topographic variation in solar radiation in a GIS environment,” International Journal of Geographical Information Science, vol. 11, no. 5. Informa UK Limited, pp. 475–497, Jul. 1997. doi: 10.1080/136588197242266.

[237]: P. Ineichen and R. Perez, “A new airmass independent formulation for the Linke turbidity coefficient,” Solar Energy, vol. 73, no. 3. Elsevier BV, pp. 151–157, Sep. 2002. doi: 10.1016/s0038-092x(02)00045-2.

[238]: M. Bashahu and D. Laplaze, “An atmospheric model for computing solar radiation,” Renewable Energy, vol. 4, no. 4. Elsevier BV, pp. 455–458, Jun. 1994. doi: 10.1016/0960-1481(94)90054-x.

[239]: J. A. Davies and D. C. McKay, “Estimating solar irradiance and components,” Solar Energy, vol. 29, no. 1. Elsevier BV, pp. 55–64, 1982. doi: 10.1016/0038-092x(82)90280-8.

[240]: C. A. Gueymard, “REST2: High-performance solar radiation model for cloudless-sky irradiance, illuminance, and photosynthetically active radiation – Validation with a benchmark dataset,” Solar Energy, vol. 82, no. 3. Elsevier BV, pp. 272–285, Mar. 2008. doi: 10.1016/j.solener.2007.04.008.

[241]: S. Mandel, “When it comes to forecasting solar irradiance a complex model is not necessarily the best,” Scilight, vol. 2020, no. 13. AIP Publishing, Mar. 25, 2020. doi: 10.1063/10.0001026.

[242]: V. Badescu et al., “Computing global and diffuse solar hourly irradiation on clear sky. Review and testing of 54 models,” Renewable and Sustainable Energy Reviews, vol. 16, no. 3. Elsevier BV, pp. 1636–1656, Apr. 2012. doi: 10.1016/j.rser.2011.12.010.

[243]: Cros, S., Liandrat, O., Sébastien, N., Schmutz, N., Voyant, C., 2013. Clear sky models assessment for an operational PV production forecasting solution. In: Proc. 28th European Photovoltaic Solar Energy Conference, Paris, France.

[244]: Sengupta, M., Habte, A., Gotseff, P., Weekley, A., Lopez, A., 2014. A physics-based GOES satellite product for use in NREL’s National Solar Radiation Database. In: Proc. Solar 2014 Conf., San Francisco, CA, American Solar Energy Soc

[245]: J. A. Ruiz-Arias and C. A. Gueymard, “Worldwide inter-comparison of clear-sky solar radiation models: Consensus-based review of direct and global irradiance components simulated at the earth surface,” Solar Energy, vol. 168. Elsevier BV, pp. 10–29, Jul. 2018. doi: 10.1016/j.solener.2018.02.008.

[246]: X. Sun, J. M. Bright, C. A. Gueymard, B. Acord, P. Wang, and N. A. Engerer, “Worldwide performance assessment of 75 global clear-sky irradiance models using Principal Component Analysis,” Renewable and Sustainable Energy Reviews, vol. 111. Elsevier BV, pp. 550–570, Sep. 2019. doi: 10.1016/j.rser.2019.04.006.

[247]: Polo, J., Antonanzas-Torres, F., Vindel, J.M., Ramirez, L., 2014. Sensitivity of satellitebased methods for deriving solar radiation to different choice of aerosol input and models. Renew. Energy 68, 785–792. http://dx.doi.org/10.1016/j.renene.2014.03. 022.

[248]: J. A. Ruiz-Arias and C. A. Gueymard, “Solar Resource for High-Concentrator Photovoltaic Applications,” Green Energy and Technology. Springer International Publishing, pp. 261–302, 2015. doi: 10.1007/978-3-319-15039-0_10.

[249]: C. A. Gueymard, “Impact of on-site atmospheric water vapor estimation methods on the accuracy of local solar irradiance predictions,” Solar Energy, vol. 101. Elsevier BV, pp. 74–82, Mar. 2014. doi: 10.1016/j.solener.2013.12.027.

[250]: J. A. Ruiz-Arias, C. A. Gueymard, and T. Cebecauer, “Direct normal irradiance modeling: Evaluating the impact on accuracy of worldwide gridded aerosol databases,” AIP Conference Proceedings, vol. 2126. AIP Publishing, p. 190013, 2019. doi: 10.1063/1.5117710.

[251]: V. Salamalikis, I. Vamvakas, P. Blanc, and A. Kazantzidis, “Ground-based validation of aerosol optical depth from CAMS reanalysis project: An uncertainty input on direct normal

irradiance under cloud-free conditions," Renewable Energy, vol. 170. Elsevier BV, pp. 847–857, Jun. 2021. doi: 10.1016/j.renene.2021.02.025.

[252]: X. Sun, J. M. Bright, C. A. Gueymard, X. Bai, B. Acord, and P. Wang, "Worldwide performance assessment of 95 direct and diffuse clear-sky irradiance models using principal component analysis," Renewable and Sustainable Energy Reviews, vol. 135. Elsevier BV, p. 110087, Jan. 2021. doi: 10.1016/j.rser.2020.110087.

[253]: C. A. Gueymard, "Clear-sky irradiance predictions for solar resource mapping and large-scale applications: Improved validation methodology and detailed performance analysis of 18 broadband radiative models," Solar Energy, vol. 86, no. 8. Elsevier BV, pp. 2145–2169, Aug. 2012. doi: 10.1016/j.solener.2011.11.011.

[254]: CropWat, Food and Agriculture Organization of the United Nations, 2024. [Online]. Available: https://www.fao.org/land-water/databases-and-software/cropwat/en/

[255]: S. Nwokolo, "A Global Review of Empirical Models for Estimating Photosynthetically Active Radiation," Trends in Renewable Energy, vol. 4, no. 2. Future Energy Service and Publishing, Oct. 2018. doi: 10.17737/tre.2018.4.2.0079.

[256]: L. Wang, W. Gong, B. Hu, A. Lin, H. Li, and L. Zou, "Modeling and analysis of the spatiotemporal variations of photosynthetically active radiation in China during 1961–2012," Renewable and Sustainable Energy Reviews, vol. 49. Elsevier BV, pp. 1019–1032, Sep. 2015. doi: 10.1016/j.rser.2015.04.174.

[257]: S. Peng, Q. Du, A. Lin, B. Hu, K. Xiao, and Y. Xi, "Observation and estimation of photosynthetically active radiation in Lhasa (Tibetan Plateau)," Advances in Space Research, vol. 55, no. 6. Elsevier BV, pp. 1604–1612, Mar. 2015. doi: 10.1016/j.asr.2015.01.002.

[258]: Y. Peng et al., "Energy performance assessment of photovoltaic greenhouses in summer based on coupled optical-electrical-thermal models and plant growth requirements," Energy Conversion and Management, vol. 287. Elsevier BV, p. 117086, Jul. 2023. doi: 10.1016/j.enconman.2023.117086.

[259]: L. J. G. Aguiar et al., "Modeling the photosynthetically active radiation in South West Amazonia under all sky conditions," Theoretical and Applied Climatology, vol. 108, no. 3–4. Springer Science and Business Media LLC, pp. 631–640, Dec. 02, 2011. doi: 10.1007/s00704-011-0556-z.

[260]: F. Ferrera-Cobos, J. M. Vindel, R. X. Valenzuela, and J. A. González, “Models for estimating daily photosynthetically active radiation in oceanic and mediterranean climates and their improvement by site adaptation techniques,” Advances in Space Research, vol. 65, no. 8. Elsevier BV, pp. 1894–1909, Apr. 2020. doi: 10.1016/j.asr.2020.01.018.

[261]: N. Proutsos, S. Alexandris, A. Liakatas, P. Nastos, and I. X. Tsiros, “PAR and UVA composition of global solar radiation at a high altitude Mediterranean forest site,” Atmospheric Research, vol. 269. Elsevier BV, p. 106039, May 2022. doi: 10.1016/j.atmosres.2022.106039.

[262]: J. F. Escobedo, E. N. Gomes, A. P. Oliveira, and J. Soares, “Ratios of UV, PAR and NIR components to global solar radiation measured at Botucatu site in Brazil,” Renewable Energy, vol. 36, no. 1. Elsevier BV, pp. 169–178, Jan. 2011. doi: 10.1016/j.renene.2010.06.018.

[263]: T. K. Akitsu et al., “The variability and seasonality in the ratio of photosynthetically active radiation to solar radiation: A simple empirical model of the ratio,” International Journal of Applied Earth Observation and Geoinformation, vol. 108. Elsevier BV, p. 102724, Apr. 2022. doi: 10.1016/j.jag.2022.102724.

[264]: C. P. Jacovides, F. S. Timvios, G. Papaioannou, D. N. Asimakopoulos, and C. M. Theofilou, “Ratio of PAR to broadband solar radiation measured in Cyprus,” Agricultural and Forest Meteorology, vol. 121, no. 3–4. Elsevier BV, pp. 135–140, Feb. 2004. doi: 10.1016/j.agrformet.2003.10.001.

[265]: B. Hu, Y. Wang, and G. Liu, “Measurements and estimations of photosynthetically active radiation in Beijing,” Atmospheric Research, vol. 85, no. 3–4. Elsevier BV, pp. 361–371, Sep. 2007. doi: 10.1016/j.atmosres.2007.02.005.

[266]: M. de Blas, A. García-Rodríguez, I. García, and J. L. Torres, “Validation and calibration of models to estimate photosynthetically active radiation considering different time scales and sky conditions,” Advances in Space Research, vol. 70, no. 7. Elsevier BV, pp. 1737–1760, Oct. 2022. doi: 10.1016/j.asr.2022.07.005.

[267]: CIE, Standard. "Spitial Distribution of Daylight-CIE Stndard General Sky." CIE S 011.1/E (2003).

[268]: A. García-Rodríguez, D. Granados-López, S. García-Rodríguez, M. Díez-Mediavilla, and C. Alonso-Tristán, “Modelling Photosynthetic Active Radiation (PAR) through meteorological indices under all sky conditions,” Agricultural and Forest Meteorology, vol. 310. Elsevier BV, p. 108627, Nov. 2021. doi: 10.1016/j.agrformet.2021.108627.

[269]: S. Martyn, “MIDAS Data User Guide for UK Land Observations, v20210705.” Zenodo, Jul. 05, 2021. doi: 10.5281/ZENODO.7357335.

[270]: Science and Technology Facilities Council, Chilbolton Facility for Atmospheric and Radio Research, C. L. Wrench, "Chilbolton Facility for Atmospheric and Radio Research (CFARR) Visible Radiometer Data," NCAS British Atmospheric Data Centre, 2023. [Online]. Available: https://catalogue.ceda.ac.uk/uuid/bf70daf01b6257b

[271]: International Organization for Standardization, "ISO 9060:2018 - Solar energy - Specification and classification of instruments for measuring hemispherical solar and direct solar radiation," Geneva, Switzerland, 2018.

[272]: J. Remund, et. al., “Worldwide Linke Turbidity Information”, Proc. ISES Solar World Congress, June 2003. Goteborg, Sweden.

[273]: Handbook AF. American society of heating, refrigerating and air-conditioning engineers. Atlanta, GA, USA: Inc.; 2009.

[274]: NASA Goddard Earth Sciences Data and Information Services Center, "NASA Goddard Earth Sciences Data and Information Services Center Datasets," [Online]. Available: https://disc.gsfc.nasa.gov/datasets/.

[275]: M. A. Mikofski, W. F. Holmgren, J. Newmiller and R. Kharait, "Effects of Solar Resource Sampling Rate and Averaging Interval on Hourly Modeling Errors," in IEEE Journal of Photovoltaics, vol. 13, no. 2, pp. 202-207, March 2023, doi: 10.1109/JPHOTOV.2023.3238512.

[276]: "ICOS Carbon Portal," https://www.icos-cp.eu/

[277]: A. Carrara et al., “Radiation measurements at ICOS ecosystem stations,” International Agrophysics, vol. 32, no. 4. Walter de Gruyter GmbH, pp. 589–605, Dec. 01, 2018. doi: 10.1515/intag-2017-0049.

[278]: M. Oh et al., “Analysis of minute-scale variability for enhanced separation of direct and diffuse solar irradiance components using machine learning algorithms,” Energy, vol. 241. Elsevier BV, p. 122921, Feb. 2022. doi: 10.1016/j.energy.2021.122921.

[279]: P. Y. Tan and M. R. B. Ismail, “Photosynthetically active radiation and comparison of methods for its estimation in equatorial Singapore,” Theoretical and Applied Climatology, vol. 123, no. 3–4. Springer Science and Business Media LLC, pp. 873–883, Feb. 13, 2015. doi: 10.1007/s00704-015-1399-9.

[280]: I. Alados, I. Foyo-Moreno, and L. Alados-Arboledas, “Photosynthetically active radiation: measurements and modelling,” Agricultural and Forest Meteorology, vol. 78, no. 1–2. Elsevier BV, pp. 121–131, Jan. 1996. doi: 10.1016/0168-1923(95)02245-7.

[281]: E. Molin, B. Stridh, A. Molin, and E. Wackelgard, “Experimental Yield Study of Bifacial PV Modules in Nordic Conditions,” IEEE Journal of Photovoltaics, vol. 8, no. 6. Institute of Electrical and Electronics Engineers (IEEE), pp. 1457–1463, Nov. 2018. doi: 10.1109/jphotov.2018.2865168.

[282]: M. T. Bembe, S. P. Daniel Chowdhury, N. Meeding, E. G. Lekhuleni, M. B. Ayanna, and S. Simelane, “Effects of Grass and Concrete Reflective Surface on the Performance of Dual Axis Bifacial Solar PV Systems,” 2018 IEEE PES/IAS PowerAfrica. IEEE, Jun. 2018. doi: 10.1109/powerafrica.2018.8521143.

[283]: M. Chiodetti, J. Kang, C. Reise, and A. Lindsay, “Predicting Yields of Bifacial PV Power Plants – What Accuracy Is Possible?,” 35th European Photovoltaic Solar Energy Conference and Exhibition; 1623-1629, 2018, doi: 10.4229/35THEUPVSEC20182018-6CO.3.4.

[283]: M. Alam, M. S. Gul, and T. Muneer, “Performance analysis and comparison between bifacial and monofacial solar photovoltaic at various ground albedo conditions,” Renewable Energy Focus, vol. 44. Elsevier BV, pp. 295–316, Mar. 2023. doi: 10.1016/j.ref.2023.01.005.

[284]: K. Sugibuchi, N. Ishikawa, and S. Obara, “Bifacial-PV Power Output Gain in the Field Test Using ‘“EarthON”’ High Bifaciality Solar Cells,” 28th European Photovoltaic Solar Energy Conference and Exhibition; 4312-4317, 2013, doi: 10.4229/28THEUPVSEC2013-5BV.7.72

[285]: Kipp & Zonen. (2015). CMP10 Pyranometer [Datasheet]. Retrieved from https://www.kippzonen.com/Product/276/CMP10-Pyranometer#.ZFuD0XbMJjU

[286]: Campbell Scientific, Inc. (2021). CR1000X Measurement and Control Datalogger [Datasheet]. Retrieved from https://www.campbellsci.com/cr1000x